Compact RF wireless power transmission system for battery-free geolocation tags

Alassane Sidibé

Université Fédérale
Toulouse Midi-Pyrénées

THÈSE

En vue de l'obtention du

DOCTORAT DE L'UNIVERSITÉ DE TOULOUSE

Délivré par :

Université Toulouse 3 - Paul Sabatier (UT3 Paul Sabatier)

Présentée et soutenue par :

Alassane SIDIBE

le 20 Juin 2023

Titre :

Compact RF Wireless Power Transmission System for Battery-Free Geolocation Tags

---

École doctorale : **GEETS - Génie Electrique Electronique, Télécommunications et Santé : du système au nanosystème**

Spécialité : **Électromagnétisme et Systèmes Haute Fréquence**

Unité de recherche :

LAAS - Laboratoire d'Analyse et d'Architecture des Systèmes

Thèse dirigée par :

Dr. Alexandru TAKACS, UT3 Toulouse

Thèse co-encadrée par

M. Jan MENNEKENS, UWINLOC Toulouse

Jury :

Simon HEMOUR, Maître de conférences, Université de Bordeaux	Rapporteur
Tân-Phu VUONG, Professeur, Grenoble INP-Phelma, Grenoble	Rapporteur
Daniela DRAGOMIRESCU, Professeure, INSA Toulouse	Examinatrice
Robert STARAJ, Professeur, Université Côte d'Azur, Nice	Examinateur
Alexandru TAKACS, Maître de Conférence, Université Paul Sabatier Toulouse	Directeur de thèse
Jan MENNEKENS, CTO à UWINLOC, Toulouse	Co-encadrant
Eric CARIOU, CEO à UWINLOC, Toulouse	Invité

“ I have far more confidence in the one man who works mentally and bodily at a matter than in the six who merely talk about it.”

Michael Faraday

Remerciements

Cette thèse a pu être réalisée grâce à la collaboration CIFRE mis en place entre le Laboratoire d'Analyse et d'Architecture des Systèmes du CNRS (LAAS-CNRS) et la société Uwinloc à Toulouse. Je tiens avant tout à remercier le ministère de l'Enseignement Supérieur, de la Recherche et de l'Innovation (MESRI) ainsi que l'Association nationale de la recherche et de la technologie (ANRT) pour le financement et la gestion de cette collaboration CIFRE.

Je ne saurai jamais assez remercier mon directeur de thèse, Monsieur Alexandru TAKACS du LAAS-CNRS, pour m'avoir offert cette magnifique opportunité tant sur le plan académique et professionnelle. A mes débuts en France durant mon Master 1, il m'a accordé sa confiance et a eu l'amabilité de m'accueillir au sein de son équipe de recherche pour un stage de quelques semaines. De là, j'ai pu développer des compétences qui ont largement soutenu la progression de mon parcours universitaire. Une seconde intégration au sein de son équipe pour cette thèse, a confirmé sa bienveillance, sa patience et sa générosité. Toujours présent et à l'écoute, il m'a prodigué conseils et orientations tout au long de mes recherches. De plus, de nombreuses opportunités de participer à des conférences nationales et internationales m'ont été possible grâce à son soutien. Ces années de travail ont été empreintes de plaisir, et je lui en serai toujours reconnaissant.

Je tiens également à exprimer ma gratitude envers Monsieur Éric CARIOU, CEO à Uwinloc, pour m'avoir accordé sa confiance et m'avoir accueilli au sein de son entreprise. Sa sympathie et son sens d'écoute envers ses collaborateurs ont toujours été très appréciés. Mes remerciements s'étendent également aux personnes qui m'ont encadré et guidé à Uwinloc. Tout d'abord, je tiens à exprimer ma reconnaissance envers Monsieur Patrick CHAN, ancien directeur produit à Uwinloc, pour avoir facilité mon intégration au sein de l'entreprise et pour ses précieux conseils. J'aimerai également exprimer ma gratitude envers Monsieur Jan MENNEKENS, CTO et co-encadrant de thèse, qui a toujours été disponible lorsque j'avais besoin d'aide et qui a généreusement partagé ses vastes connaissances scientifiques et techniques. Merci également à Bruno FRANCISCATTO, qui m'a encadré pendant une période importante de cette thèse. Un grand merci à René STOLL, doté d'une expertise remarquable, pour son accompagnement et son humilité. Il a été un binôme pour moi au sein de l'entreprise, et nos échanges enrichissants sur les aspects techniques relatif aux antennes et au fonctionnement des certains outils ont été inestimables. Mes remerciements s'adressent également aux autres collaborateurs de Uwinloc qui ont fait partie de cette belle aventure.

Je remercie également les partenaires des différents projets auxquels j'ai participé. Leur solide expertise a été mise en avant pour garantir le bon déroulement des activités. Je tiens particulièrement à mentionner Laura López MIR de Eurecat Centre Tecnològic en Catalogne, qui a fourni un effort considérable et a toujours été présente pour me guider dans la gestion du projet Madras. Grâce aux nombreux échanges techniques avec elle, j'ai pu développer d'autres compétences et à me familiariser à certains processus de fabrication pour l'impression de l'électronique flexible.

Mes pensées s'orientent également à mes collègues au sein du laboratoire. L'atmosphère conviviale et l'esprit d'équipe au sein de l'équipe MINC m'ont permis m'épanouir pleinement dans mon travail. Je tiens à exprimer ma gratitude envers Abderrahim OKBA, ancien doctorant de l'équipe, pour ses conseils précieux et son accompagnement à l'utilisation des logiciels de simulation et à la participation certaines campagnes de mesure à mes débuts. Gaël LOUBET, un collègue d'une grande rigueur et ponctualité dans son travail, je tiens à le remercier pour sa contribution déterminante à l'aboutissement de certains travaux.

Mon appréciation va également à Mohammed ABO KASSEM, qui a fourni un travail remarquable dans la conception de cartes électroniques et la conduite de campagnes de mesures. Un grand merci est également dû aux stagiaires qui ont grandement contribué à la progression de mes travaux. Mes pensées vont également aux autres doctorants que j'ai eu le plaisir de côtoyer au laboratoire, pour leur amitié et les bons moments que nous avons partagés. Un remerciement à Samuel CHARLOT pour son appui technique et pour m'avoir rendu possible les fabrications en salle blanche sur substrat flexible.

Je ne peux pas clore sans exprimer ma gratitude envers Allah, le Créateur, le tout Puissant, le Miséricordieux, le Guide sans qui rien ne serait possible. Enfin, un merci tout particulier s'adresse à ma famille qui réside à Dakar. J'éprouve une profonde reconnaissance envers ma mère, Nanténin SIDIBE, et à mon père, Adama SIDIBE, pour m'avoir donné la vie, m'avoir éduqué en m'inculquant des valeurs solides et avoir pris soin de moi depuis ma naissance. Je leur dois ma réussite. Merci à tous mes frères et sœurs qui ont été un soutien indéfectible tout au long de ces années.

Système Compact de Télé-alimentation par Ondes RF pour des Étiquettes Géolocalisables et Autonomes en Énergie

Résumé:

L'expansion considérable des systèmes électroniques dans un monde de plus en plus connecté a entrainé un besoin permanent d'énergie pour un fonctionnement en continu, sans nécessiter d'interruptions fréquentes pour la recharge ou le remplacement de batterie. De plus, les objets connectés intègrent davantage de fonctionnalités qui nécessitent une consommation d'énergie croissante. Ainsi, l'autonomie en énergie est devenue un enjeu majeur pour de nombreux systèmes électroniques. Cette limitation de la durée de fonctionnement peut être résolue grâce à des approches alternatives d'alimentation qui ne dépendent pas des batteries conventionnelles. Ce qui pousse au développement des dispositifs sans batterie. Par ailleurs, l'émergence de nouvelles technologies et de nouveaux secteurs d'activité pour les objets connectés tels que le textile, le médical, l'industrie 4.0, le transport et les chaînes de distribution, incite à la miniaturisation et à l'adaptabilité géométrique de ces systèmes afin de pouvoir s'intégrer et fonctionner efficacement dans des environnements variés et complexes. Ainsi, l'usage et le développement de matériaux non conventionnelles tels que les matériaux flexibles, organiques et biodégradables sont souvent privilégiés pour faciliter l'intégration des dispositifs électroniques.

Cette thèse s'inscrit dans le cadre d'une collaboration CIFRE entre le LAAS-CNRS et la société UWINLOC. Grâce à son expertise, la société a développé une solution de géolocalisation dédiée à l'identification et à la traçabilité des actifs au sein d'une zone industrielle de type entrepôt de stockage. Cette solution permet une meilleure gestion des flux de production et une optimisation de l'inventaire des objets. Elle se distingue des autres solutions de traçabilité, par le fonctionnement de son étiquette géolocalisable sans batterie, et par sa précision de localisation atteignant l'ordre du centimètre grâce à la technologie Ultra-Wide Band (UWB). L'alimentation de l'étiquette géolocalisable est assurée par la technique de télé-alimentation via les ondes électromagnétiques ou de collecte d'énergie radiofréquence (RF) au travers d'une source émettrice dédiée. La société vise à réduire la taille de ses étiquettes géolocalisables et à cibler d'autres secteurs d'activités tels que le commerce de détail, la santé en produisant une version d'étiquette flexible, robuste et bas coût. Pour relever les défis scientifiques et industriels, la thèse porte sur un système compact de télé-alimentation par ondes RF pour des étiquettes géolocalisables et autonomes en énergie.

L'objectif de la thèse est d'une part, de miniaturiser et d'intégrer de manière optimale les antennes dédiées à la télé-alimentation, et d'autres part d'optimisation les performances radiofréquences du système. Pour cela, il a été nécessaire de se familiariser, voir en revue les types de dispositifs sans batterie, la technique de récupération d'énergie (RF), les typologies de circuit redresseur (pour la conversion d'un signal RF en courant continu).

Une partie des travaux de recherche a été dédiée aux activités de recherche au sein du laboratoire sur les aspects de télé-alimentation par ondes RF et sur les réseaux de capteurs sans fils. Nous avons donc étudié et conçu un circuit de récupération d'énergie RF communément appelé rectenna (association d'antenne et de redresseur), optimisé pour un fonctionnement dans la bande ISM 868 MHz à des faibles densités de puissance. Cette rectenna satisfait les exigences en termes de compacité car elle est considérée comme électriquement petite. Elle offre de bonnes performances en termes d' efficacité de conversion à des faibles niveaux de puissance, et présente un coût de fabrication réduit grâce l'utilisation de substrats et composants du commerce. Elle a ensuite été utilisée pour l'alimentation des réseaux de capteurs sans fil dédiés au suivi de l'état de santé du béton

(mesure des paramètres de température et d'humidité de la structure du béton) utilisant les technologies de communication LoRaWAN ou Bluetooth Low Energy (BLE). La compacité et la consommation en énergie des réseaux de capteurs ont été prises en compte afin de faciliter l'intégration et d'assurer un fonctionnement à longue portée. Nous avons pu valider, à travers de cette étude, la faisabilité de récupérer l'énergie et de faire fonctionner des nœuds de capteurs sans fils embarqués dans un environnement contraignant tel qu'à l'intérieur d'une cavité d'une structure en béton armé.

La seconde partie des travaux est consacrée à la problématique de la thèse en rapport avec l'entreprise UWINLOC, autour de l'étiquette géolocalisable et autonome en énergie. A travers le projet Européen SMARTEES, nous avons d'abord acquis un large savoir-faire dans le processus de développement de l'étiquette sur un substrat flexible. En effet pour faciliter cette pré-étude, nous avons uniquement étudié l'étage de récupération d'énergie de l'étiquette. Plusieurs prototypes d'antenne, de redresseur et de rectenna ont été conçu sur un substrat flexible approprié de type PET à base de matériau polymère, pour le développement de l'étiquette géolocalisable. La caractérisation préalable des propriétés diélectriques du substrat a été nécessaire afin de garantir la fiabilité des résultats de simulation et de mesure. Les résultats ont été satisfaisants et nous avons pu garantir un fonctionnement de l'étiquette associée à la rectenna en PET, comparable à l'étiquette de UWINLOC sur un substrat rigide. La problématique de la miniaturisation des antennes de l'étiquette a été étudié à travers des techniques de miniaturisation sans dégrader significativement l'efficacité de rayonnement. D'une part, le choix d'un substrat rigide présentant des propriétés diélectriques intéressantes, nous a permis d'avoir un degré de liberté sur la conception des antennes plus petites en sacrifiant légèrement les performances. D'autre part, l'utilisation de techniques de fabrication avancées sur du substrat flexible a permis d'obtenir des antennes de dimensions plus importantes tout en maintenant une meilleure efficacité, pouvant ainsi être pliées jusqu'au demi ou au tiers de la taille normale à plat. La comparaison des résultats expérimentaux des deux solutions nous ont permis de cerner leurs limites et de conclure sur la solution la plus viable pour la miniaturisation. Dans la même perspective de développer des étiquettes flexibles à bas coût, d'autres travaux ont été possible grâce au projet MADRAS. Ce projet a pour objectif, le développement de matériaux innovants pour de l'électronique flexible. Dans cette thèse, nous avons abordé la conception des deux antennes (pour la télé-alimentation et pour la transmission du signal UWB) de l'étiquette sur différents types de matériaux en tenant compte des différentes contraintes liées à la dimension, la robustesse et aux performances souhaitées. Plusieurs expérimentations ont été réalisées, ce qui nous a permis d'aboutir à une version finale de l'étiquette flexible et compacte avec des résultats satisfaisants.

Compact RF Wireless Power Transmission System for Battery-free Geolocation Tags

Abstract:

The significant growth of electronic systems in an increasingly connected world has led to a constant need for energy to enable continuous operation without frequent interruptions for battery recharging and replacement. Moreover, Internet of things (IoT) objects embed more functionalities that require increasing power consumption. As a result, energy autonomy has become a major concern for many electronic systems. The limitation of the life span can be addressed through alternative power supply approaches that do not rely on conventional batteries, leading to the emergence of battery-free devices. Additionally, the emergence of modern technologies and sectors for IoT objects, such as textiles, medical applications, Industry 4.0, transportation and retail and transport) calls for the miniaturization and conformability of these systems to effectively be integrated and operate in various and complex environments. Therefore, the use and development of unconventional materials, such as flexible, organic and bio-degradable materials, are often favored to facilitate the integration of electronic devices.

This thesis is part of a CIFRE collaboration between the LAAS-CNRS and UWINLOC company. UWINLOC has developed a geolocation solution dedicated to asset tracking and identification in an industrial area, such as a storage warehouse. This solution enables better production flow management and optimized inventory of objects. The developed solution distinguishes itself from other tracking solutions, thanks to the battery-free operation of the geolocation tag and achieving a high localization accuracy around few centimeters thanks to the Ultra-Wide Band technology (UWB). The geolocation tag is remotely powered thanks to wireless power transmission (WPT) technique via a dedicated RF power transmitter. The company aims to reduce the size of its geolocation tag and target other sectors such as retail and healthcare by developing a flexible, robust, and low-cost version of the tag. To address scientific and industrial challenges, the thesis focuses on a compact RF wireless power transmission system for battery-free geolocation tags.

The purpose of this thesis is, on one hand, the miniaturization and the optimal integration of the antennas dedicated for the RF energy harvesting and on the other hand, the optimization of RF-to-DC conversion efficiency. Thus, a study of the state of art on battery-free devices, RF energy harvesting or WPT techniques, different antenna types, and rectifier circuits (for RF-to-DC converter).

A part of this thesis was dedicated to the laboratory-based research activities on RF energy harvesting and wireless sensor networks. Therefore, we have studied and designed an RF energy harvesting circuit commonly known as a rectenna (combination of an antenna and a rectifier circuit), optimized for operation in the 868 MHz ISM frequency band at low power densities level. The proposed rectenna meets the requirements for compactness as it is considered electrically small. It offers good power conversion efficiency at low power levels and does not require an expensive and complex manufacturing process The prototype was then used to supply Wireless Sensor Nodes (WSN) dedicated for Structural Health Monitoring (SHM) applications. The WSN must measure the physical parameters of the concrete structure (temperature, humidity and resistivity) and transmit the data using LoRaWAN or Bluetooth Low Energy (BLE) communication technologies. The compactness and energy consumption of the WSN were considered to facilitate the integration and ensure long-range operation. This work enabled us to implement a proof a concept and demonstrate the feasibility of harvesting energy and transmitting data from the WSN embedded in harsh environments such as into a concrete cavity.

In addition, other activities focused on the design of antennas and rectennas working at several frequencies (dedicated to BLE and Wi-Fi applications), to maximize the harvested power, and prototyped on flexible materials such as polyimide (Kapton) to target applications requiring device conformability.

The second part of the work addresses the main topic of this thesis related to UWINLOC company, focusing on the development of a battery-free geolocation tag. Through the European project SMARTEES, the objective was to acquire crucial knowledge with regard to the development of the flexible geolocation tag. Thus, it was decided that the studies carried out were to be concentrated solely on the energy harvesting technology of the tag. Several prototypes of antennas, rectifiers, and rectennas were designed on a selected flexible substrate, a PET-based polymer material. Prior characterization of the dielectric properties of the substrate was necessary to ensure reliable simulation and measurement results. The obtained results were satisfactory, and we were able to ensure the functionality of the geolocation tag associated with a prototyped PET-based rectenna, comparable to the current version of the tag on a rigid substrate. The challenge of miniaturizing the antennas of the tag was addressed through miniaturization techniques without significant degradation of the radiation efficiency. On one hand, the choice of a rigid substrate with interesting dielectric properties (lower loss tangent) allowed us to slightly sacrifice antenna performances for a reduction of the overall size. On the other hand, the use of advanced manufacturing techniques on flexible materials enabled the design of larger antennas while maintaining better efficiency and allowing them to be folded to half or one-third of their initial flat size. The comparison of experimental results between the two proposed solutions helped us identify their limitations and conclude on the most suitable solution for the antenna miniaturization. In the frame of developing low-cost flexible tag, further work was performed through the MADRAS project. This project aims to develop innovative and advanced materials for flexible electronics. In this thesis, we addressed the design of the two antennas of the tag on several types of materials, considering the requirements related to size, robustness, and targeted performance. Several experiments were conducted, leading to a definitive full version of the flexible and compact geolocation tag with satisfactory results.

Acronyms

AC	Alternative Current
Ag	Silver
AJWG	Arjowiggins
BLE	Bluetooth Low Energy
CPW	Coplanar-Waveguide
CPWG	Coplanar-Waveguide Grounded
CW	Continuous Wave
DC	Direct Current
EH	Energy Harvesting
EIRP	Effective Isotropic Radiated Power
EM	Electromagnetic
ESA	Electrically Small Antenna
EUT	Eurecat
FCC	Federal Communications Commission
FF	Far-Field
FF-WPT	Far-Field Wireless Power Transmission
FR4	Flame Retardant 4
GNK	Genesink
GS	Ground-Signal
GSG	Ground Signal Ground
HB	Harmonic Balance
Ic	Integrated circuit
IFA	Inverted F-Antenna
IME	In-Mold Electronic
IoT	Internet of Things
ISM	Industrial Scientific Medical
McBIM	Material communicating with the Building Information Modelling
MPPT	Maximum Power Point Tracking
NCF	Nanocellulose Foil
NFC	Near-Field Communication
NP	Nano-Particle
NW	Nano-Wire
OOK	On Off Keying
OLAE	Organic and Large Area Electronics
PCB	Printed Circuit Board
PCE	Power Conversion Efficiency
PEC	Perfect Electric Conductor
PET	Polyethylene Terephthalat
PMIC	Power Management Integrated Circuit
PMU	Power Management Unit
PU	Poly-Urethane
PVDC	Poly-Vinylidene Chloride
RF	Radio Frequency
RFEH	Radiofrequency Energy Harvesting
RFID	Radio Frequency Identification
SHM	Structural Health Monitoring
SMD	Surface Mount Device

SoC	System On Chip
UHF	Ultra-High Frequency
UGM	Uwinloc Geolocation Module
UTAG	Uwinloc Tag
UWB	Ultra-Wide Band
UWL	Uwinloc
TPU	Thermoplastic Polyurethane
VNA	Vector Network Analyser
WP	Work Package
WPT	Wireless Power Transmission
WuRx	Wake-up Receiver

Table of contents

List of figures

List of tables

Preamble

This thesis started in February 2019, was established thanks to a CIFRE funding, involving the UWINLOC Company and the LAAS-CNRS laboratory in Toulouse. UWINLOC (UWL) is a French company specialized in the design, production and marketing of an industrial geolocation system able of continuously identifying and locating a large volumes of assets in both indoor and outdoor environments. The UWL system comprises a low cost, robust, and reliable battery-free geolocation tags, beacons for Wireless Power Transmission (WPT) and reception of Ultra-Wide Band (UWB) signals from tags, and server for calculations and 3D visualization. The developed solution stands out from others available on the market due to its low cost, low weight, battery-free operation, and localization accuracy enable by UWB technology.

Faced with the rapid growth of wireless systems and the numerous technological challenges, the company had to upgrade its technology through this specific collaboration with the laboratory. Among the major technological challenges, we can note: the integration for electronic devices with increasingly advanced features, the miniaturization required for portability and space-saving, limited energy autonomy due to conventional battery usage, manufacturing costs and reliability according to environmental conditions. In scientific research, the field of Radiofrequency Energy Harvesting (RFEH) or WPT, is also constantly evolving to provide an alternative to battery-dependent power supply techniques. Works in this field are mainly focused on indoor environments for low power electronic devices in the absence of other energy sources, such as solar. The aim of this thesis is to address the company technological and economical challenges through the study of a compact RF wireless power transmission for battery-free geolocation tags.

The objectives of the thesis are driven by both the needs of the company for the development of a competitive geolocation tag and the laboratory's research topics focused on powering battery-free wireless devices for Structural Health Monitoring (SHM) in harsh environments. The objectives involve proposing a battery-free Wireless Sensing Node (WSN) wirelessly powered by a rectenna (a combination of antenna and rectifier circuit) in order to monitor physical parameters of a concrete structure. Since they have to be embedded in harsh environments, the rectenna must exhibit high efficiency for low RF power levels while maintaining a compact size. For UWL requirements, the current size and the format of the geolocation tag, measuring 70 mm x 50 mm x 10 mm, often pose constraints in use-cases that require smaller and/or conformable devices to match the shape of the objects to be located. Another improvement sought is to maximize the operating distance of the tag from the RF energy source, which depends on the transmission channel and the RF-to-DC power conversion efficiency of the tag. Therefore, the objective of the thesis is to propose a miniaturization solution for the geolocation tag by reducing the antenna size, optimizing the integration of its antennas with electronic parts, and the overall enhancing of the system's radio performance. To fulfill this purpose, this manuscript presents different chapters that provide the global work carried out during the research activities.

Chapter 1: Introduction

It highlights a detailed state of the art around the activities carried out during these years of research: A global review will be proposed around the battery-free devices in order to better target the needs. Different existing Energy Harvesting (EH) techniques will be presented with particular emphasis on RFEH and WPT. The origin, functioning principles, and various solutions developed in these fields will be discussed.

Chapter 2: Compact Rectenna for Wireless Sensing Applications.

This chapter focused on the development of compact rectennas for wireless devices. We proposed a highly efficient and miniaturized rectenna operating at 868 MHz. Firstly, the topology of the rectifier stage will be presented, followed by a comparative study of Schottky diodes. Subsequently, two electrically small antennas will be designed and characterized for the integration with the rectifier circuit. The advanced performance of the proposed rectenna was demonstrated through a comparison with other rectennas in the state-of-the-art operating at the same frequency to conclude on the added value of our proposition. This rectenna is intended to power supply wireless sensor nodes embedded in harsh environment. This study will be presented in the next chapter.

Chapter 3: Battery-free Wireless Sensing Node for Structural Health Monitoring Applications.

This chapter discusses the work done to wirelessly power sensing nodes based on Bluetooth Low Energy or LoRaWAN wireless communication technology. The purpose of this work, which is a part of another thesis, is to design a « communicating material », embedding WSN which monitor the physical parameters of the structure. The WSN was designed to be compact and low power and able to achieve long range communication. Its architecture and operating mode will be presented. To ensure the operation of the WSN embedded into concrete cavities, techniques for maximizing the harvested DC power have been investigated. Experimental results will be presented through wireless power transmission thanks to the highly efficient and compact rectenna developed in chapter 3. We will subsequently conclude on the feasibility of wireless power transfer through concrete and the ability to transmit and receive data. A part of this chapter will be focused on the design and implementation of the first existing tag combining the UWB and BLE technology for harsh environments.

Chapter 4: Development of an UHF Energy Harvesting Front-end for the Flexible Geolocation Tag.

European projects have facilitated the development of the future geolocation tag. The works during this thesis also contributed to the FLexUtag project of Smartees, funded by the European Union Hoziron 2020 research and innovation programme under grant number 761496. The objectives of the project were to design the first prototype of the flexible geolocation tag based on the current rigid tag developed by UWL, with a focus on miniaturization, low-cost manufacturing processes, and target new potential markets. The entire design and integration on a flexible material is focused on the EH part of the tag. Thus, the tasks were divided into 3 parts:

- To ensure proper functioning of the tag, the first phase involved defining the specifications and selecting the appropriate polymer-based flexible material. The chosen material need to exhibit interesting RF performance as well as being suitable for a simple and cost-effective manufacturing process.
- The second step focused on the characterization and prototyping of the samples. The dielectric properties of the materials was carefully measured prior to design the antennas and rectifier circuits for the validation.
- The final phase consisted of gathering the knowledge acquired in the previous phases to design a conclusive prototype of rectenna on a flexible substrate, and to evaluate its performance through its integration on the electronic part of the rigid tag.

Chapter 5: Miniaturization of the Antennas for the Geolocation Tag

This part will present the different steps that enable the miniaturization of the geolocation tag. The electronic part of the tag has already been reduced on a small module by UWL, so the miniaturization efforts will focus on the antennas dedicated to the EH and UWB features. Three solutions were proposed. The first approach was focused on reducing the size of antennas based on a rigid substrate. A second approach involved modifying the tag's geometry using a semi-flexible substrate to achieve an overall size reduction when it is bent. The design and characterization of the new antennas to facilitate the curvature of the tag will be presented in this chapter. The third approach was about switching to the same design on a full flexible material. The results of these flexible prototype will also be presented. Finally, a comparison of all prototypes will allow for a discussion on the advantages and drawbacks of each approach, and leading to conclusions regarding the technological and economic progress compared to the current UWL tag.

Chapter 6: Development of a flexible battery-free geolocation tag based on advanced materials.

The development of a compact and low-cost tag for UWL purposes was carried out through the Madras project. funded by the EU Horizon 2020 program under grant agreement No. 862492. The objectives of this project are, to develop new advanced materials and improved manufacturing processes for large-scale production for Organic and Large Area Electronics (ELOA) devices. UWL is a project partner and is the end user of the geolocation flexible tag demonstrator. Unlike in chapter 4, this flexible tag was completely integrated (UHF and UWB antennas) on a flexible substrate with innovative materials. The specifications will be presented, followed by a discussion on the materials developed by the partners involved. A first antenna for EH features designed to validate the properties of the developed materials, will be presented . A second phase was focused on both antennas design (EH and UWB) including the over-moulding step. The performance and the effect of plastic used for injecting molding on the performance will be analyzed.The final phase involved the development of the entire flexible geolocation tag after several studies. The different choices made in the selection of used materials and proposed antenna designs to ensure satisfactory performance and rigidity of the tag will be presented.

Appendix: Exploitation of flexible Polyimide based material for antenna and rectenna design.

In appendix is dedicated to the work on the development of antennas and rectenna on flexible substrate-based Polyimide material. The results have been presented in two conference papers which will be provided in this chapter.

I. General Introduction

In this first chapter of the manuscript, we will address the problematic of the energy autonomy of the advanced wireless devices faced to the technological advances in our daily lives. This technological challenge of new wireless electronic devices can be overcome through energy harvesting techniques. The operating principle and the opportunities of each of them will be briefly presented. Since, this thesis focuses on the energy autonomy aspect of the geolocation tags, we will present before the different topologies of existing battery-free devices while highlighting the intended application, and the operating mode. These various aspects will finally lead us to introduce the topic of RF energy harvesting or wireless power transmission, which is more specifically related to this research work.

1. Battery-less devices : Trends, challenges and Opportunities

Over the course of the 21st century, our daily lives have been significantly improved by new technologies and the development of smart electronics devices. Autonomous vehicles, drones, 3D printing machines and electric transportation such as trains, buses, bikes, and cars, have contributed to the advancement. Simultaneously, the Internet is considered as the greatest progress of the century, offering numerous opportunities through artificial intelligence, big data, social networks, ease of communication and information sharing and/or events, and access to remote services such as digital libraries, online booking services, e-commerce, and transactions. The convergence of the internet and new technologies gave rise to the Internet of Things (IoT). The first IoT object is attributed to a simple Coke machine developed by David Nichols and his colleagues from Carnegie Mellon University in the early 1980s. Its invention was based on several micro-switches connected to the Internet to make an inventory of drinks and also check the freshness of them [1]. Since then, a large number of IoT objects have flooded our daily lives and become an emerging paradigm that simplifies, enhance comfort, and improve security our life [2]–[4]. According to the study conducted by IoT analytics, the number of IoT objects is estimated to exceed 17 billion by 2023, representing almost a 40% increase since 2020. As a result, the rapid evolution of wireless electronic devices push us to focus on sustainability and energy autonomy. The continuous innovation of electronic devices leads us to a heavy reliance on battery power for uninterrupted long-term operation. This energy source has major consequences such as:

- The size of batteries is a constraint for the miniaturizing IoT devices. A lot of research has already been conducted to develop micro-batteries for IoT applications [5], [6]. The use of conventional batteries can also be disadvantageous for textile, wearable and flexible electronics applications. The weight of such devices is a parameter that is no longer negligible for portability and user comfort. Nevertheless Technological advances on flexible battery based on organic materials are in progress [7]–[10].
- Battery operation also requires frequent manual replacement, resulting to a significant maintenance cost.

- The environmental impact of batteries has become increasingly unfavorable with the growing number of deployed IoT objects. Alternatives in this area are also being researched, such as disposable paper batteries. The batteries aim to reduce the environmental impact of single-use electronics for applications such as point-of-care diagnosis, smart packaging, and environmental sensing [11].
- Reliability is critical in certain applications. When a battery reaches the end of its lifespan, it can lead to the shutdown of devices, including associated sensors or transmitters/receivers, resulting in data loss and/or communication interruptions.

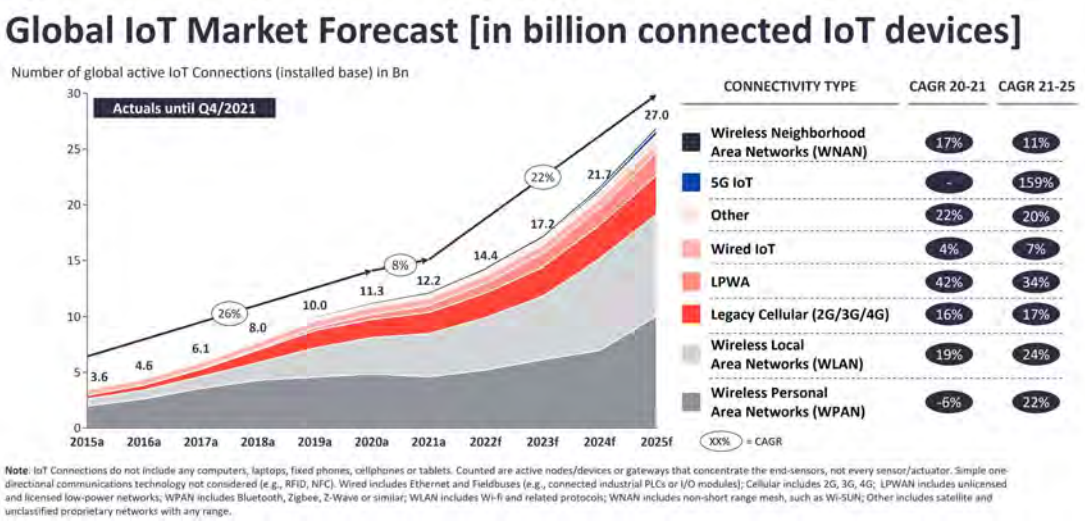

Figure I.1. State of number of connected IoT devices from IoT Analytics Research 2022 [3].

As a result, it is obvious that battery-free operation of IoT devices and more generally wireless electronic devices can overcome the numerous disadvantages mentioned earlier. The concept of battery-devices refers to the capability of electronic devices to operate using alternative energy sources, independently of the batteries as a primary power source. Indeed, those alternative energy sources enables the devices to harvest sufficient energy for its operation.

1.1. Energy harvesting techniques for battery-less devices

With the enormous democratization of the use of connected and communicating objects for long-term applications, conventional methods of energy supply are revealing their limitations. Researchers and engineers are faced with the challenges of reducing the energy dependence of smart devices. To address this issue in an increasingly environmentally friendly society, the development of battery-free or battery-less devices require the implementation of energy harvesting (EH) techniques. Ambient EH is a viable solution for long term-operation mainly by means of a transducer for low power electronic devices. EH technologies have also demonstrated their relevance for next generation portable and wearable systems such as electronic skin [12]. The most common sources of ambient energy include thermal, mechanical, solar, and radio frequency [13].

- Solar energy is widely used as an energy source for self-powered systems due to its abundance in the environment. It is obtained through solar cells, electronic devices that convert sunlight energy into electricity. Sustainable solar powered battery-free sensing systems and IoT devices are proposed in the literature [14]–[16]. However, the availability of solar power is unpredictable and depends on factors such as climate, solar panel size and orientation, and the time of day and season.

- Thermal energy is an alternative to solar energy for powering wireless sensors, as shown in [17], [18]. This approach involves converting temperature gradients into electrical power using a thermoelectric generator (TEG) based on the Seebeck effect [19]. However, the power conversion efficiency of this method is limited.
- Piezoelectric energy harvesting utilizes mechanical deformation to generate electrical energy and has gained interest in portable and healthcare applications. [20], [21].
- RF energy harvesting is a promising solution for indoor applications. Electronic devices can be powered by harvesting RF waves from the environment, either from existing wireless communication transmitter (with a risk of capturing a very weak signal) or from specific energy sources that can focus radio waves directly onto the harvester device. This technique involves capturing electromagnetic waves using an antenna and converting them into DC power through an RF-to-DC conversion circuit to power supply active circuits. With the proliferation of wireless technologies operating in different frequency bands, the power density of ambient RF power has thus increased (depending on location). More details on RFEH technique will be provided later in this discussion.

However, key questions arise about the viability of such an EH solutions for long-term operation.

How much renewable power density is available in the surrounding environment ?

Answering these questions involves evaluating the power density of the available ambient energy sources and evaluating the power consumption of the target device. Due to fluctuation of the amount of ambient energy available, which depends on several factors such as climatic conditions, geographical position, duration of exposure, the harvested power is generally variable. As a result, it rarely reaches the power threshold required for operating active electronic components in battery-free devices. Table I.1 summarizes the state of the art of ambient energy source, indicating their equivalent power density level and harvested DC power. Solar energy is the most abundant energy source, while radiofrequency exhibits the lowest available power density.

Table I.1. Ambient energy harvesting sources and their corresponding power densities and harvested dc voltage [22].

Energy Source	Ambient Environment	Device	Power density	Harvested DC power
Ambient Light	Indoor Outdoor	Solar Cell	mW/cm² 100 mW/cm²	10 µW/cm² 10 mW/cm²
Vibration/ Motion	Human	Piezoelectric Electrostatic	0.5 m at 1 Hz 1 m/s² at 50 Hz	4 µW/cm²
	Industry	Piezoelectric Electromagnetic	1 m at 5 Hz 10 m/s² at 1 kHz	100 µW/cm²
Thermal	Human Industry	Thermoelectric	20 mW/cm² 100 mW/cm²	30 µW/cm² 1-10 mW/cm²
Radiofrequency	GSM 900 MHz Wi-Fi	Antenna	µW/cm² 0.015 µW/cm²	0.1 µW/cm² 0.001 µW/cm²

Among these techniques, our work will focus on the functioning of battery-less devices through harvesting electromagnetic waves. Several studies has measured the power level of radio waves as Wi-Fi, Bluetooth and cellular communication waves and evaluated the energy potential in a specific location. For example, in the core Montreal city, outdoor dynamic measurement of ambient RF power density were conducted, covering a frequency range of 400-2700 MHz. These measurements yielded a low power level below -35 dBm with a broadband omnidirectional antenna (N6850A) [23]. The overall RF power density was found to be below 1 µW/cm² [23], [24]. By employing a harvesting circuit network, it become possible to harvest a few microwatts of power over several frequency bands [25], [26]. In most cases, as seen in Table I.1 the amount of harvested energy is so low that it is impossible to power active circuits.

1.2. Trends for developed battery-free devices

With the increased use of IoT applications and advancements in wireless communication technologies, devices must operate continuously without interruption due to a lack of energy for the power supply. The use of battery-free devices is becoming increasingly necessary as we seek ways to power the growing number of devices in our daily lives. Battery-free devices can significantly reduce production and marketing costs and provide the opportunity for use in areas with difficult access to avoid maintenance. However, energy consumption is a key parameter for designing reliable battery-free devices. The power consumption depends on the number of features to ensure by the device, and in the case of battery-free wireless, the data transmission require a specific transceiver (resulting in additional energy consumption depending on the technology used, such as Bluetooth, Wi-Fi, LoRa, Zigbee, etc.). Moreover, the solution becomes more complex when transmitting confidential data that require encryption techniques (which also cost more energy). Apart from energy harvesting, it is possible to extend the battery lifespan by using low-power active components and reducing the overall power consumption through the duty cycling approach. The duty cycling method enables the deep sleep mode of the wireless devices. In this state, the active components are turned off and consume only a few nanoamps until they wake up after a programmed timeout. This approach has been implemented as a Wake-up Receiver (WuRx) through an RF envelope detector to listen for On-OFF Keying (OOK) modulated signals while the main transceiver remains in standby mode [27]. Nowadays, this method is better known as deep-sleep or wake-up mode in IoT communication modules that enable energy harvesting techniques. In this state, all nodes in the circuit are deeply turned off and discharged as soon as the harvested voltage reaches the cold start activation voltage, enabling them to enter in normal operating mode. This functionality is implemented in Texas Instrument and E-Peas Power Management Integrated Circuit (PMIC) state machine [28], [29].

Overall, we can distinguish two categories of battery-free electronic devices:

- The first category includes devices that operate by directly harvesting enough energy for their operation and do not require an energy storage element such as supercapacitor. In this category we can mention passive Radio Frequency Identification (RFID) tags. These tags consist of a single antenna and a low-power chip called RFID chip which simply harvest the transmitted signal from the reader and then transmit back an identification signal to the reader. Passive RFID tags are commonly used in applications such as access control, inventory management, supply chain management, asset and equipment tracking, tool gate system, contactless payment. Nowadays, RFID tags are equipped with sensors to detect environmental changes for multiple purposes.

For instance, a passive RFID temperature sensor has been developed to monitor the temperature of the surrounding environment of perishable foods, such as food and drugs, in the cold supply chain [30].

In the medical field, researches have led to the development of an epidermal RFID tag that allows reliable monitoring of human body temperature [31]. With the development of IoT Smart Home applications, RFID Sensor battery solutions have been proposed to enable the reading of environmental conditions from distances of up to 7.9 m from the reader [32].

- The other category of battery-less devices has a more complex architecture to ensure diverse and advanced features, and they require boosting the harvested power for their operation. These devices often require the use of several antennas for transmission and reception and consume more power. Two components that have greatly facilitated the development of this category of battery-less devices are the supercapacitor and Power Management Unit (PMU), also known as Power Management Integrated Circuit (PMIC). Supercapacitor unlike standard batteries, have a fast charging and discharging time, an unlimited loads cycles of which can be cycled several times over several months. They also have a wide operating temperature range and are relatively small and lightweight. The role of PMU is to manage the flow of power between the harvester and the storage element in order to supply a stable voltage to the load according to the requirements. The power management solution incorporates various features to optimize the energy transfer from the harvester to the active components. These include Maximum Power Point Tracking (MPPT) feature to maximize the energy transfer from the harvester to the supercapacitor, a booster or DC-DC convertor to step up the input voltage, and as well as cold-start procedure to ensure functionality even with an empty energy supercapacitor.

  Thanks to the availability of efficient supercapacitor and ultra-low power PMU, various battery-free devices enabling wireless communication capabilities have emerged [33]–[35]. One notable example is the design of a battery-free cell phone by researchers from the University of Washington. This innovative device operates by harvesting RF signal and consumes only a few microwatts of power. It support real-time sense of speech, actuation of earphones and switch between uplink and downlink communications [36]. In response to the pandemic situation, researches on battery-free devices enable the development of a battery-free temperature monitoring device that can be fitted inside the ear for an accurate body temperature measurement of a subject Wireless battery-free body sensing device [37]. For short-range communication such as Near Field Communication (NFC), a battery-less soil moisture measurement system has been proposed. It is powered by the magnetic field generated by the reader and uses a dynamic NFC/RFID integrated circuit with energy harvesting capabilities [38]. To maximize harvested DC power and capture almost any incoming field of any polarization, an orientation-independent UHF battery-less tag has been developed [39], [40]. It embeds an energy efficient pulse generator in the 3-5 GHz UWB band and can be wirelessly power up to a distance of 12 m using a 2 W Effective Radiated Power (ERP) source in the UHF 865-868 MHz band.

Apart from energy autonomy, the aspect of miniaturization is a challenge for several applications. As mentioned earlier, battery size can be bulky for applications such as wearable, textile and medical applications. Thus, advancements in wireless power transmission and energy harvesting technologies can help to reduce the overall size and weight of battery-free devices.

Wireless devices operates using an antenna, which often occupy a larger or smaller area depending on the operating frequency and desired performance, particularly in terms of radiation efficiency. For RF energy harvesting, the antenna efficiency is a critical parameter due to the low power density available. The use of flexible material allows for greater flexibility and versatility in incorporating IoT devices in a wide variety of products. We will now discuss the concepts of wireless energy transfer and RF energy harvesting, which are relevant to the topic of this thesis.

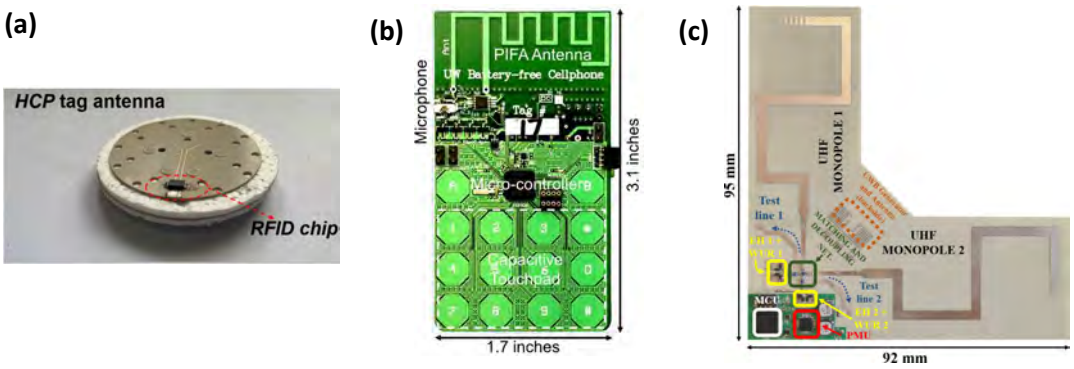

Figure I.2. Examples of developed wireless battery-free devices in the state of the art : (a) Miniaturized and Highly Sensitive Epidermal RFID Sensor for Reliable Skin Temperature Monitoring [32]; (b) First battery-free cellphone from Washington University [36]; (c) Dual-monopole UHF/UWB battery-less tag [39].

2. Far-Field Wireless Power transmission (FF-WPT) and RF Energy Harvesting (EH)

The concept of wireless power transmission (WPT) was born with the ambition of eliminating the use of cables and transmitting electricity wirelessly through the air [41]. It allows the distribution of electrical energy from one device (the transmitter) to another (the receiver) without the requirement of any physical support such as cables. It's important to note that while energy harvesting is often associated to far field wireless power transmission, it is a separate concept. Energy harvesting refers the process of capturing and converting the energy at the receiver level to generate Direct Current (DC) for power supply. Depending on the distance between the transmitter and receiver, and also the frequency, various methods of WPT can be employed, which can be classified into two main categories : Near Field WPT and Far-Field WPT.

- Near-Field (NF) WPT is a technique used for short-range power transmission over few centimeters. It employs methods such as magnetic resonance, electromagnetic induction (inductive or capacitive) techniques to transfer energy. In this approach, an electromagnetic (EM) fields is created by the transmitter coil, which induces a current in a nearby coil (the receiver). Among the different techniques, inductive WPT has become the most widely used for powering devices due to its high efficiency. Recent advances allow its use in many commercial devices as for electric vehicles [42], [43]. The rapid growth of near-field WPT technique is encouraged in medical applications, such as a neurostimulation solution presented in [44]. The state of the art of the near-field power transfer is based on three main technologies: Qi (87-205 kHz), A4WP (6.78MHz) and Near-Field Communication (NFC) (13.56MHz). The NF WPT is particularly suitable for high-power devices or systems where the distance between the transmitter and the receiver is relatively short.

- Far-field (FF) WPT is used for longer distances, typically up to several meters to several kilometers. It involves the transfer of power through beams of electromagnetic radiations using both microwaves and lasers. The microwave WPT consists of the transmission of power through EM waves using a transmitting antenna. At a certain distance, a receiving antenna captures theses waves and converts them into DC current. While far-field WPT offers the advantage of transmitting the power over long distances, the efficiency trends to decrease as the distance increases. This technique is mainly used in low-power applications within the Internet of Things (IoT) domain [45], [46]. Laser power transmission is an emerging technology that can be classified in FF WPT techniques. Compared to the other WPT techniques, the laser power transfer exhibits superior working distance and high-power density.
  However, this technique requires a line of sight to the receiver, which is not suitable for daily life applications and movable devices in time [47].

Due to the limited lifespan of battery powered devices, the high cost of batteries and their regular replacement, WPT techniques become a ubiquitous alternative solution for wirelessly powering devices. The main limitation of the wireless power technique is the decrease of power as distance increases. The transfer efficiency of the different WPT techniques for near and far-field presented in Figure I.3. We will focus on the far field wireless power transmission technique via microwaves, which is the most suitable for powering battery-free devices.

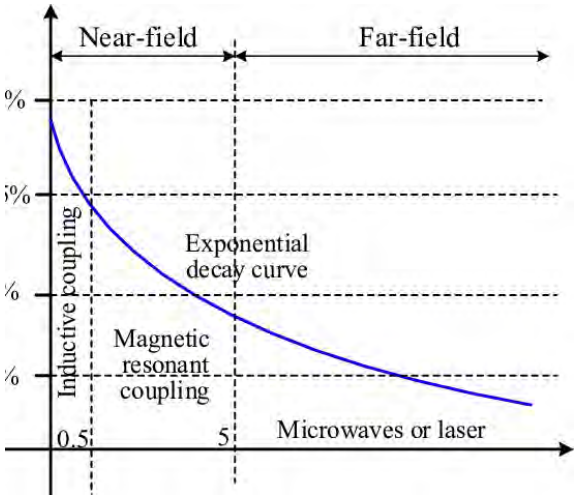

Figure I.3. Comparison of the efficiency for different WPT Techniques [2].

2.1. History

Major scientific discoveries at the end of the 19th century have allowed us to enjoy the technology of wireless energy transmission and energy harvesting. Already in 1964, the work carried out by the physicist James Clerk Maxwell allowed to demonstrate the propagation of electromagnetic waves in vacuum and more precisely with his theory on Maxwell equations [48]. About ten years later, Heinrich Hertz experimentally demonstrated the process of wireless transmission of radio waves using an antenna and an oscillator, validating the theory established by Maxwell's equations [49]. Thus, he becomes the precursor of wireless communication. In 1890, French physicist Edouard Branly, made significant contribution by highlighting the phenomenon of radioconduction in 1890. Through its device called the coherer or radioconductor, he enabled the detection of electromagnetic waves [50].

Thanks to the numerous scientific advances, the technique of power transmission without material support was first explored by Nikola Tesla [51]. He performs experiments of wireless energy transfer using the principle of the coil resonance.

His invention, the tesla coil, enabled him to generate hight alternating current. He implemented remarkable experiments that earned him his famous photograph taken in 1899 in his laboratory, showing lightning generated by his giant transformer as seen in Figure I.4. His ambitions to deliver energy from a greater distance have led him to several successful experiments on the possibility of powering light bulbs located several kilometres from his laboratory. Aware of the potential of transmission of energy by radio waves, he undertook the construction of his station the Wardencyffle Tower or Tesla Tower for the purpose of transmitting electricity on a global scale. Unfortunately, this ambition project was never realized. His genius allowed him to be ten years ahead of the current technology with a specific approach to the prospects of wireless energy transmission.

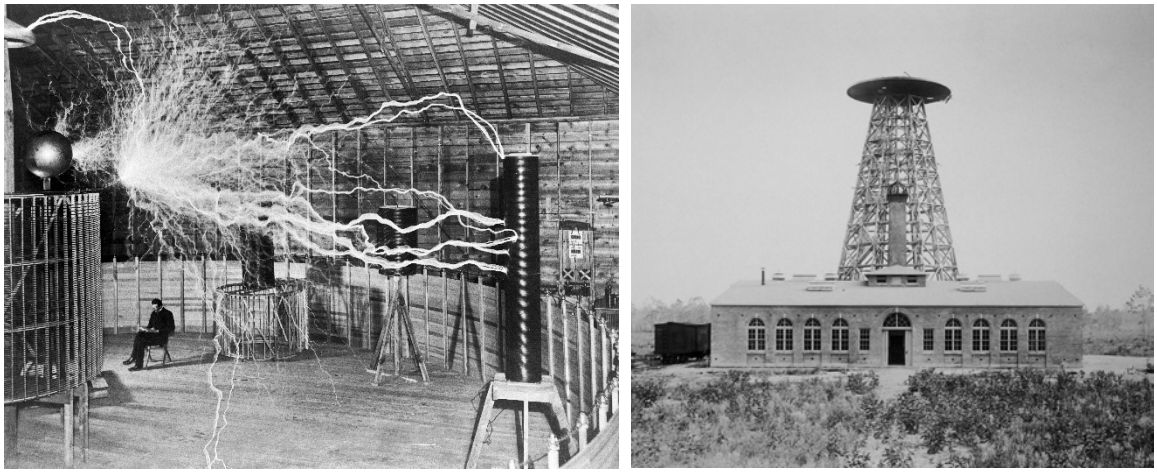

Figure I.4. (Left) Tesla sitting in his Colorado Springs laboratory with his "magnifying transmitter" generating millions of volts, (Right) Tesla Wardencyffle tower.

After several years, this principle of wireless power transfer gained significant attention in scientific research, particularly in the aim of having a satisfactory receiver for microwave power transmission initially established by Tesla. A breakthrough came in 1963 with the development of the first rectifier antenna by William C. Brown [52]. This rectifier antenna known as rectenna (rectifying antenna) is a passive element combining an antenna and a rectifier circuit. Its purpose is to convert the EM waves captured by the antenna into an RF signal, which is then rectified and filtered to produce a DC voltage. An arrangement of 28 rectennas yielded an output DC power of 4 W and 7W for an estimated conversion efficiency of 50 % and 40 %, respectively. William Brown was able to demonstrate the operation of a small size helicopter fed by microwave energy transmitted from a ground-based source through a rectenna array. Its rectenna helicopter consists of 4480 IN82G diodes which efficiently converts and supplied approximately 270 W of power to the helicopter's rotor [53], [54]. In this experiment, the helicopter reached a flying altitude of 50 feet, powered by 5 kW magnetron operating at a frequency of 2.45 GHz. This marked a significant milestone in 1964, as it became the first wirelessly powered helicopter demonstrator by microwaves energy, as shown in the Figure I.5.

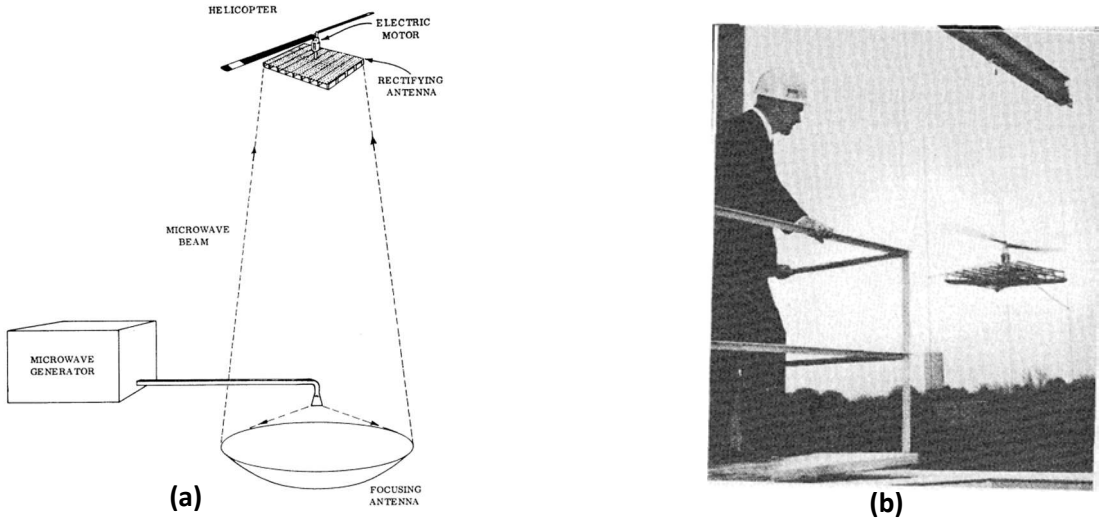

Figure I.5. (a) The basic elements of a microwave-powered helicopter system, (b) Microwave-powered helicopter in flight 60 ft above a transmitting antenna.

Indeed, William Brown is considered as the precursor of the development of rectenna and has greatly contributed to scientific research in the field of microwave energy harvesting [55]. In the coming years, other activities based on W. Brown's research have contribute to the development of the rectenna to wirelessly power satellites. Huge potential applications for RF energy harvesting have emerged since and will be discussed later on this chapter. Now we can address the part that interests us in the wireless power transmission, the rectenna.

2.2. Rectenna development

The rectenna is composed of two main parts: an antenna and a passive rectifier circuit, which includes an RF diode and a low-pass filter. As demonstrated earlier by W.C Brown, the purpose of the antenna is to capture the surrounding electromagnetic waves that match its resonant frequency and then convert them into RF power. A portion of this RF power, depending on losses, is delivered to the rectifier circuit. Given the low power levels harvested by the rectenna, it is crucial to incorporate of a Power Management Unit (PMU) to ensure a sufficient power threshold for the operation of active elements. The conventional architecture of the WPT system is depicted in the Figure I.6.

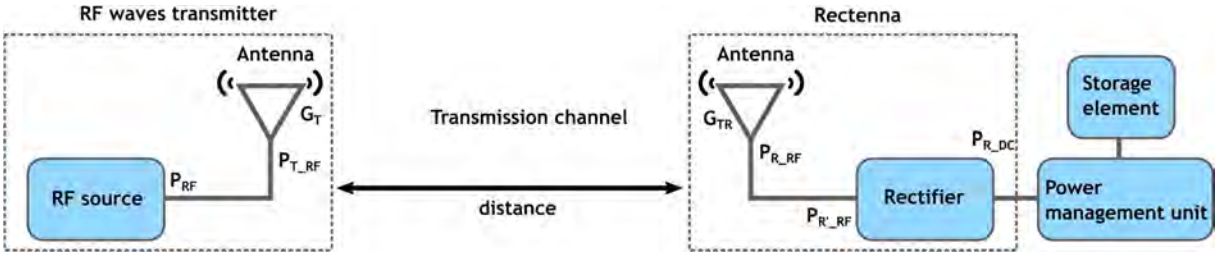

Figure I.6. Architecture of a conventional far-field WPT system.

The wireless power transmission technique involves transmitting power from the RF source through its antenna to the load connected to the output of the rectenna. Initially, the RF source emits a signal with a power level P_{RF}. Depending on factors such as cable and mismatch losses, the antenna, with a gain of G_T, radiates a signal with an equivalent power level P_{T_RF}. The transmitted wave is characterized by its wavelength ($\lambda = c/f$) which defines its periodicity in free space. The received wave is influenced by the transmission channel and the distance (d) between the transmitting and receiving antennas.

The received power by the antenna with a gain G_R in the free space (no multiple paths of the wave), assuming a direct line of sight path of the wave, can be calculated can be computed using the Friis equation defined by the equation (I.1). In this equation, the received power considers the free space losses, which is determined by the factor $\lambda^2/(4\pi d)^2$. However, in real case scenarios, outside the free space environment, the propagation of the wave can be altered by several disturbances (interference, reflection and diffraction phenomena) producing a variation of amplitude and phase.

$$P_r = \frac{P_t G_t G_r \lambda^2}{(4\pi d)^2} \quad \text{(I.1)}$$

The combination of the antenna and rectifier circuit involves an impedance matching to maximize power transfer. A portion of the received power $P_{R'\_RF}$ feeds the rectifier input. The rectifier is used to convert this RF signal into a DC signal with a power level of P_{R_DC}, which can be stored in a storage element through the PMU. The Power Conversion Efficiency (PCE) of the rectifier is influenced to several factors including its topology, the types of components used, its operating frequency, the RF input power level and the output load. Now let's take a look at the different existing rectifier topologies.

2.2.1. Rectifier topologies

The choice of the rectifier topology depends on several parameters: the kind of applications, the size of the prototype, the operating frequency, the available RF power level at the input, the sensitivity and the targeted optimization (the conversion efficiency or the output DC voltage). Since, the first studies by W.C. Brown, several rectifier topologies have been developed and are listed in Figure I.7. Various studies have compared the performance of these rectifier topologies [56]–[59]. In rectifier architectures, there are two main parts: the rectifier and the low-pass filter. The rectifier is responsible for rectifying the RF signal at its input, while the filter is designed to extract the DC component of the signal and eliminate any ripples present in the rectified signal. The DC component of the rectified signal is obtained using a low pass filter, generally consisted of a shunt capacitor and the resistive load.

- The half-wave rectifier, also known as single diode rectifier, is the simplest existing topology that requires only one diode and rectifies half cycle of the received input signal. Theses rectifiers, with fewer components in their architecture, minimize losses and exhibit good performance at low power levels [60]–[65]. Among the types of half-wave rectifiers, there is the serial diode rectifier used for positive alternation and shunt diode rectifier for negative alternation as represented in Figure I.7 (a) and (b).
- The voltage doubler rectifier also known as full-wave rectifier or single stage Greinacher rectifier, consists of two diodes and can rectify both the negative and the positive cycles of the RF input signal. Its topology is presented in Figure I.7 I. It is known for increasing the level of the DC output voltage [66]–[70]. A comparative analysis of the voltage doubler rectifier and single series-type rectifier was conducted in the design of the rectenna [71]. The study showed that the voltage doubler exhibits better RF-to-DC conversion efficiency than the single series-type for output loads exceeding 100 Ω. This highlights the importance of considering the output load for optimizing the performance.
- The use of charge-pump topologies is necessary in certain applications that require a significant output voltage at least 1 V, to supply any active electronic components such as in battery-free sensing and the Radio Frequency Identification (RFID) [72], [73]. The voltage multiplier technique was earlier demonstrated in 1976 by John F. Dickson [74].

The output voltage of the rectifier is boosted by means of a combination of diodes and cascaded diode-capacitor stages. Some designs are based on Dickson topology [75]–[77]. Additionally, the voltage doubler or charge pump configuration enables wider bandwidth rectifier operation, as the input impedance slightly varies with the frequency. The rectifier proposed in [78] uses the Dickson charge pump for increasing the bandwidth and improving the dc voltage of the output load.

- CMOS technology rectifiers are also investigated to achieve higher efficiency compared to commercial Schottky diode [79], [80]. However, it requires rigorous design knowledge and involves a lengthy, expensive, and complex manufacturing process. As a result, it is not suitable for rapid prototyping purposes.

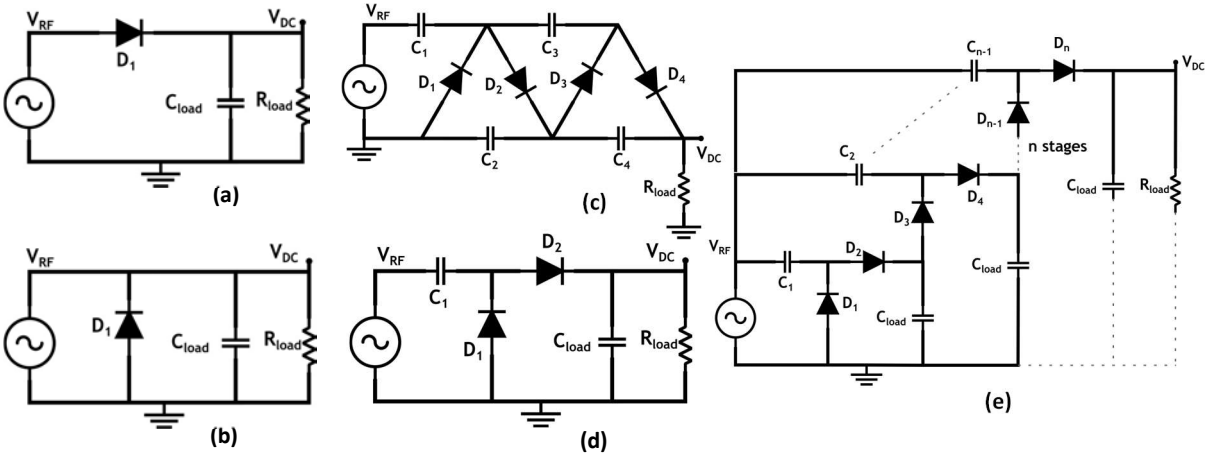

Figure I.7. Rectifier topologies : (a) Series diode rectifier, (b) Shunt diode rectifier, (c) single stage Greinacher rectifier ; (d) Cockcroft-Waltron rectifier, (e) N-stage Dickson rectifier.

The choice of topology is crucial in the design of an RF rectifier. The more diodes is used, the higher the losses due to the equivalent resistance (junction resistance and series resistance) of the diodes, resulting in lower conversion efficiency of the rectifier. The input impedance of the rectifier is also affected by its non-linearity. Any impedance discontinuity between the source (or the antenna in the case of a rectenna) and the rectifier can cause signal reflection and resulting losses due to impedance mismatch. The equivalent circuit model of diode implies that it has a complex impedance different from the conventional 50 Ω input impedance. To maximize the conversion efficiency, it is important to achieve good impedance matching between the source and the rectifier.

2.2.2. Existing impedance matching techniques

The combination of an antenna and a rectifier to from a rectenna requires an impedance matching network in order to maximize the power transfer. This need of impedance matching network has already been highlighted by William Brown when he fed a helicopter with a rectenna node. In his prototype, the proximity of the diode chains to obtain the required power density has changed the impedance and much of the power is reflected back. He solved this issue by implementing an matching network consisting of a plane network of spaced rods in an appropriate manner and at an appropriate distance from the plane of the diode network [55]. It is either challenging to implement in energy harvesting circuit while, the input impedance of the rectifier is a function of the RF input power, the frequency and the output load. A comprehensive review of the rectenna's impedance matching architecture is presented in [81]. In the case of a bad impedance matching between the source and the load (the antenna and the rectifier in our case of use), standing waves can be created, resulting in the reflection of a portion of the incident power back to the power source.

The insertion loss of the matching network, which includes actual lumped elements and transmission lines, was quantified for low power rectennas in [82].

- Impedance matching with lumped element is achieved by means of a matching network, typically consisted of reactive Surface Mount Device (SMD) components such as inductors and capacitors connected in series or in parallel configurations. One of the simplest and most common solution is the L-network, which combines an inductor and a capacitor. Lumped element circuits are useful for miniaturization and suitable for low frequency [83]–[85]. This technique with lumped component also offers tunabilty during the prototyping phase, allowing for easy modification of the rectifier's input impedance to target different frequency bands with the same design.
  However, this kind of matching network is narrow band, more sensitive parasitic effects, challenging to design at high frequencies, and dissipate more power than transmission lines [86]. The implementation can be complex, particularly considering the component tolerance range and the frequency dependent characteristics of inductance. Additionally, the precise positioning of components during hand soldering can be critical in achieving the desired performance.
- Distributed element matching networks generally consist of transmission lines such as microstrip or coplanar wave guid, where the electrical length is proportional to the wavelength at the operating frequency. These networks offer advantages such as wider bandwidth and lower insertion losses. Several topologies exists, including microstrip transmission lines, open-end stubs, radial stubs [87], [70], [88] and coupled transmission lines [89]. They are used to compensate the capacitive reactance of the Schottky diode and minimize impedance variation when the frequency or input power changes. Broadband rectifier designs with transmission line based matching network have been carried out in various experiments [89]–[92].
- In certain designs, a trade-off is made by combining transmission lines and lumped SMD components to achieve both good efficiency and reduced design size. Several studies have investigated the used of hybrid matching networks [93]–[95]. The transmission line part of the matching circuit enables fort tuning the imaginary part of the high-frequency input impedance of the rectifier, while the inductance compensates for the capacitance of the diode [96], [78].
- Another approach for impedance matching is the conjugate matching technique, which does not involve the use of any lumped or distributed components. In this approach, the input impedance of the rectifier is properly adjusted to match the conjugate impedance of the antenna. The conjugate impedance matching means that the same real part and opposite imaginary part. This methods not only allows for size reduction but also improves operating efficiency by eliminating insertion losses in the matching network. Conjugate matching often requires a co-design of the antenna and rectifier to achieve highly-efficient rectenna [99], [100], [98], [101]. Otherwise, conjugate matching can be performed by tuning the antenna impedance as for the patch rectenna with an integrated impedance matching network proposed in [102].
- As mentioned earlier, the non-linearity of the diode induces a variation of the rectifier's input impedance as a function of the input power level. To address this issue and to achieve efficient rectifier with a high RF input power dynamic, specific impedance matching technique must be employed. A rectifier with an immunity to the input power fluctuation was designed with a self-tuning impedance which consists of a varactor reversely biased by the output voltage of the rectifier to compensate the variation of the input impedance [97]. Another method involves the use of paired diodes for capacitive self-compensation, which enhances the rectifier's dynamic power range (19).

Additionally, an L-matching network consisting of an open stub and a short stub can also be employed for impedance matching (18). These techniques contribute to improving the rectifier's performance and enable efficient power transfer across a wide range of input power levels.

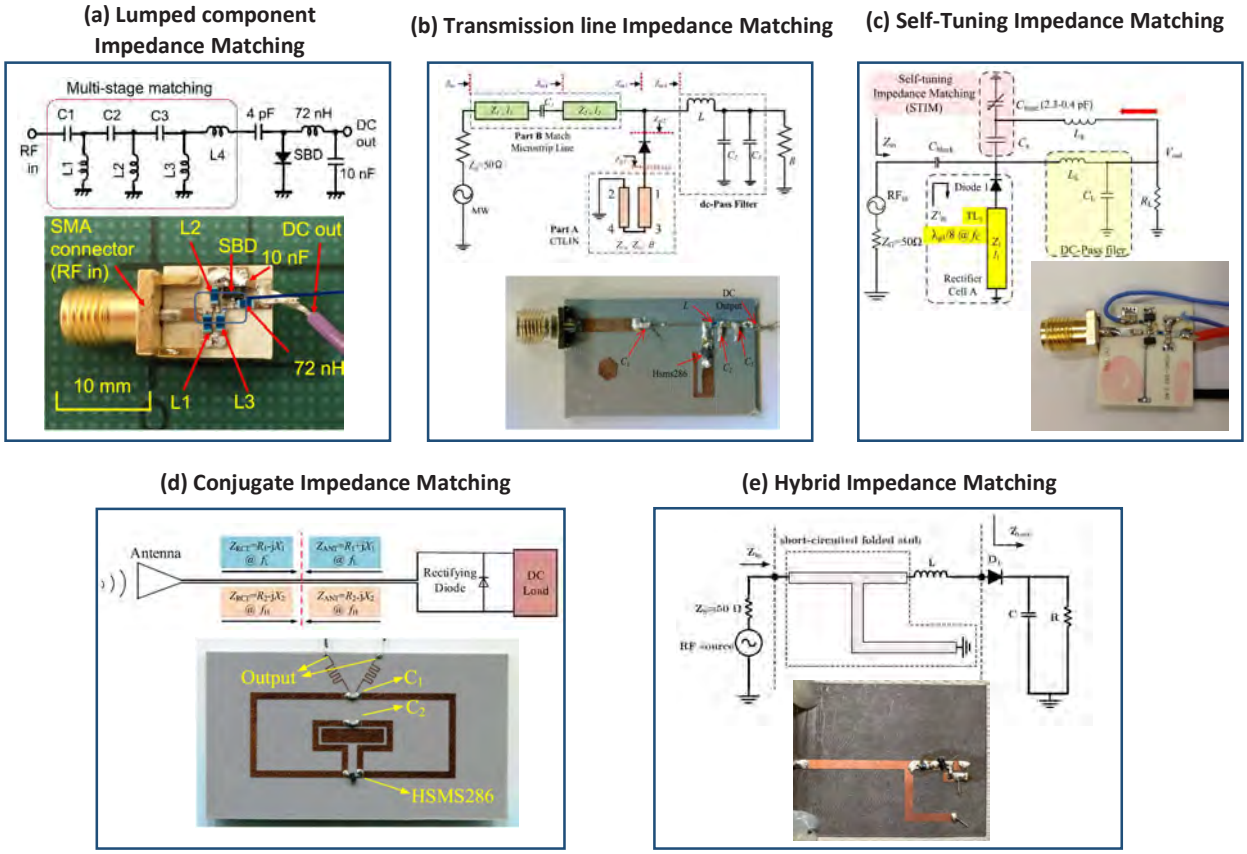

Figure I.8. Rectifier design based on different impedance matching techniques: (a) Lumped component impedance matching [84]; (b) Transmission line impedance matching [89]; (c) Self-tuning impedance matching [97]; (d) Rectenna based on conjugate impedance matching [98]; (e) Hybrid impedance matching network based on SMD inductor and short circuited folded stub [65].

3. Conclusion

In this chapter, we have provided a review of the different battery-less device solutions, discussed the current trends, highlighted the associated challenges. Our research work focuses on developing a battery-free device solution based on harvesting energy through a far-field wireless power transmission technique. The operating frequency is established in the ISM 868 MHz band, considering its availability and the high maximum power level allowed by the standard. We have examined different rectifier circuit topologies and impedance adaptation techniques according to the requirements. Building upon these insights, we have first designed a compact highly efficient and cost-effective rectenna for low power levels and suitable for the targeted frequency. This rectenna is specifically dedicated to powering battery-free devices designed for Structural Health Monitoring (SHM) applications.

II. Compact Rectenna for Wireless Sensing Applications

1. Introduction

Over the past decades, the rapid growth of wireless systems has driven their miniaturization, enabling the integration of multiple functionalities in a rather limited area. However, this trend poses challenges in terms of power consumption, battery capacity, size and efficiency. In order to deal with this problematic, we will discuss in this chapter, the development of compact a rectenna dedicated to power supply wireless sensing nodes.

The overall design has been essentially designed on a rigid substrate. We will provide a comprehensive overview of the rectifier part, including simulation and optimization techniques employed during the design process. Moreover, considering the importance of size reduction, different antenna structures will be presented and evaluated. The objective is to propose a compact and efficient rectenna operating at the frequency of 868 MHz, and optimized for low power levels. Through this design approach, we aim to overcome the limitations associated with power supply in wireless sensing nodes. By developing a compact rectenna, we can effectively address the power consumption and battery size concerns, while ensuring efficient wireless power transfer at the desired frequency. This will enable reliable and continuous operation of battery-free wireless sensing systems, contributing to advancements in various fields such as structural health monitoring.

2. Rectenna for FF-WPT

A rectenna stands for a *rect*ifier and an*tenna* that is used to convert electromagnetic waves to DC power in order to power supply active components such as microcontrollers, transceivers and sensors. The architecture of a typical rectenna is illustrated in Figure II.1. The first stage involves the antenna, which captures the electromagnetic waves at the same frequency band from various sources or data transmitters. It generates a an RF signal (P_{RF}) that is then provided to the connected rectifier. An adequate matching network is used to optimize the power transfer from the output of the antenna to the input of the rectifier diode. Once the RF signal is rectified by the diode, it is then filtered to get a DC voltage. This DC voltage is then boosted, managed and stored in a storage capacitor for supplying the load and active components.

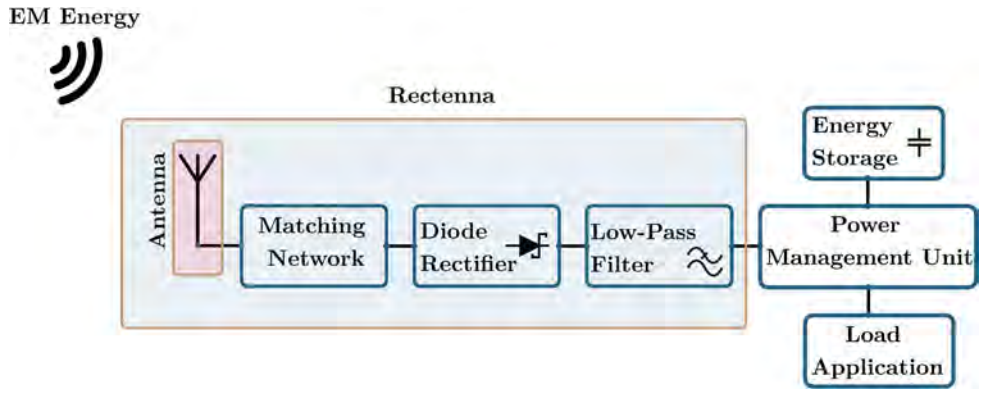

Figure II.1. Schematic of a rectenna connected to a power management unit for supplying power to the load application using the harvested DC power from incident electromagnetic waves.

The limitation of RF energy harvesting (RFEH) systems lies in the among of harvested DC power. It is constrained by the relatively low ambient power density, typically bellow 1 µW/cm². For instance, when considering a rectifier working at 900 MHz with antenna gain of +1 dBi, the received RF power at the input of the rectifier is estimated at -10.5 dBm. Indeed, the power level at the input of the rectifier is relatively low, and it will be further affected by various losses within the rectifier circuit. These losses can significantly impact the efficiency of the energy conversion process, resulting in a lower DC output power available for the load. The Figure II.2 illustrates the general relationship between the RF input power and the Power Conversion Efficiency (PCE) of a rectifier. The maximum PCE achievable is limited by the RF input power, the output load, the presence of harmonic effects, the breakdown voltage, and the junction voltage.

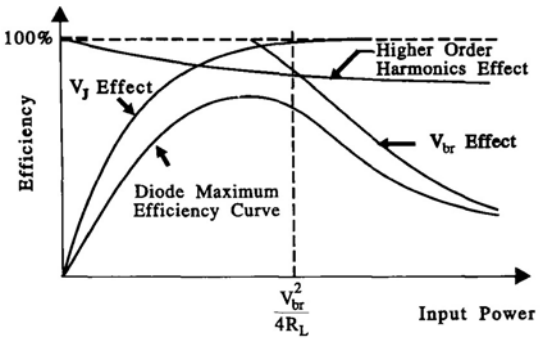

Figure II.2. General relationship between the RF input power and the conversion efficiency.

Our work consists of the design of a highly efficient rectenna for low input power levels and optimized for an output load of 10 kΩ. As depicted in Figure II.2, the efficiency tends to decrease at low power region. However, by carefully selecting the appropriate Schottky diode, and designing an efficient matching network, we can optimize the rectenna's performance in this low-power region.

2.1. Rectification circuit

The rectification circuit named rectifier is dedicated to convert the RF signal into a DC power. Our aim is to harvest very low power level, specially below -10 dBm, at the European Industrial Scientific and Medical (ISM) 868 MHz frequency band. Additionally, we have the requirement of optimizing the overall size of the rectifier to b as small as possible for integration into a wireless sensor node. To achieve these goals, it is essential to select a suitable rectifier circuit topology that is efficient at low input power levels. As mentioned earlier, Schottky diodes are commonly used in rectifier circuits for their low forward voltage drop and fast switching characteristics and must be wisely chosen.

2.1.1. Choice of the diode

The key component of a rectifier circuit is the diode, which enables the conversion of the alternative current (AC) into a direct current (DC). Its primary characteristic is its ability to flow the current in one direction. Consequently, when the current flows through a diode, there is a voltage drop across it, known as the forward voltage. The equivalent electrical model of a diode is represented in Figure II.3. Intrinsically, it is modelled by a series parasitic resistance (R_s) and a junction capacitance (C_J) in parallel with a junction resistance (R_J). These last two junction elements, the junction capacitance and resistance, are dependent on the bias voltage as expressed in equations (II.1) and (II.2).

$$R_j = \frac{nkT}{q(I_s + I_b)} \quad \text{(II.1)}$$

$$C_j = \frac{C_{j0}}{\left[1 - \frac{V_d}{V_j}\right]^m} \quad \text{(II.2)}$$

$$I_b = I_s \cdot \left[\exp\left(\frac{qV_d}{nkT}\right) - 1\right] \quad \text{(II.3)}$$

Where I_b is the bias current, I_s is the saturation current, n is the ideality factor, K the Boltzmann constant, T is the temperature, q is the electron charge, C_{j0} is the zero-bias junction capacitance , V_d is the voltage across the diode, V_j is the junction voltage and m is the gradient coefficient. The diode package includes parasitic elements (inductance L_p and capacitance C_p) to be consider on the equivalent model.

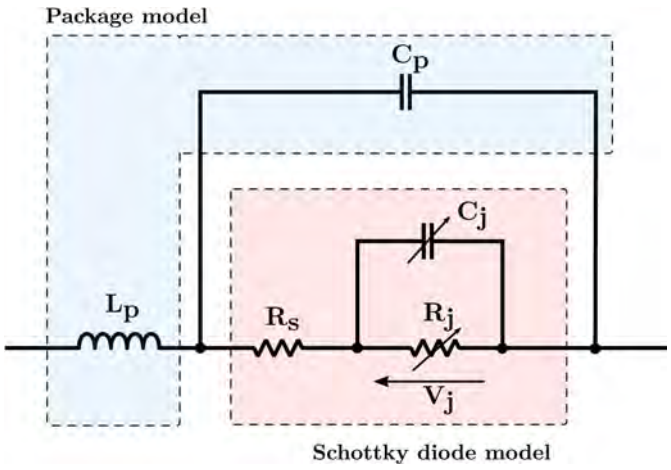

Figure II.3. Linear equivalent electrical model of the Schottky diode model with parasitic elements of the package.

The Schottky diode is used in general purposes of rectification particularly in RF applications. Its current-voltage characteristic is compared to that of a P-N junction diode and shown in Figure II.4. Except its high reverse current and low breakdown voltage, the advantages of using Schottky diode instead of conventional diode or junction P-N diode are multiple:

- Low forward voltage is possible with Schottky diode (V_F) and its fast rate of switching due to the higher current density in the Schottky diode.

- Low junction capacitance (C_j) due to the absence of depletion region thus no more charges are stored.
- Less noise due to low nonlinear impedance
- High cut-off frequency

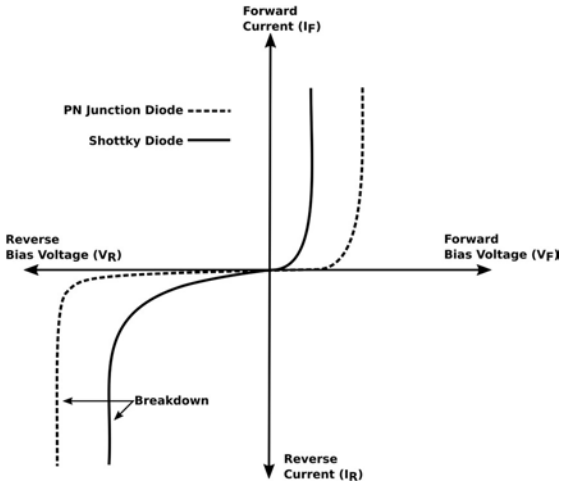

Figure II.4. Current vs. voltage characteristic of Schottky and P-N diode

Therefore, the choice of the appropriate type of Schottky diode is crucial for designing an efficient rectifier circuit. A commercial SMD Schottky diode is used for our rectifier design. We selected the one with interesting properties that meet the functional requirements of the rectifier mentioned before. In the Table II.1, is reported the fundamentals electrical specifications of the commonly used Schottky diode. The HSMS285x series from Avago and SMS760 series from Skyworks are frequently employed in the literature for low RF power design due to their low forward voltage characteristics. On the other hand, Schottky diode with high breakdown voltage is suitable for high power applications. For instance, the HSM286x series has been employed in rectifiers designed to handle incident power levels up to +24 dBm, as demonstrated [103], [104].

Table II.1. Electrical specifications of the most used Schottky diode

Diode series	V_F (V) [I_F = 1 mA]	B_v (V)	Rs (Ω)	C (pF)	Used on references
HSMS285x	250	3.8	25	0.18	[65], [85], [105]
HSMS286x	350	7.0	5.0	0.18	[106]–[108]
SMS7630	135-240	2	20	0.14	[109], [110], [77]
MA4E1317	700	7	4.0	0.02	[111]–[113]

To improve the Power Conversion Efficiency (PCE) at higher frequency, it is important to minimize the junction capacitance and series resistance of the Schottky diode. The MA4Ex family of Schottky diode from MACOM is known for its high cut-off frequency, making it well-suited for Millimetre-wave applications. In a design proposed in [111], the MA4E1317 GaAs Schottky diode was used to achieve a high PCE of 72.6% at 915 MHz, using a high input power of +19 dBm. Others commercially available diodes, such as BAT15-04R type from Infineon Technologies, are also used in RFEH applications [114].

For our purpose, we require a Schottky diode with low-power handling capability, low forward voltage and low series resistance is required. According the information provided in the datasheet [115] and the previous comparison, the Skyworks SMS7630 series offers the best trade-off in terms of DC voltage and efficiency for low power range.

2.1.2. Rectifier design

In the general introduction (chapter I), several rectifier topologies were discussed, each with its own advantages and disadvantages. A trade-off was made between the DC output voltage and the PCE for the topology selection. In the present work, we have chosen to use the Greinacher voltage doubler topology for the rectifier design. For the Schottky diode, we have selected the SMS7630-005LF model. It consists of a pair of series-connected, identical single diodes within the same packaging. The choice of this diode is based on its suitability for low-power applications, low forward voltage, and low series resistance, which aligns with our design requirements.

In order to perform accurate simulations, we first started by creating the spice model of an single diode with the electrical characteristics provided in the datasheet [115]. However, this model does not include the parasitic effects of the package. To incorporate the package parasitic elements in our global simulation model, we considered two types of the SOT-23 plastic diode package model, as illustrated in Figure II.5, each with its respective component values provided in Table II.2. We considered an accurate and concise microwave model of SOT-23 package diode established by Skyworks (SK) [117] and by Hewlett Packard (HP) [118]. By including these parasitic models of the diode package in our simulation, we aimed to obtain the realistic behaviour of the diode in practical operating conditions.

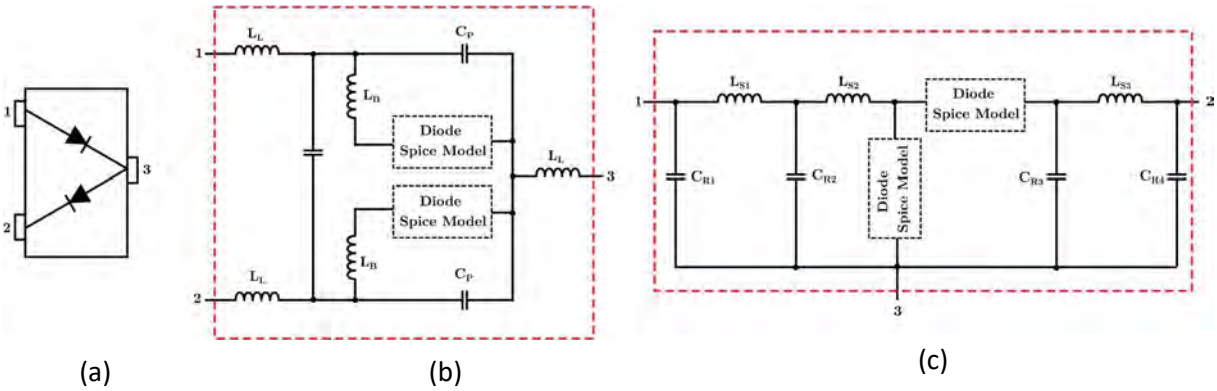

Figure II.5. SOT-23 Package Circuit models of the Schottky diode: (a) General Package style; (b) Model by HP Inc.; (c) Model by Skyworks (SK).

Table II.2. Elements value of the SOT-23 Package model.

L_L	L_B	C_P	C_C	L_{S1}	L_{S2}	L_{S3}	C_{R1}	C_{R2}	C_{R3}
0.5 nH	1 nH	0.08 pF	0.06 pF	0.65 nH	0.05 nH	0.7 nH	0.13 pF	0.01 pF	0.015 pF

The architecture of the rectifier, as presented on Figure II.6 , consists of the selected Schottky diode model, le matching network and low pass-filter at the output, and two capacitors. A series capacitor at the input (C_D) is required to enable the full-wave rectification of the input signal. The second capacitor C_F is a part of the low pass-filter, to reduce the ripple on the DC output signal. Both capacitors have a fixed value of 100 pF. The performance of the rectifier is influenced by the non-linearity of the diode, which results in a dependence of the input power and the output load.

We target to design an efficient rectifier at lower input power (around -15 dBm), and a resistive load (R_L) of 10 kΩ is selected to globally emulate the input impedance of the Power Management Unit (PMU) component for upcoming implementations. The matching network plays an important role in maximizing the power transfer from the input to the rectifier, thereby enhancing the power conversion efficiency (PCE).

We have opted for a lumped component matching network in order to reduce the size of the circuit, knowing that the half-wavelength at the targeted frequency (868 MHz) is relatively high (86.4 mm) for an impedance matching with transmission lines. Miniaturization of the circuit is preferred to the detriment of the decrease in the PCE due to insertion losses caused by the components. The entire circuit is designed on microstrip coupled transmission line, using a 0.8 mm thick FR4 substrate.

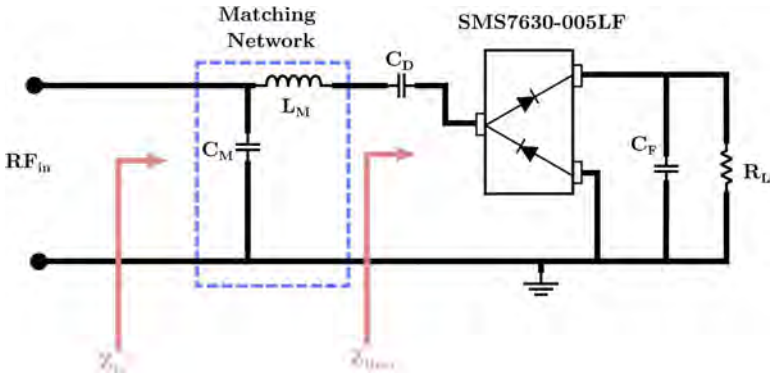

Figure II.6. Designed rectifier topology without matching Network.

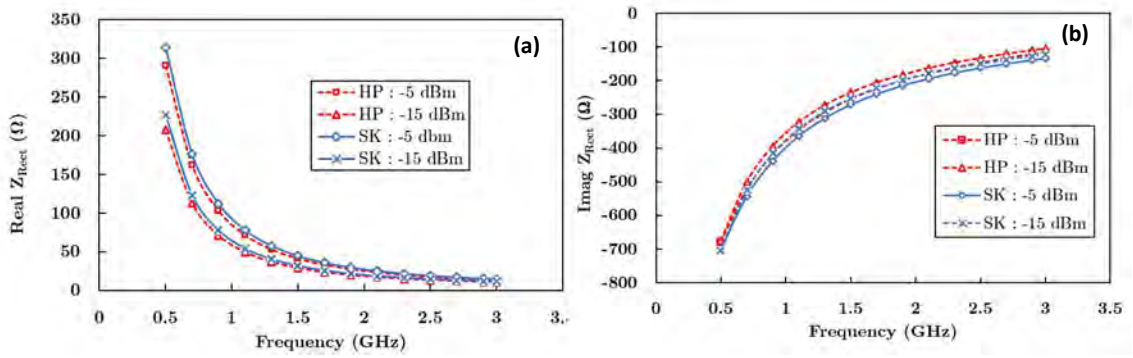

Figure II.7. Simulation the input impedance of the rectifier without matching network: HP Model on blue line and Skyworks (SK) Model on red dashed line: (a) Real part of the input impedance; (b) Imaginary part of the input impedance.

Preliminary, the spice parameters of the diode and parasitic parameters of both models are integrated into ADS simulator for the design of the rectifier circuit without a matching network. As shown in Figure II.7, the rectifier circuit exhibits a high real part of the impedance (> 50 Ω) before 1 GHz and exponentially decreases with increasing frequency. The real part is lower for -15 dBm. The negative imaginary part of the impedance increases but remains lower than -100 Ω from 500 MHz to 3 GHz. Both models display similar impedance trends, with a maximum deviation of 23.5 Ω and 27.9 mΩ for the real and imaginary part, respectively. To match the impedance of the rectifier circuit at 868 MHz to an impedance of 50 Ω, an L-network (series inductor L_M and shunt capacitor C_M) impedance matching network is selected. With the consideration of the transmission line model on the design, an inductor of 33 nH (LQW15AN) and a shunt capacitor of 4 pF (GRM1555C2) is obtained for optimal operating frequency around 868 MHz. The first simulation is performed using the ADS harmonic balance (HB) tool and transmission line model, as presented in Figure II.8 (a), to estimate the rectifier's performances.

ADS simulator also provides a useful EM simulation tool for the analysis of planar circuit layout at RF and microwave frequency named Momentum. To simulate the rectifier properly and accurately, we used Momentum Microwave (Mom µW) simulation. The layout of the rectifier was generated from the schematic design and the Scattering (S)-Parameters were created by setting pins across the SMD component location, as shown in Figure II.8 (b). Once obtained, a co-simulation of HB+Momentum was performed. However, it is important to specify certain parameters to ensure accurate simulated performances.

- Port setup: The differential port were used, and the calibration type at each pin is defined as Delta gap. This accounts for the parasitic effects that are not included in the schematic component model used.
- Mesh setup: The simulation results are improved with higher mesh density. In our design, the mesh density was set to 500 cells/wavelength. The edge mesh was also enabled to capture the details near the edges of the layout.

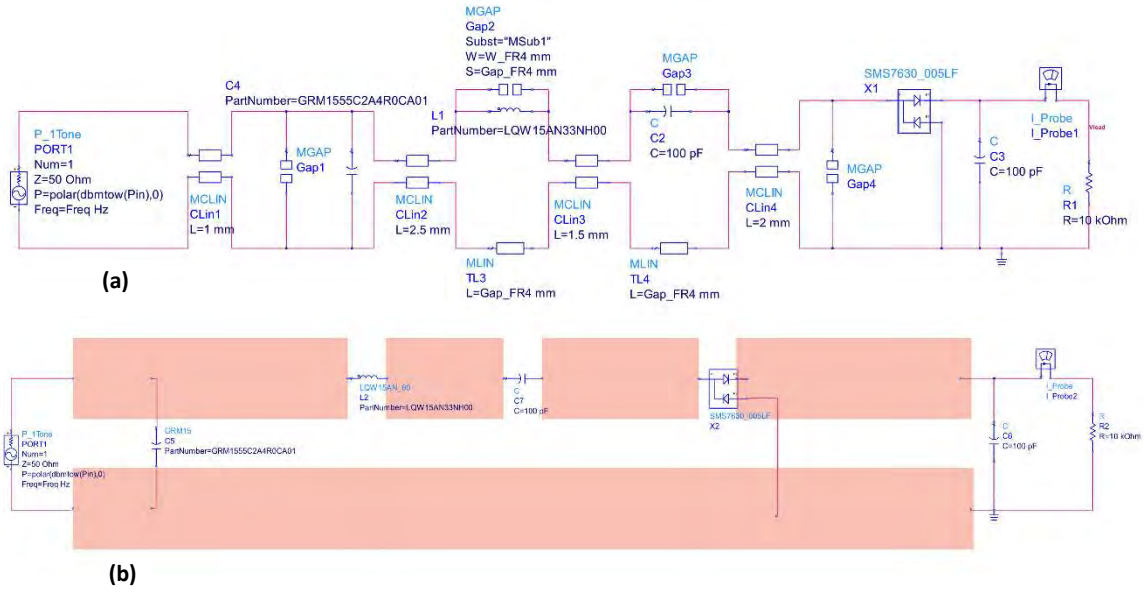

Figure II.8. Schematic of the rectifier design on ADS software: (a) HB Simulation with transmission lines model and (b) Co-simulation with EM model on Momentum.

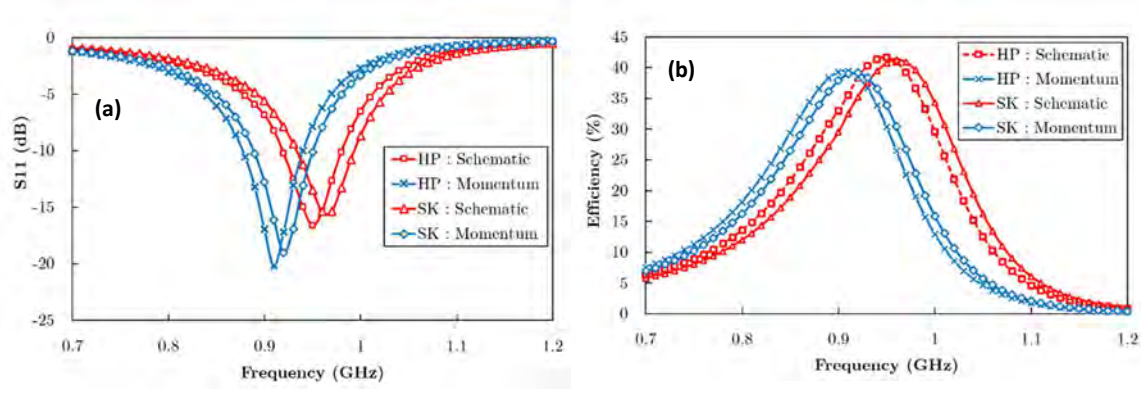

Figure II.9. Comparison between SK and HP model on schematic and Momentum simulation: (a) Return loss at -15 dBm and (b) PCE of the rectifier at -15 dBm.

The return loss (S11) in decibel of the rectifier was then computed using both diode package model, as shown in Figure II.9. There is a significant difference on the resonance frequency between Momentum simulation and Schematic. This deviation of 40 MHz can be attributed to the consideration of coupling effects in the co-simulation. The same behaviour is observed on the efficiency with a peak of 39%. In conclusion, when comparing the simulation results, the two models show a slight difference. However, for a rapid hand prototyping of a rectifier in the ISM 868 MHz band, this difference is not significant, and the measurement results will depend on several factors, which will be discussed later on.

Afterward, the designed rectifier was prototyped on 0.8 mm-thick FR4 substrate using the same components as previously mentioned in the simulation steps. The prototype occupies a surface area of 14 mm x 5 mm, excluding the SMA connector. To characterize the rectifier, it was connected to an RF power generator, and the harvested DC voltage was measured across the 10 kΩ load using a digital multimeter. The measurement results closely match to the co-simulation results obtained with EM model on Momentum, and particularly with the HP model of the diode package. However, there is still a shift in the resonance frequency, which can be justified by the use of SMA connector, soldering effects and component tolerances. The exact location of the component on the prototype cannot be accurately determine in the Momentum simulation, and this may slightly modify the global impedance of the rectifier.

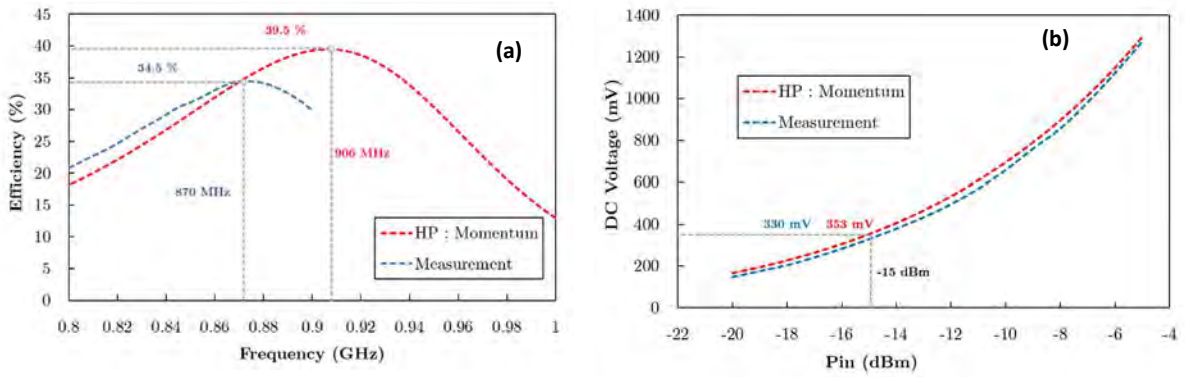

Figure II.10. (a) PCE of the rectifier at -15 dBm; (b) Harvested DC voltage at the resonance frequency.

As depicted in Figure II.10 (a), the prototyped rectifier achieved a PCE of 34.5% (at -15dBm) close the targeted frequency at 868 MHz. However, the efficiency can be further improved by choosing the optimal load, which is different from the chosen value of 10 kΩ for our specific applications. Concerning the harvested voltage, the presented design can exhibit a DC voltage of 330 mV (or an output power of 11 µW) for a RF input power of -15 dBm at 868 MHz and there is only 23 mV lower than the simulation result at the resonant frequency (906 MHz). Therefore, it can be concluded that the HP model of the diode package and co-simulation with Momentum provide simulation results close to the measurements. These models will be used for the next design iterations. We can also note that the performance of the designed rectifier is sufficient to power supply active components through an energy management system. For instance, it can be effectively used with the commercial PMU AEM30940 ([119]) from e-peas semiconductors, which has an ultra-low-power start up. The PMU typically required a cold start from 380 mV input voltage and 3 µW input power.

With an RF input power of -10 dBm, the rectifier can also complete the cold start requirements of another PMU, the BQ25570 [119] from Texas instrument, which has a minimum cold start input voltage of 600 mV and an input power of 15 µW. These satisfactory results from the prototyped rectifier allow to move on to the design of the antenna intended to form the rectenna.

2.2. Antenna Design

Toward having a compact design, the size of the radiative part of the rectenna is crucial for an efficient devices. Generally, the antenna part occupies around 80% of the total rectenna size, mainly due to the geometrical elements dependent on the wavelength. In order to maintain efficient performance while reducing the physical size of the antenna, an original topology of 3D folded dipole antenna (3DFDA) operating at ISM 868 MHz frequency band is proposed. As required to convert the ambient EM waves to RF signal, the antenna should reach a minimum radiative gain of +1 dBi on an overall planar area of around 60 mm x 30 mm. Hence, the choice of an Electrical Small Antenna (ESA) is made. An ESA is defined as an antenna that is physically small compared to the wavelength of the electromagnetic waves to transmit. Wheeler's formula (II.4) is used to determine the size of an electrically small antenna, where the antenna sphere is smaller than the radian sphere, also defined as Wheeler Cap as represented in Figure II.11 [121], [122]. In the formula (II.4), λ represents the wavelength at the operating frequency, k is the free-space wavenumber, and a is the minimum antenna sphere radius.

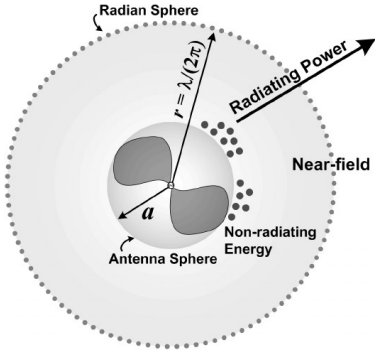

Figure II.11. The antenna and radian sphere view of an electrically small antenna [123]

$$k.a < 1 \; with \; k = \frac{2\pi}{\lambda} \tag{II.4}$$

Reducing the electrical length of the antenna results in a decrease of the radiation efficiency and bandwidth. However, for applications in the ISM European 868 MHz frequency range (with a bandwidth of 3 MHz), the reduction in bandwidth is not a limiting factor. The target is to achieve a minimum antenna gain of +1 dBi while ensuring a compact design. A comprehensive understanding of the effects of antenna size reduction on quality factor (Q), bandwidth and gain, allows for the proposal of a compact antenna without significant performance degradation. For further details on the fundamentals of electrically small antennas, including their limitations and potential applications, a detailed review can be found in [124], [125]. Based on the expression in formula (II.4), for an operating frequency of 868 MHz, the antenna sphere must have a radius of less than 55 mm in order to be considered electrically small. Since the sphere represents the maximum extent of the antenna's electric field, it should have a radius larger than the largest dimension of the antenna structure to ensure that it is electrically small. In this case, the dimensions of the rectangular surface of 60 mm x 30 mm dedicated to the antenna design fit comfortably within the calculated sphere size (radius of 55 mm), satisfying the condition for an electrically small antenna.

The proposed design is based on a dipole antenna. It is selected thanks to the symmetry of its shape and radiation pattern, its low-cost manufacturing, and its ability of receiving balanced signals. To realize such antenna, a half wavelength dipole antenna at the resonance frequency of 1.12 GHz was designed.

Starting from the antenna on Figure II.12 (left), a T-match connection is added in order to improve the input impedance matching to 50 Ω at the targeted frequency. This structure acts as an impedance transformer and is generally used in RFID applications for conjugate impedance matching [126]. The resonance frequency of the antenna is greatly influenced by the width and the length of the T-match structure. The simulations were performed using the High Frequency Structure Simulator HFSS software from Ansys.

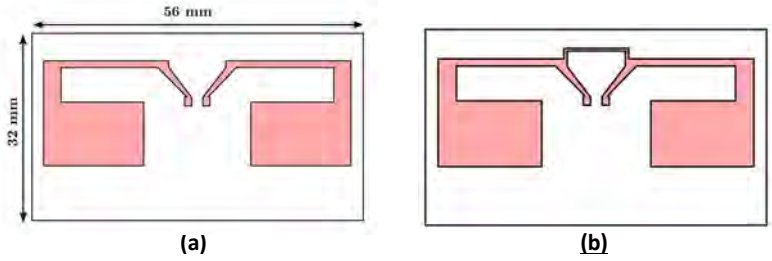

Figure II.12. Geometry of the proposed compact antenna with (b) and without (a) T-Match structure.

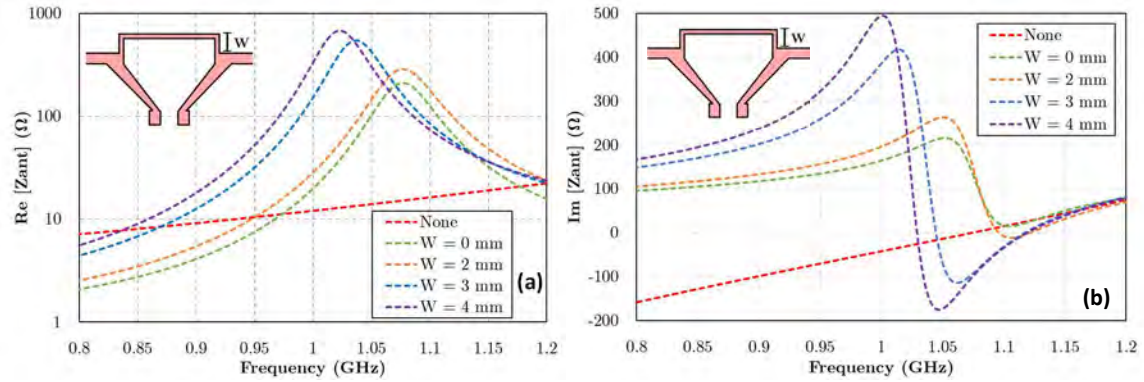

Figure II.13.Simulation of the antenna as function of W parameters: (a) Simulated real part of the impedance, (b) Simulated imaginary part of the impedance.

By connecting the two parts of the dipole antenna with a horizontal line (W = 0), both the real part and the imaginary part of the impedance increase significantly. Figure II.13 illustrates the tuning of W parameter, which helps to find the resonant frequency of the antenna for a normalized impedance of 50 Ω. Without T-match structure, at 1.12 GHz, the impedance of the antenna is [17.4+j·28.4j] Ω, while with W = 3 mm and W = 4 mm, the input impedance becomes [56+j·5.6] Ω and [52.6+j·2.8] Ω, respectively. It is also important to note that as the length (L) of the short-circuited line increases, the antenna resonates at higher frequencies, as shown in Figure II.14. With the W parameter fixed at 3 mm and the L parameter fixed at 10 mm, the resonant frequency of the antenna is guaranteed to be around 1.12 GHz. These fixed parameters ensure that the antenna operates at the desired frequency range.

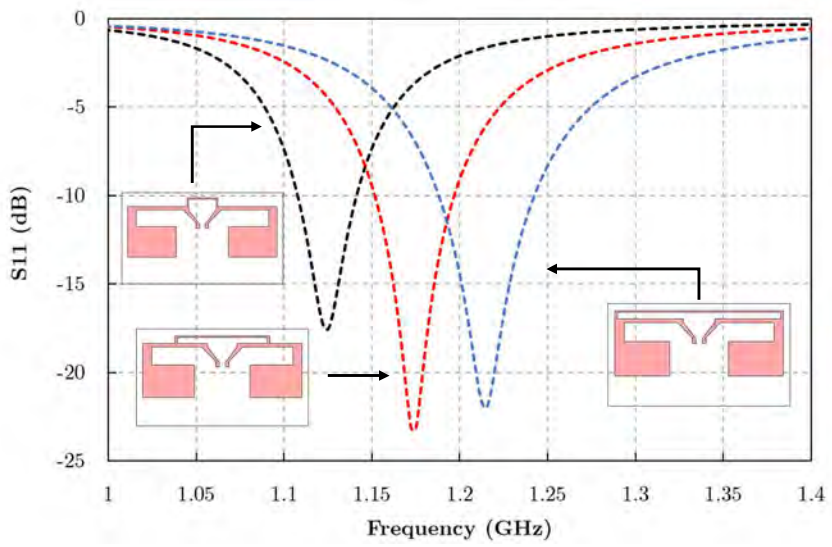

Figure II.14. Simulated return loss of the antenna for different configurations; L = 10 mm (black), L = 30 mm (red) and L = 51.4 mm (black).

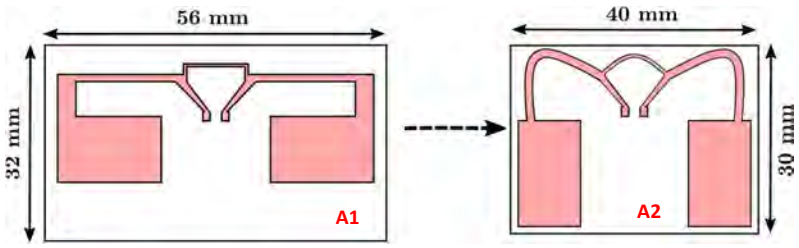

Figure II.15. Geometry of A2 antenna obtained from A1 planar antenna size reduction.

By modifying the planar shape of the antenna, specifically the bottom part, we can further improve compactness. In this design, the horizontal arms of the planar dipole are folded in a spline shape, reducing the overall planar length. This modified antenna, named A2, is smaller compared to the previous A1 antenna, with an area reduction factor of about 2/3. The resonant frequency of the A2 antenna is 1.15 GHz, which is close to the resonant frequency of the A1 antenna. This demonstrates that the compactness of the antenna can be improved without significantly affecting its resonant frequency.

Beyond these interesting conclusions, we need to operate the antenna at 868 MHz for our applications. We opted reducing the electrical length by modifying the 3D configuration of the antenna while keeping the preliminary design unchanged. In the same perspective, a paper has introduce a technique of operating/resonant frequency of the antenna by connecting two metal strands [62]. Inspired by this technique, we investigated the addition of two vertically connected metal arms to the planar antenna using a short transmission line, as seen on the photo in Figure II.16. The width of the arms was adjusted to match the substrate size, and the height was adjusted to achieve a resonant frequency at 868 MHz. The position of the connection line at the edge of the planar antenna was carefully optimized through simulations. As a result, we obtained an operating frequency as close as possible to 868 MHz, with a bandwidth of 30.7 MHz and a maximum gain of +1.5 dBi for A1 ; and a bandwidth of 20 MHz and a maximum gain of +1.1 dBi for A2.

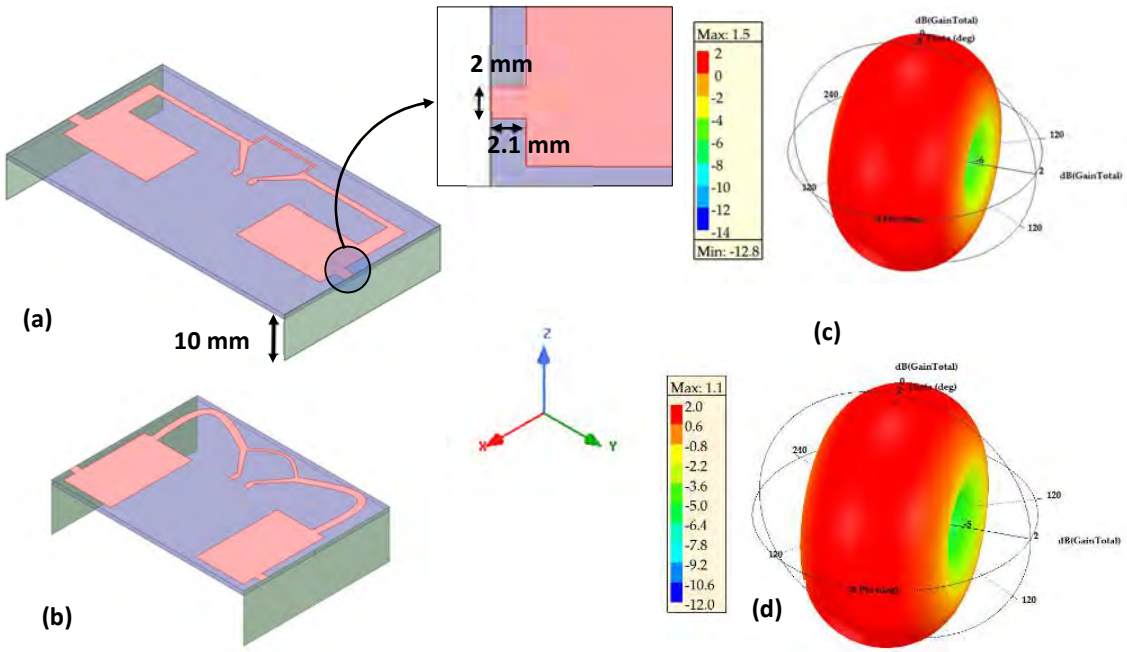

Figure II.16. Geometry of the 3D configuration antenna with the connected metallic arms: (a) Antenna A1 with a dimension of 56 mm x 32 mm; (b) Antenna A2 with a dimension of 40 mm x 30 mm. Simulated 3D gain polar plot at 868 MHz : (c) A1 antenna and (d) A2 antenna.

Subsequently, both antennas were manufactured in an FR4 substrate with a thickness of 0.8 mm. Dipole antennas usually require a balanced-unbalanced (balun) circuit or transition for coaxial measurements. The absence of balun can result in current flowing on the outer surface of the coaxial conductor, leading to measurements interference. However, for the purpose of prototyping and testing convenience using RF cables, we opted for a surface mount coaxial U.FL connector [127]. This connector allows us for easy prototyping and testing with RF cables. It offers several advantages, including low cost, small size, lightweight, and easy mounting. It is strongly used for characterization and RF connections for embedded antennas, especially in IoT applications. Before conducting the measurements on the antennas, a 3D model of the U.FL connector was considered on the simulation for accurate results. Based on the simulation results, we concluded that there was a non-significant difference in antenna performance with the U.FL connector. At the prototyping level, the pads of the connector were soldered to the feed pads of the antenna. The return loss (S_{11}) and the gain measurements were conducted in an anechoic chamber. A compatible coaxial cable was connected to the vector network analyser (VNA) and plugged into the connector for the measurements. The simulation results of the antenna with connector and the measurements are compared.

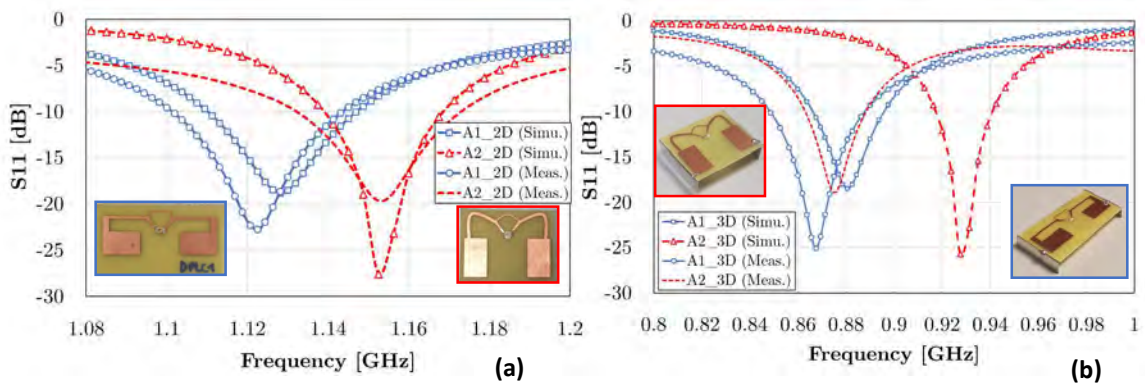

Figure II.17. (a) Comparison between the measured and simulated reflection coefficient of the A1 (blue line) and A2 (red line) antennas on 2D configuration; (b) 3D configuration with vertically connected metal arms of 10 mm.

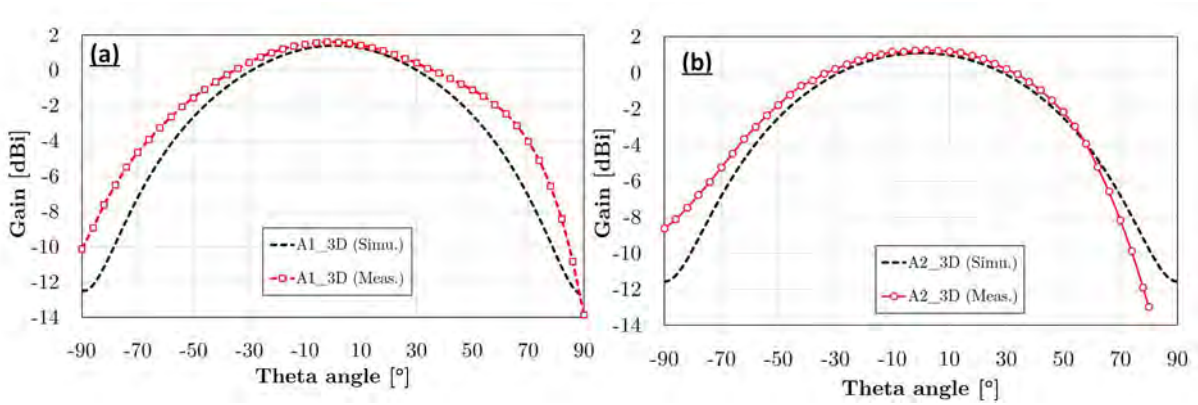

Figure II.18. Simulated (black) and measured (red) of the radiation pattern (gain plot in the E-plane): (a) 3D_A1 antenna and (b) 3D_A2 antenna at the resonant frequency.

As plotted on Figure II.17 (left), the measured return loss of A1 and A2 in the 2D configuration (A1_2D and A2_2D) fits well with the simulation results. This indicates that the measurements obtained with the U.FL connector are reliable. However, a frequency shift is observed in the results with antennas on 3D configuration, featuring two 10 mm high metal arms (A1_3D and A2_3D). This difference can be explained by the soldering effect and assembling tolerances, such as imperfect shape of the metal arms and their connection to the planar dipole. For the measurement of the antenna radiation pattern and gain, a far-field setup with a horn antenna in an anechoic chamber is used. As presented in Figure II.18, the radiation pattern plotted on a half slice in the E-plane remains unaffected by the metallic arms. The measured gain in the E-plane for A1_3D correlates well with the simulation, exhibiting a maximum gain of +1.54 dBi at 868 MHz. While regarding the smallest design A2_3D, there is a slight reduction in the gain of 0.4 dBi compared to A1_3D version.

In conclusion, we have successfully achieved the challenge of miniaturizing the antennas while maintaining satisfactory gain and the bandwidth characteristics. Two interesting design of compact antennas, namely A1_3D and A2_3D, were obtained with dimensions of 56 mm x 32 mm x 10 mm ($0.0004 \cdot \lambda^3$) and 40 mm x 30 mm x 10 mm ($0.0003 \cdot \lambda^3$), respectively. These antennas can be considered as electrically small antennas and ensure a maximum gain on the E-plane of at least +1 dBi, which is +1.05 dBi less than the gain of a half-wave dipole antenna (+2.15 dBi). Table II.3 compares the performances and size of theses antennas with state-of-the-art designs operating in the ISM 868 MHz or ISM 915 MHz frequency bands. It should be note that the proposed antennas were implemented on a FR4 substrate, which is generally more lossy compared to the substrates used in other state-of-the-art designs.

Our proposals are smaller than the 3D antennas in [130] and [131], and exhibit a good trade-off between size, gain and bandwidth, making them suitable candidates for compact energy harvesting systems.

Table II.3. Comparison with the different antennas for compact wireless devices in the state of the art.

Ref.	Freq. (MHz)	Type	Max gain (dBi)	BW (MHz)	Substrate	size (mm x mm x mm)
[128]	878	Dual Band PIFA	+1.8	80 (855-937)	Duroid 5880	80 x 45 ($0.03\cdot\lambda^2$)
[129]	868	UCA PIFA	+0.71	23 (857-880)	FR4	34 x 80 ($0.02\cdot\lambda^2$)
[62]	915	Slot loaded DB folded dipole	+1.87	--	Arlon 25N	60 x 60 x 60 ($0.006\cdot\lambda^3$)
[130]	868	3D single arm bowtie	+0.19	90	Ultralam	50 x 50 x 10 ($0.0006\cdot\lambda^3$)
[131]	868	Strip-SSRR antenna	+1.7	14.3 (863-877)	Foam ($\varepsilon_r \approx 1$)	26.4 x 26.4 x 33.8 ($0.00056\cdot\lambda^3$)
This work	868	A1_3D	+1.54	32 (865-897)	FR4	56 x 32 x 10 ($0.0004\cdot\lambda^3$)
		A2_3D	+1.1	26 (862-888)		40 x 30 x 10 ($0.0003\cdot\lambda^3$)

BW: Bandwidth, PIFA: Planar Inverted F-Antenna, DB: Dual Band

2.3. Implementation of the rectenna

The rectifier and the antenna designed on the previous section, were integrated on the same Printed Circuit Board (PCB), resulting in a compact rectenna with an improved power conversion efficiency without the need of additional transition connectors. Figure II.19 illustrates how the small rectifier was seamlessly integrated between the dipole arms without increasing the antenna's size. The pitch of the antenna input was carefully adjusted to match the input coupled lines of the rectifying circuit. By using the A1_3D and A2_3D antennas, we were able to create the R1_3D and R2_3D rectennas, respectively.

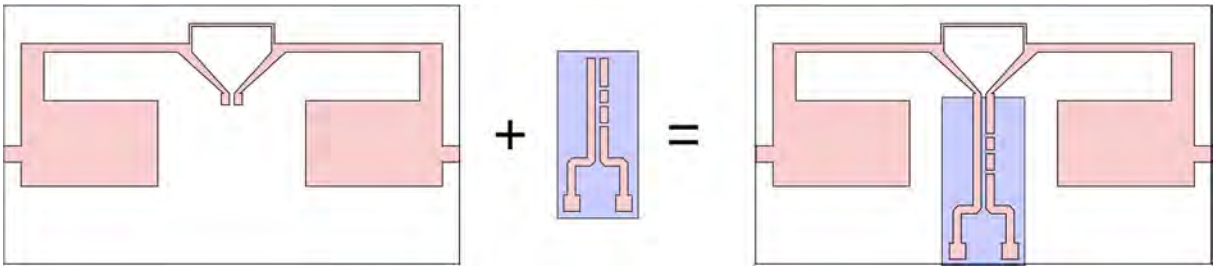

Figure II.19. Formation of the R1_3D rectenna with the antenna connected to the rectifier. Top layer of the rectenna on pink and bottom layer representing the ground plane on purple.

The rectennas performances were evaluated in an anechoic chamber to minimize any RF wave interferences. The measurement setup consists of a Patch antenna with a gain G_t around +9 dBi at 868 MHz, which was connected to the RF signal generator Anritsu MG3694B. The signal generated is a Continuous Wave (CW) with a power level of P_{RF}. The antenna radiates an EM field to the rectenna under test, which was positioned at a distanced (d) of 1.5 m in the far-field region of the transmitting patch antenna. The harvested DC voltage (P_{DC}) was measured using a multimeter across a resistive load connected to the rectenna's output. To automate the measurement process, a homemade data acquisition interface implemented in LabVIEW was used. The setup is shown in Figure II.20 (d).

The respect of the free space conditions enables the computation of the rectenna efficiency η (%) using equation (II.5), which represents the ratio between the measured harvested DC power and the received RF power converted by the antenna.

$$\eta\ (\%) = 100 \cdot \frac{P_{DC}}{P_{RF}} = 100 \cdot \frac{P_{DC}}{S \cdot A_{eff}} \qquad (II.5)$$

$$S = \frac{P_t \cdot G_t}{d^2 \cdot 4 \cdot \pi} \cdot 100 \qquad (II.6)$$

$$A_{eff} = \left(\frac{G_r \cdot \lambda^2}{4 \cdot \pi}\right) \qquad (II.7)$$

The efficiency of the rectenna or power conversion efficiency (PCE) is expressed through the RF power density (S) in µW/cm² at a distance (d) from the centre of the transmitted antenna and the effective aperture area (A_{eff}) of the receiving antenna, considering the antenna gain G_r. These equations assume a perfect alignment of the transmitting and receiving antennas in E-plane at the same height. The Figure II.20 (a) shows the evolution of the harvested DC voltage across the resistive load between 820 MHz and 920 MHz for different power density level. The measurement results for the R1_3D rectenna prototype are represented by dashed lines, while the results for the R2_3D rectenna are represented by solid lines. The maximum performance of the R1_3D rectenna prototype is achieved at 865 MHz, while for the R2_3D rectenna, it is achieved at 867 MHz. These maximum functioning frequencies are independent of the receiving power level.

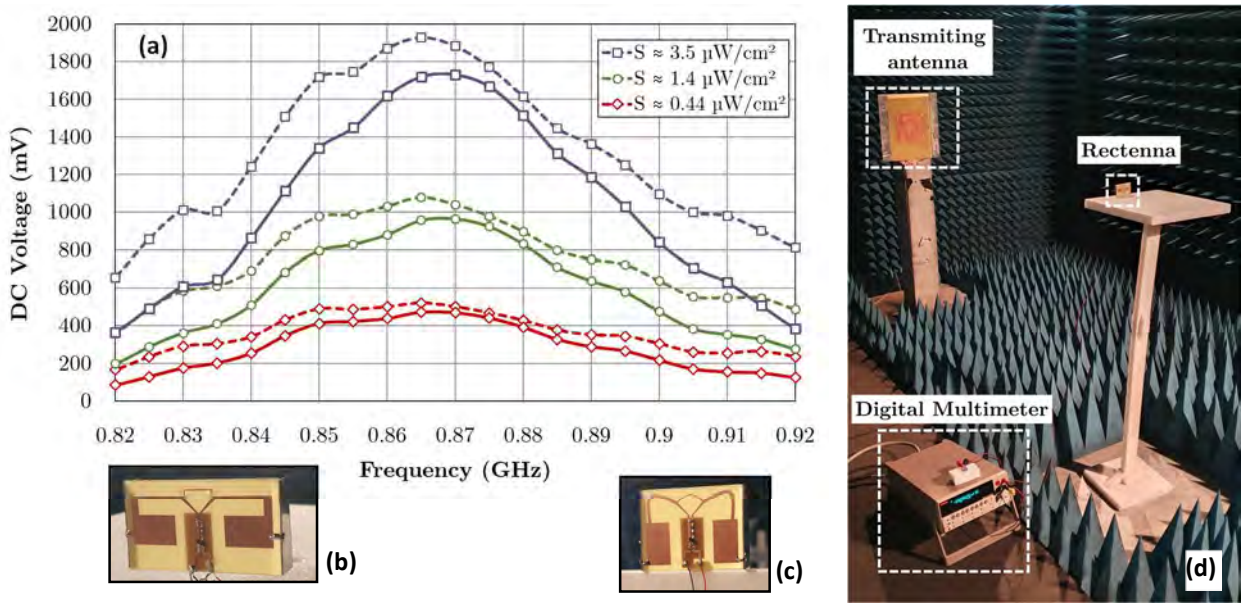

Figure II.20. (a) Harvested DC voltage across the 10 kΩ load as function of the power density levels for R1_3D (dashed lines) and R2_3D (solid lines); (b) Photo of the R1_3D; (c) Photo of the R2_3D; (d) Photo of the measurement setup in an anechoic chamber.

We can also remark that voltage obtained with both rectennas is relatively similar for low power density levels below 0.5 µW/cm². The small enhancement in the antenna gain of +0.4 dBi for R1_3D does not significantly improve the rectenna performance due to the non-linearity of the diode; resulting in a slow increase in the harvested voltage for input power lower than -13 dBm (as observed in Figure II.10 (b)). The prototyped rectennas can exhibit more than 400 mV with a power density higher than 0.5 µW/cm² (equivalent to received power of around -12 dBm) at 868 MHz.

The experimental power conversion efficiency is estimated to be more than 60% at this power density level. These measured performances demonstrate the feasibility of powering an Integrated Circuit (IC) as the BQ25505 [9], which requires a minimum cold start voltage at least equals to 330 mV, using a low power density of 0.3 µW/cm² from the incident EM waves.

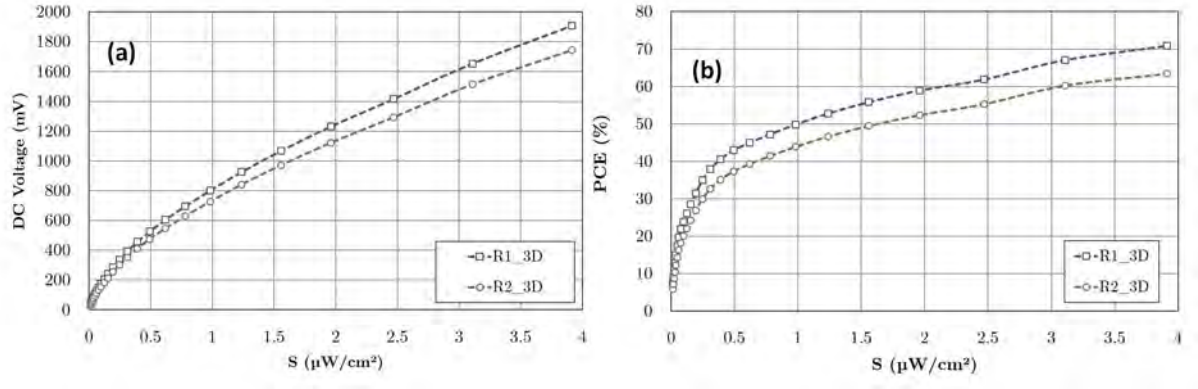

Figure II.21. Measurements obtained at 868 MHz with the power density variation across the 10 kΩ resistive load for the manufactured rectennas: (a) The measured DC voltage; (b) The power conversion efficiency.

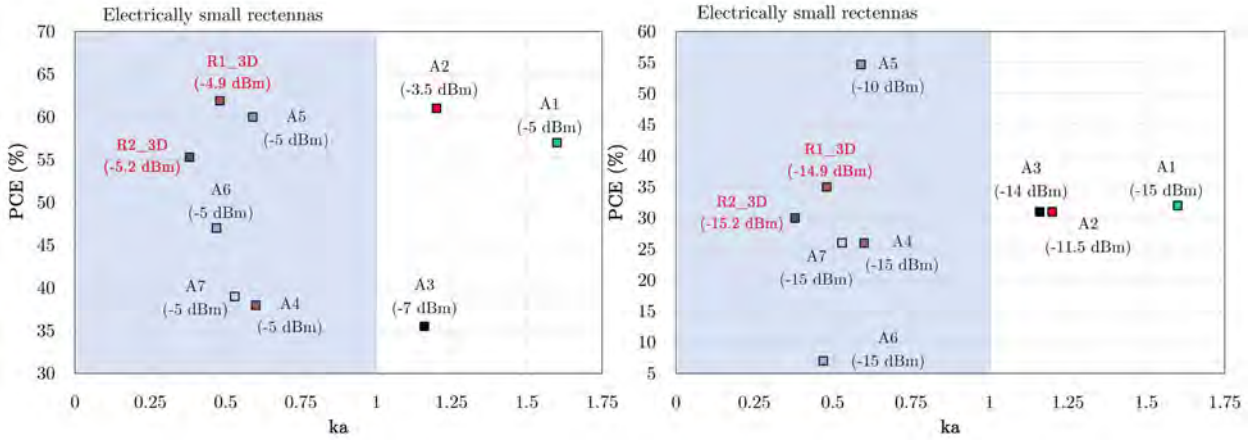

Figure II.22. These plots of the PCE versus the electrical size (ka) compare our rectennas with those in the state of the art for about -5 dBm (right) and -15 dBm (left).

The Table II.4 reports the overview of the key characteristics and performances of the proposed rectennas compared to those in the state-of-the-art operating with similar illuminating power density. Furthermore, the graph in Figure II.22 represents the PCE of rectennas as function of the electrical size. It can be observed that our rectennas is not only electrically small (ka<1), but also outperform others with a PCE exceeding a 55% with a RF input power of about -5 dBm. Among the rectennas, R1_3D is stands out as the most promising candidate, despite the use of a non-optimum load of 10 kΩ as in A5 and A1. Our proposal demonstrates a remarkable advantage, particularly when considering lower available power received by the rectenna, approximately -15 dBm.

This highlights the robustness and effectiveness of our design in extracting usable power from low-intensity RF signals. Additionally, it is interesting to note that the PCE of R2_3D is comparable to that of A1, which is a high gain antenna of 3.47 dBi with a low loss tangent of 0.0009, and an optimum load of 2.5 kΩ). Hence, this makes R2_3D a good candidate for achieving the best trade-off between compactness and efficiency.

3. Conclusion

The works presented in this chapter, introduce original and electrically small rectennas functioning at 868 MHz. The design and architecture of the rectennas were carefully chosen based on specific requirements, including small size, high efficiency for low RF input power, and cost-effective manufacturing. All prototypes were implemented on FR4 substrate using readily available SMD components.

The first part of the study focused on the development of an efficient voltage doubler rectifier using a series-pairs SMS7650-005LF Schottky diodes. The rectifier was optimized for RF input power around -15 dBm. To emulate the input impedance of a power management unit and to ensure the needs of powering wireless sensing devices, a resistive load of 10 kΩ was chosen. The rectifier demonstrated good performance under these conditions. In the second part, compact 3D antennas were designed and thoroughly characterized in an anechoic chamber. Both proposed antennas A1_3D and A2_3D are considered electrically small antennas, with dimensions of 52 mm x 32 mm x 10 mm and 40 mm x 30 mm x 10 mm, respectively. Additionally, they achieved a gain higher than +1 dBi. The antennas were carefully optimized and demonstrated reliable performance. The final stage involved integrating the rectifier and the antenna to form a complete rectenna prototype. They independently achieve an RF-to-DC conversion efficiency of over 40 % when subjected to an illuminating power density of 1 µW/cm² across a non-optimum load of 10 kΩ. Comparing the proposed rectennas with the designs reported in Table II.4, our rectennas are ultra-compact and exhibit outstanding performances. The obtained experimental results have confirmed the suitability of the proposed rectennas for RF wireless power transmission. However, further optimization is still possible for our rectennas. This includes exploring the use of lower loss tangent substrates, such as those used in A1, A6, and A7, and increasing performance by adopting complex-conjugate impedance matching between the antenna and rectifier without the use of lumped components that may introduce additional losses. In the next studies, presented in chapter III, the proposed rectenna will be used as a power-harvesting solution for a battery-free wireless sensing node and potentially be embedded in inaccessible environment requiring good performances for low received power.

Table II.4 Study of the compact and electrically small rectennas in the state of the art.

Geometry	References	Freq. (GHz)	Diode	Substrate	Input Power (dBm)	S ($\mu W/cm^2$)	PCE (%)	R (Ω)	Gr (dBi)	Rectenna size (mm x mm x mm)	ka
2D	[132] = A1	0.800	2* SMS7630-0079	Taconic TLY-5-0100 (er =2.2; tanδ =0.0009)	-15 -10 -5 -5.5*	0.13* 0.4* 1.4* 1	32%* 44%* 57%* 54%*	2.5¤	3.47	130 x 140 x 0.254	1.6 (a = 95.6 mm)
	[69] = A2	1.8	SMS7630	Teflon F4B (er =2.55 ; tanδ =0.001)	-11.5 -7.1 -3.5	1.6 4.5 10	31% 54% 61%	12	3	45 x 45 x 0.8	1.2 (a = 32 mm)
	[65] = A3	0.86	HSMS2850	FR4 (er =4.4 ; tanδ =0.02)	-14* -7 * -4*	0.21 1.1 2.2	31% 35.5% 37%	10	2.6	110 x 60 x 0.8	1.13 (a = 62.7 mm)
	[133] = A4	0.920	SMS7630	(er =3.4; tanδ =0.0015)	-15 -10 -5	NR	26%* 34% 38%*	8	0.8	45.5 x 43 x 0.2	0.6 (a = 31.5mm)
	[134] = A5	0.868	HSMS2852	FR4 (er =4.28 ; tanδ =0.02)	-20 -10 -5	NR	33.8% 54.7% 60%	10¤	0.23	54 x 32 x 1.6	0.59 (a = 32.2mm)
	[135] = A6	0.915	HSMS286C	Taconic TLY & Duroid 5880 (er =2.2; tanδ =0.0009))	-15 -10 -5 0	0.27** 0.85** 2.7** 8.7**	7%* 25%* 47%* 65%*	5.1	1.27	Circular (R=49.4)	0.47 (a = 24.7 mm)
3D	[131] = A7	0.868	HSMS-285B	Taconic TLY-5 (er =2.2; tanδ =0.0009)	-15 -10 -8.4 -5	0.23* 0.7* 1* 2.2*	26%* 32%* 34%* 39%*	2.193¤	1.8	19.21 x 19.21 x 52.06	0.53 (a = 29 mm)
	This work R1_3D	0.868	SMS7630 005LF	FR4 (er =4.4 ; tanδ =0.02)	-14.9 -8.9 -4.9	0.25 0.95 2.5	35% 49.8% 61.9%	10	1.7	52 x 32 x 10	0.48 (a = 26.5mm)
	This work R2_3D	0.868	SMS7630 005LF	FR4 (er =4.4 ; tanδ =0.02)	-15.2 -9.2 -5.2	0.25 0.95 2.5	30% 43.9% 55.3%	10	1.1	40 x 30 x 10	0.38 (a = 20.7mm)

*Estimated from graph or calculated from given data and figures; ¤ Optimum load, NR: Not reported

III. Battery-free Wireless Sensing Node for Structural Health Monitoring Applications

1. Introduction

The development of a wireless power system through a rectenna aims to feed low-power consumption devices. It eliminates the need for batteries, reduces the weight of the device, and provides longer operating times. This is particularly beneficial for inaccessible systems that require maintenance, such as battery replacements. Building upon the rectenna developed in the previous chapter, this section presents the implementation of wireless sensing nodes to be embedded in reinforced concrete beams. These nodes are designed to measure physical parameters such as temperature, humidity, and resistivity, and store the data for structural health monitoring. While similar concepts exist with RFID technology, it is limited by data storage capacity and short reading distances. Multiple wireless powered sensor implementations based on LoRaWAN and BLE technology will be discussed, including their advantages and disadvantages across various designs.

The second part of this work focuses on combining BLE technology for wireless sensor data communication with UWB for geolocation functionality. This design serves as a proof of concept to test the power supply of the sensing nodes using the EH stage of a geolocation module developed by UWINLOC company. The geolocation module (UGM) will be detailed in Chapter **Error! Reference source not found.**

The research was made possible via the McBIM (Material communicating with the Building Information Modeling) project, funded by the French National Research Agency (ANR). This project aims to implement a communication system for civil engineers [136]. It is part of a colleague Gael Loubet's thesis, conducted within our team in the laboratory. Further details and in-depth results on the entire system and the different implementations of battery-free sensing nodes are presented in his manuscript [137]. In our work, we had only focused on their functioning thanks to RF Wireless Power Transmission facilities.

2. Remotely Powered Battery-free wireless sensor nodes

2.1. Introduction of the targeted application : Structural health monitoring

The main objective of the application is to accurately predict the state of health of the material, specifically a concrete beam in the McBIM project. The goal is to ensure safe usage and anticipate potential damages by providing timely maintenance solutions. The study involves measuring various

physical parameters of the structure and/or the environment throughout its lifecycle, including manufacturing, drying, construction, operation, demolition, and recycling.

Parameters such as temperature, humidity, pH, corrosion, deformation or stress, crack detection, and location are commonly measured [138]–[141]. These physical measurements need to be stored, processed, and exchanged using a new concept called communicating material, which is introduced as a novel paradigm for industrial information systems [142].

The technical solution proposed for this project is to design a communicating concrete that incorporates a low-energy wireless sensor network capable of managing and exchanging data with a Building Information Modeling (BIM) platform. As depicted in Figure III.1, the communicating concrete solution consists of a Wireless Sensor Network (WSN) comprising two types of nodes: sensing node (SN) and communication node (CN). The task of the SN is to periodically monitor and transmit the physical data to a remote server using the BIM standard. Since the SNs need to be embedded in concrete, they must meet the requirements of the IoT paradigm, being completely wireless, low power, and robust throughout the structure's lifespan. On the other hand, the CNs are responsible for retrieving, processing, storing, and exchanging the data transmitted by the SNs with other CNs. Ensuring the autonomy of SNs in concrete is critical, and battery-powered solutions are not feasible due to their limited lifespan. Ambient Energy Harvesting (EH), which efficiently powers devices without batteries using ambient energy sources, serves as a viable alternative. Among various EH solutions, RF EH or WPT solutions are considered most suitable for wireless sensors embedded in an air cavity within reinforced concrete due to their specific advantages.

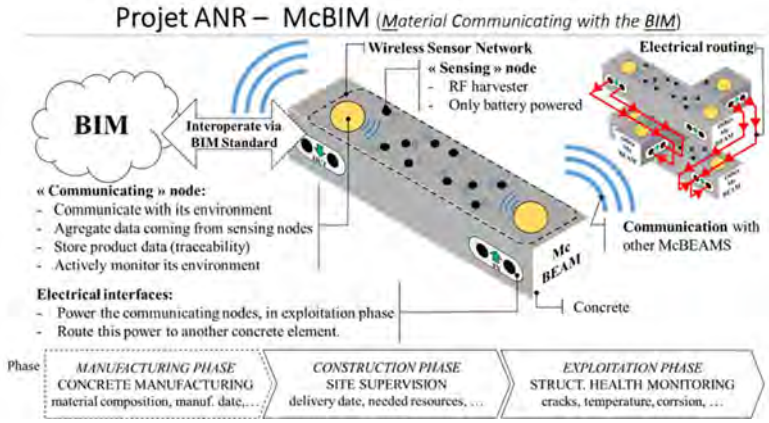

Figure III.1. Description of the ANR McBIM Project

The integration of sensing nodes (SNs) into concrete beam cavities can be done in various ways, each with its own advantages and disadvantages. One option is to integrate only the sensors into the concrete and wire them to the rest of the devices (microcontroller electronic board, rectenna, and data transmitting antenna), allowing access to the SN for maintenance or hardware/software modifications. Another option is to embed the entire electronic part of the SN into the concrete while placing the antennas externally. This approach restricts access to the SN once the concrete has been molded but helps protect it from damage or tampering, except for the antennas. However, these first two solutions do not account for the effect of concrete on the propagation of electromagnetic waves.

In this project, the most secure solution is adopted, which involves embedding the entire battery-free sensing node (including the electronic and antenna components) into the concrete cavity. This approach presents two main challenges: (1) Harvesting electromagnetic waves transmitted through wireless power transmission; (2) Transmitting the data measured by the sensors via wireless communication. The attenuation of electromagnetic waves through concrete depends on its

composition, the density of metallic reinforcement, porosity, and dielectric properties, which are influenced by the condition of the concrete (wet or dry).

However, this study does not cover the investigation of these factors and instead focuses primarily on the feasibility of wireless energy transmission through a dry concrete structure. Considering the low available power density for energy harvesting and the attenuations within the concrete structure, the proposed strategy is to periodically receive data from the sensors instead of continuous data reception. The harvested power also depends on the targeted frequency, as higher frequencies result in greater free space losses. Moreover, the maximum emitted power is regulated based on frequency band and regional location [143]. For the purposes of this study, it is considered sufficient to obtain measurements, for example, once an hour, once a day, once a week, or once a month to monitor the structural health of reinforced concrete in different life cycle phases. As mentioned earlier, this work is part of a larger project and another PhD thesis. The overall system architecture and the communicating node are presented in that thesis.

2.2. LoRaWAN-based Sensing Node (LSN)

The proposed wireless system, intended to wirelessly power a sensor node embedded in a concrete cavity, is illustrated in Figure III.2. The aim is to wirelessly power the sensor node using a wireless power transfer (WPT) interface, which includes a rectenna, and transmits data through LoRaWAN (Long Range Wide-Area Network) frames to a gateway. Initial communication tests conducted through reinforced concrete walls confirmed the suitability of LoRaWAN technology. Despite its advantage of providing long-range communication capabilities (up to tens of kilometers), it consumes relatively higher power compared to Bluetooth Low Energy solutions, which will be presented later. The sensing node performed measurements in a punctual and temporal manner, without the need for internal storage memory, in order to reduce power consumption. The different components used in the system are generic and have been carefully selected to ensure efficient operation and low power consumption. Unidirectional data communication is employed from the sensing node to the communicating node. The transmitter of the sensing node is responsible for transmitting a small amount of data collected by the sensor, over a distance of at least a few tens of meters, from inside the material (in this case, reinforced concrete) to the communicating node(s). For the communication functionality of the sensing node, the compact and cost-effective module CMWX1ZZABZ-091 LoRaWAN from Murata [144] is utilized. This module incorporates an SX1276 LoRa transceiver from Semtech [145] and an STM32L072CZ microcontroller from STMicroelectronics [146]. To facilitate wireless data transmission, a conventional monopole antenna known as the Whip antenna (ANT8WHIP3H) is employed. Concerning the energy harvesting features, the rectenna captures electromagnetic (EM) waves emitted by a dedicated RF source, and then transfers the harvested energy to a power management unit (PMU) (Texas Instruments BQ25504). This energy is stored in a 22-mF supercapacitor (AVX BZ01CA223ZSB). Once a sufficient amount of energy is accumulated (determined by an activation threshold of 5.25 V), it is used to power the active components through a dc-to-dc regulator (Texas Instruments TPS6303x). The supercapacitor is discharged until it reaches a deactivation threshold of 2.30 V.

The active components consist of a LoRaWAN communication module (Murata CMWX1ZZABZ-091), which includes a microcontroller unit (MCU) and a LoRa transmitter, as well as a temperature and humidity sensor (Texas Instruments HDC2010). During this study, various prototypes were developed. However, we will focus solely on the energy harvesting aspect in order to enhance performance of the SN in a challenging environment with relatively low available power density.

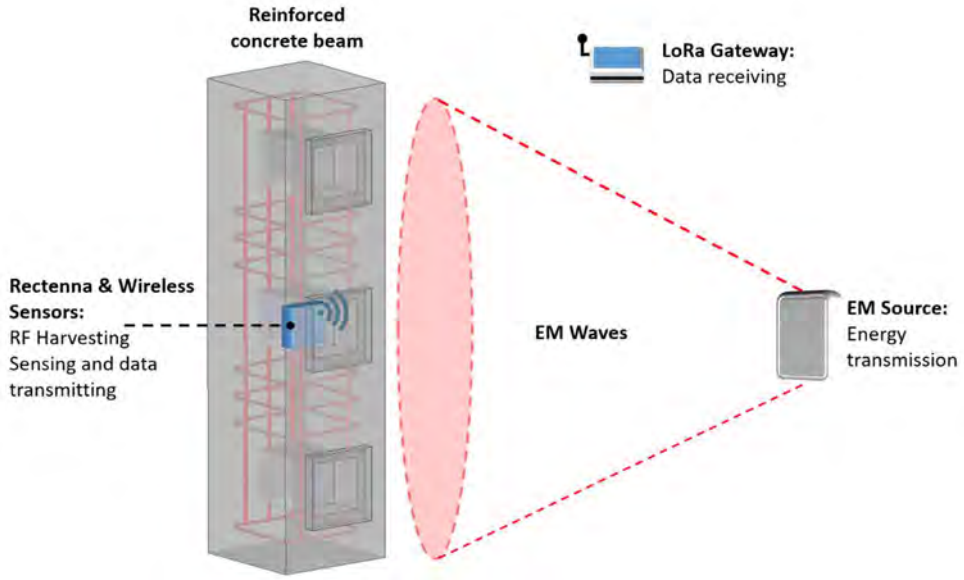

Figure III.2. Schematic of the proposed wireless power system for the sensor node.

2.2.1. Prototype 1 of the proposed sensing node (LSN1)

At the sensing node level, the initial prototype involved two separate antennas: one for capturing electromagnetic waves for energy harvesting and the other dedicated to LoRaWAN communication. Figure III.3 illustrates the implementation of this architecture. For the energy harvesting aspect, we used the rectenna developed in Chapter II, which proved suitable for testing the prototyped sensing node. Its compact size facilitated integration with the sensing node and embedding within the concrete cavity. Among the two developed rectennas, R1_3D was chosen due to its higher antenna gain and compact power conversion efficiency (PCE) compared to R2_3D. Experimental results for the R1_3D rectenna, with dimensions of 52 mm x 32 mm x 10 mm, demonstrated a PCE of 35% with an equivalent power density of 0.25 µW/cm² or an RF input power of -14.9 dBm. This corresponds to a harvested DC voltage of 336 mV or 11.3 µW on a 10 kΩ load. These promising results indicate the rectenna's ability to meet the cold-start condition of the BQ255504 power management unit (PMU) in the sensing node, which requires a minimum cold-start input power of 15 µW. It's important to note that these performances were achieved in an anechoic chamber and are expected to degrade when the rectenna is embedded in the concrete structure. Therefore, optimization of the energy harvesting component in the sensing node is necessary to ensure proper operation within the concrete cavity. Indeed, the objective is to optimize the sensitivity of the rectifier in order to maximize the harvested DC power at low input power levels.

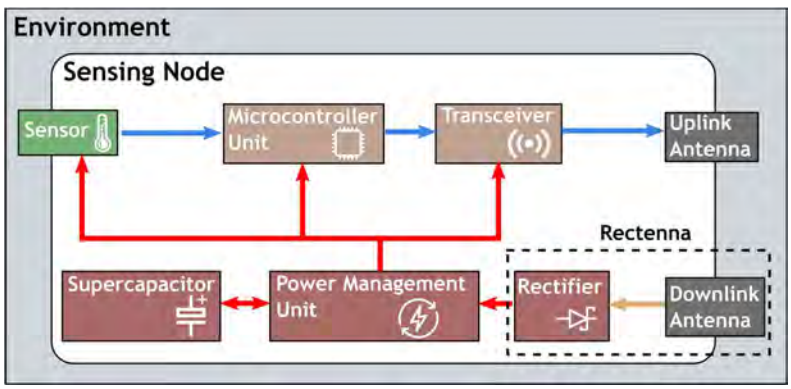

Figure III.3. Bloc diagram of the proposed generic architecture of the sensing node V1.

Optimizing the rectenna's sensitivity to low RF input power levels can be achieved through various methods. These include using a specific rectifier topology (such as a multiband rectifier or a resistance compression network), employing CMOS technology instead of commercial Schottky diodes, increasing antenna gain, and optimizing the transmitting signal. For our experimentation purposes, we aim to choose the simplest solution to implement while still using the previously developed rectenna. Thus, the most suitable solution was to enhance the antenna gain of the rectenna. However, it is challenging to design an antenna suitable for operation within a concrete cavity. Additionally, the propagation of waves through concrete depends on several factors, including the composition, density, moisture, and porosity of the concrete material. These factors significantly impact the antenna's performance, leading to impedance mismatch and alterations in its radiation pattern. The propagation behavior of electromagnetic waves through concrete varies depending on the operating frequency. Higher frequencies have limited ability to penetrate concrete. Therefore, the choice of frequency in the European ISM 868 MHz band was made carefully. This frequency allows for better wave penetration, offers high maximum power emission according to the standard ([147]), and is available for LoRaWAN technology. In existing literature, some studies have investigated antennas embedded in concrete for different applications. For instance, a microstrip patch antenna operating at 2.5 GHz was designed for civil engineering applications [148]. Another study [149] presented the design of a UHF RFID tag antenna suitable for embedding in a concrete floor. This antenna consisted of a ceramic patch, a parasitic patch, and a metal cavity, which improved the overall antenna gain. To improve the antenna, gain and minimize the influence of the cavity on radiation, we considered two approaches: (1) Covering the concrete beam hole with a metal cavity to reduce losses when the rectenna is embedded in the concrete; (2) Using the grounded bottom side of the sensing node, which would serve as a reflector plane. Both methods would increase the maximum gain of the antenna in a specific direction and consequently enhance the power harvested by the rectenna. However, they may also reduce the beamwidth of the antenna. Additional simulations were conducted to ensure impedance matching to 50 Ω and determine the optimal distance between the antenna and the reflector plane, as well as the bottom of the cavity.

- *Antenna gain enhancement with reflector plane*

The antenna, when positioned at a specific distance from the metal plane, generates a unidirectional radiation pattern. Theoretically, it is known that the antenna should be placed at a distance of a quarter-wavelength from the reflector plane to ensure that the reflected wave is in phase and enhance the antenna gain. In Figure III.4, the SN PCB board, which acts as the reflector plane, is positioned parallel to the co-polarization plane of the antenna. Through simulations, an optimal distance of 6 cm (approximately λ/5.5 at 868 MHz in free space) was determined to concentrate the maximum gain in a single E-plane lobe and minimize back lobe radiation.

Additionally, the width of the metallic arms was adjusted to 8 mm (instead of the initial 10 mm). The performance of the two antennas, namely the 3D dipole antenna (DA) and the DA with a rectangular reflector plane (DARP) measuring 140 mm x 90 mm, is presented in Figure III.5. For the DARP, the antenna was connected to the PCB board using a nylon stem to maintain the simulated height of 6 cm. The return loss (S11) plots demonstrate that both antennas are well-matched, with a slight frequency shift of 15 MHz due to fabrication tolerances, such as imperfect shape of the metallic arms and the connection with the planar dipole. The measured gain in the E-plane is +1.54 dBi for DA and +5 dBi for DARP, which closely aligns with the simulated gain of +5.68 dBi for DARP.

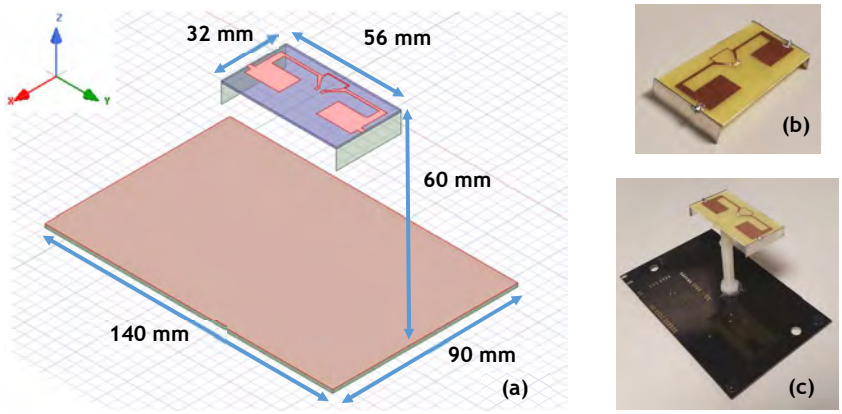

Figure III.4. (a) Simulation model and geometries of the DARP antenna; (b) Manufactured DA antenna; (c) Manufactured DARP antenna.

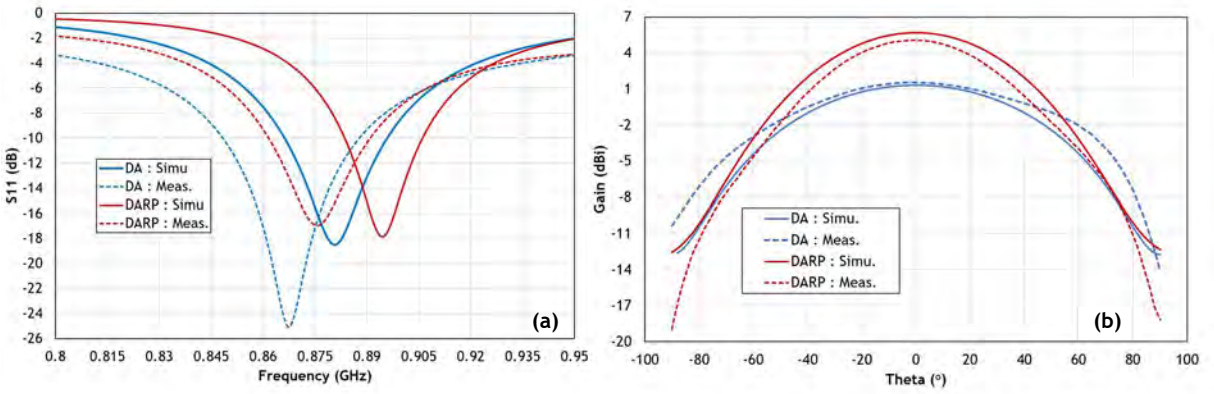

Figure III.5. (a) Comparison of the simulated and measured reflection coefficient of DA and DARP antennas; (b) Simulated and measured radiation patterns (gain in dBi) of the DA and DARP antennas in the E-plane at 868 MHz.

- *Antenna gain enhancement with metal cavity.*

Through simulations, the size of the metal cavity and the positioning of the antenna from the bottom side were optimized to increase the antenna gain and prevent detuning of the antenna within the concrete. A smaller metal cavity with dimensions of 120 mm x 130 mm x 100 mm was designed to fit the 150 mm x 150 mm x 150 mm, concrete beam hole without its cover. The antenna was placed 10 cm from the bottom of the cavity, and the metallic arms were adjusted to 7.5 mm. The antenna with the metallic cavity (DAMC) was prototyped using an aluminium plate, adhering to the dimensions obtained from the simulations. Figure III.7 illustrates the comparison between simulation and experimental results for both antennas. The measured return loss (S11) values for the DA and DAMC antennas were -18.8 dB and -22.2 dB, respectively.

The radiation pattern of the manufactured antennas was measured in an anechoic chamber, and the measured and simulated gain in the E-plane (a vertical cut plane orthogonal to the antenna's horizontal plane) aligned well. Consequently, by incorporating the metallic cavity, the antenna gain improved by a factor of 2.5, reaching up to +4.5 dBi. Therefore, with both methods, the antenna gain has more than doubled. However, it is worth noting that the simplest solution is to utilize the bottom side of the SN board as a reflector plane. On the other hand, the antenna with the metallic cavity still offers the advantage of a better aperture angle.

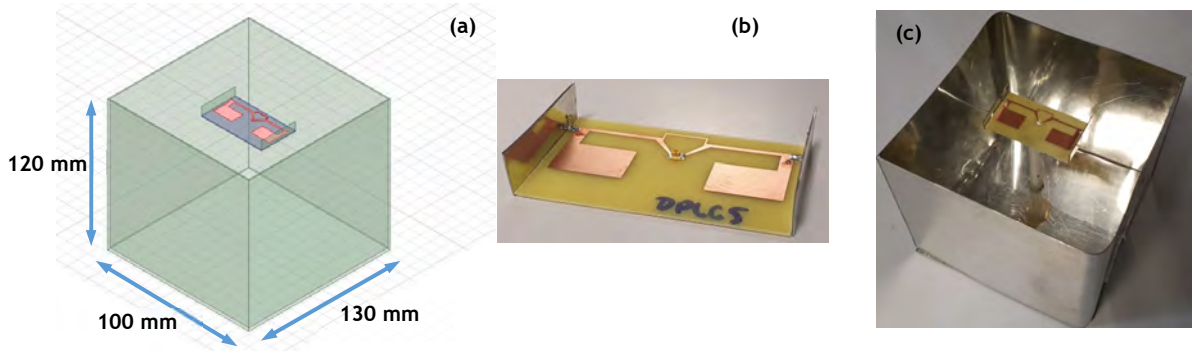

Figure III.6. Simulation design and photo of the manufactured prototype of the antenna with and without the metal cavity.

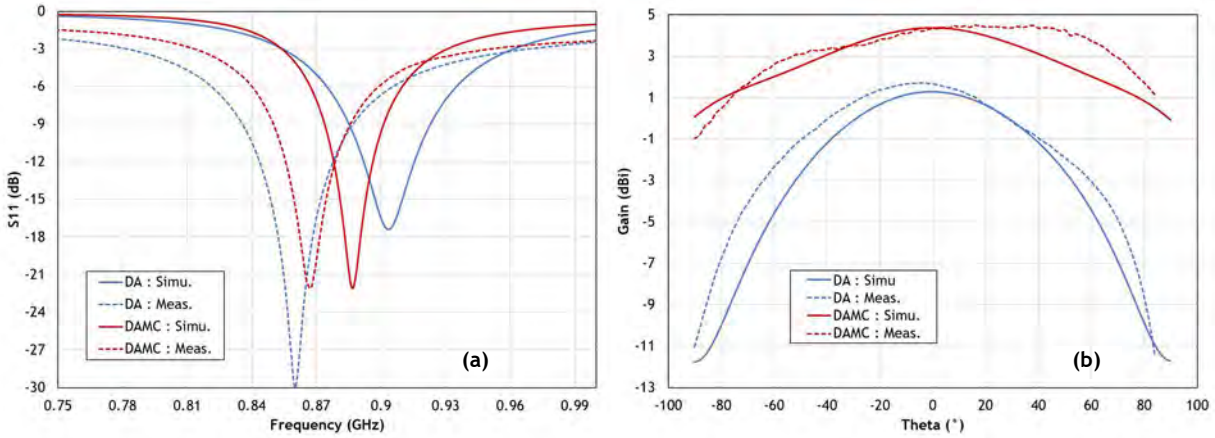

Figure III.7. (a) Comparison of the simulated and measured reflection coefficient of DA and DAMC antennas; (b) Simulated and measured radiation patterns (gain in dBi) of the DA and DAMC antennas in the E-plane at 868 MHz.

- *Rectenna performances with the improved antenna*

The final design involves replacing the DA antenna with a rectenna to evaluate its performance with the improved gain achieved through the reflector plane and the metal cavity. Two prototypes were tested: the rectenna placed inside the metal cavity named RMC, and the rectenna positioned on the bottom of the SN PCB board named RPB. Their performances will be compared with the one without any reflector structure, referred to as RA. The experimental setup was placed inside an anechoic chamber. It involved illuminating the rectenna under test, positioned in the far-field region of the transmitter, with a linearly polarized E-Field. The transmitting patch antenna was connected to an Anritsu MG3694B power generator via a coaxial cable. To ensure accurate measurements, the insertion losses through the RF cable used to connect the RF source to the transmitting antenna were measured using a power meter and subtracted from the transmitted RF power. The harvested DC voltage across a 10 kΩ load was measured using a multimeter. The measured DC voltage of the rectenna as a function of frequency indicates that the use of a reflector does not shift the optimum working frequency of the rectenna. All prototypes exhibit their maximum harvested DC voltage close to the targeted frequency of 868 MHz. There is a clear improvement in the harvested DC voltage with the use of a reflector. While the rectenna RA without reflecting element, achieves a voltage of 1.97 V, the rectennas RPB and RMC achieve voltages of 2.7 V and 2.6 V, respectively, representing a growth rate of at least 31%. When it comes to higher received power by the rectenna, RA demonstrates higher efficiency than the other prototypes, reaching a maximum efficiency of 70%.

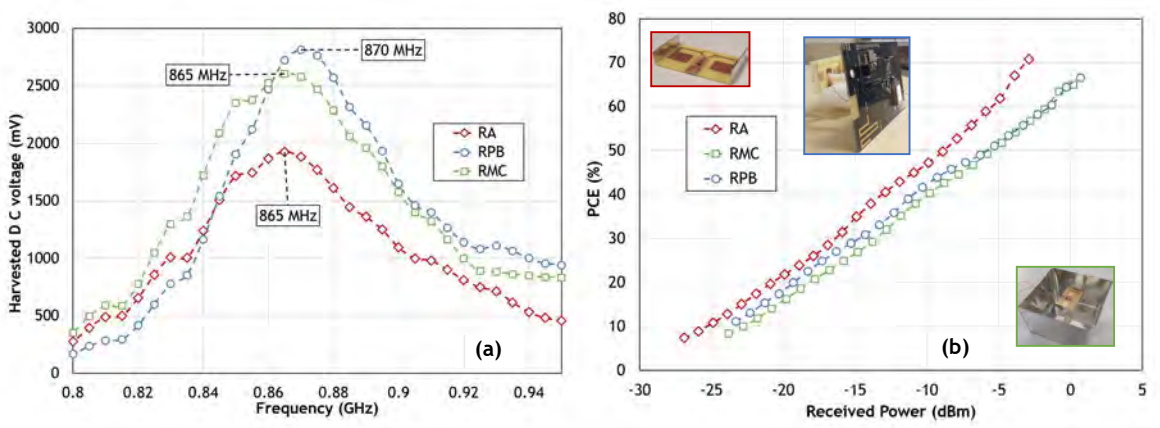

Figure III.8. (a) Measured dc voltage of the manufactured rectennas over the frequency in anechoic chamber at a power density of about 3.4 µW/cm². (b) Computed RF to dc conversion efficiency over the received power by the rectenna at 868 MHz across a 10 kΩ load.

The increase in antenna gain does not necessarily result in an increase in rectenna power conversion efficiency (PCE) due to Schottky diode saturation when receiving excessive power (with a higher gain antenna). However, both RMC and RPB maintain a good efficiency of about 65% with a received power of 0 dBm or an equivalent power density of 3.9 µW/cm². The primary goal of increasing antenna gain was to enhance the rectenna's sensitivity for operating the PMU in cold-start mode at low power levels. The summary Table III.1, presents the harvested DC power and PCE obtained with each rectenna. It is worth noting that with the flat reflector plane (representing the ground plane of the SN), the rectenna's sensitivity has been halved from 0.31 µW/cm² to 0.16 µW/cm² for a minimum cold-start input power of 15 µW. Additionally, the sensitivity has decreased by a factor of 2/3 with the metal cavity. With the same power density reaching the rectennas (0.98 and 3.91 µW/cm²), the RF received power is higher thanks to the reflectors, resulting in more than doubled harvested DC power.

Table III.1. Summary table of the rectennas performance for different power density level at 868 MHz and sensitivity assessment for cold-start working conditions of the PMU BQ25504.

Rectenna	Antenna gain (dBi)	Power density (µW/cm²)	RF Received Power (dBm)	Harvested DC Power (µW)	PCE (%)
RA	+1.4	0.31 (S)	-13.9	15.48	34.9
		0.98	-8.9	64.26	49.8
		3.91	-2.9	363.7	70.8
RPB	+5	0.16 (S)	-13.3	15.49	33.1
		0.98	-5.3	151.0	51.1
		3.91	+0.7	783.6	66.6
RMC	+4.5	0.19 (S)	-12.8	16.85	32.0
		0.98	-5.8	129.5	49.2
		3.91	+0.2	682.0	65.0

*S refers to sensitivity

Therefore, it can be expected to operate the battery-free sensing node embedded in the concrete cavity at a lower power density, allowing for a greater distance or faster operation with the same power density.

- *Battery-Less System Performance Measurements*

In this section, we focus the study on the wireless power transmission aspect for the operation of the sensing node. The SN used for the experimentation has been fully characterized and tested, as presented in the PhD manuscript [150]. In the paper, the SN, referred to as SN4, requires 11 mJ for the initialization step without any sensor and 143.4 mJ for the full process with the HDC2010 temperature and humidity sensor. The interesting performance achieved by the rectenna with the PCB board as reflector plane (RPB), allows for the embedding of the complete rectenna connected to the SN within a cavity of a reinforced concrete beam, which was manufactured specifically for the experiments and has the dimensions presented [151]. The open concrete beam cavity has a depth of 25 cm, and its cover (depicted in Figure III.10 (c)) has a height of 100 mm. Therefore, the entire battery-free SN, when embedded in the concrete, will reside within an empty cavity of 150 mm x 150 mm x 150 mm. Before conducting the SN experiments, we investigated the influence of concrete on the rectenna's performance. For this purpose, we set up the experimental setup shown in Figure III.10 (a). The transmitting antenna, connected to the RF power generator, is positioned on the roof at a distance of 1.56 m from the top of the concrete beam. Additionally, the rectenna within the concrete cavity is placed to match the polarization of the transmitting antenna, at different heights from the bottom of the cavity, as illustrated in Figure III.9 (a). The direct wave path transmitted by the patch antenna is attenuated over a distance of 1.56 m in the air and an additional 100 mm by the thickness of the concrete cover. Preliminary measurements have revealed that the operating frequency of the rectenna is not affected by the concrete structure. With an EIRP (Effective Isotropic Radiated Power) of +32 dBm, without considering the disruption of wave propagation, the harvested DC power varies non-linearly depending on its height within the cavity. At the bottom of the cavity (d = 0 mm), the rectenna captures fewer electromagnetic waves, resulting in a harvested DC power of 82.35 µW. When the rectenna is closer to the surface of the concrete cover at 1.5 cm, its radiation pattern is also altered, resulting in a harvested power of 56 µW. The best trade-off was found at a maximum power of 219.83 µW when the rectenna is positioned at 5 cm within the cavity. At this particular position of the rectenna in the cavity, we then evaluated its performance as a function of the EIRP power to determine the operating sensitivity of the sensing node. As shown in Figure III.9 (b), the harvested DC power varies almost exponentially with the EIRP power level. With a minimum EIRP of +22.7 dBm, the rectenna can provide 15 µW for the cold-start functioning of the developed SN. According to the standards defined by ETSI, we can emit a maximum power of 2W or +35.15 dBm EIRP.

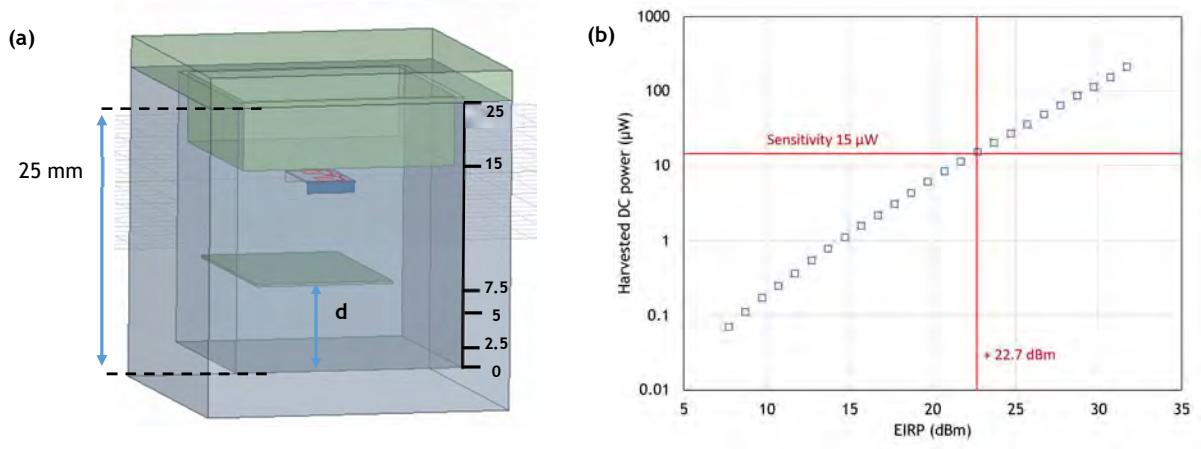

Figure III.9. (a) 3D view of the rectenna RPB position inside the covered concrete cavity (top green part is the cover); (b) Harvested dc voltage of the rectenna RPB over the EIRP of the RF source positioned at 170 cm far away from the rectenna fully embedded in the covered concrete cavity at 868 MHz across a 10 kΩ load.

Therefore, with such a limitation, we expect the SN to operate at a distance of at least 2 meters. After characterizing the rectenna in both the anechoic chamber and the embedded concrete cavity, a complete sensing node prototype was characterized. In these experiments, the output of the rectenna was no longer connected to the 10 kΩ load, but rather to the input pins of the sensing node. The EIRP power remained constant at +32 dBm at a frequency of 868 MHz. The voltage evolution at the output of the rectenna and across the storage capacitor was measured using a LeCroy WaveRunner 6100 oscilloscope. During operation, when the RF power generator is turned on, the rectenna harvests electromagnetic waves and supplies power to the PMU (BQ25504). It then stores the available power in the supercapacitor until the voltage across the capacitor exceeds 5.25 V as shown in Figure III.11. At that point, it supplies power to the active components of the sensing node until the voltage drops below 2.30 V. During each discharge cycle, the temperature and humidity is measured by sensors, and a LoRaWAN frame is transmitted.

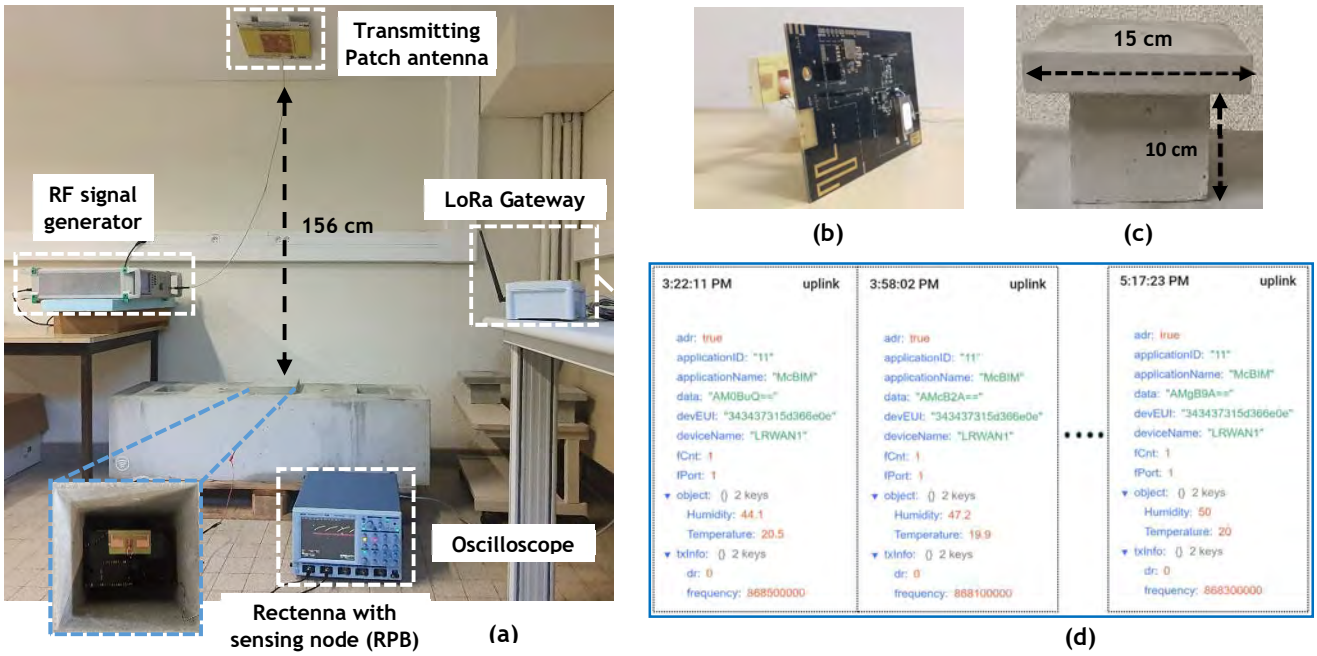

Figure III.10. Experimental setup of WPT system (the rectenna R2 with the sensing node acting as a battery-free wireless sensor was placed inside the covered concrete cavity, the RF source and the LoRa gateway); (b) Bottom view of the sensing node connected to the rectenna; (c) The cover of the hole/cavity (sized 15 cm x 15 cm x 15 cm) where the rectenna was embedded; (d) Received data from the LoRa gateway.

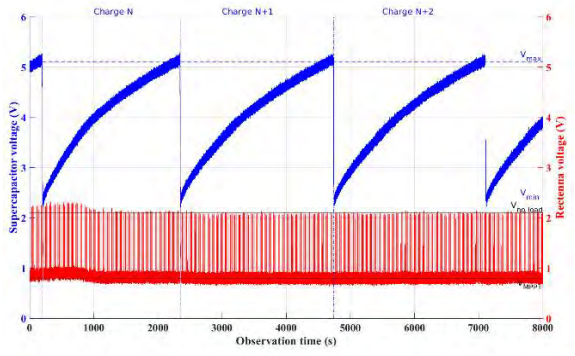

Figure III.11. Voltage waveforms at the ports of the super capacitor (blue upper curve) and rectenna output voltage (red lower curve) for a +32 dBm EIRP power.

Based on the experimental results, it takes approximately 36 minutes for a complete charge of the supercapacitor and the transmission of temperature and humidity data to a local LoRaWAN gateway. These preliminary findings demonstrate the feasibility of wirelessly transmitting both power and data through concrete. Beyond the minimum operation of the PMU, the transmission of sensor data can be monitored periodically, corresponding to the transmitted EIRP power level. This is particularly useful in critical use-cases where the need for data at reduced time intervals is necessary for statistical purposes. Considering the high-power consumption and large size of the current prototype (140 mm x 90 mm x 60 mm) presented in Figure III.10 (b), further efforts have been made to obtain an advanced prototype with improved power efficiency and reduced dimensions.

2.2.2. Prototype 2 of the proposed sensing node (LSN2)

The earlier prototyped SN allowed us to validate the major functionalities and the feasibility of communication and power transmission through concrete. However, the SN board was designed to be larger in size to accommodate the addition of auxiliary components for other functional tests. The size of the PCB is also influenced by the 868 MHz IFA transmitter antenna, which requires minimum ground plane dimensions for optimal radiation efficiency. As the choice of the transmission antenna is a constraint for miniaturization, we considered using a single antenna for both wireless power transmission and data communication. This eliminates the need for a dual-band antenna design. To achieve this, an RF circulator is required to separate the transmitted and received signals at the antenna input. As the principle depicted in Figure III.12, the antenna captures the electromagnetic waves transmitted by the power source and directly feeds the RF signal to the rectifier input port without injecting it into the transceiver. Once enough power is stored in the supercapacitor, the data from the sensor is transmitted through the transceiver to the second port of the circulator. The circulator must have very low insertion losses (typically around 0.5 dB) and high isolation between the ports. For ease of prototyping, the previously developed compact 3D antenna in the chapter II was chosen. In this iteration, the entire prototype was manufactured using a 1.6 mm thick FR4 substrate. A modified version of the dipole antenna with a T-match structure associated with metal arms was adapted for easy connection with the circulator. The selected circulator is the C11-1FFF/OPT. N from Aerotek (Hanover, Maryland, United States of America) [152]. The PCB antenna is connected to the main port of the circulator, while the other PCB, which includes the integrated rectifier, sensors, LoRaWAN module, energy management element, and microcontroller, is connected to the other two ports. The size of the SN PCB, including the 60 mm x 80 mm electronics, serves as the ground plane for the transmitting/receiving antenna, as shown in Figure III.13 (a). This version of the sensing node with a pass plane is named SNP1, and a more compact version of the electronic board with the antenna without a ground plane is named SNP2.

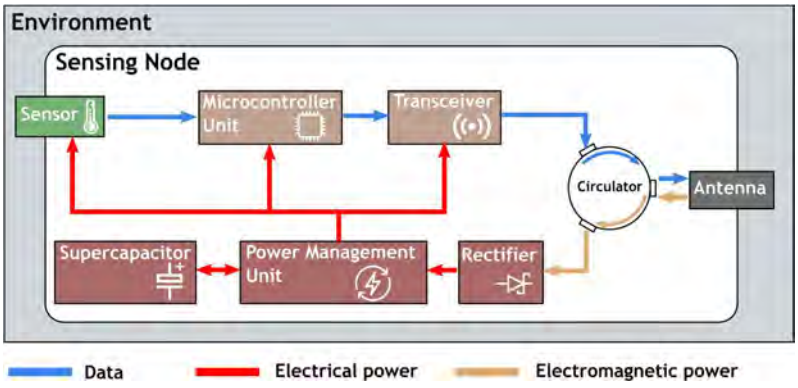

Figure III.12. Bloc diagram of the proposed generic architecture of the sensing node V2.

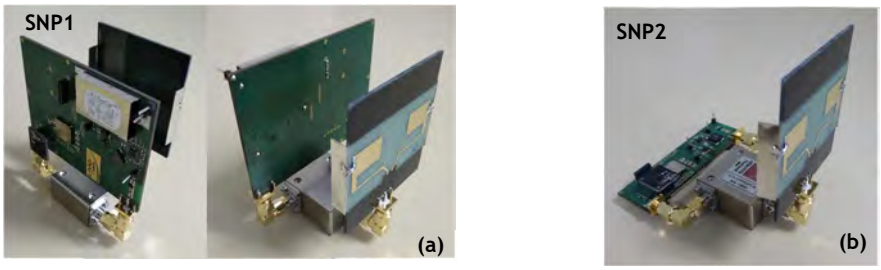

Figure III.13. Photographs of the prototypes of the sensing nodes: (a) SNP1 with the PCB as reflector plane; (b) SNP2 without reflector plane.

According to antenna simulation results, the antenna has a gain of +1 dBi, which is reduced by 0.4 dBi due to the size and thickness of the PCB. However, with the ground plane at a distance of 50 mm imposed by the position of SMA connectors and the circulator, the antenna gain is +2.2 dBi. Before conducting experimental testing of the SN, the antenna reflection coefficients were checked to ensure their suitability at 868 MHz. The test conducted in the harvesting aspect with SNP1 prototype, which benefits from gain enhancement thanks to its reflector plane, is presented here. Further results of SNP1 and SNP2 were obtained and presented in [150]. Placing SNP1 in the concrete will significantly reduce the wireless communication range and the power level received by the rectenna, leading to a higher data emission rate. Once enough power is received, the SN is powered on and can perform its full operational cycle (power-up, initialization, measurement, pre-processing, LoRaWAN transmission) in 1.6 seconds, consuming 92 mJ of energy with an input power of +4 dBm. A more detailed study of the SN's energy consumption based on the received RF power level for different types of sensors is presented in [137]. Preliminary tests confirmed the functionality of the second prototype. The SN, embedded in the cavity of a reinforced concrete beam, is wirelessly powered and controlled up to several meters by the communicating node. A power source was developed to emit a CW signal of variable power at 868 MHz. The duration of the initial charge with an empty capacitor and the recharge time of SNP1, considering the estimated RF power received by the rectenna, were measured and illustrated in Figure III.14. It can be observed that the sensitivity of SNP1 is achieved at -14 dBm, which aligns well with the previous result obtained with SN, demonstrating a sensitivity of -13.9 dBm when powered by the same rectenna (RA) used here. Beyond a certain RF power value at the rectifier input, the harvested DC voltage remains almost constant due to the saturation of the Schottky diode.

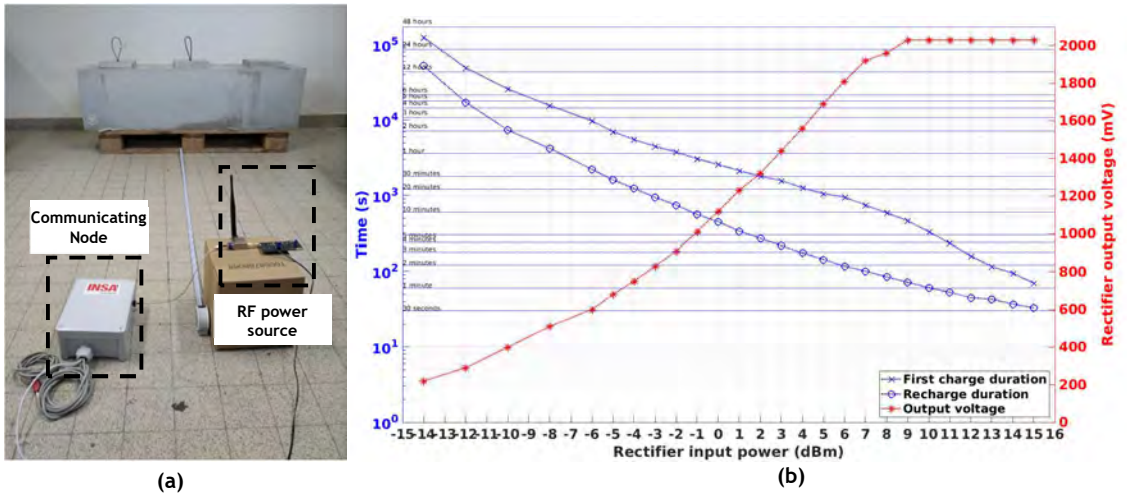

Figure III.14. (a) Photo of the experimental setup with the sensing nodes embedded in a reinforced concrete beam; (b) Durations of the first charge and recharges, and rectifier output voltage against the RF power applied at the input of the sensing node for a frequency of 868 MHz.

The duration of the initial charge increases from approximately 34 hours to 1 minute, and the recharge time decreases from approximately 14 hours to 30 seconds, as the received RF power by the rectenna increases from approximately -14 dBm to +15 dBm, respectively.

The experimental tests conducted on the prototyped SN serve as a proof of concept for wireless power and data transmission through concrete. The SNs can be remotely powered by an RF power source, and the measured data are accurately received by the communicating node. However, there is still room for improvement due to the limitation of the maximum distance achieved between the source and the SN, which is currently 7 meters. To enhance the sensitivity of the SN, which directly impacts the duration of the initial charge, recharge time, and thus the maximum distance, it will be necessary to reduce its overall power consumption.

2.3. Bluetooth Low Energy-based Solution (BSN)

In this section of the project, we present the development of a wireless sensing node based on Bluetooth Low Energy (BLE) technology. The objective was to create a more compact sensing node with communication technology that consumes less energy, thereby extending the node's lifespan and increasing sensitivity to wireless power transmission (WPT) features. For this purpose, wireless power transmission is always performed at 868 MHz, allowing for initial testing. The architecture used for the first prototyped LoRa-based sensing node (V1), with two separate antennas, is also employed for this BLE-based node, as depicted in Figure III.3.The choice of BLE technology was based on its numerous advantages compared to other technologies. It boasts low power consumption, utilizes cost-effective chipsets, and offers higher data rates than LoRaWAN. As a result, it becomes feasible to transmit large amounts of data in a single transmission. Additionally, with BLE technology, monitored data can be accessed using various wireless devices, including smartphones, tablets, and even smartwatches.

The Bluetooth Low Energy (BLE) wireless communication technology is specifically designed for low-power operation and operates within the 2.4 GHz Industrial Scientific and Medical (ISM) frequency band, ranging from 2.402 GHz to 2.48 GHz [153]. This frequency band is divided into two sets of channels: 3 advertising channels and 37 data channels. BLE supports various modes of operation depending on the type of connection, including point-to-point, mesh, and broadcast. For this project, the broadcaster or advertising mode is employed to minimize the energy consumption of the sensing node (SN). By utilizing the advertising channels, potential interference with other Bluetooth and WiFi devices, which also operate within the same frequency band, can be avoided. In this configuration, the SN device transfers data in the form of advertising packets on the three primary advertising channels, without establishing any incoming connections. On the other hand, the communicating node (CN) is configured in observed mode, continuously scanning for advertisements in passive mode. The broadcast event corresponds to the duration of the primary advertising channels: 37, 38, and 39. These channels are transmitted at the respective frequencies of 2.402 GHz, 2.426 GHz, and 2.480 GHz [154].

When designing a system with low energy consumption, choosing the right components, including the Bluetooth Low Energy (BLE) System-on-Chip (SoC), is crucial. There are several BLE transceivers available in the market, and it's important to consider their key relevant features when sizing the global system. Table III.2 provides a comparison of these transceivers based on key relevant parameters. One notable observation is that most of the commercialized transceivers have similar sensitivity levels, typically around -95 dBm. This sensitivity enables coverage ranges of several tens of meters. The default transmitting power for these transceivers is generally set at 0 dBm. In terms of current consumption, the QN908x transceiver has the lowest values for both receive (Rx) and transmit (Tx) current. However, it should be noted that the QN908x has higher current consumption in deep sleep mode compared to the RSL10 transceiver.

The resolution of the Analog to Digital Converter (ADC) is another important parameter to consider. Most of the transceivers support at least 10 bits of resolution, ensuring accurate analog-to-digital conversion. By considering these key features, the appropriate BLE SoC can be selected to optimize energy efficiency in the overall device design.

Table III.2. Comparison of the key parameters of most used BLE transceiver in IoT applications.

Parameters	QN908x [155]	QN9090 [156]	nRF52833 [157]	BlueNRG-LP [158]	RSL10 [159]	EFR32BG22 [160]	DA14531 [156]
Sensitivity (dBm)[1]	-95	-97	-95	-97	-94	-98.9	-94
Tx power (dBm)	- 30 to +2	Up to +11	-20 to +8	-20 to +8	-17 to +6	-27 to +6	-19.5 to +2.5
Rx Current (mA)	3.5	4.3	6.0	3.4	3.0	3.6	2.2
Tx Current (mA)[2]	3.5	7.4	6.0	4.3	4.6	4.1	3.5
Deep sleep mode current (nA)	1000	350	1300	900	100	1050	1200
Supply voltage (V)	1.62 to 3.6	1.9 to 3.6	1.7 to 5.5	1.7 to 3.6	1.1 to 3.3	1.71 to 3.8	1.1 to 3.3
ADC	16-bit 8-channel	12-bit 8-channel	12-bit	12-bit 8-channel	8 to 14-bit	12-bit	10-bit

[1]The sensitivity is specified in 1Mbps mode.
[2]Value obtained for 0-dBm TX power with DC-DC.

2.3.1. Prototype 1 of the BLE-based sensing node (BSN1)

a. Architecture and Design of the proposed Wireless Sensing Node

The Sensing Node (SN) incorporates various sub-systems to fulfil its functionalities, as depicted in Figure III.15. These sub-systems include:

- Two single-band rectifiers: These enable the conversion of RF signals to DC power at different frequencies.
- Power Management Unit (PMU): The PMU plays a vital role in managing, boosting, and storing the harvested power from the rectifiers. It ensures efficient power utilization and distribution to the other components of the SN, such as the sensors and BLE SoC.
- Temperature and relative humidity sensor: This sensor measures and provides data on temperature and relative humidity levels in the SN's environment.
- Resistivity measurement circuit: This circuit is responsible for measuring resistivity, which is a property related to electrical conductivity. It enables the SN to gather information about the resistivity of the surrounding materials.
- BLE System on Chip (SoC) transceiver: The BLE SoC transceiver facilitates wireless communication using the Bluetooth Low Energy protocol. It allows the SN to transmit data wirelessly to other devices or systems.

The SN is wirelessly powered via a rectenna, which consists of an integrated on-board rectifier designed for low power input levels, as well as an external antenna. The PMU is set up to manage, boost and store the available power from the rectifier. Then, it supplies power to the sensors and BLE SoC, even during deep sleep mode when the energy stored in the capacitor is depleted, and the SN is discharged. The resistivity sensing is not reported in the work, but it is discussed on Gael Loubet thesis in [150].

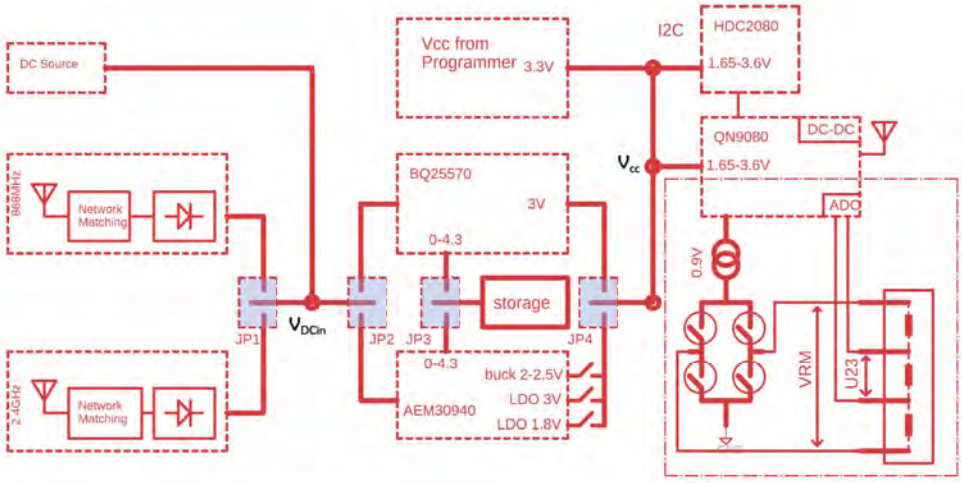

Figure III.15. Block diagram of the architecture of the implemented Sensing Node.

With the SN, it is possible to inject a current into the concrete in order to compute the electrical resistivity by measuring a potential difference thanks to probes embedded in the concrete. The evolution of this physical parameter will allow estimating the corrosion rate.

- *RF-to-DC conversion circuit : Rectifier*

The WPT technique has been chosen to wirelessly power the implemented sensing node (SN). It involves generating and transmitting time-varying electromagnetic waves across space from a power source connected to an antenna to the receiving antenna of the SN. Similar to the LoRaWAN-based solution, the same rectenna was used for harvesting the energy. The voltage doubler rectifier design was integrated into the SN board and connected to the compact 3D antenna with metal arms through an SMA connector, as designed in the previous chapter. We have chosen to use two separate single-band rectifiers at different frequencies instead of a dual-band rectifier. This choice allows us to avoid power dependence on a single rectifier (in case of damage) and eliminates the need for designing a dual-band antenna.

By using a single-band rectifier, we can also optimize the power conversion efficiency through better matching network design. Previous research has compared single-band and dual-band rectifiers. In [162], a rectifier operating at 2.45 GHz and another working at 2.45 GHz and 5.8 GHz (based on two subrectifiers) are introduced. Without an impedance compress network, the single-band rectifier exhibits 10 % more conversion efficiency compared to the dual-band rectifier operating at the same frequency (2.45 GHz) with an input power of 0 dBm (which is not low enough to observe the difference). This decrease in efficiency is also observed in [163] when comparing a single-band and dual-band rectifier operating at 900 MHz. In the implementation of the SN, our strategy is to use the same rectifier design and select the working frequency by tuning the L-matching network of the rectifier presented in chapter II. The L-type matching network components for the 868 MHz rectifier are 33 nH and 4pF, while for the 2.45 GHz rectifier, they are 3.9 nH and 2.1 pF. Prompt experiments with the implemented SN show a DC voltage across a 10 kΩ load of 286 mV and 236 mV for the 868 MHz and 2.45 GHz rectifiers, respectively, with an input power of -15 dBm. It was expected that the higher the frequency, the higher the insertion loss of the components. In this design, we have not considered simultaneous operation of both rectifiers. The choice of frequency will be made in advance, and the DC voltage output will be selected through a jumper to feed the PMU.

- *Sensing Sub-systems*

This subsystem is dedicated to measuring the targeted parameters, formatting the data, and wirelessly transmitting the collected data to the observer. It is powered by the DC power available from the PMU, which stores energy in the capacitor from the power output of the rectifier. The BLE SoC and active sensors are supplied when there is sufficient energy stored in the capacitor. The output selection can be made using jumper J1, depending on the chosen rectifier. In this work, we have opted to use two commercially available PMUs. These PMUs have been tested and characterized, and their performances are compared to determine the advantages of each based on the available electromagnetic power density and the input power requirements of the sensors to be used. For temperature and humidity sensing, we have chosen the HDC2080 integrated sensor from TI, which has low power consumption [205]. Depending on the application, the input (the DC voltage source) and the PMU can be selected using jumpers J1 and J2. The sensors and BLE transceiver can also be powered from an external DC source if needed. Wireless data communication is enabled by the ultra-low power BLE QN9080 SoC [155], and a conventional Meandered Inverted-F Antenna (MIFA) designed at 2.45 GHz, as suggested in the application note [165].

Knowing that the instantaneous available power from the harvester is insufficient to continuously supply the BLE transceiver and active sensors, we have decided to manage, boost, and store the harvested power in a storage capacitor using two independent power management units (PMUs) in order to determine the best option. The value of the storage capacitor was determined based on the amount of energy required to fully operate the SN. The first PMU selected is the BQ25570, which is a low-power PMU with a minimum input DC power requirement of around 15 µW for 100 µF [122]. It offers similar performance to the previously used BQ25505 for the LoRaWAN-based SN. However, during our investigation of the recent PMUs available in the market, we found out the AEM30940 PMU from e-peas [121], which has interesting features. It is a full-featured, energy-efficient PMU that can generate the appropriate regulated supply voltage. It has an ultra-low power start-up with a typical input power of 3 µW and can be configured to store energy using various elements such as a supercapacitor, conventional capacitor, thin film battery, Li-Ion battery, LiFePO4 battery, etc. The PMU offers a range of supply voltages, including a Low Voltage (LV) supply (1.2 V to 1.8 V) for the microcontroller and a High Voltage (HV) supply (1.8 V to 3.3 V) for the transceiver. Additionally, a voltage path for a rechargeable battery is possible using the DC-DC boost converter (2.2 V to 4.5 V). For our proposal, we have selected the HV LDO option as it consumes less power compared to the boost converter.

Before sizing the supercapacitor and the activation and deactivation voltages of the PMU, it is necessary to quantify the amount of energy required to operate the SN. To achieve this, the BLE transceiver is programmed to operate exclusively as a broadcaster, transmitting the measured temperature and humidity data in advertising mode. A research paper has investigated packet collisions in BLE advertising mode [166]. Increasing the advertising time and the number of packets can reduce the probability of packet collisions but also increases the energy consumption. After careful consideration, we found out a trade-off by sending four advertising packets over the three allocated channels (37, 38, and 39) with an advertising interval of 250 ms. These packets are transmitted to the observer, which is a QN9080 NPX development board configured in observer mode [167].

To configure the PMUs using the manufacturer's provided configuration tools, we evaluated the total power required by the sensors and transceiver. This can be carried out by conducting a power budget analysis (summing the consumed power at each stage) or using the power measurement tool in the NXP software (MCUXpresso IDE). The current consumption profile of the SN during broadcasting is depicted in Figure III.16, with a DC voltage of 3 V. The operation of the sensing node involves the following steps:

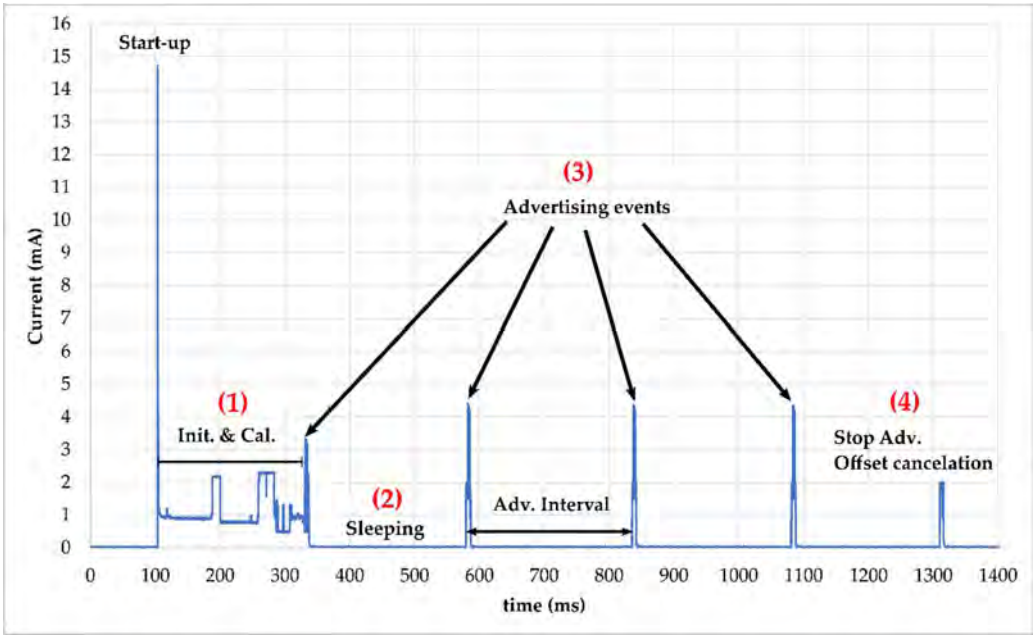

(a)

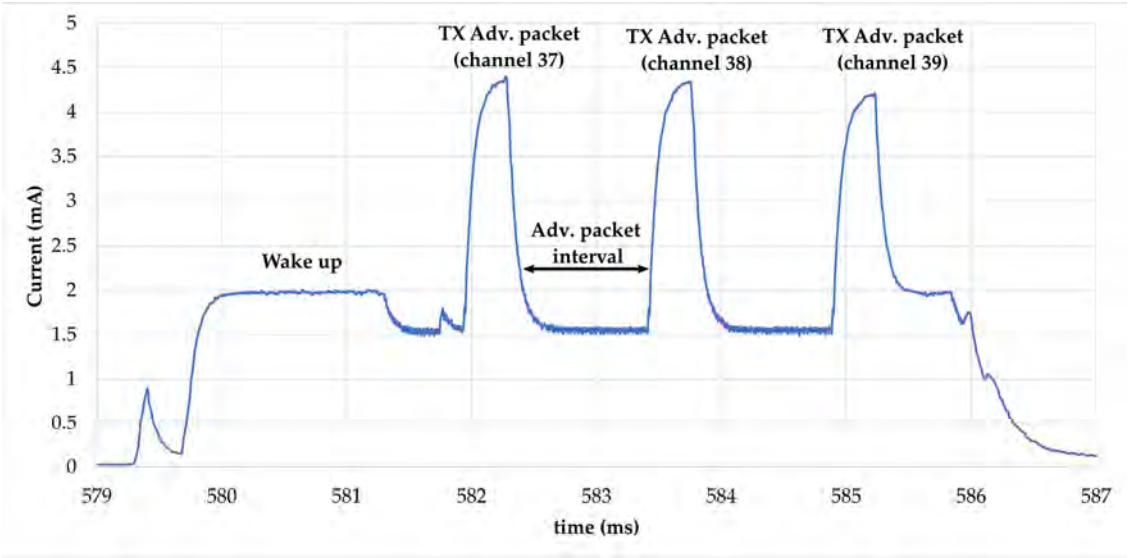

(b)

Figure III.16. (a) Current consumption profile of the BLE SN during broadcasting obtained with the power measurement tool of MCUXpresso IDE software; (b) Current consumption profile of the BLE SN during an advertising event.

(1) Power-off Mode: When there is no available or sufficient power, the SN remains in a power-off state with no hardware activity. The average current consumption during this mode is 27 µA.

(2) Start-up and Initialization: Upon receiving power, the SN started with an inrush current followed by the initialization of the registers and calibration of the sensors. This stage accounts for a significant portion of the power consumption during the broadcasting phase. The SN has a high peak demand of 14.6 mA during the start-up process.

(3) Advertising Events: After the initialization phase, the SN generates subsequent advertising events to avoid restarting the Microcontroller Unit (MCU). These events contribute to additional power consumption, as observed in the subsequent advertising events.

The advertising interval is set to 250 ms, and a timer of 1 second is implemented to send four advertisements. Each advertising event begins with the MCU waking up and transmitting packets on the designated channels (37, 38, 39). A detailed view of the advertising packets is shown in Figure III.16 (b).

(4) 4. Advertisement Stop: The last phase of current consumption occurs when the function to stop advertising is executed after the 1-second timer expires. An additional function is programmed for resistivity measurement, which involves cancelling the measured current across dedicated probes.

Table III.3. Current consumption during each state of a broadcasting event

	State description	Time duration (ms)	I (µA)
1	Deep-sleep mode : Between advertising events	234	31.4
2	First state (start-up, init., cal. and 1st adv. Event)	241	1074
3	A full advertising event	8	1758
4	Offset cancelation and stop advertising	11	1032
5	Total broadcasting event (from start-up to stop adv.)	1216	282

The total average current consumption during a broadcasting phase is approximately 282 µA over a duration of 1216 ms. It can either be computed thanks to the equation (III.1) but is less accurate due to approximations in time duration of each state.

$$I_{average} = \frac{\sum I_i T_i}{\sum T_i} = \frac{I_2 \cdot T_2 + 4 \cdot I_1 \cdot T_1 + 3 I_3 T_3 + I_4 T_4}{4 \cdot T_1 + T_2 + 3 \cdot T_3 + T_4} \quad \textbf{(III.1)}$$

The energy consumption of the SN is then calculated to be 1028.7 µJ (Econs) with a DC voltage of 3 V. However, this method of calculating power consumption may not be accurate due to the variation in offset voltage, which introduces an error for measured currents below 150 µA, as described in the datasheet [168]. An alternative method was employed by increasing the advertising interval and measuring the voltage across a resistor using a digital multimeter (Keithley 2000). The resulting current was found to be 3.3 µA instead of 31.6 µA in a deep sleep state. By computing the equation (III.1), the correct value of the average current is 260 µA, resulting in an energy consumption of 946 µJ (Econs). Therefore, the final storage capacitor is determined using the equation (III.2) for both PMUs. The maximum threshold voltage (activation) is set at 4.2 V, and the minimum threshold voltage (deactivation) is set at 2 V. To account for the tolerance of the capacitance value in the worst-case scenario, 20% is subtracted from the required value. It should be noted that the calculated value of 111 µF is not a standard value. For the prototype, a low leakage current storage capacitor of 150 µF [169] from Würth Elektronik is selected to meet the requirements.

$$E_{cons} = \frac{1}{2} \cdot C_{stor-20\%} \cdot \left(V_{max}^2 - V_{min}^2\right) \quad \textbf{(III.2)}$$

b. Implementation and experimental results of the BSN1

The first proposed solution of the Bluetooth Low Energy Sensing Node (BSN1), which includes two PMUs and two rectifiers operating at different frequency bands, has been successfully prototyped. The nomenclature of each subsystem of the SN can be seen in the photo of Figure III.17. The output of either the 2.45 GHz rectifier or 868 MHz rectifier input can be used for the power supply. However, only the experimental results of the SN using the 868 MHz rectifier are presented in this study, as there are no available results for the 2.45 GHz rectifier at this time. The full schematic and layout view of the designed SN1 is presented in Appendix 1.

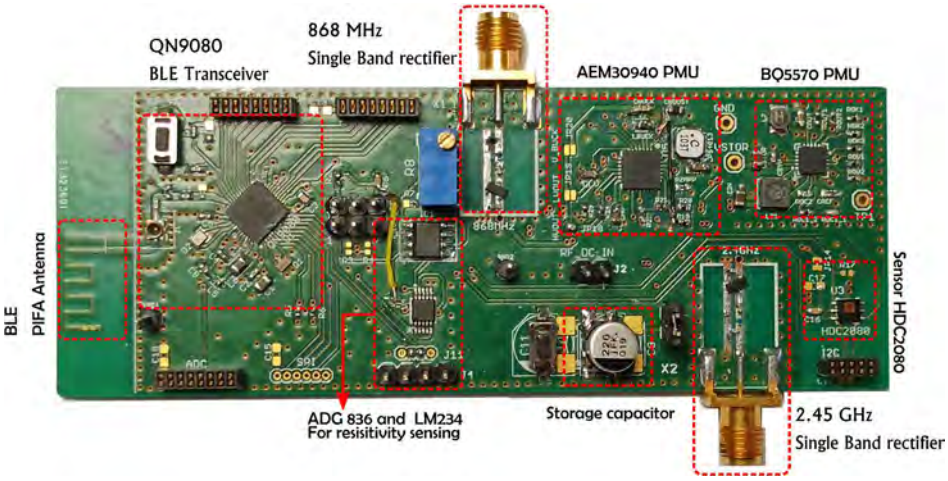

Figure III.17. Photo of the fabricated Sensing Node with the nomenclature of each part.

- *A comparison of the performance of the two Power Management Units*

The performance evaluation of the prototyped Sensing Node (SN) involved two main aspects: measuring the charge time of the storage capacitor and comparing the performance of each Power Management Unit (PMU). Experimental results were obtained using a continuous wave input signal provided to the 868 MHz rectifier. The charge and discharge behaviour of the storage capacitor were captured using an oscilloscope, as illustrated in the experimental setup shown in Figure III.18.

To ensure accurate measurements and avoid any influence from the input impedance of the measuring devices (such as voltmeter, probes, and oscilloscope), the time duration of a single event or the time between each data emission was determined by calculating the time difference between the received timestamped packets.

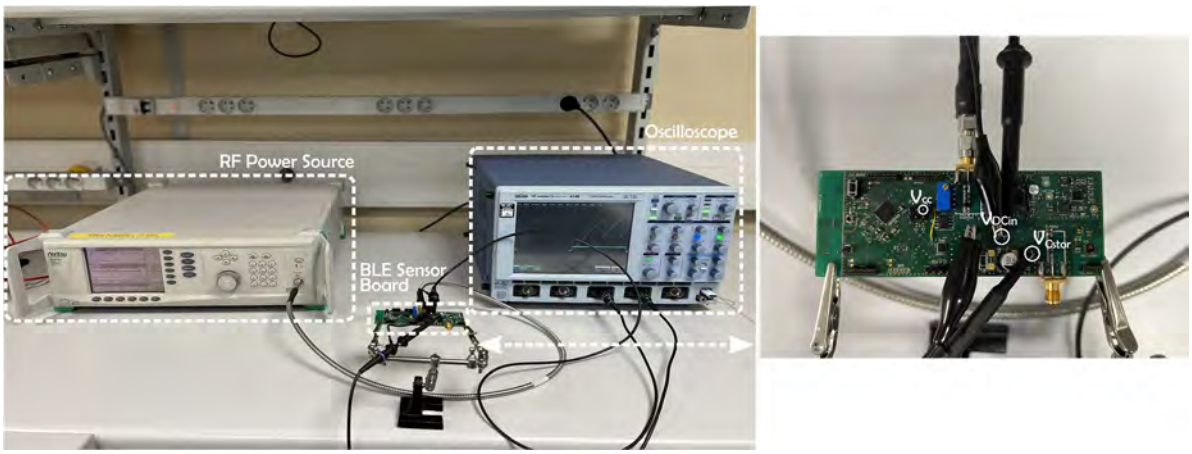

Figure III.18. Experimental setup of measuring the charging evolution of the storage capacitor.

With a RF input power of -6 dBm at the rectifier input, the voltages evolution over time for each PMU configuration was captured using the oscilloscope, and the results are reported in Table III.4. The data clearly shows that the configuration with the BQ25570 PMU requires a longer cold start time compared to the one with the AEM30940 PMU. In the AEM30940 configuration, the cold start procedure is completed, allowing for the execution of 4 advertising events. Based on these findings, it can be concluded that the AEM30940 PMU appears to be more suitable for the application, especially when considering a low RF input power during the cold-start procedure.

Table III.4. Comparison for an RF power of -6 dBm (868 MHz) at the input of the rectifier.

PMU component	Minimum Input DC power (µW)	Activation threshold voltage (mV)¤	Deactivation threshold voltage (mV)	First charge duration (s)	Recharge duration (s)
BQ25570 [120]	15*	4.195	1.936	114	21
AEM30940 [121]	3	4.22	1.87	34	21

¤obtained for an -6 dBm RF input power of the rectifier at 868 MHz *for a storage capacitor of 100 µF.

A quantitative comparison has been conducted between the two PMUs in terms of their first charge and recharge durations, considering various input power levels (from -5 dBm to -14 dBm), as presented in Figure III.19. The first charge duration includes the cold start time before reaching the deactivation threshold. It has been observed that the evolution of the first charge duration exhibits an insignificant dynamic range for both PMUs, regardless of the input power. However, the recharge duration remains relatively similar for input power levels above -8.5 dBm. The difference between the PMUs becomes more apparent at low RF input power levels. As a result, the AEM30940 PMU demonstrates promising results with reasonable charge duration, particularly for low power input levels. Regarding the second charge or recharge state, the BQ25507 PMU proves to be more efficient for RF input power below +10 dBm due to its low input power range for normal charging (as specified in the datasheet with a minimum of 5 µW). For the minimum 15 µW required for the cold-start operation of the BQ25507, the BSN1 sensitivity is achieved at -13.8 dBm, which is consistent with the experimental results of the rectifier. For an RF input power of -14 dBm, the harvested DC output power across a 10 kΩ load is measured to be 14.48 µW.

Consequently, we can estimate that for the AEM30940 PMU (which requires a minimum cold start input power of 3 µW), the input sensitivity is approximately -19 dBm. This corresponds to the power required at the rectifier input to deliver a DC power of 3.14 µW across a 10 kΩ load.

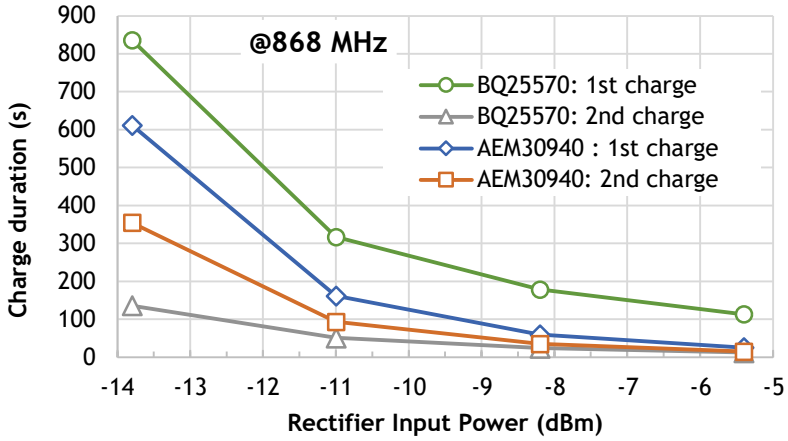

Figure III.19. Charge duration of the BSN1 using an 868 MHz rectifier for different selected PMU.

- *Radiated performance evaluation.*

In order to finalize the implementation of the first prototype BLE-based sensing nide (BSN1) in real wireless conditions, it is connected to a compact 3D antenna developed in Chapter II. In this characterization step, the BSN1 is specifically configured with the selection of the AEM30940 PMU, considering its suitability for low RF power levels during the cold start mode, as demonstrated in previous experiments. The setup, illustrated in Figure III.20, consists of an RF source comprising an RF signal generator connected to a patch antenna via a coaxial cable.

The BSN1, acting as the broadcaster under test, is positioned at a distance of 2 meters from the RF source. The observer, represented by the QN9080 Development Kit, receives the transmitted data from the BSN1.

Figure III.21 shows the first start duration and the recharge periodicity of the storage capacitor as a function of the Effective Isotropic Radiated Power (EIRP). The measurement and data transmission periodicity can be controlled by the RF power source, which determines the equivalent power density level at the surface of the antenna connected to the BSN1.

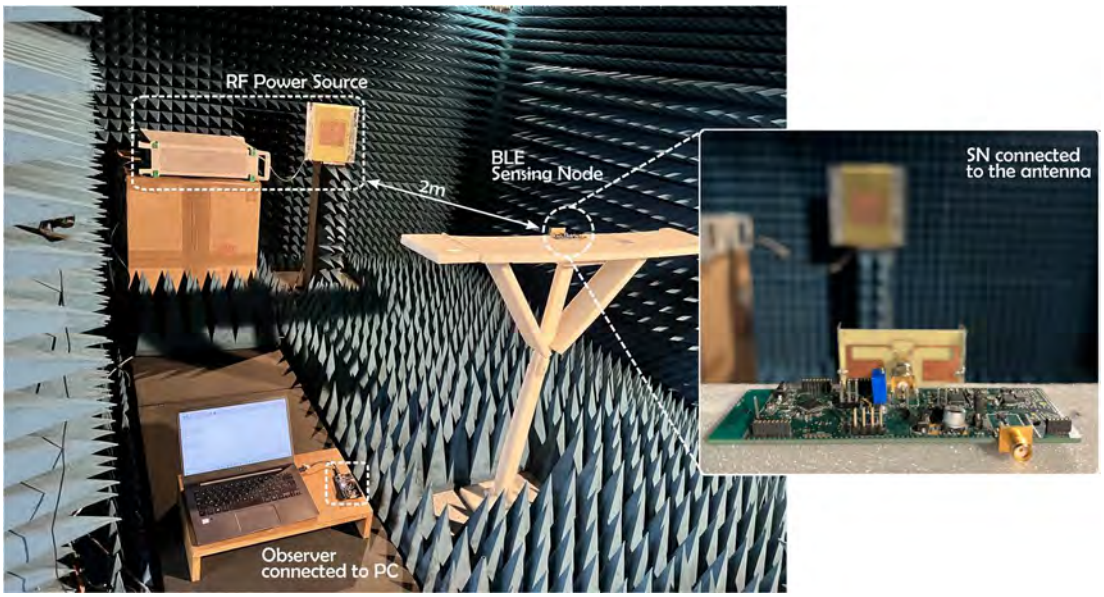

Figure III.20. Measurement setup of the charge duration of BSN1 connected to an antenna in a anechoic chamber.

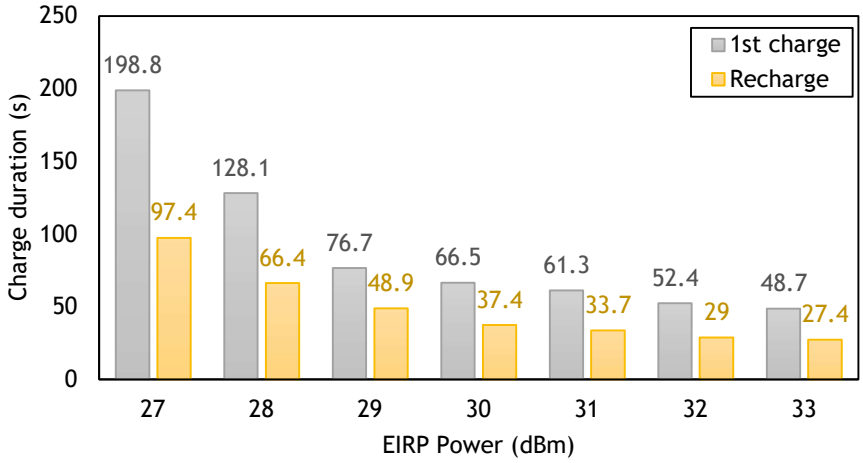

Figure III.21. Measured charge duration of the BSN1 or BLE emission rate with a connected antenna in anechoic chamber with different EIRP power level.

For an EIRP power of +33 dBm, which roughly corresponds to the limit set by the FCC standard in the 868 MHz band, the BSN1 located 2 meters away from the source can transmit regular data within less than half a minute in its normal cycle. The BSN1 measurements were conducted up to an EIRP power of +27 dBm. However, considering the low power level required for the cold start (3 µW) of the AEM30940, the BSN1 can operate with an estimated minimum EIRP power of +19 dBm at 2 meters. Regarding the maximum distance, with a fixed EIRP power of +33 dBm, the BSN1 can be positioned up to 8 meters away from the source to maintain operation.

However, this will result in a relatively long measurement periodicity of approximately 7 minutes in its normal cycle. Unfortunately, due to time constraints, it was not possible to conduct tests on the prototype in the concrete cavity to gather statistical data on its performance. Nevertheless, a second, more advanced prototype with fewer components and smaller dimensions has been developed and will be presented in the next section.

2.3.2. Prototype 2 of the BLE-based sensing node (BSN2)

The initial prototype of the BLE-based sensing node (BSN1) demonstrated promising performance in monitoring temperature and pressure parameters using wireless power transmission (WPT) technology. Building upon the comparison of the two power management units (PMUs) discussed earlier, version 2 of the BLE Sensing Node (BSN2) was developed with a focus on miniaturization, incorporating fewer features and components. The BSN2 includes essential functions for our application as presented in Figure III.22 (a), such as the BLE QN9080 transceiver paired with a MIFA antenna, a single 868 MHz rectifier for RF-to-DC conversion, the AEM30940 PMU, a storage capacitor, the HDC2080 temperature and humidity sensor, and an analog circuitry for driving an external resistivity sensor (which is not the primary focus of this work) designed to monitor corrosion issues in reinforced concrete structures. The 868 MHz rectifier used in the BSN2 is identical to the one employed in the previous prototype. Vias are strategically placed at its RF input to facilitate connection to a flexible antenna, eliminating the need for an SMA connector. The entire circuitry is designed to fit within a compact 47 x 36 mm² PCB area, as depicted in Figure III.22 (b). The complete schematic and layout can be found in appendix 2. The configuration and programming of the BLE module in the BSN2 remain unchanged from the BSN1. Once powered on, the sensing node (SN) operates in broadcasting mode, transmitting temperature and humidity data to the central node (CN) over the course of 4 advertising events. During each advertising event, the same data frame is broadcasted across BLE channels 37, 38, and 39.

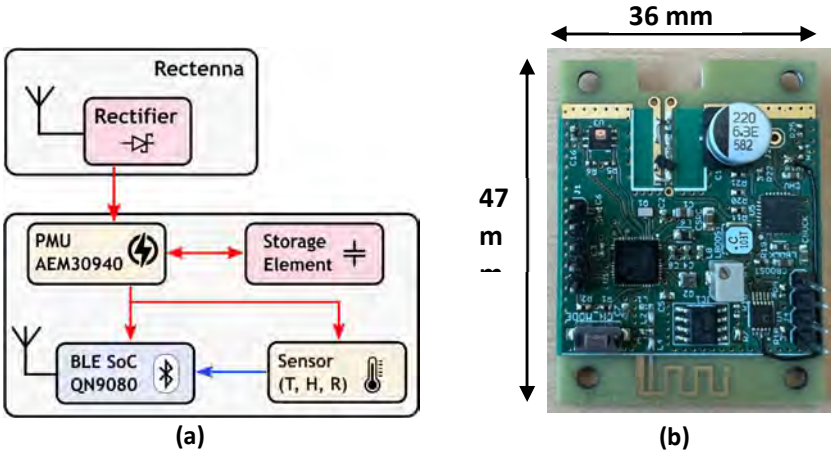

Figure III.22. (a) Bloc diagram of the battery-free BLE SN; (b) Photo of the manufactured compact battery-free BLE SN without antenna.

The implemented power management algorithm involves utilizing two voltage levels at the input of the storage element C_store, which is a standard 220 µF capacitor of type EEEFK0J221P. The voltage levels are set at V_{HIGH} = 4.23 V and V_{LOW} = 1.94 V. It's worth noting that the sizing of C_store considered the DC power consumption of the analog circuitry responsible for driving the external resistivity sensor. The BSN2 prototype has been successfully built, and initial experimental tests were conducted as illustrated in the setup shown in Figure III.23.

These tests involved using a high-impedance oscilloscope to measure the voltage at the storage capacitor terminals and the output DC voltage (HVOUT) of the PMU. When the voltage at the capacitor terminals reaches V_{HIGH}, the HVOUT output of the PMU supplies a voltage of 2.84 V to the sensor and the BLE module during the measurement and data transmission phase. This continues until the capacity is discharged to the V_{LOW} level, at which point the cycle resumes as long as the rectifier can provide sufficient energy to recharge the storage element.

The voltage evolution of across the storage capacitor (V_cstore) and HVOUT is illustrated in Figure III.24 (a) for a continuous wave (CW) signal at 868 MHz with a power level of +6 dBm. In order to supply power to the rectifier input, a feeding technique was employed, which involved soldering two PCB pin headers into the rectifier input holes. The RF signal generator was connected to the rectifier input pins using an SMA transition with dual-ended alligator clips. However, it should be noted that the feeding technique used in this setup is not ideal, as it does not provide a reliable 50 Ω impedance match. Consequently, the RF input power delivered to the rectifier may not precisely correspond to the power level defined at the signal generator. The graph depicted in Figure III.24 (b) demonstrates that the periodicity of measurement and data transmission is dependent on the power available at the rectifier input. Regardless of the power level, approximately one-third of the first charge duration is allocated for the cold start phase, during which the voltage of the capacitor transitions from empty to the V_{LOW} voltage of 1.94 V. The sensitivity of the BSN2 with pin header corresponds to the minimum RF power level to ensure a full cycle is obtained at 0 dBm (approximately 12 minutes for an empty supercapacitor and 7 minutes for the recharge phase). It cannot be considered reliable due to the uncertainty surrounding the feeding technique used. The use of pin headers and SMA transitions with alligator clips does not guarantee a 50 Ω impedance match, thus affecting the accuracy and consistency of the RF input power to the rectifier.

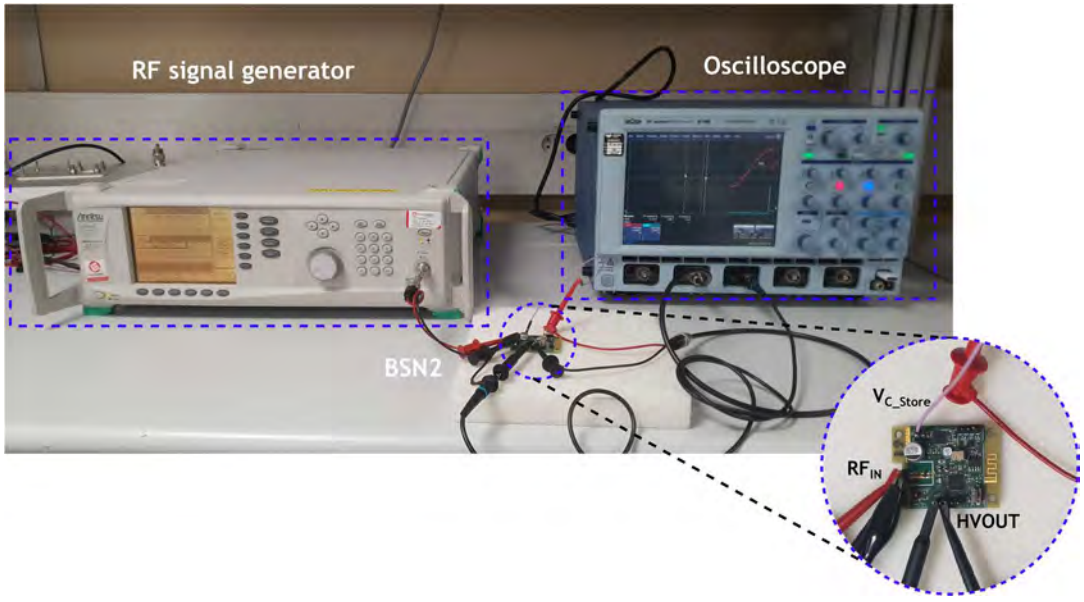

Figure III.23. Experimental setup of the BSN2 powered by cable and connected to the digital oscilloscope.

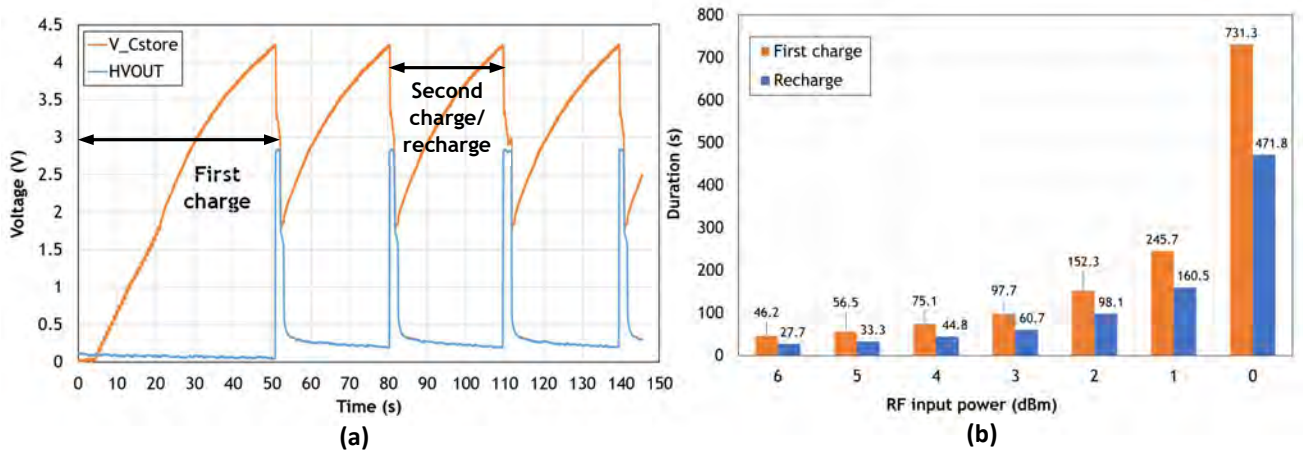

Figure III.24. (a) Measured voltage at the input port of the storage capacitor (V_Cstore) and at the output of the power management unit (HVOUT) as function of time. Experimental results obtained for a RF input power of +6 dBm. (b) First charge and recharge duration of the BSN2 as a function of the RF input power.

Figure III.25. Photo of the manufactured of battery-free SN prototype including a flexible antenna manufactured on transparent PET substrate operating in ISM 868 MHz frequency band.

Table III.5. Charging durations as a function of the RF power

EIRP (dBm)	P_Rx (dBm)	1st charge (s)	Recharge (s)
32.7	-3.33	54	27
30.7	-5.33	105	49.83
28.7	-7.33	200	96
26.7	-9.33	420	206.25
24.7	-11.33	1073	501.33

To obtain more reliable results, radiating measurements were conducted in an anechoic chamber. The BSN2, positioned at a distance of 2 meters, was wirelessly powered by an RF source connected to a linear polarized patch antenna. The antenna used for the BSN2 was the flexible PET substrate antenna developed in Chapter IV, which is a modified dipole with a T-match structure operating at 868 MHz and providing a gain of +1.2 dBi. The connection between the antenna and the BSN2 was established electrically using metallic paste and mechanically using nylon screws as seen in Figure III.25. In order to measure the recharge time, the time interval between two emissions from the BSN2 was detected through software measurements performed at the Communicating Node (CN) level. As for the duration of the first charge, it was obtained by first emptying the storage element and residual voltages, and then timing the period between the activation of the power source and the first data reception at the CN.

Table III.5 presents the data for P_RX, which corresponds to the power received by the antenna connected to the BSN2 or at the rectifier input. As expected, the duration of the first start charge and the recharge phase vary according to the EIRP of the RF source, ranging from 54 seconds (EIRP = +33.9 dBm) to 1073 seconds (EIRP = +25.9 dBm) for the first charge, and from 27 seconds (EIRP = +33.9 dBm) to 501 seconds (EIRP = +25.9 dBm) for the recharge duration. The duration of the first charge is twice that of the recharge, and the sensitivity is approximately -12 dBm. This sensitivity value is lower than the expected value of approximately -19 dBm, possibly due to the mismatch losses between the PET antenna connected to the BSN2 and the effect of the rigid PCB on the antenna's radiation pattern. The BSN2, which was derived from the initial prototype BSN1 measuring 110 mm x 40 mm, has undergone optimization to select a more suitable PMU for low power levels and achieve a significantly reduced size for easy embedding in a smaller concrete cavity. The resulting BSN2 now measures 47 mm x 36 mm. However, the transition made to connect a flexible antenna does not provide the expected performance. In comparison, the BSN1 with its SMA connector offers a shorter charge duration (measurement periodicity) while consuming the same amount of energy. As a perspective for future work, it would be crucial to co-design the antenna and rectifier circuit to ensure proper impedance matching and improve overall performance.

3. Battery-Free Wireless Tag combining UWB and BLE Technologies (UBT)

The work presented in this study addresses the requirements of UWINLOC Company, which aims to integrate Ultra-Wide Band (UWB) and Bluetooth Low Energy (BLE) functionalities. The objectives include :

- Investigating the feasibility of powering the BLE Sensing Node's (BSN) transceiver stage (BLE chip and sensors) using the Uwinloc Geolocation Module (UGM) that incorporates a harvester. It architecture and parameters regarding the input impedance at each port is presented in the chapter V and VI.
- Additionally, the study focuses on exploring the UWB features with external sensors to obtain both location and physical parameters such as temperature and humidity.
- Another aspect is to evaluate the ability to receive UWB signals through a concrete structure.

To achieve the objectives, we have proposed and implemented an architecture that utilized the Uwinloc Geolocation Module (UGM) provided by UWINLOC Company. Additionally, the project drew upon the prior knowledge and understanding of BLE technology gained from previous studies on BSNs. The outcome of this work is a highly promising proof of concept for a battery-free UWB/BLE tag (UBT) that combines the advantages of both technologies. The UBT demonstrated integrated sensing capabilities for temperature and humidity measurements, along with localization functionality. This achievement serves as a significant milestone in showcasing the feasibility and potential of the developed solution. It should be noted that works on the aspect of geolocation with battery-free systems are present in the literature. In [33], a solution for a UWB positioning system for space applications is proposed. It is remotely powered through WPT (Wireless Power Transfer) with a power source of 2 watts Effective Radiated Power (ERP) in the UHF band at 868 MHz."

3.1. Architecture and Design of the Proposed Tag Prototype

The developed tag integrates various components, including a geolocation module (UGM), which enables RF energy harvesting and facilitates UWB transmission for precise location tracking. It also incorporates a temperature/humidity sensor and a BLE transceiver. The tag operates wirelessly, receiving power from a far-field wireless power transmission (WPT) system.

To manage the harvested power effectively, a Power Management Unit (PMU) is employed. The PMU boosts the received power, stores it in a capacitor, and handles its distribution as illustrated in Figure III.26.

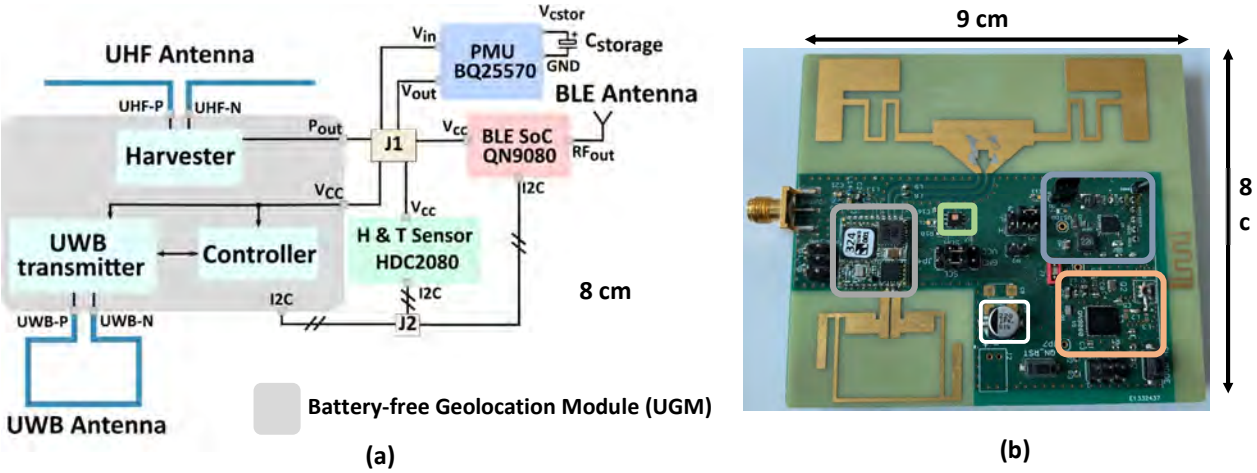

Figure III.26. (a) Architecture of the battery-free UWB-BLE tag; (b) Photo of prototyped tag.

The proposed solution was prototyped on a 1.55 mm thick FR-4 substrate. The incorporation of a jumper (J1) allows for versatile combinations and configurations, enabling the tag to support multiple functionalities based on the specific requirements or desired operation. This flexibility allows for customization and adaptation of the tag to be used in two different modes, depending on the desired functionality:

- Geolocation Mode (UWB mode): In this mode, the harvested power (Pout) obtained from the harvester is connected to the input pin (Vcc) of the UGM, enabling UWB geolocation functionality. Other chips or components are disconnected by configuring the appropriate jumper setting (J1). Additionally, the tag can support humidity and temperature sensing by supplying power to the sensor through the suitable combination of jumper settings. It is important to note that this configuration does not allow simultaneous geolocation through UWB and BLE sensing. Jumper J2 is used for I2C communication, either by the UGM or the BLE System on Chip (SoC).
- Temperature and Humidity Monitoring Mode (BLE mode): In this mode, the harvested DC power is managed by the PMU, which stores the energy in the capacitor. The BLE transceiver and active sensors are then powered when sufficient energy is available in the capacitor. By configuring the appropriate jumper settings on J1, the tag can operate in this mode, enabling temperature and humidity monitoring through BLE communication.

3.2. Bluetooth Low Energy sensing and communication

For data transmission, we have selected the QN9080 BLE SoC and a conventional meandered Planar Inverted-F Antenna (PIFA) designed at 2.4 GHz, which has been used in previous BSN designs. However, considering that the instantaneous power available from the harvester is insufficient to power the BLE transceiver and active sensors, we have incorporated a 220 µF storage capacitor and the BQ25570 low-power PMU. The DC output voltage of the PMU is set at 1.9 V to achieve the best balance in terms of low power consumption for the BLE transceiver and sensors. To optimize energy consumption of the prototype, the BLE transceiver is programmed to operate exclusively as a transmitter (broadcaster), transmitting the measured temperature and humidity data in advertising mode. This configuration is the same as that used for BSN1 and BSN2. We have chosen the HDC2080 integrated low-power temperature and humidity sensor from Texas Instruments (TI).

The operation of the sensor and the BLE SoC requires an energy consumption of approximately 756 µJ for 3 advertising events and 942 µJ for the broadcasting phase. The PMU is configured with minimum and maximum DC voltage thresholds set at 1.97 V and 3.55 V, respectively. The storage capacitor (($C_{storage}$), chosen for the system is the EEEFK0J221P from Panasonic, with a capacitance value of 220 µF. This capacitor was carefully selected to store sufficient energy for the active components and to minimize leakage current. During the first charge (considering cold start phase) from an empty state (Vstorage = 0 V) to the maximum voltage allowed by the PMU (Vstorage = 3.55 V), the maximum energy stored by the capacitor is approximately 1.39 mJ. During each subsequent recharge, before each sensing and data transmission cycle, the capacitor stores around 960 µJ of energy. The minimum voltage allowed at the output of the capacitor before the advertising stops is set at 1.97 V.

3.3. Harvester and Ultra-Wideband Module

The battery-free geolocation module (UGM), developed by UWINLOC Company, is specifically designed for real-time asset tracking. The UGM version utilized in this study incorporates two differential inputs for energy harvesting purposes. One input is dedicated to the proposed solution, while the other is connected to an SMA connector for additional experimentation (not discussed in this paper). The harvester employed in the UGM, is based on the Greinacher doubler topology, optimized to extract low-power density from a dedicated RF energy source operating at 868 MHz within the Industrial Scientific Medical (ISM) frequency band. To minimize power consumption, various aspects were considered, including the reduction of the power required by the microcontroller and transmitter, and leakage current of the first storage capacitor (60 µF) within the harvester block (refer to Figure III.26.(b) for UWB operation). Further details regarding the energy harvesting circuit can be found in the associated patent of the company [170]. The UGM module consumes approximately 5 to 10 µJ for a single UWB transmission. Once sufficient energy is stored, the tag emits an ultra-wideband pulse through the UWB antenna towards UWB beacons (not discussed in this paper). Accurate triangulation algorithms are then employed to compute the precise 3D position of the tag.

The design of the antenna plays a critical role in achieving the best trade-off between high sensitivity at low power density reception, UWB transmission range, and localization accuracy. To minimize the need for additional lumped components and avoid insertion losses, the UWB and Ultra High Frequency (UHF) antennas are designed to possess an impedance that is the complex conjugate of the input impedance of the UWB transmitter (25-j·9 Ω) and harvester (30-j·250 Ω). The UHF antenna, used for capturing electromagnetic waves for energy harvesting feature, utilizes a modified folded dipole antenna with a T-match structure at 868 MHz. To compensate for the high imaginary part of the UGM's input impedance, Coplanar Wave Guided Grounded (CPWG) coupled transmission lines are employed as shown in Figure III.27. The simulation results indicate that the maximum gain achieved at the desired frequency is approximately +1.13 dBm in the YoZ plane (Phi = 90°) for the theta angle of the radiation pattern set to 90°. This corresponds to the horizontal position of the tag (H-pos) for the experiments. Similarly, for the vertical position of the tag (V-pos), the antenna exhibits a gain of 0 dBi at a theta angle of 0° in the YoZ plane, as shown in Figure III.27 (d). The UWB antenna utilized in the design is based on a novel modified loop antenna, specifically designed to exhibit a wideband behaviour (refer to Figure III.27 (a)). However, due to the presence of the UHF antenna and the wider ground plane, the radiation pattern of the antenna has been altered to become more directional in a certain direction. To improve the radiation pattern, two crossed arms are incorporated at the corner of the loop. According to the simulation, the antenna achieves a maximum gain of +3.8 dBi at 4 GHz.

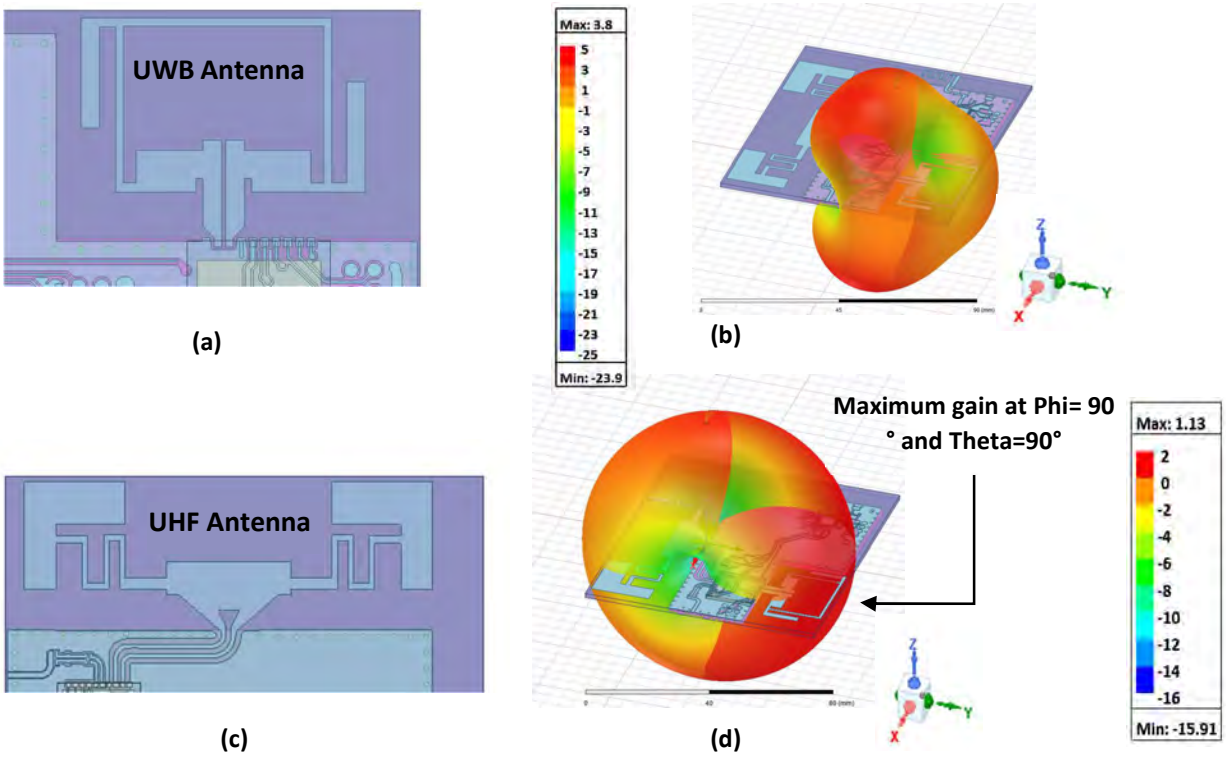

Figure III.27. Antenna design and simulation of the tag: (a) Proposed design of the UWB antenna; (b) 3D Radiation pattern of the UWB antenna at 4 GHz; (c) Proposed design of the UHF antenna; (d) 3D Radiation pattern of the UHF antenna at 868 MHz.

3.4. Experimental Results

3.4.1. Bluetooth Low Energy Performances

In the conducted measurements in the anechoic chamber, the tag was configured to operate in BLE mode with the harvester, PMU, sensors, and the BLE SoC. The setup involved a dedicated RF source consisting of a transmitting patch antenna placed at a distance of approximately 2 meters from the tag as seen in Figure III.28. The RF source was connected to an RF signal generator (Anritsu MG3694B) through a cable, with cable losses accurately measured using a power meter (with an average loss of -0.5 dB), to provide power (PRF) at a frequency of 868 MHz to the tag. Prior to the measurements, all the capacitors in the system were manually discharged to ensure accurate measurement of the cold start phase. The BLE receiver, acting as an observer or listening device, was connected to a laptop. The QN9080 development kit was utilized to enable this functionality. During the measurements, the emission rate, which represents the time elapsed between two consecutive temperature/humidity measurements sent by the battery-less tag through the advertising channels during the broadcasting phase, was evaluated. This was achieved by calculating the time difference between each broadcasting phase. It also correspond to recharge, or second charge duration evaluated before on the BSN prototypes. The measured results include the first time required for the cold start procedure (initial startup) and the average emission rate as a function of the Effective Isotropic Radiated Power (EIRP) of the RF source, which was placed at a distance of 2 meters from the tag. These results are depicted graphically in Figure III.29.

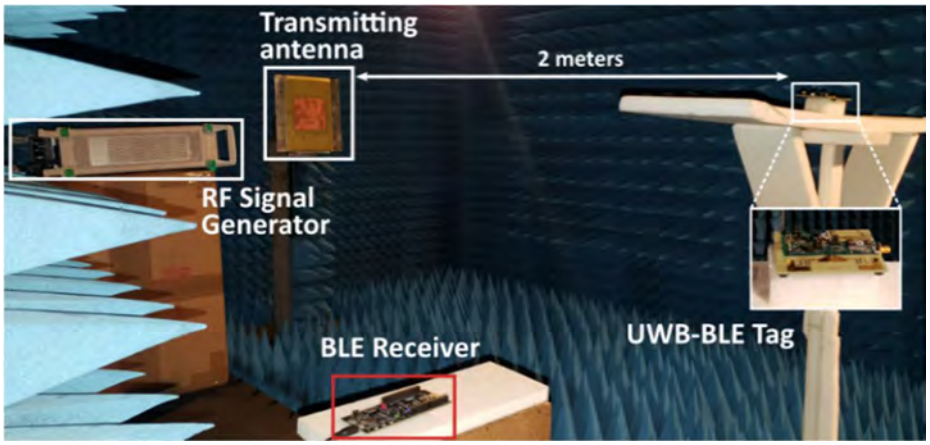

Figure III.28. Measurement setup for the evaluation of the BLE performances of the tag in an anechoic chamber.

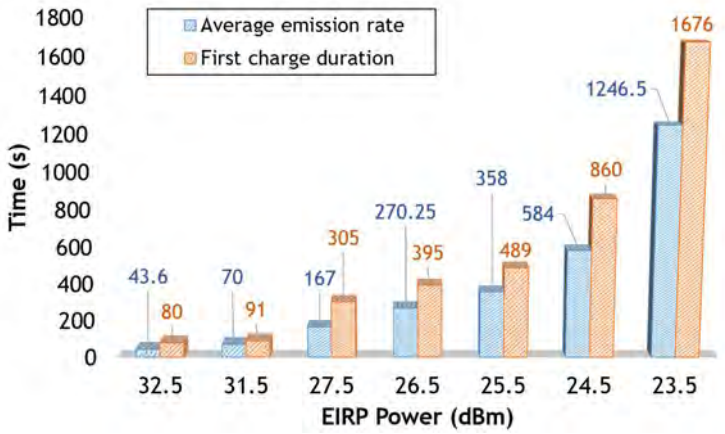

Figure III.29. Measured BLE emission rate and the time of the cold start phase as function of the EIRP power of the 868 MHz RF source located at 2 m far away the tag.

The measurement operated in an anechoic chamber, allows to enable the Friis equation for the calculation of the received power at the output of the UHF antenna. Since the transmitted power is greater than +23.5 dBm EIRP, which corresponds to an estimated received power of -12.65 dBm at the input of the harvester, the first charge duration is less than 28 minutes. By extrapolating the results using Friis equation, and considering a maximum EIRP power of +33 dBm, it is estimated that the maximum range would be around 6 meters. This estimation assumes an average equivalent emission rate of 1246 seconds.

3.4.2. Ultra-Wideband Performances

The prototyped tag is now configured to work with the geolocation module (UGM) exclusively for preliminary results. The evaluation of the emission rate was conducted under the same conditions as the BLE tests, using the setup depicted in Figure III.29. However, instead of the BLE receiver, a UWB beacon was employed. Two different testing positions were chosen for the tag: the horizontal position (H-pos), which was used in the BLE tests, and the vertical position (V-pos), where the tag was placed vertically facing the transmitting antenna. According to simulations, the UHF antenna exhibited lower gain in the V-pos compared to the H-pos. To enable swift monitoring of the tag's location/position changes, a maximum emission rate of approximately 10 minutes was set. When comparing the emission rate between the two positions, a larger time difference was observed at lower power levels due to the nonlinearity of the harvester and losses. The UHF antenna of the tag, operating at 868 MHz, demonstrated a simulated gain of +1.13 dBi (in H-pos), while the RF source, with an EIRP of +18 dBm, was positioned 2 meters away from the tag.

Using Friss equation, it can be estimated that UWB emission is possible as long as the received RF power at the rectifier's input exceeds -20 dBm. After evaluating the UWB communication capability between the tag and the beacon in an anechoic chamber, we proceeded to evaluate the UWB localization performance in a real-world scenario.

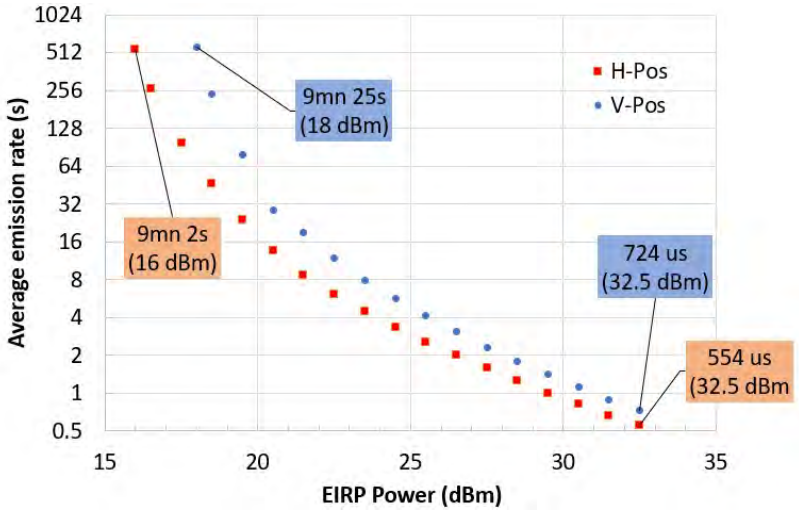

Figure III.30. Average emission rate of the tag in localisation mode without sensor.

For this purpose, an indoor test was conducted in a 300 m² test warehouse containing multiple obstructions from UWINLOC company. The configuration of the test area and the number of beacons were specific to the company and were not detailed in this study. Further details about the method and device used for detecting the UWB pulse can be found in [171]. Two prototyped tags were placed separately within the test area, as shown in Figure III.31. The energy sources were configured according to the ESTI standard [147], with continuous wave (CW) signals at the RFID frequency band and power levels set at 2 W.

The beacons, which receive the UWB signal, were positioned in the corners and facades of the test area at a height of 5-6 meters. The coordinates of these beacons were known as shown in Figure III.32 (a). Out of the 13 configured beacons, 11 of them successfully received the UWB signal. The tag's location was then calculated using an algorithm, and the position was displayed on the software's graphical interface developed by Uwinloc (Figure III.32 (b)). The accuracy of the calculated position depends on the tag's position relative to the beacon locations. Based on the available tests up to the date of submission, the position accuracy was found to be lower than 1 meter, although this value is highly dependent on the tag's position and orientation. The real-time position of the tags on the map was obtained by filtering their unique identification through the user interface. Ongoing work involves evaluating the tag's performance in a harsh environment by embedding it in a concrete beam and implementing the sensing capability in UWB mode.

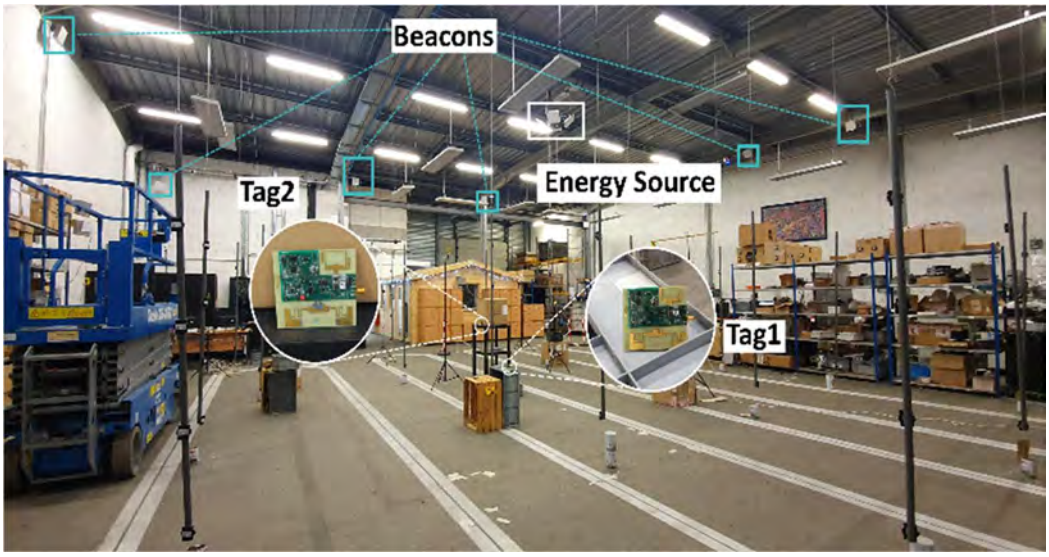

Figure III.31. Geolocation setup of the tags in the 300 m² test area. Thirteen beacons (only six are visible here) and two tags (placed at various position) have been used.

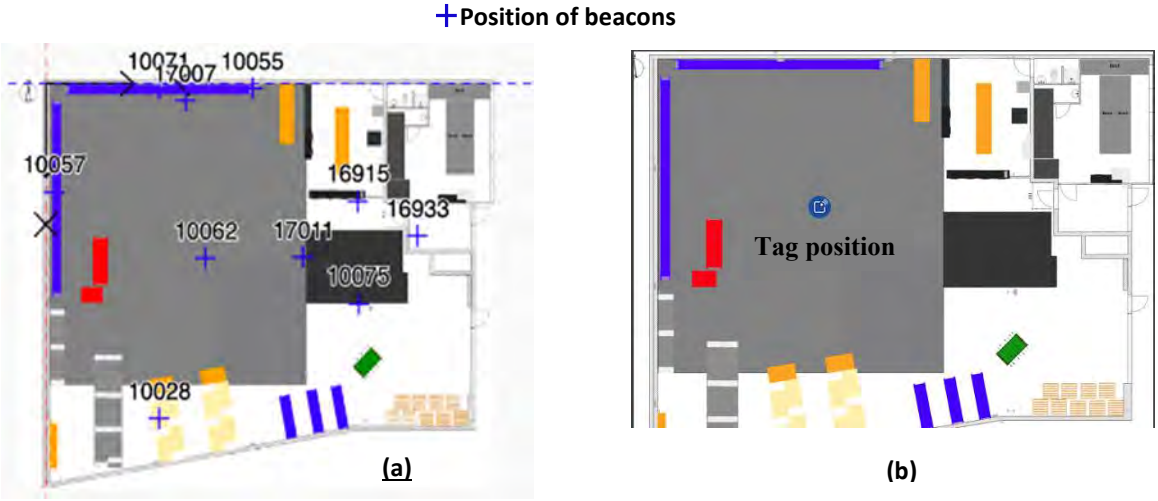

Figure III.32. (a) Mapping of the geolocation tag in the test area: each beacon (fixed position) is represented by its unique identification. (b) The position of the geolocated tag: only one tag was shown inside the overall volume of the test area (1800 m³).

4. Conclusion

In this chapter, we have successfully implemented various battery-free devices using a Wireless Power Transmission System. The objective was to deploy a full compact, battery-free solution for monitoring the physical parameters of concrete structures. To achieve this, we used the rectenna developed in the previous chapter, given its compact size (electrically small) and outstanding performance. Various battery-free sensing node was proposed, and they vary in size, power consumption, and communication technology for data transmission. The Table III.6 provides a summary of all the solutions and their distinct characteristics. The first two proposed solutions are based on the LoRaWAN protocol (LSN1 and LSN2). The LSN1 prototype, being the initial version, has larger dimensions and requires separate connected rectenna for the power supply through WPT. Building upon this prototype, improvements have been made to reduce size, overall power consumption, and the addition of other functionality such as resistivity measurement. This led to the development of LSN2, which used a single antenna for both data uplink and power downlink.

However, the overall power consumption remains relatively high, around 20 mJ at a transmitter power of +4 dBm for 5470 bits/s. As a result, the measurement and data transmission periodicity is relatively long, set at 5 minutes with a relatively high RF power of +10 dBm at the rectifier input. After successfully reducing the overall size of the board (from LSN1 to LSN2), lower-energy solutions were introduced using the Bluetooth Low Energy (BLE) communication protocol. With the BLE-based solutions (BSN1 and BSN2), the overall power consumption is below 1 mJ, enabling shorter measurement intervals (charging and recharging times). The BSN2 prototype, which is half the size of the BSN1 version, is less efficient at lower power levels due to the choice of flexible antenna and its connection to the board. Its association with the PET antenna introduces impedance mismatch and radiation pattern modification.

In conclusion, we have successfully prototyped a battery-free sensing node, LSN1, with dimensions of 140 mm x 90 mm and a total consumption of 21 mJ. Through improvements, we developed BSN2, measuring 47 mm x 35 mm and requiring 946 µJ for operation. However, from a LoRaWAN-based solution to a BLE-based solution, the data transmission range reduced and may result in decreased performance in the presence of SN embedded into the concrete structure due to the bad wave propagation through concrete at higher frequency.

Additionally, we present a unique solution of a multifunctional battery-free tag that combines geolocation in UWB mode and wireless sensing in BLE mode. The prototyped tag is based on an electronic module developed by UWINLOC Company, enabling RF energy harvesting at 868 MHz and UWB signal transmission at 4 GHz. In UWB mode, we measured the average emission rate and placed the tag within a 300 m^2 indoor test area to obtain a preliminary estimate of localization accuracy. The experimental results confirm that the localization accuracy is less than 1 meter but strongly depends on the tag's position and the presence of obstacles within the test area.

Table III.6. Table reporting the developed sensing node prototypes and their characteristics and performance.

Proposed solutions and Photos	**Dimensions**	**Communication technology**	**Features**	**Energy Harvesting solutions**	**Energy consumption for transmission / Tansmitted data bytes**	**Duration (seconds) of the First charge / recharge**
LSN1 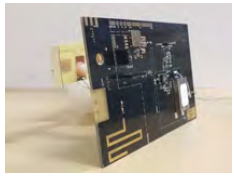	140 mm x 90 mm (w/o) antenna 140 mm x 90 mm x 70 mm (with antenna)	LoRaWAN (CMWX1ZZABZ-091) with printed antenna	Sensors (HDC2010); strain gauge; Resistivity sensor; thermodiodes; PMU(BQ25504); Supercapacitor (22 mF)	External rectenna using a 3D compact antenna	<20 mJ (PTx = +4 dBm and a high data rate of 5470 bit/s) / 4 data bytes	90 / 70 (for P_{RX} = +10 dBm)
LSN2 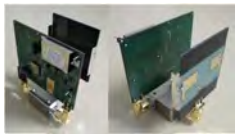	80 mm x 60 mm (w/o antenna) 90 mm x 80 mm x 65 mm (with antenna)	LoRaWAN (CMWX1ZZABZ-091) with the same antenna used for RFEH		External 3D antenna and integrated rectifier circuit		300 /60 (for P_{RX} = +10 dBm)
BSN1 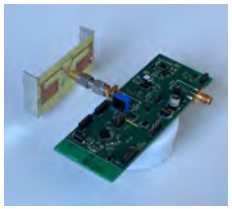	110 mm x 40 mm (w/o antenna) 110 mm x 100 mm (with antenna)	Bluetooth Low Energy (QN9080) with IFA antenna	Sensors (HDC2080); Resistivity sensor; PMU(AEM30940 & BQ25570); Supercapacitor (150 µF)	External 3D compact antenna and integrated rectifier circuit	946 µJ at PTx = 0 dBm / 3 data bytes	198.8 / 97.4 (for P_{RX} = -8.8 dBm)* 48.7 / 27.4 (for P_{RX} = -2.8 dBm)*

BSN2 	47 mm x 35 mm (w/o antenna) 80 mm x 85 mm (with antenna)	Bluetooth Low Energy (QN9080) with IFA antenna	Sensors (HDC2080); Resistivity sensor; PMU (AEM30940); Supercapacitor (220 µF)	External transparent PET antenna and integrated rectifier circuit	946 µJ at P_{TX} = 0 dBm / 3 data bytes	420 / 206.25 (for P_{RX} = -9.3 dBm)* 54 / 27 (for P_{RX} = -3.3 dBm)*
UBT 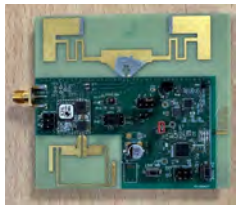	90 mm x 80 mm	Bluetooth Low Energy (QN9080) with IFA antenna &	Sensor (HDC2080); PMU(BQ25570); Supercapacitor (220 µF)	Integrated antenna and harvester circuit of the UGM	960 µJ at P_{TX} = 0 dBm / 3 data bytes	395 / 270.25 (for P_{RX} = -10.24 dBm)* 80 / 43.6 (for P_{RX} = -4.2 dBm)*
		Ultra-Wide Band (UWB) Uwinloc Geolocation Module	Harvester and UWB chip; Capacitor (33 µF)		20 µJ at P_{TX} = 0 dBm / 4 data bytes	Emission rate : 0.55 (for P_{RX} = -4.2 dBm)* 542 (for P_{RX} = -20 dBm)*

*Measurements performed in anechoic chamber; ¤ Measurements performed without antenna; P_{RX} is the received power at the frequency of 868 MHz, by the sensing node at the input of the rectifier or harvester; P_{TX} is the output power of the transmitter

IV. Development of an UHF Energy Harvesting Front-end for the Flexible Geolocation tag

1. Introduction

The works presented in this chapter is in the interest of UWINLOC Company [172], which develops and commercialises an indoor accurate and reliable location solution using a battery-free tags. The UWINLOC solution presented in Figure IV.1, consists of five parts enabling geolocation features for asset tracking. The battery-free geolocation tag is wirelessly powered using far-field Wireless Power Transmission (WPT) technique with electromagnetic (EM) waves radiated by a Radiofrequency Identification (RFID) source named Ultra High Frequency (UHF) exciter, operating at the frequency of 868 MHz. Initially, a reference tag with known relative coordinates is placed into the cell. When the tag to be geolocated harvests enough power from the source, it transmits a signal using Ultra Wide Band (UWB) technology at 4 GHz. This signal emitted from the tag, is then received by several beacons. The real time 3-Dimensional (3D) position of the tag is then accurately computed thanks to triangulation algorithm.

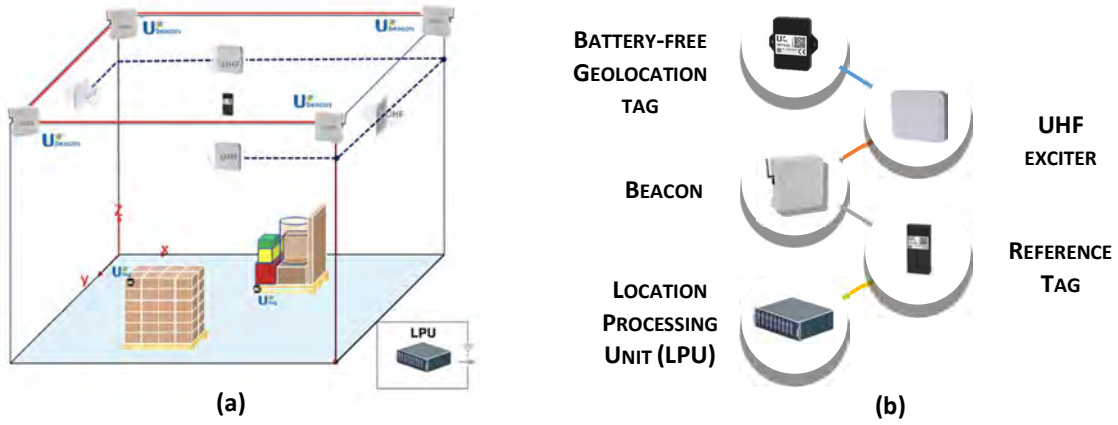

Figure IV.1. UWINLOC Geolocation system: (a) Reference cell; (b) Main part of the system.

The company is faced to certain scientific challenges in the development of their geolocation solution to target different markets. The development of outstanding geolocation tag relies on its ability to improve the following aspects:

- Reduction of overall size of the tag, including the size of antennas.

- Increase in RF-to-DC conversion efficiency, achieved through the energy harvesting system ; the rectenna.
- Improvement of the link budget between the UHF energy source and the geolocatable tag.

To address these identified scientific challenges, the thesis will focus on studying and proposing an optimized solution for a compact RF wireless power transmission system for the battery-free geolocation tag. The objective is to find innovative approaches to overcome these challenges and enhance the performance and functionality of the geolocation solution.

Thus, with trends in the flexible electronics markets [173]–[176], UWINLOC has set its sights on developing a miniaturized and sustainable flexible version of its geolocation tag. The current rigid version of the tag (Utag) has some limitations to be integrated and be attached to assets in complex uses-cases. This development will enable the tag to be attached to small items or curved surfaces in industrial environments, opening up possibilities for more diverse applications. The main target markets for these flexible geolocation tags include healthcare, logistics, and retail.

This chapter focuses on the research conducted as part of the European SMARTEES project, which stands for SMART Emerging Electronics Servicing. The project received co-funding from the European Union's Horizon 2020 research and innovation program under grant agreement No. 761496, with a duration of nine months. UWINLOC Company participated in this project with the aim of developing a flexible and compact battery-free geolocation tag for asset tracking. The objective of this project is to develop and build an application experiment through the flexible, low-cost, and efficient development of the geolocation tag. It will go through the investigation of the feasibility of manufacturing printed rectifiers, antennas, and rectennas using screen printing and inkjet printing techniques.

The project involves four partners: UWINLOC, LAAS-CNRS, IMEP-LAHC, and Eurecat. Eurecat, a leading technology center in Catalonia and the largest private research organization in Southern Europe, is leading the project. Eurecat is specialized in providing industrial and business sectors with advanced technology and expertise to meet their innovation needs and enhance their competitiveness in a rapidly evolving environment [177]. The overall studies were carried out on the RF Energy Havesting (RFEH) part of the Utag in order to fulfil the objective of acquiring crucial knowledge with the regards to the development of the flexible geolocation tag. The project progress was organized into three technical Work Packages (WP):

- WP1: This phase involved studying and comparing various materials such as substrates and conductive inks, and defining the fabrication techniques and processes.
- WP2: Building upon the technical specifications determined in WP1, this phase focused on material characterization and validation of the fabrication process, including the evaluation of the electrical and dielectric properties of the materials through the design of a rectifier and an antenna.
- WP3: This step involved prototyping. Multiple rectennas were fabricated and tested on flexible materials, thanks to the knowledge acquired in the previous WPs. The performance of the flexible rectennas was then compared with the harvester stage of the current geolocation tag, which is built on a rigid substrate.

2. Specifications

2.1. Choice of materials

The preliminary step in this project is to as evaluate and select the appropriate material for our application. The performance of the antenna, and the rectifier, relies on the selection of materials (substrate, conductive ink, and protective materials) for design and manufacturing purposes. In general, a transmitting antenna can be modelled by an equivalent circuit of a transmission line, as shown in the figure Figure IV.2. The equivalent input impedance of the antenna is determined by both a resistive part (Ra) and a reactive part (Xa).

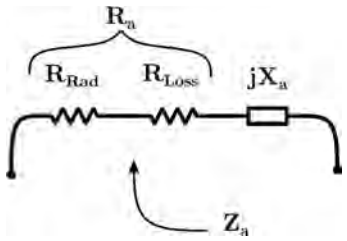

Figure IV.2. Equivalent circuit model of an antenna in transmitting mode.

The resistive component of the antenna represents the radiation resistance and the loss resistance. The loss resistance consider various ohmic losses that occur in the antenna, including dielectric losses related to the material's loss tangent, ohmic losses due to the conductivity of the conductive ink, and losses from nearby objects. This resistance quantifies the power dissipated by the antenna. The radiation resistance of the antenna reflects its ability to efficiently radiate electromagnetic waves. It depends on the antenna type and its geometry relative to the wavelength. To achieve higher antenna efficiency, it is important to maximize the radiative resistance and minimize the losses. The antenna efficiency can be evaluated using equations (IV.2) and Figure IV.3. The power radiated by the antenna, as defined by $P_{radiated}$, is reduced by both losses caused by impedance mismatch between the antenna and the source and the previously mentioned losses represented by R_{Loss}.

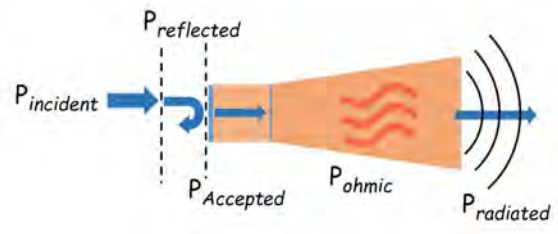

Figure IV.3. Diagram of the incident power dissipation through a transmitting antenna.

$$\eta_{ant} = \eta_{mismatch} \cdot \eta_{rad.} = \frac{P_{radiated}}{P_{incident}} \quad \text{(IV.1)}$$

$$\eta_{mismatch} = \frac{P_{accepted}}{P_{inc}} \quad and \quad \eta_{rad.} = \frac{P_{radiated}}{P_{accepted}} \quad \text{(IV.2)}$$

As mentioned earlier, the radiation efficiency of the antenna is significantly influenced by the dielectric properties of the substrate, including its relative permittivity (or dielectric constant), loss tangent, thickness, and the resistivity of the conductive ink.

The relative permittivity (ε_r) of a material determines its ability to store electrostatic energy and be polarized by an electric field. The dimensions of an antenna are theoretically related to the relative permittivity and the thickness of the substrate used. Higher dielectric constant results in smaller antennas since they affect the guided wavelength (λ_g). The guided wavelength is the wavelength of the signal propagating inside a transmission line. In the case of a microstrip transmission line (MTL), its value can be calculated using equation (IV.3).

$$\lambda_g = \frac{c}{f\sqrt{\varepsilon_{eff}}} \quad \text{(IV.3)}$$

where c represents the speed of light, f is the resonant frequency, and ε_{eff} is the effective dielectric constant. The effective dielectric constant is determined by the width of the microstrip transmission line (MTL) and the thickness of the substrate. Consequently, altering the dielectric constant causes a shift in the impedance of the circuit or antenna. Numerous studies have highlighted the influence of the dielectric constant on the dimensions and performance of antennas [178], [179]. For instance, a high-dielectric-constant and flexible cellulose composite nanopaper, with a range of 726.5 to 1.1 GHz, has been utilized in the design of a miniaturized antenna. It is mentioned that the proposed antenna, employing the nanopaper substrate, is approximately half the size of an antenna printed on conventional nanopaper or plastic film [180]. Miniaturizing antenna will have an impact on the radiation resistance, depending on the effective radiation surface of the antenna relative to the wavelength. Regarding the loss tangent or dissipation factor (tanδ) of the substrate, it is the results of signal propagation losses along the transmission line and, more precisely, for the dissipation of electromagnetic energy within the substrate. Therefore, a cost-effectiveness analysis was conducted to find the optimal solutions. Table IV.1 shows the potential substrates that can be used. Among them, Kapton 300 HN and PET Melinex 506 have the lowest loss tangent. For the next phase of this project, PET Melinex 506 was selected as the chosen substrate due to its low cost, despite its limited temperature tolerance. However, it is recommended to characterize the dielectric properties of the substrate to ensure reliable simulation results.

Table IV.1. Substrates potentially usable in the project

References	Substrates	Thickness (um)	Dielectric constant @1KHz	Loss tangent Tan δ @1GHz	Cost
[181]	Kapton 500 HN	125	3,5	0,0026	High
[181]	Kapton 300 HN	75	3,5	0,002	High
[182]	PET Melinex 506	125	2,9	0,002	Low
None	PEN Q65FA	125	2,9	0,005	Medium

Conventional screen-printing inks are known to be cheaper and is suitable for the requirements. Copper and silver inks for screen printing are significantly more cost-efficient compared to gold inks. A list of inks usable according to the manufacturing process of Eurecat is presented in Table IV.2. Silver inks are predominant especially because of their stability in normal room conditions, and their high conductivity. Finally, silver Dupont 5000 was used as the best alternative.

Table IV.2. Conductive inks potentially usable in the project

Inks	Printing technology	Thickness per layer (um)	Resistivity Rsq (mΩ/sq/mil)	Solid content %	Viscosity (PaS)
Copper (Dupont PE510)	Screen	6-10	<35	76-79	16-22
Silver (Dupont 5000)	Screen	8-9	<15	58-62	3.5-16
Silver (Norcote ELG4105)	Screen	8.6	<20-25	95.5	4.5-5.5
Silver ANP (DGP 40LT-15C)	Inkjet	2-4	11 (uΩ/cm)	30-35	10-17

2.2. Architecture of the implemented solution

As stated before, the purpose of this project is to develop and build an application experiment through the flexible, low-cost, and efficient development of the geolocation tag. In this regard, an intermediate design step was go through a differential rectified with connected to a 50 Ω antenna via a RF connector, to form a rectenna. The technical task was to design and simulate the rectifier according to the material specifications. The rectifier is intended to be optimized for maximum efficiency at the lowest input power, considering a targeted load impedance of 10 kΩ for characterization. Regarding the rectifier topology, there are two categories of rectifiers according to the input. Single ended rectifier receiving the RF signal between the wire and the ground, and differential rectifier with two signals of opposite polarity. Figure 29 shows schematics of a single ended doubler rectifier and a Greinacher rectifier in with differential inputs. The differential design has the advantage to cancel the noise from the wire but requires more components and thus induces losses. It also presents the ability to be directly connected to a conventional dipole antenna without any transition.

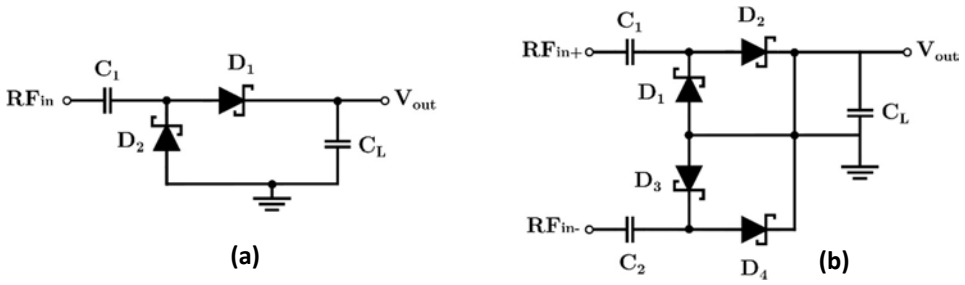

Figure IV.4. Schematics of the single-ended rectifier(a) and differential rectifier (b).

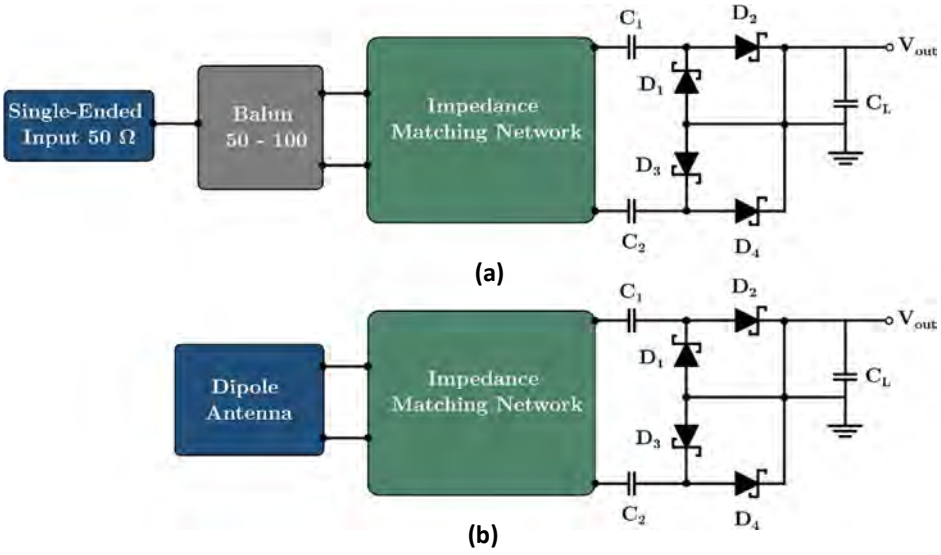

Figure IV.5. (a) Differential rectifier design architecture with a single-ended input; (b) Differential rectenna design.

The Greinacher rectifier with differential input has been chosen for the next simulations. The proposed design architecture is presented in Figure IV.5. A matching network is required to achieve a 100 Ω input impedance from the complex capacitive input impedance of the rectifier with Schottky diodes. The next stage involves a balun, which converts the input from the matching network to a single-ended input 50 Ω impedance, facilitating the characterization of the RF connector.

This balun will not be included in the final rectenna design because the targeted antenna for the rectenna development will be a differential antenna (printed folded dipole). The need to generate a balanced signal from an unbalanced signal (or vice versa) and to match the impedance has led to the use of various balun devices in RF applications.

- Transformer Balun

The transformer is generally used to decrease or increase the AC voltage level. However, such devices are also employed to prevent the flow of current between the source and the load. The simplest approach to obtain a balun is by using a transformer device. The impedance ratio can be established based on the ratio between the number of turns in the primary (N1) and secondary (N2) windings of the transformer. This relationship is expressed by equation (IV.4) when the source impedance and the load impedance are not matched.

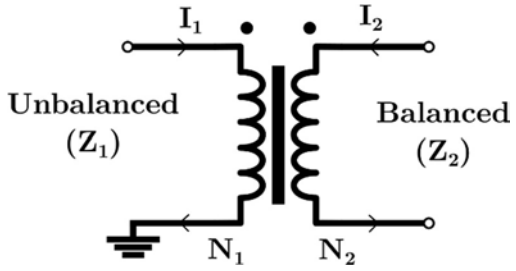

Figure IV.6. Schematic of the voltage transformer balun.

$$\frac{Z_2}{Z_1} = \left(\frac{N_2}{N_1}\right)^2 \quad \text{(IV.4)}$$

Mini-Circuits and Coilcraft are among the manufacturers that offer a variety of mini-RF balun transformers with a wide frequency range. These transformers are commonly used in applications such as antennas, mixers, and push-pull amplifiers across different frequency ranges. Despite their advantages, including small size, wide frequency range, and low losses, it is worth noting that they are relatively expensive.

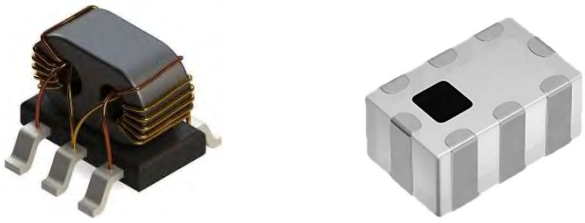

Figure IV.7. Examples of SMD Transformer Balun. (a) Balun coil with ferrite core assembled with SMD pads; (b) SMD balun transformer.

In the field of Radio Frequency Integrated Circuits (RFIC), integrated baluns are commonly based on transformer baluns. For instance, a new design approach of an integrated balun for 60 GHz applications in 65nm CMOS technology was proposed in [183] as seen in figure Figure IV.8 (b).

Another approach, targeting a lower frequency range, was presented in [184]. It consists of a stacked multi-layer transformer balun operating at 128 MHz. Figure IV.8 (d).provides a 3D view of the balun, showing the four-layer pattern of the stacked coil.

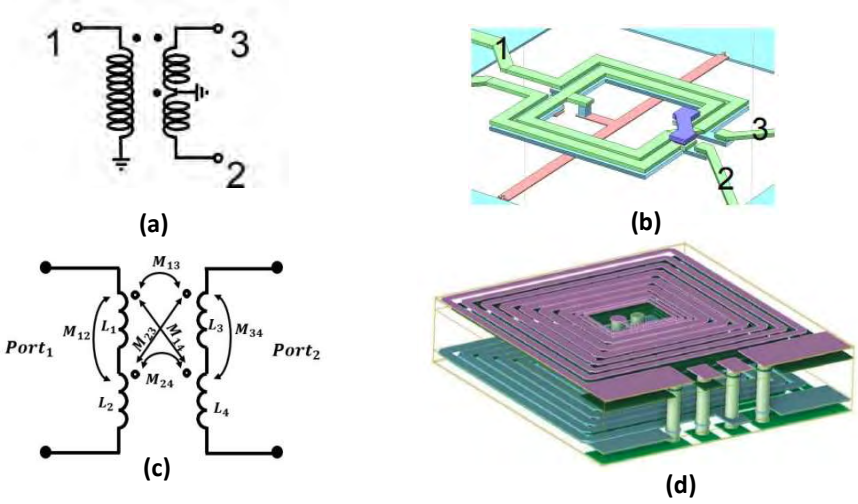

Figure IV.8. (a) Circuit model of classical transformer balun configuration simulated; (b) Image of the transformer balun simulated using Sonnet software [183]; (c) Circuit equivalent of the proposed balun using 4 layer PCB, (d) 3- D view of the balun with four-layer pattern of the stacked coil model [184].

- Planar Balun

One of the widely used planar microwave baluns is the Marchand Balun, which is employed to generate balanced output from an unbalanced input. It was initially introduced by Nicolas Marchand in 175] as a wide-band conversion transformer. Over time, it has proven to be highly useful in Microwave Integrated Circuit (MIC) or Microwave Monolithic Integrated Circuit (MMIC) designs, particularly for mixers, amplifiers, and oscillators [185]–[187].The conventional structure of the Marchand balun is based on microstrip-coupled lines, as illustrated in Figure IV.9. The two coupled quarter-wavelength transmission lines ensure good isolation, a 180° phase-shift between the outputs, and the rejection of harmonics in the even-mode.

Although the Marchand balun offers broad bandwidth, it is more complex to design, requires a specialized manufacturing process, and is not suitable for low-frequency applications due to the significant physical size of the microstrip lines.

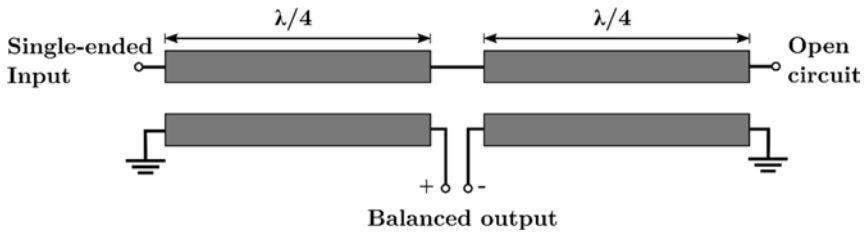

Figure IV.9. Conventional Marchand balun structure.

- Lumped LC Balun

The LC Balun is a lumped component network used to convert a single-ended input to a differential output (or vice versa) with a phase shift of ±90°, while also allowing impedance transformation. It consists of two capacitors and two inductors, as depicted in Figure IV.10. This circuit acts as a resonant circuit and is typically used for narrowband applications. The LC Balun offers several advantages, including ease of design, low cost, and tunability. When operated at the resonant frequency (f_0), the circuit analysis can be simplified, and we can derive the following equations (IV.5) and (IV.6) to calculate the values of the inductor (L) or capacitor (C). X represents the reactive impedance obtained at resonance, considering the input impedance of the source and the load.

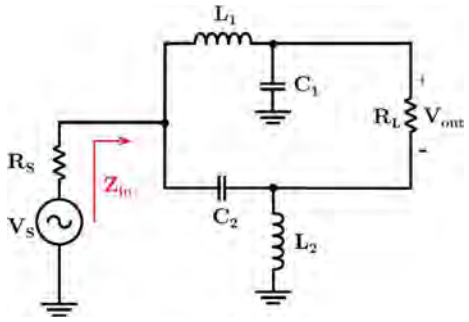

Figure IV.10. Schematic of the LC Balun network.

$$L \cdot w_0 = \frac{1}{C \cdot w_0} \Rightarrow Z_0 = \sqrt{\frac{L}{C}} = \sqrt{R_s \cdot R_L} \quad \text{(IV.5)}$$

$$L = \frac{X}{2\pi \cdot f_0} \; and \; C = \frac{1}{2\pi \cdot X \cdot f_0} \quad \text{(IV.6)}$$

Previous studies have focused on rectifiers with a differential topology using commercially available RF Schottky diode series pairs. A differential doubler rectifier with odd harmonics suppression characteristics is designed at 1.83 GHz in [188]. It achieved an efficiency of 28% with a 7.29 kΩ load resistance when receiving an input power of -15 dBm. Another differential rectifier architecture composed of a pair of voltage double stages with a balun component has been suggested in [189]. This design in Figure IV.11 (b), has the particularity to provide a balanced output voltage for biasing analog IC. The RF-to-dc conversion efficiency was evaluated to 30% at 900MHz for a dc load of 10 kΩ for an RF input power of +5 dBm. However, this kind of architecture with a commercial SMD balun does not favour miniaturization and can induce insertion losses of at least +1 dB.

Furthermore, a particular rectifier design using resistance compression network with the same differential with double stage Schottky diode is presented in [190]. Experimental results indicate that it can achieve an efficiency of 15% for low RF input power at -5 dBm across an output load of 2 kΩ at a frequency of 915 MHz. Despite using fewer lumped components to avoid additional insertion losses, this double-stage differential rectifier topology cannot achieve an efficiency higher than 30% with the unoptimized load.

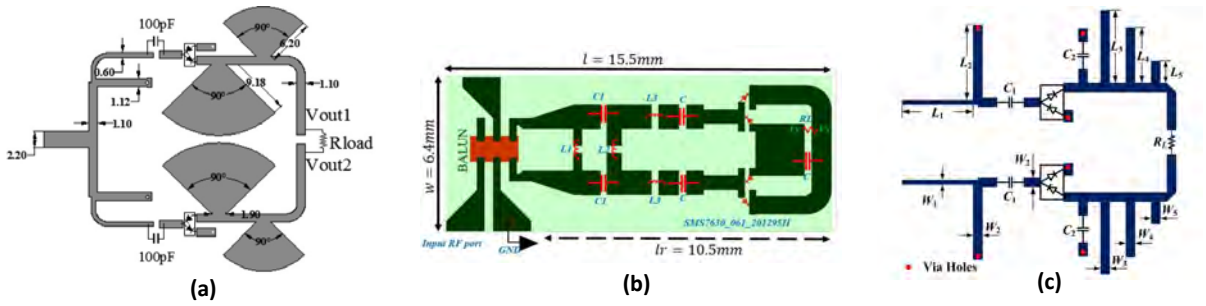

Figure IV.11. Layout of differential rectifier design with series pair Schottky diode presented on the state of the art : (a) Differential doubler topology rectifier with odd harmonics suppression at 1.83 GHz [188]; (b) RF differential rectifier optimized over a wide bandwidth in [189]; (c) Differential rectifier using resistance compression network designed at 915 MHz [190].

3. Evaluation of rectifier performances on rigid substrate

As the targeted application is on the narrow band of the ISM 868 MHz, we have chosen to implement a lumped element LC balun design, which is simple and highly adjustable. The design and simulation of the balun are conducted using ADS software from Keysight. The first step was to design the LC balun network that ensures the impedance transition from 50 Ω to 100 Ω. The component values are determined using equations (IV.5) and (IV.6) at 868 MHz. When selecting the inductor, it is crucial to consider the numerical value deviation based on the frequency. Therefore, instead of relying on ideal components from an empirical model, we used standard components from the Murata library in the simulations. The values of the components, specifically a 15 nH inductor and a 3.3 pF capacitor, were adjusted to achieve the desired return loss. The balun design, along with the corresponding return loss, is presented in Figure IV.12 (b). The return loss plot is depicted on the Smith chart, illustrating the impedance matching performance of the LC balun network.

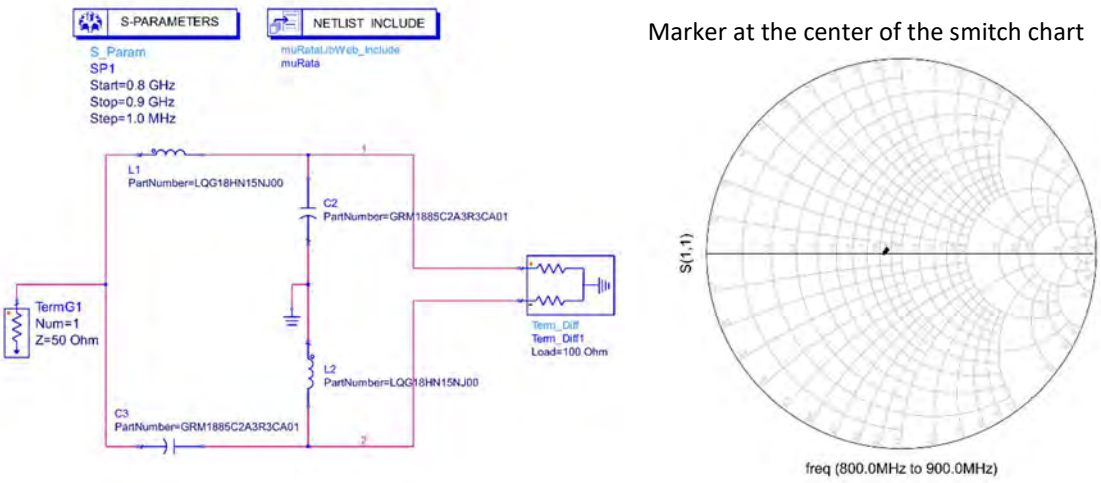

Figure IV.12. (a) Schematic view of the balun circuit; (b) Simulated return loss on smith chart with the marker at 868 MHz.

A preliminary rectifier circuit has been designed following the validation of the balun on simulation. The circuit employs a series Schottky diode and is optimized for low input power at -15 dBm. To emulate the load of the input impedance of the active stage of the tag, a resistive load of 10 kΩ has been chosen. It is important to consider the insertion losses of the components to be used in order to minimize any significant loss of input power. The dc resistance of the inductor plays a critical role as higher resistance leads to greater losses and lower conversion efficiency of the rectifier. Prior to implementing the circuit on the chosen flexible substrate, the design was first carried out on a rigid FR4 substrate (thickness: 0.8 mm, dielectric constant: 4.4, dielectric loss tangent: 0.02) to establish correlations between simulations and measurements. The design is based on the schematic depicted in Figure IV.5 (a), using two differentially connected Greinacher rectifier topologies. A carefully selected Schottky diode type, the HSMS-285C series pair from Avago, has been chosen for our specific applications. This diode is a zero bias Schottky diode optimized for low power signal levels (Pin <-20 dBm) and frequencies below 1.5 GHz. It is suitable for low-power level applications [191]. The simulation model of the HSMS285C diode has been imported into the ADS software high-frequency diode library to ensure accurate simulation results. This model allows for the consideration of the diode's non-linearity. The quality factor, or Q-factor, of the inductor is a crucial parameter to consider in our rectifier design. It is a measure of the energy storage capability and lossiness of the inductor. The Q-factor is directly proportional to the frequency and inversely proportional to the DC resistance of the inductor. Higher resistance leads to increased losses and a lower Q-factor. To ensure accurate simulation results that closely match the measurements, the inductor model used in the design incorporates the Q-factor value. This model, referred to as INDQ, is detailed in [192].

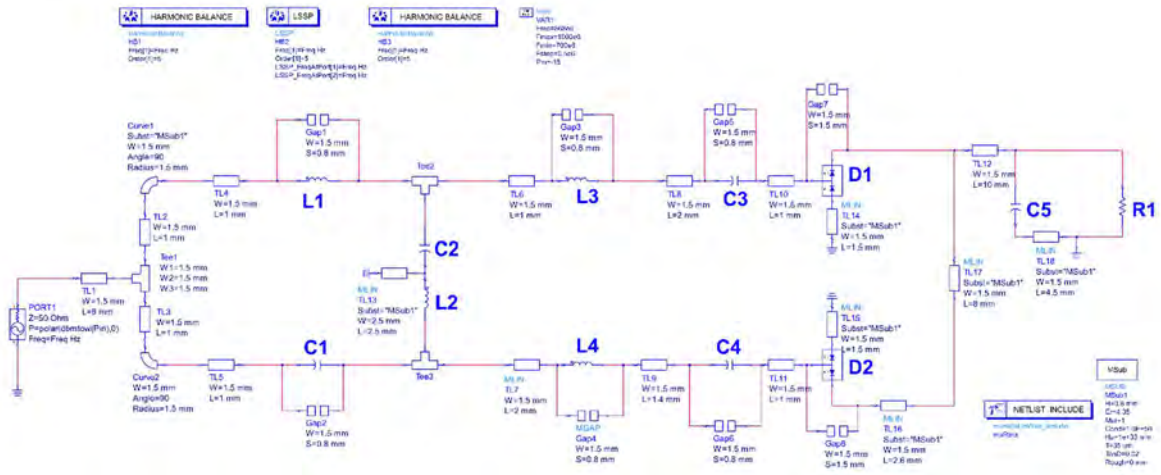

Figure IV.13. Schematic of the differential rectifier implemented on ADS Keysight.

The rectifier was designed using microstrip technology on an FR4 substrate. Several steps of optimization were operated on the transmission lines length to improve the return loss under -10 dB at the desired frequency band. Following the balun stage of the rectifier, a pair of lumped inductors were employed to match the output impedance of 100 ohms to the input impedance of the double-stage rectifier. This matching ensures efficient power transfer between the stages. The final design of the rectifier with microstrip transmission lines and gaps (as close as possible to the prototyped rectifier) is presented in Figure IV.13. Table IV.3 provides a list of the components used in the design, along with their respective values and part numbers.

Table IV.3. List of component of the differential rectifier design on rigid substrate.

Component name	Part Number	Value
L1=L2	LQP18MN15NG02	15 nH
L3	LQP18MN6N8C02	6.8 nH
L4	LQP18MN33NG02	33 nH
C1=C2	GRM1885C2A7R5CA01D	7.5 pF
C3=C4=C5	GRM1885C1H101JA01	100 pF
D1 = D2	HSMS-285C-BLKG	--
R1	--	10 kΩ

Instead of the S-Parameter simulation tool, the Large-Signal S-Parameter (LSSP) simulation is used to compute the return loss of the rectifier. This approach takes into account the non-linear behaviour of the components, which is crucial at low input power levels. Specifically, the design was optimized for an RF input power of -15 dBm. As seen in Figure IV.14 (b), the simulated design is precisely matched at the targeted frequency band with a return loss under -10 dB. Subsequently, the proposed rectifier design was fabricated on an FR4 substrate, and an SMA connector was added to provide RF input power for characterization purposes, as shown in Figure IV.14 (a). During the measurement, a slight frequency shift was observed compared to the simulation results. This discrepancy can be attributed to the inaccuracies in the adopted simulation models as well as the effects of soldering. The frequency shift also affected the maximum RF-to-DC conversion efficiency, which was measured at 25% compared to the simulated value of 28%, as depicted in Figure IV.15 (a). However, it is important to note that despite this discrepancy, the measured efficiency remains within an acceptable range. Furthermore, a comparison of the DC output voltage across the load was performed between the simulation at the targeted frequency of 868 MHz and the measurement at the resonant frequency of 840 MHz. The prototyped rectifier achieved an output voltage of 282 mV at an input power of -15 dBm. The measurement showed an average offset of only 15 mV over the range of RF input power, indicating a relatively stable and reliable performance of the rectifier. After the validation of the rectifier topology on FR4 substrate, the same topology was adapted for an improved design on flexible PET substrate. The design process involved modifying the dimensions and layout of the components to suit the characteristics of the PET substrate. Careful consideration was given to the material properties and manufacturing processes specific to the flexible substrate.

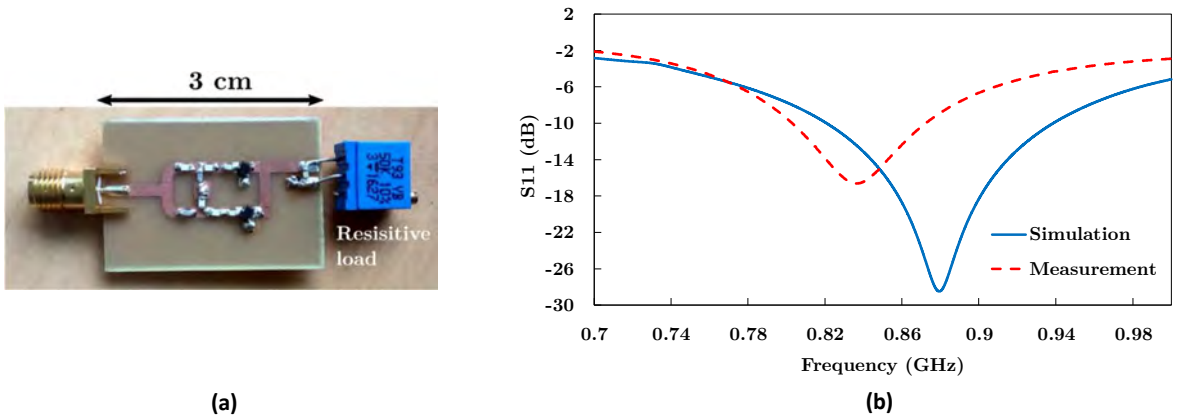

(a) **(b)**

Figure IV.14. (a) Photo of the fabricated rectifier; (b) Simulated (blue line) and measured (red dashed line) return loss of the differential rectifier at an RF input power of -15 dBm.

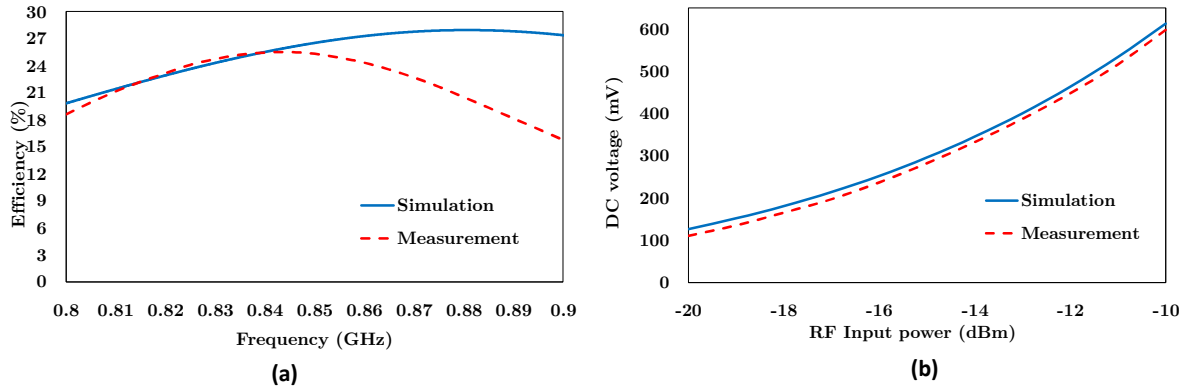

Figure IV.15. Comparison between simulation and measurement of the designed rectifier : (a) RF-to-DC conversion efficiency as function of the frequency at -15 dBm ; (b) DC output voltage as function of the RF input power (868 MHz for the simulation and 840 MHz for the measurement).

4. Rectenna Design on flexible PET substrate

4.1. Material characterization

With the objective of prototyping an optimized design of rectifier and antenna, the PET MELINEX 506 material is used as substrate. The two main RF parameters needed for the simulation step are dielectric constant (D_k) or relative permittivity (ε_r) as well as the Dielectric Loss Tangent ($\tan\delta$) of the material with both at the range of frequencies of energy harvesting to ensure accurate simulation results. Any material is defined by its permittivity expressed in equation (IV.7) and whose value depends on the frequency. The real part of the dielectric constant (ε'), known as the absolute permittivity, defines the material's energy storage capacity, while the imaginary part (ε'') accounts for energy dissipation and allows for estimating losses. In the case of a lossless material or medium, the imaginary part is equal to zero. In practical design applications, engineers primarily focus on the dielectric constant of materials, which can be calculated using equation (IV.8).

$$\varepsilon^* = \varepsilon' + j \cdot \varepsilon'' \tag{IV.7}$$

$$D_k = \varepsilon_r = \frac{\varepsilon_m}{\varepsilon_0} \quad with \ \varepsilon_m = \varepsilon' \tag{IV.8}$$

where ε_m is the absolute permittivity of the material and ε_0, the vacuum permittivity. The loss tangent is a quantitative factor that indicates how much power loss is induced by the material. Through the permittivity, it can be obtained via the ratio of the imaginary part to its real part as in equation (IV.9).

$$tan\delta = \frac{\varepsilon''}{\varepsilon'} \tag{IV.9}$$

An initial development phase was conducted to characterize the material at 868 MHz and validate the parameters provided in the datasheet. There are several techniques available for characterizing the dielectric properties of materials, and the choice of technique depends on factors such as the type of material (solid, liquid, gas), frequency, expected accuracy, and thermal stresses. Some of these techniques include the coaxial probe, transmission line, free space, resonant cavity, parallel plate, and measurement of inductance methods, as discussed in [193], [194]. In order to accurately characterize the material using simple and efficient methods, considering the targeted frequency range, planar transmission line techniques were selected for extracting the dielectric parameters.

The transmission line method is a convenient, easy and fast dielectric properties extraction technique. However, it has limitations in terms of frequency range (not a frequency-dependent behaviors) and accuracy compared to the resonant cavity or parallel plate method.

- *Resonant methods of transmission line : Open T-stub resonator method*

In this section, the T-resonator test method is studied from a theoretical perspective and experimentally validated for the extraction of dielectric parameters. The T-resonator method, which uses an open-circuit T-stub, is a widely used technique for characterizing dielectric properties. This method has been demonstrated in various research studies [195]–[198]. In RF engineering, an open-ended stub refers to a transmission line with a stub length equal to one-quarter of the wavelength of the target frequency. By measuring the resonant frequencies of the open-ended stub, the effective permittivity of the material can be determined. It is important to note that, in this context, the substrate is considered as an inhomogeneous and non-magnetic material. The electrical length of the stub is directly proportional to the guide wavelength, and this relationship can be mathematically expressed using equation (IV.10).

$$l_{stub} = \frac{n \cdot \lambda_g}{4} \quad with \quad \lambda_g = \frac{c_0}{f_n \cdot \sqrt{\varepsilon_{eff}}} \tag{IV.10}$$

where n is a positive odd integer, λ_g is the guided wavelength, c_0 is the speed of light in the vacuum. The guide wavelength is dependent on the effective permittivity of the material and the operating frequency. Once the dielectric constant is determined, the loss tangent or dissipation factor (tanδ) needs to be determined as well.

The quality factor of a resonant structure is a measure of its ability to store energy and is directly influenced by the losses caused by the substrate, which is represented by the dissipation factor. The quality factor Q_0 of a resonator can be evaluated by measuring the transmission coefficient (S_{21}) and determining the upper and lower frequencies at which the insertion loss reaches 3 dB at each resonant frequency. This relationship is expressed by equation (IV.11); where f_0 is the resonant frequency at a specific mode, f_h is the upper frequency at 3 dB insertion loss, and f_l is the lower frequency at 3 dB insertion loss.

The obtained quality factor Q_0,, as defined by equation (IV.12), considers the losses induced by the resonator. $Q_{dielectric}$ represents the losses induced by the dielectric material, $Q_{conductor}$ represents the losses induced by the conductor, and $Q_{radiation}$, represents the losses induced by radiation from the open-ended structure. Given the various parameters that affect the quality factor, the loss tangent has not been determined using this method under conditions of rapid and less precise characterization. However, we can also evaluate the attenuation per guided wavelength (in dB/λ_g)**.**

$$Q_0 = \frac{f_0}{BW_{3dB}} \quad with \quad BW_{3dB} = f_h - f_l \tag{IV.11}$$

$$\frac{1}{Q_{dielectric}} = \frac{1}{Q_0} - \frac{1}{Q_{conductor}} - \frac{1}{Q_{radiation}} \tag{IV.12}$$

A preliminary design of an open-ended T-stub was designed with the standard dielectric parameter of the PET Melinex 506 as provided in Table IV.1, and its structure is shown in Figure IV.17 (a). Once the T-stub was simulated on ADS with a stub line (l_{stub}) of 73.66 mm, it was fabricated using screen printing on the same PET substrate with silver ink, and then measured using a vector network analyzer. The inkjet manufacturing process was utilized for this project, specifically using the Dimatix Inkjet printer DMP-2850 from Fujifilm [199]. This printer enabled the deposition of fluidic materials on an A4 substrate using a disposable piezo inkjet cartridge. In addition to inkjet printing, mask-based printing technologies were also employed in this project. These technologies involve the use of analog masks (such as screens, cylinders, plates, etc.) to deposit the desired patterns. Among them, screen-printing was particularly utilized, although it typically results in a higher layer thickness compared to inkjet printing.

The geometry of the stub allows for the determination of the relative permittivity from the effective permittivity as referenced in [200]. In microstrip design, the relationship between the effective and relative permittivity is important, especially when the ratio of the transmission line width to the substrate thickness is equal to or greater than one. The effective permittivity of the inhomogeneous substrate can be calculated using equation (IV.13), which takes into account the width of the conductor (w = 0.32 mm) and the substrate thickness (h = 125 µm). The flexibility and the low heat stability of the substrate did not allow the use of standard SMA connector to be soldered. It was therefore more judicious to use end-launch connector from Southwest Microwave [201]. These connectors provide a reliable and efficient means of connecting the microstrip transmission line without compromising the substrate's integrity.

The measurement of the stub was operated up to a frequency of 4 GHz to capture at least 3 harmonics (or 3 nodes) . By analyzing the measured resonant frequencies, we were able to determine the effective permittivity of the substrate using equation (IV.10) and then calculate the relative permittivity using equation (IV.13). The measured resonant frequencies and their corresponding effective permittivity values are listed in Table IV.4. The values of relative permittivity varied slightly with frequency, with an average value of 3.44 and a standard deviation of 0.17. Subsequently, we performed a retrosimulation on ADS using a relative permittivity value estimated at 3.5, compared to the measured value of 2.9. Figure IV.18 demonstrates a good correlation between the retrospective simulation and the measurement results.

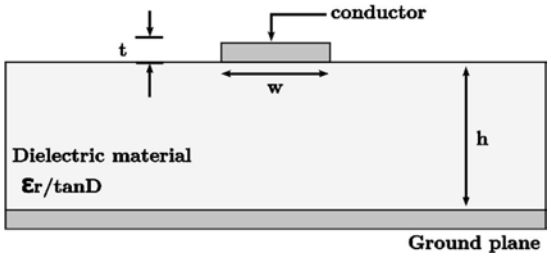

Figure IV.16. Cross section view of microstrip transmission line geometry.

$$\varepsilon_{eff} = \frac{\varepsilon_r + 1}{2} + \left[\frac{\varepsilon_r - 1}{2\sqrt{1 + 12\left(\frac{h}{w}\right)}}\right] \quad if \quad \frac{w}{h} \geq 1 \tag{IV.13}$$

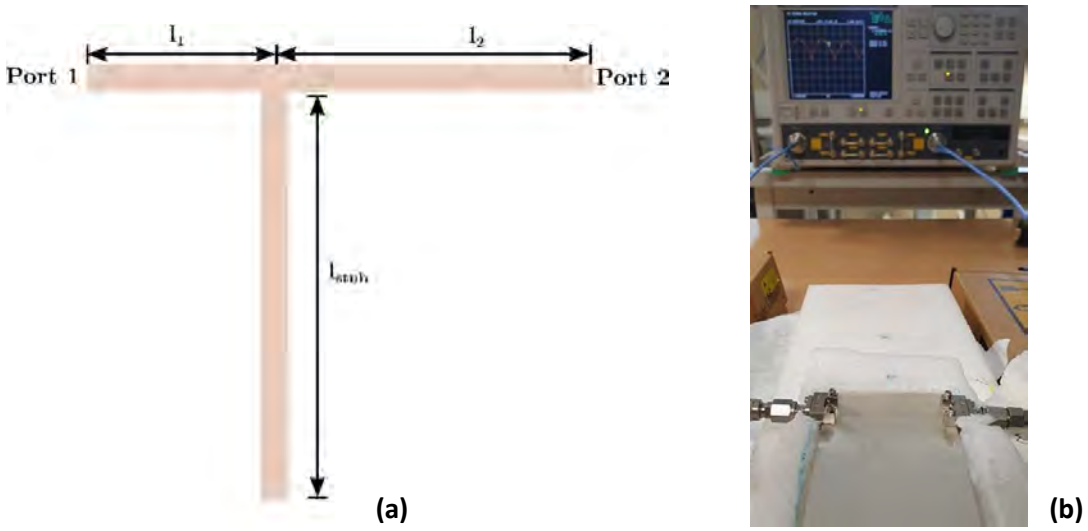

Figure IV.17. (a) Structure of the designed microstrip quarter-wavelenght open-ended stud resonator (l1= 15 mm and l2=35mm; (b) Photo of the S-parameters measurement setup for the prototyped structure.

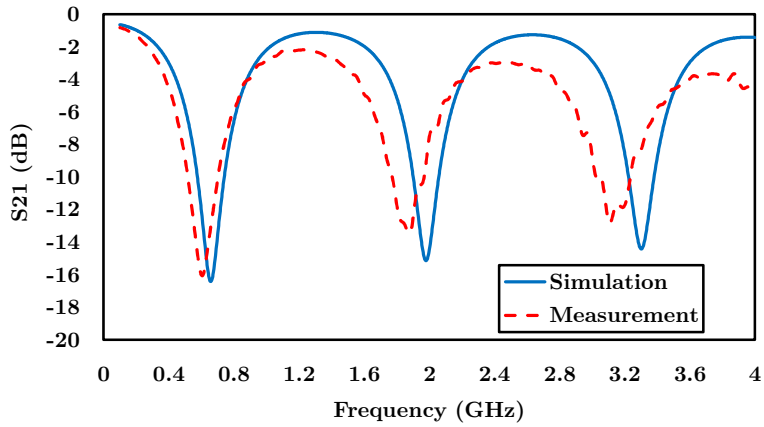

Figure IV.18. Comparison between the measured and retro-simulated transmission coefficient of the microstrip open-ended stub resonator with εr *= 3.5.*

Table IV.4. Extracted effective and relative permittivity of the PET material for microstrip T-stub resonator method.

n	Resonant Frequency (GHz)	ε_{eff}	ε_r
1	0.607	2.87	3.63
3	1.879	2.64	3.31
5	3.108	2.68	3.37

Another design of an open-ended T-stub resonator was implemented using Coplanar Waveguide with Ground (CPWG) on the same substrate in order to compare the results with the microstrip design. CPWG transmission lines have advantages over microstrip lines, such as reduced dispersion and prevention of unwanted modes from propagating. This technique has also been proposed for the characterization of microwave [202]. By using the effective permittivity value obtained through the analysis, the relative permittivity can be calculated using equations (IV.14) to (IV.18) from [200]. The

CPWG T-stub line is designed with a width (w) of 0.35 mm and a gap of 0.4 mm to ensure a characteristic impedance of 50 ohms for the transmission line.

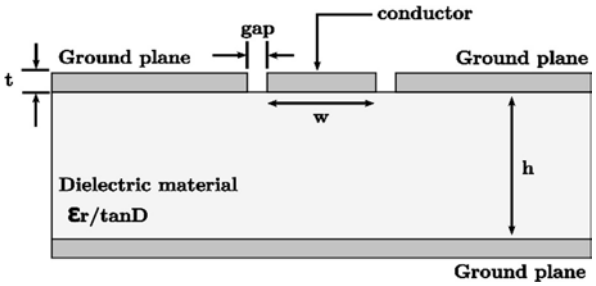

Figure IV.19. Cross section view of Coplanar waveguide with ground transmission line geometry.

$$\varepsilon_{eff} = \frac{1 + A \cdot \varepsilon_r}{1 + A} \quad with \quad A = \frac{K(k') * K(k_1)}{K(k) * K(k_1')} \tag{IV.14}$$

$$k = \frac{a}{b} \tag{IV.15}$$

$$k' = \sqrt{1 - k^2} \tag{IV.16}$$

$$k_1 = \frac{\tanh\left(\frac{\pi \cdot w}{4 \cdot h}\right)}{\tanh\left(\frac{\pi \cdot b}{4 \cdot h}\right)} \tag{IV.17}$$

$$k_1' = \sqrt{1 - {k_1}^2} \tag{IV.18}$$

where w is the width of the trace, b is the length between the two adjacent ground plane on the top layer (w+2*gap), t is the thickness of the metallization and h the thickness of the substrate. The function K(x) is the elliptical integral of the first kind. The relative permittivity of the substrate was determined to be 3.44 ± 0.08. The retrosimulation of the resonator with a relative permittivity of 3.5 is compared to the measurement in Figure IV.20 (b) and the difference is more significant at the harmonic frequencies.

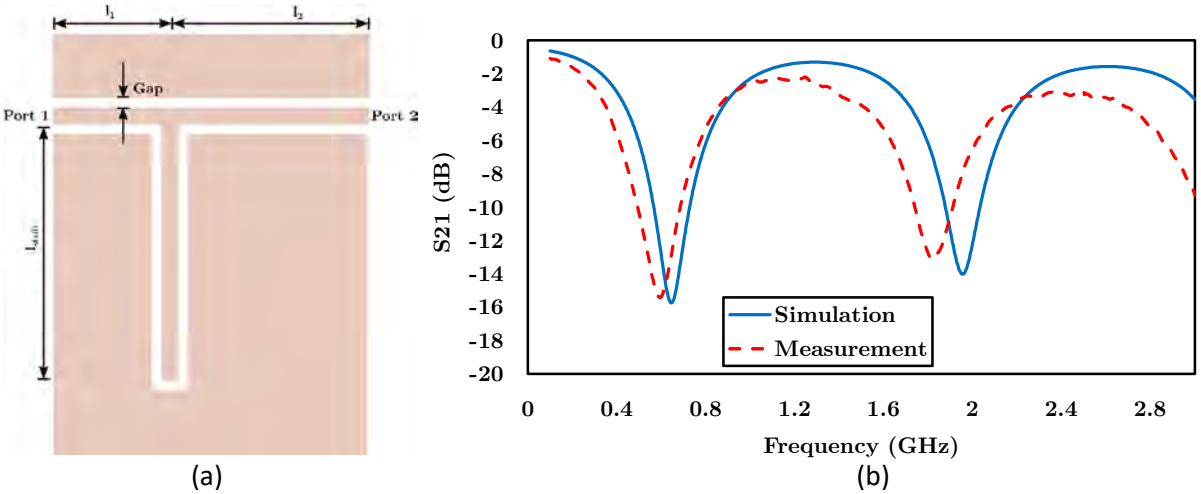

(a) (b)

Figure IV.20. (a) Structure of the designed CPWG quarter-wavelength open-ended stud resonator; (b) Comparison between the measured and retrosimulated transmission coefficient of the CPWG open-ended T-stub resonator with εr *= 3.5.*

Table IV.5. Extracted effective and relative permittivity of the PET material for CPWG T-stub resonator method.

n	Resonant Frequency (GHz)	ε_{eff}	ε_r
1	0.593	2.94	3.52
3	1.879	2.81	3.36

- *Half-wavelength transmission line resonator methods*

A fast dielectric constant extraction method from a CPWG transmission line was evaluated. This method for fast determining dielectric properties of substrate materials was presented in [197].based on the ungrounded coplanar waveguide structures containing two simple straight lines. It consists of measuring the resonant frequency of a half-wavelength transmission line, as the resonant frequency is inversely proportional to the square root of the effective permittivity. The phase response of the transmission line reveal a phase shift at it resonant frequency. To apply this method, three transmission lines with different lengths (70 mm, and 90 mm) were used. The resonant length can be calculated by the equation (IV.19). The designed transmission lines followed the same dimensions (gap and width) as presented in the GCPW T-stub method. In order to perform the measurement on lines of different lengths, a calibration was performed before to bring the reference of the measurement back to the beginning of the line to be measured. A test structures designed for flexible substrate characterization. A test structure was specifically designed for the characterization of flexible substrates. The test structure consists of two transmission lines (50 Ω GCPW lines) and an associated SOLT (Short, Open, Load, Thru) custom calibration kit. The use of GCPW lines facilitates the measurement of S-parameters using a standard on-wafer setup, with the test structures positioned on a metallic chuck. Addition it can be equipped with standard SMA end-launch connectors for convenient connection and measurement purposes.

$$l = \frac{\lambda_g}{2} = \frac{c}{2.f.\sqrt{\varepsilon_{eff}}} \qquad \text{(IV.19)}$$

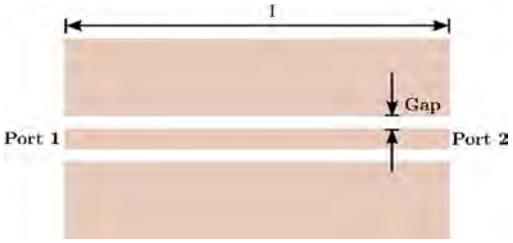

Figure IV.21. Structure of the designed CPWG half-wavelength transmission line.

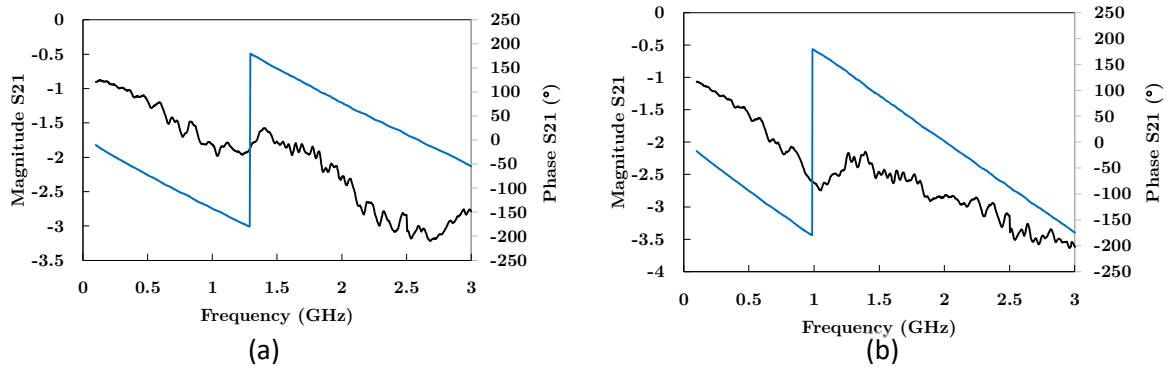

Figure IV.22. Measured Magnitude and phase of the transmission coefficient S21: (a) line of 70 mm; (b) line of 90 mm.

Table IV.6. Extracted effective and relative permittivity of the PET material for half wavelength transmission line method.

L (mm)	Resonant Frequency (GHz)	ε_{eff}	ε_r
70	1.284	2.78	3.32
90	0.982	2.88	3.44

The relative permittivity based of the measured frequency shift of the transmission coefficient and the equation (IV.19), is reported in Table IV.6. The relative permittivity for a length of 90 mm is equal to the mean of the value obtained with the two previous methods. This last method allows us to confirm the value of the obtained relative permittivity. However, the loss tangent of the substrate was not measured due to concerns about the accuracy of the method. Instead, the attenuation or transmission loss was determined to be 0.024 dB/mm with an uncertainty of ± 10%. This provides an estimate of the loss experienced by the signal as it propagates through the substrate.

4.2. Evaluation of the rectifier performance on PET Substrate

For the rectenna design as part of the project, it was important to evaluate the performance of the differential rectifier with a balun on a PET substrate. This preliminary step was necessary to validate the dielectric properties of the previously characterized substrate and evaluate the performance of the rectifier on the flexible substrate. For the subsequent designs of the rectifier and antenna, the dielectric constant was set at 3.5 and the loss tangent at 0.08.

The rectifier based on a topology as shown in Figure IV.13, is designed on CPWG to facilitate characterization with an End-Launch connector as used for substrate characterization. To accurately predict the experimental results of the rectifier on PET, a co-simulation model using Momentum features in ADS was employed. Momentum enables electromagnetic simulation of RF designs, expanding the accuracy range of circuit models and accounting for potential coupling and edge effects.

The rectifier circuit can be divided into two parts for simulation: (1) from the RF input of the rectifier to the differential input of the Schottky diode, (2) from the Schottky diode to the output load. Consequently, EM simulation of the rectifier layout was only performed on the first part to accurately compute S-parameters. Following the EM simulation, the model of the rectifier, including the S-parameters results, was created and simulated in the schematic view using the appropriate components. The co-simulation model of the rectifier, including the balun, is depicted in Figure IV.23 (a). The components used for the rectifier simulation are listed in the Table IV.7.

The simulated rectifier was subsequently printed on the PET substrate using silver ink by the Eurecat partner. The integration of electronic components onto the printed rectifier on the flexible material was performed silver resin using a vacuum pickup tool and silver resin as the bonding material. Specifically, the EpoTek H20E [203], which is an epoxy system consisting of a silver resin paste and a silver resin hardener, was utilized. The process involved depositing the silver Epotek H20E onto the designated footprints of the rectifier. Then, all the components were picked up and placed onto the conductive resin. To ensure proper contact and conductivity between the footprint and the components, the entire circuit with the mounted components was placed in an oven and thermally cured for 10 hours at 50°C. This process facilitated the formation of good contact and conductivity. Afterwards, the prototyped rectifier was characterized using an end-launch connector at the input port. The DC performance of the rectifier is measured using a DC probe arm controlled by a micro-positioner, as illustrated in Figure IV.23 (b).

Table IV.7. List of component of the differential rectifier design on flexible PET substrate.

Component name	Part Number	Value
L1=L2	LQW15AN8N7G00	8.7 nH
L3=L4	LQW15AN43NG00	43 nH
C1=C2	- -	1 pF
C3=C4=C5	- -	33 pF
D1 = D2	HSMS-285C-BLKG	--
R1	--	10 kΩ

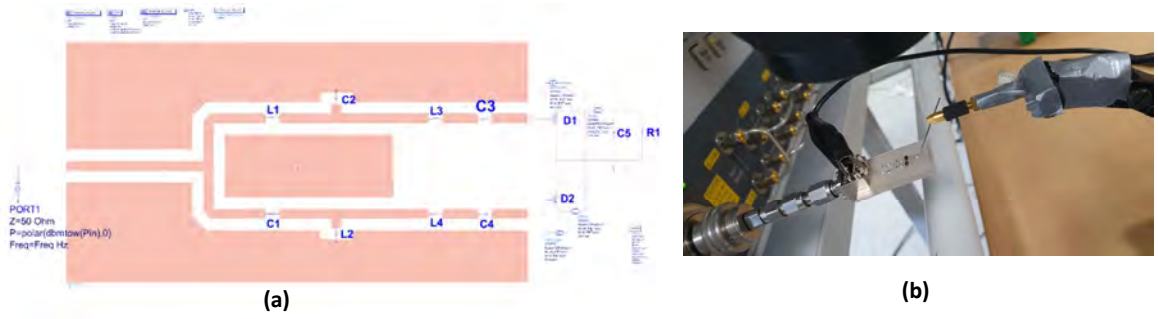

Figure IV.23. Flexible rectifier designed on PET substrate: (a) Schematic view of the co-simulation model; (b) Photo of the prototyped flexible rectifier under measurement.

The measured and retro-simulated return loss and RF-to-DC conversion efficiency, considering the dielectric properties of the selected PET substrate (dielectric constant of 3.5 and dielectric loss tangent of 0.08), are presented in Figure IV.24. The obtained results validate the rectifier simulation with a slight difference probably due to the test fixture used and component tolerances. The rectifier achieves a maximum measured DC voltage of 236 mV (18% of efficiency) at 842 MHz. However, performance is degraded compared to the results obtained with the rigid substrate rectifier (FR4).

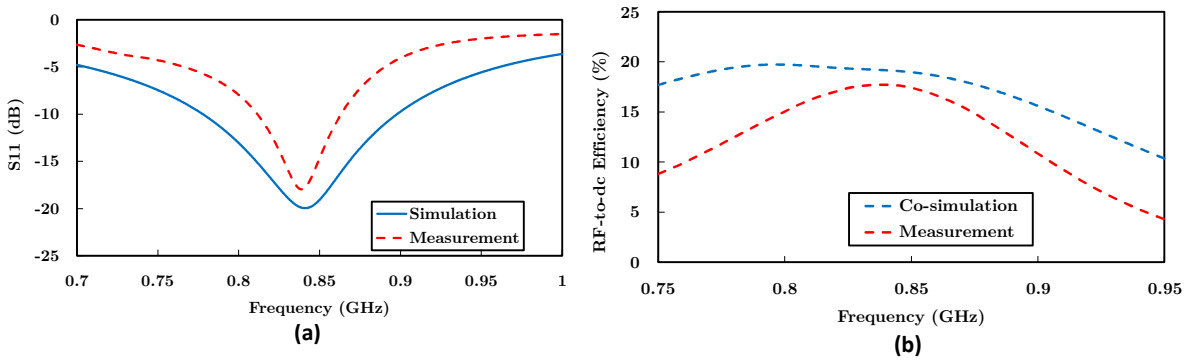

Figure IV.24. Comparison between simulation and measurement of the flexible rectifier on PET : (a) Return loss as function of the frequency at -15 dBm ; (b) RF to dc conversion efficiency as function of the frequency (Input power of -15 dBm).

The final objective is to carry out a study on the flexible rectenna, as depicted in Figure IV.5 (b), focusing on the interface between the differential rectifier and the antenna without balun. The differential rectifier, which has been previously presented and tested, is now adapted and optimized to achieve a differential input impedance of 100 Ω. To simplify the single-layer screen printing process, the final circuit is designed on coplanar waveguide without ground plane. The coupling effect is modelled using a coupled CPW transmission line in the simulator, and the impedance matching to 100 Ω is ensured by using a pair of two 56nH inductors (LQW18AN56NJ00). Both, the schematic model and the co-simulation model (EM model from Momentum) of the rectifier, are simulated using harmonic balance and LSSP simulator techniques (as illustrated in Figure IV.25).

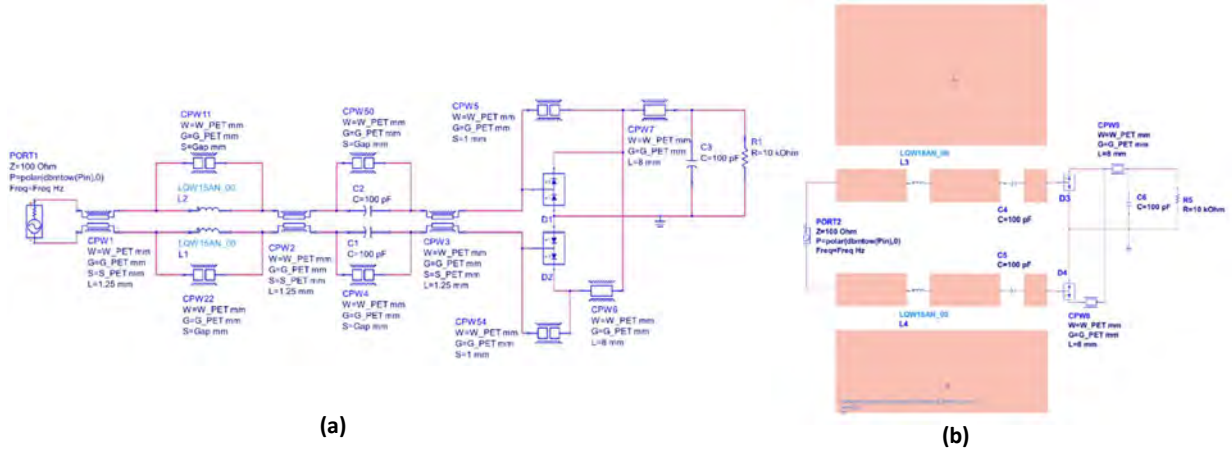

(a) (b)

Figure IV.25. Schematic view of the differential rectifier to be interfaced to the antenna: (a) Rectifier with equivalent transmission line mode; (b) Rectifier simulated using Momentum with layout of the RF part.

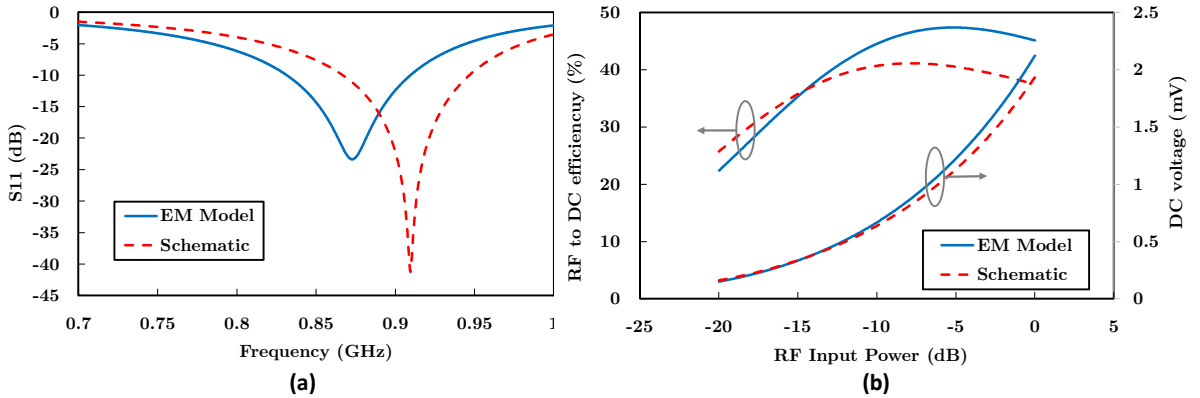

(a) (b)

Figure IV.26. Comparison between EM model and schematic of the rectifier: (a) Return loss at -15 dBm; (b) RF to DC conversion efficiency and DC output voltage at 867.5 MHz.

As previously noted, there is a huge difference between the schematic and EM models of the rectifier that is note here. The final tuning of component value and transmission line length for the prototyping is based on the co-simulation with the EM model. The simulation results presented Figure IV.26 with a lumped inductor of 56 nH are very encouraging for the final implementation of the rectenna. Through this, we can note that a loss of around 10% in efficiency was linked to the use of the balun. Fewer components in the circuit means less insertion loss, and therefore greater efficiency. With the prototyped rectifier, we can expect to have a rectifier working at 867.5 MHz and provide a DC voltage of 334 mV across the 10 kΩ load. The maximum conversion efficiency is located at -5 dBm but the rectifier can reach up to 35% at -15 dBm.

4.3. Design and implementation of the flexible antenna

After evaluating the performance of the rectifier on the PET Melinex 506 substrate, our focus now shifts to the design of the antenna. The primary criterion for the desired antenna is to achieve a positive realized gain within the European ISM 868 MHz band, while also considering miniaturization as a design constraint. The proposed design on PET is based on the electrically small 3D antenna on FR4 substrate presented in Chapter II, which offers several advantages such as shape symmetry, desirable radiation pattern, easy and cost-effective fabrication, and the ability to receive balanced signals. The antenna is designed at 100 Ω input impedance. The planar structure of the antenna, featuring a UFL connector, is depicted in Figure IV.27.

Although the measurement technique used with the U.FL connector does not allow balanced feeding of the antenna, it was chosen for its accessibility, small size, and ease of implementation. Moreover, it was observed that its use did not have a significant impact on the measured results compared to the simulation.

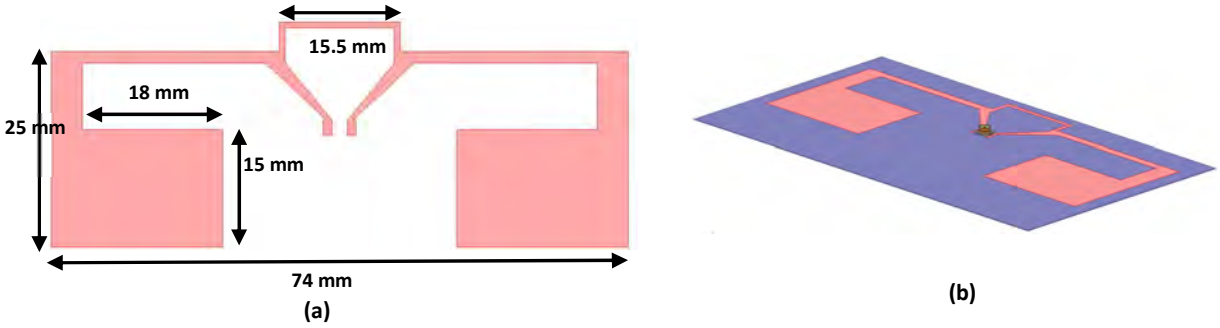

Figure IV.27. Proposed UHF antenna: (a) Pattern with the dimensions; (b) Dimetric view of the antenna with an UFL connector.

The performance of the antenna was evaluated in terms of impedance matching and radiation characteristics. The simulation considered the thickness of the silver layer (9 µm) and the U.FL connector model. A 100 Ω impedance was defined at the lumped port of the simulation. The antenna exhibits a maximum gain of +1.3 dBi with an aperture angle of 92° at 867.5 MHz. Next, the return loss of the prototyped antenna, as shown in Figure IV.28, indicates a good correlation with the simulation. Below -10dB, the bandwidth is obtained from 853 MHz to 884 MHz. A slight frequency shift is observed, likely due to inaccuracies in the extracted dielectric parameters and potential errors during the measurements. However, the prototyped antenna is well-matched within the targeted frequency band for our application (865 MHz to 868 MHz) and exhibits an omnidirectional radiation pattern. The measured maximum gain is +1.65 dBi on the YoZ plane at 867.5 MHz. However, the measured gain is slightly higher (+0.5 dBi) than the simulated realized gain of +1.1 dBi at Phi=90° and theta=0°. This difference can be attributed to the overestimation of dielectric loss and measurement inaccuracies caused by the UFL cable.

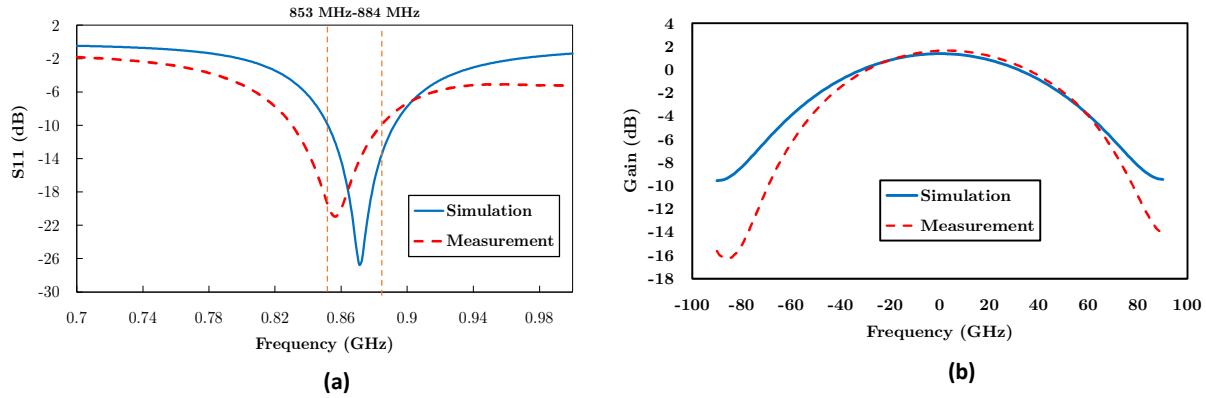

Figure IV.28. Comparison between simulation and measurement of the designed antenna: (a) Return loss; (b) realized gain on the YoZ plane at 867.5 MHz.

After experimentally validating the antenna, adjustments were made to its input pads to facilitate direct connection to the rectifier to form a rectenna on the sample substrate. These minor modifications do not have a significant impact on the performance of the antenna. Additionally, changes were made to the layout of the rectifier in the DC part (after the Schottky diode) to simplify its characterization using a specific connector. Research led to the selection of Clincher connectors from Amphenol, which are low-cost and flexible rigid connectors.

A study was conducted to investigate the effect of placing the rectifier between the arms of the antenna, and it was found that there was no significant difference. However, further investigation was required to understand how the bending angle of the substrate affects the performance of the antenna. It is known that the bending of the prototype can affect the current distribution and subsequently impact the antenna's performance. To demonstrate this, simulations of the antenna were carried out using HFSS, as depicted in Figure IV.29. The simulations show that the proposed dipole antenna design with varying the bending radius has a good impedance matching (S11 below -10 dB) over a bandwidth of 46 MHz. The return loss at 867.5 MHz is consistently below -15 dB, except at a radius of curvature of 5 cm, which represents the antenna's flat configuration. The radiation pattern of the antenna remains unaffected by the bending radius. As a function of the radius, the realized gain has a deviation of ±1 dBi.

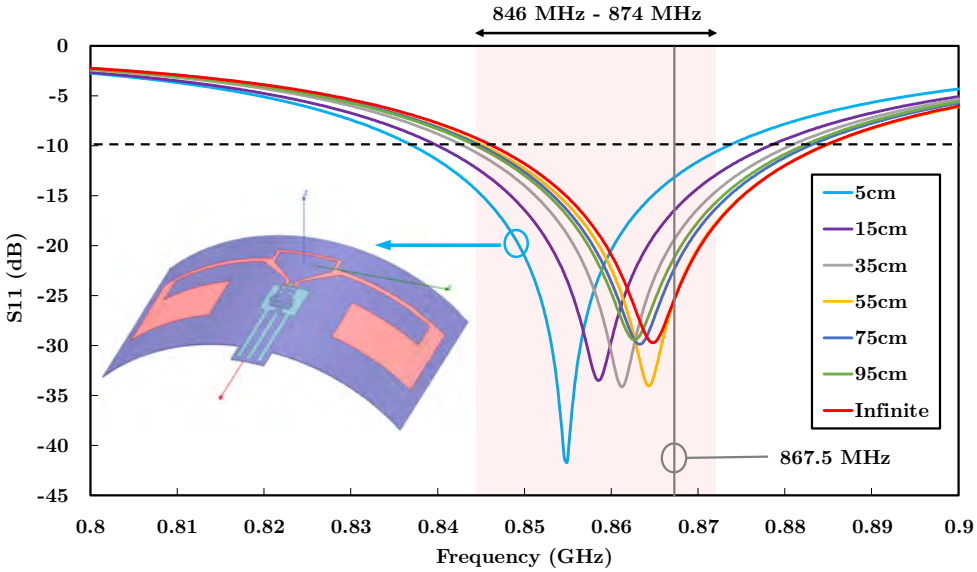

Figure IV.29. Evolution of the return loss as for different bending radius of the flexible antenna.

4.4. Evaluation of the rectenna performance

The fabrication process of the designed rectenna involved screen-printing and the hybridization of surface-mount (SMD) components, which was carried out by Eurecat. Similar to the previous part, the Epotek H20E conductive paste was used due to its ability to provide good ohmic contact. However, it should be noted that there were some process variations and soft system failures with the pick and place instrument (Autotronik BS281), resulting in an alignment margin of approximately 100 µm. Another important consideration was the potential short circuit between pads or adjacent lines. This issue could arise from the spread of the conductive paste after deposition, which is due to semi-liquid nature of the conductive paste. To prevent unexpected short circuits, a margin of around 700 µm was desired to ensure sufficient separation between pads and lines. Once the components were properly placed on the substrate with the conductive paste, the entire assembly was subjected to curing in an oven at 150°C for 10 minutes. For experimentation under bending conditions, a non-conductive adhesive paste (Loctite AA3525) was also used to enhance the mechanical stability of the prototype. Figure IV.30 shows a photo of the final prototypes after the printing and hybridization steps.

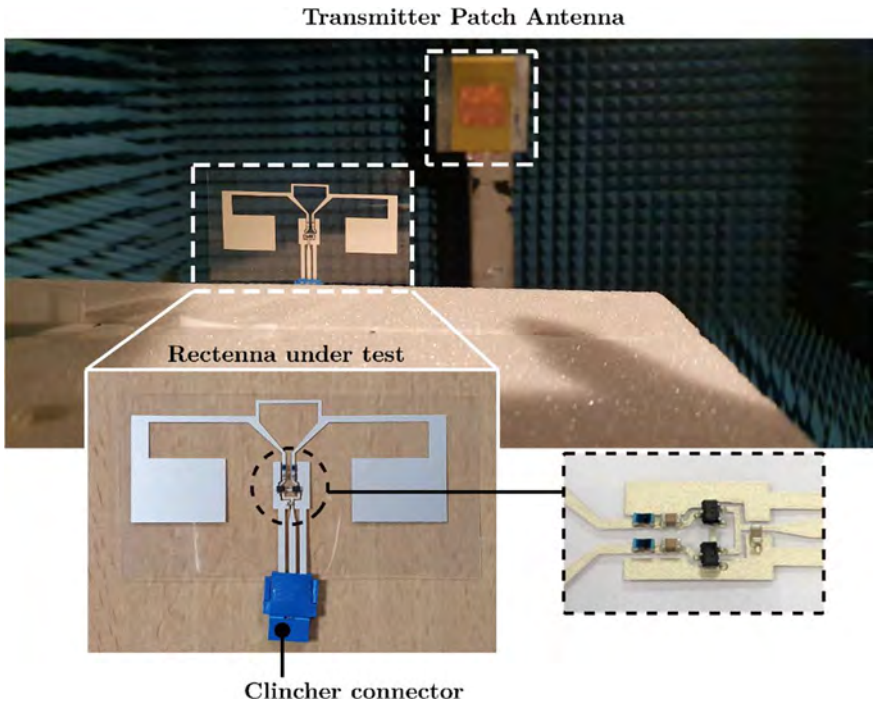

Figure IV.30. Test setup environment with rectenna in foreground and transmitter in background

To evaluate the overall performance of the rectenna, a test environment was set up in an anechoic chamber to minimize reflections and obstacles. The transmitter consisted of a patch antenna with a gain of +9.4 dBi connected to an RF signal generator. The rectenna, with an antenna gain of +1.1 dBi, was placed at a distance of 2 meters from the transmitter. For accurate measurements, it was crucial to ensure perfect alignment and co-polarization between the rectenna and the transmitter antenna. This alignment was necessary to compute the Friis equation. Measurements were conducted on three different samples to evaluate the variability in performance. Among the samples tested, one sample (R1) was manufactured by Eurecat, while the other two samples (R2 and R3) were manufactured in the laboratory using rectennas printed on a flexible substrate provided by Eurecat. The main difference between the samples lies in the hybridization technique, with R1 being manufactured using an automated process at Eurecat, and R2 and R3 being manually assembled in the laboratory. Additionally, the curing times in the oven were different for each sample. The samples (R2 and R3) were cured for 10 hours at 50°C, while the sample R1 underwent a curing process at 150°C for 10 minutes. In terms of performance, both R1 and R2 demonstrated similar results, with a maximum DC voltage of approximately 1.19 mV and 1.2 mV, respectively, for an equivalent power density of 2.2 µW/cm². The R3 sample exhibited slightly lower performance, with a maximum voltage of 1.1 mV. As illustrated in Figure IV.31, the rectenna R1 demonstrated interesting performance at 870 MHz, with a maximum DC voltage of 1.19 V and an efficiency of 54% at a power density of 2.2 µW/cm². These results indicate that the rectifier and the antenna combination achieved a working frequency in the targeted frequency band. An additional prototype was fabricated with Loctite glue deposited on the top of the SMD component to increase the mechanical stiffness of the electronic part of the rectifier circuit. In this sense, we can observe in Figure 56 that the rectenna performances with (w.) the glue are altered (compared to green curves). An alternative should be investigated to minimize this effect. The curvature of the rectenna is proved to have no significant effect on the overall performance as demonstrated first with the antenna in different bending conditions. The prototypes proved to have high-performing characteristics in terms of both voltage output as well as high efficiency.

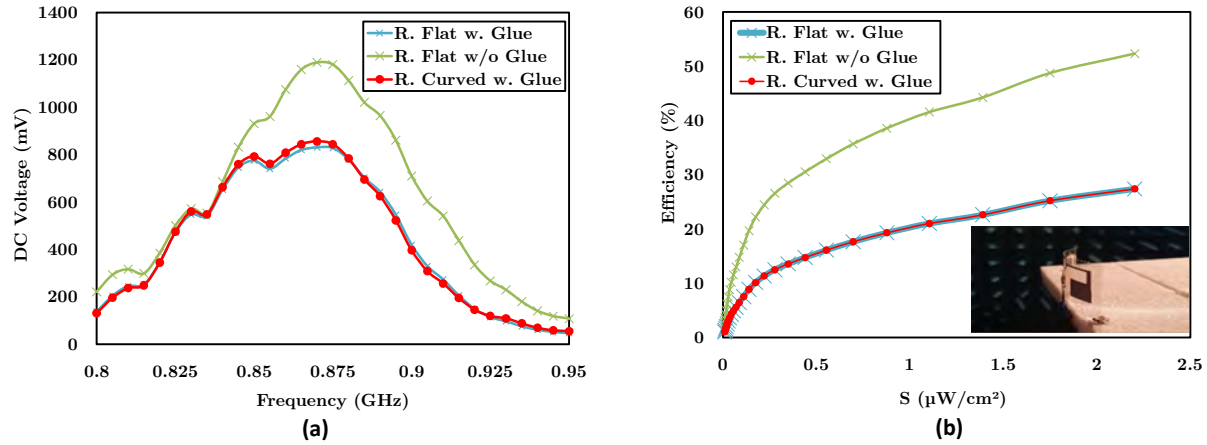

Figure IV.31. Experimental results with a comparison between the rectenna (sample R2) with and without Loctite glue, and curved rectifier (a) DC output voltage with 2.2 µW/cm²; (b) Conversion efficiency at 868 MHz.

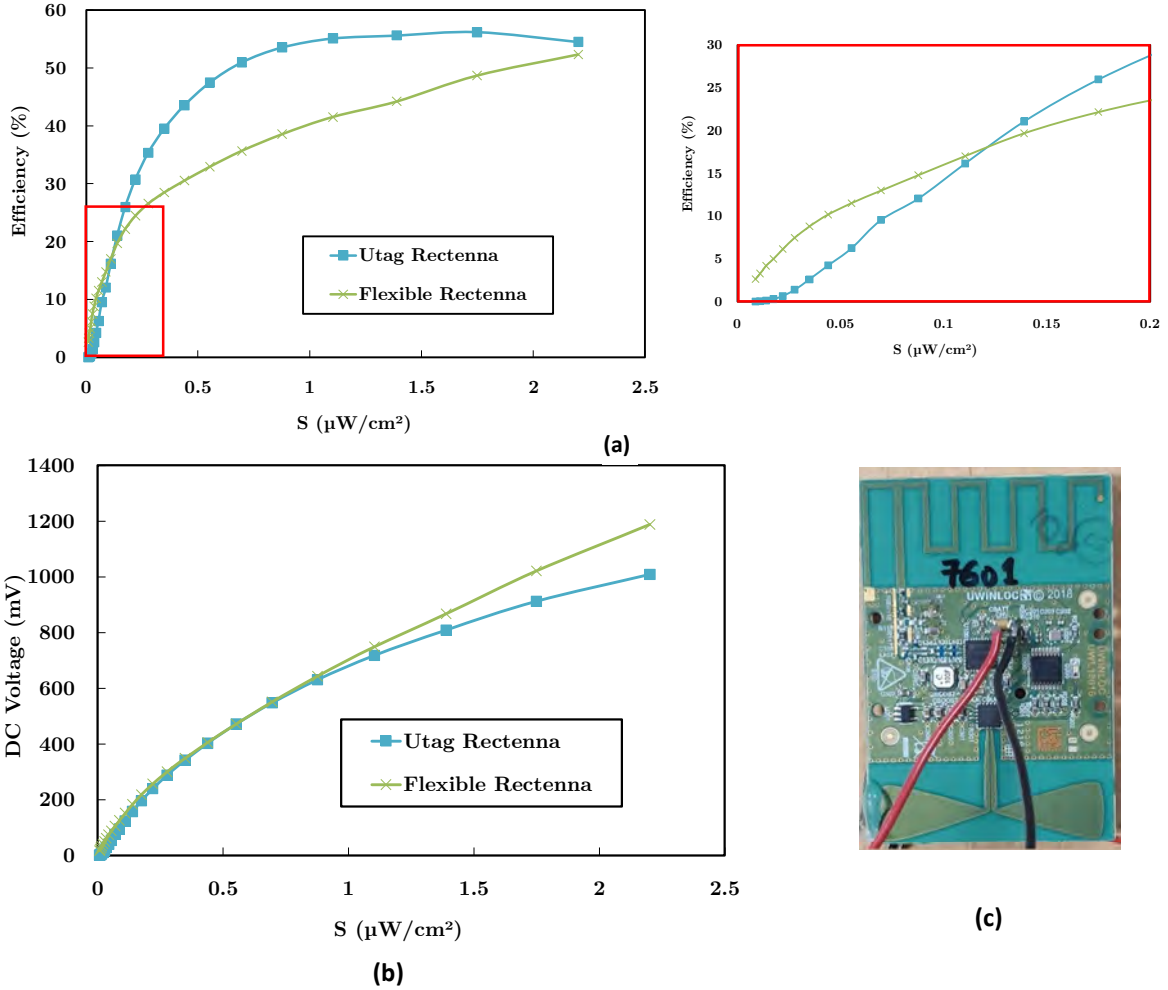

Figure IV.32. Experimental results of the comparison between the flexible rectenna R1 and the Rectenna from Utag : (a) Conversion efficiency at 868 MHz; (b) DC output voltage at 868 MHz; (c) Photo of the modified Utag with DC output connection across the capacitor.

It was crucial to compare the performance of rectenna of flexible substrate with that of the UWINLOC tag (Utag) harvester. The functionality of the Utag was modified to focus only on the rectifier part, excluding any connection with the included power management unit and other active circuits on the board. In this configuration, the Utag received antenna, a printed Inverted F-Antenna (IFA) designed for 868 MHz (gain of -0.5 dBi) was used with the rectifier part and the output is connected to a 10 kΩ resistive. The experimental setup and conditions were the same as previously described with the rectenna sample R1. The Utag rectenna exhibited higher efficiency within a specific power density range, exceeding 0.13 µW/cm² (equivalent received power of -19.3 dBm), despite its relatively low gain as illustrated in Figure IV.32. Below this power density range, the rectifier in the Utag was not optimized to achieve the minimum DC voltage required for its functioning (sensitivity of the Utag is at -20 dBm). These results can be attributed to the fact that the Utag is fabricated on a rigid substrate (I-Tera MT40) with a lower loss tangent of 0.0031. Additionally, the rectifier circuit in the Utag is optimized, using an integrated circuit (Ic) with reduced losses compared to a Schottky diode. However, if prioritizing DC voltage over efficiency, the flexible rectenna is more suitable because its higher antenna gain than that of Utag (printed IFA antenna).

5. Conclusion

The study in this chapter related to the Smartees project has successfully validated the performance of an efficient flexible rectenna on a flexible substrate as a viable alternative to conventional rigid PCBs. Considerations on this project were made not only regarding performance but also the cost of materials and the manufacturing process. Through extensive research based on the specifications, the PET substrate from Melinex and the silver conductive ink from Dupont were identified as the optimal choices for our application. Dielectric properties of the substrate were carefully analyzed to ensure accurate simulation results. The selection of the antenna type was based on defined specifications, and simulation results demonstrated that a modified dipole antenna with a T-match structure met the requirements, achieving a measured gain of +1.1 dBi at 867.5 MHz. The rectifier circuit, based on a differential topology, was designed and optimized for low input power (-15 dBm) with a 10 kΩ output load. Both the rectifier and the antenna were individually optimized, and their integration resulted in a rectenna with promising performance for the geolocation tag. The prototyped rectenna was accurately tested and the results demonstrated an efficiency up to 52% for an estimated power density of 2.2 µW/cm² (or an equivalent received power of -5.7 dBm).

The mechanical stability of components on the flexible substrate is a crucial factor for mass production. It was observed that using Loctite glue on top of the rectifier led to a reduction in performance.

In future iterations, different conductive pastes can be explored to improve mechanical stability while maintaining rectifier performance. Additionally, a more detailed study can be conducted to further investigate this effect of the rectifier circuit. The results also demonstrated satisfactory performance, comparable to rectenna of the Utag (its own antenna and rectifier from the harvesting part).

This project provided valuable insights into the available flexible and low-cost technologies in the market. The technical achievements of the designed rectenna are promising for future developments and product definitions. However, it is important to address the issue of prototype stiffness. While the performance of the prototypes remains stable under different bending angles, the fragility of the hybridized components on the flexible substrate could be a limitation. In future iterations, alternative techniques such as injection molding should be considered to enhance the mechanical robustness of the prototypes.

V. Miniaturization of the Antennas for the Geolocation Tag

1. Introduction

This chapter, like the previous one, falls within the scope of the thesis on the battery-free geolocation tag. One of the research areas on the tag miniaturization is discussed here As presented earlier, the tag comprises three main parts: the two antennas, and the electronic part consisting of the microcontroller, the harvesting part and the UWB chip. The Ultra-High Frequency (UHF) antenna or receiving antenna and the Ultra-Wide Band antenna or transmitting antenna enable energy harvesting and geolocation signal transmission, respectively. The global size reduction of the Utag (65 mm x 45 mm) can be investigated through the antenna miniaturization. The shape of the antennas takes a considerable size on the tag and mostly for the UHF antenna working at a lower frequency of 868 MHz. The electronic part has been previously integrated into a single module and will not be intrinsically detailed. We specifically focused the study on redesigning the UHF antenna for energy harvesting purposes, while keeping the UWB antenna unchanged from the current version of the tag. However, slight modifications were made to the UWB antenna to ensure it matches the complex impedance of the module and to accommodate its specific location on the tag surface.

Several techniques for miniaturizing printed antennas have been explored in the literature [204]. One approach involves making structural modifications to the antenna geometry within the available space or volume. This can include incorporating a larger radiating structure or adding additional elements to the antenna shape. For example, the use of a coupling element, such as a rectangular ring, has been shown to reduce size and increase bandwidth of the antenna [205]. Another technique involves designing electrically small antennas using coupling between capacitively loaded loop and Egyptian axe dipole structures etched from opposite copper sides. This approach enables the creation of a single-substrate Huygens dipole antenna with compact dimensions [68]. Meander lines are also commonly employed in the design of small antennas. These lines reduce the physical dimensions of the antenna while increasing the electrical dimensions, thereby achieving a lower resonant frequency [206]. Meander antennas are commonly used in UHF and RFID applications [207]–[209]. Space filling properties using fractal geometry is also used to miniaturize antennas [210]. For compact nonplanar antennas, a 3D or spherical shape can be employed to achieve miniaturization. This technique allowed us in the chapter II to propose an electrically small antenna by adding metal arms connected perpendicularly to the planar structure of the antenna. Additionally, a dipole-type RFID tag antenna is wound into a spherical shape to make it compact in a volume. [211]. Reactive loading elements can also be used for miniaturization [212]. This technique is employed in [213], [214] through an LC load (a combination of a lumped inductor and an interdigitate capacitor). Miniaturization can also be achieved by reducing the guided wavelength through the use of a higher permittivity material, such as a ceramic—polymer composite [215], [216].

Recent research efforts have focused on developing small antennas using metamaterials [217]. Overall, these various techniques offer ways to miniaturize printed antennas and optimize their performance for specific applications.

For the miniaturization technique selection for your application, it is important to consider factors such as ease of implementation and cost-effectiveness in the manufacturing process. The first approach of the work was to design a compact antenna on a rigid substrate without significantly degrading the efficiency. Then, advanced manufacturing process were employed to further investigate a compact antenna design on the rigid substrate. Additionally, the advantages of flexible materials were considered in order to design conformal antennas. The antennas can be shaped and integrated into various form factors and irregular surfaces, optimizing space utilization.

2. Electronic module of the geolocation tag

In the latest version of the geolocation tag, significant improvements have been made to the electronic part. It has been integrated onto a compact castellated holes PCB measuring 15 mm x 15 mm, facilitating easy integration into the geolocation tag as shown in Figure V.1. This electronic module incorporates all the necessary circuits and functionalities, including microcontrollers, a UWB transmitter chip, and energy harvesting components.

The energy harvesting part, equipped with a power management subsystem, converts AC power to DC power, but also manages and stores the harvested power in a capacitor, and supplies power to the active components. The module operates in the Industrial Scientific Medical (ISM) frequency band at 868 MHz and enables an ultra-low power cold start procedure, typically consuming around 3 µW from an empty storage element. It can harvest a wide range of RF input power, from -18 dBm to +10 dBm. Once a sufficient amount of energy is stored in the 150 µF ceramic capacitor, the tag can transmit an ultra-wideband pulse at a central frequency of 4 GHz. The UGM requires no more than 40 µJ for a single UWB message, which includes a unique identification (from the start-up point to the data sending). To accommodate the energy harvesting and UWB features, the Uwinloc geolocation module (UGM) offers two differential inputs. The impedance at the RF input pins is Zin_UHF ([8-j·250] Ω) at 868 MHz for an input power of -18 dBm, while Zout_UWB ([25-j·9] Ω) at 4 GHz is the impedance at the RF output pin. Therefore, the antennas are directly designed at the corresponding RF input and output pins, avoiding the need for additional lumped components, reducing insertion losses, and minimizing the overall size compared to the previous version of the tag.

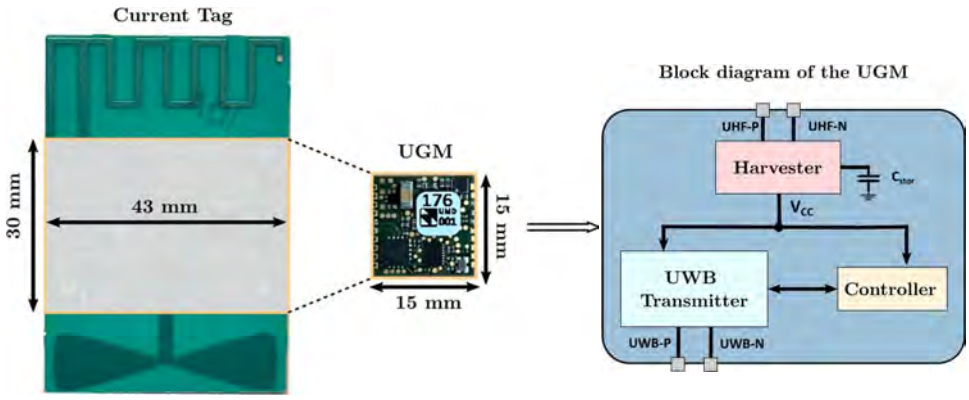

Figure V.1. Size reduction of the electronic part from the current version and simplified block diagram of the UGM.

In order to accurately estimate the mismatch losses, the RF input and output impedance was measured with the same setup used for the antenna characterization as seen in the experimental setup in Figure V.7 (a). It allows to accurately evaluate the impact of impedance mismatch on the performance of the tag. The design of the antennas is particularly important to achieve the best compromise in terms of high sensitivity at low power density to be received, UWB transmission range, and accuracy for localisation. Thus, we tried to propose antenna designs that are both compact and have good performance.

3. Rigid substrate antennas (Rtag)

For our initial optimization strategy, we have chosen to focus on developing a small-sized antenna on a rigid substrate. Our objective is to fit the entire tag within a 50 mm x 50 mm square area. In contrast to the current version of the tag (Utag) that utilizes a printed Inverted F-Antenna (IFA), we explored alternative options due to constraints related to the required size of the ground plane and the feeding technique. To address these challenges, we decided to design complex conjugate antennas that are specifically matched to the corresponding RF inputs of the UGM module. This approach allows us to optimize the performance of the antennas and ensure efficient signal transfer avoiding impedance matching network. The prototyped tag named Rtag, including the optimized antenna design, was implemented on a rigid substrate called Itera MT-40, manufactured by Isola with a dielectric constant of 3.45 and a low loss tangent of 0.0031 [218].

3.1. Simulation of the proposed antenna

- *Design of the UHF antenna*

Given its large size, we started the simulation with the UHF tag antenna on the 50 mm x 50 mm area. The design process for the UHF antenna involves four main steps, which are illustrated in Figure V.2.

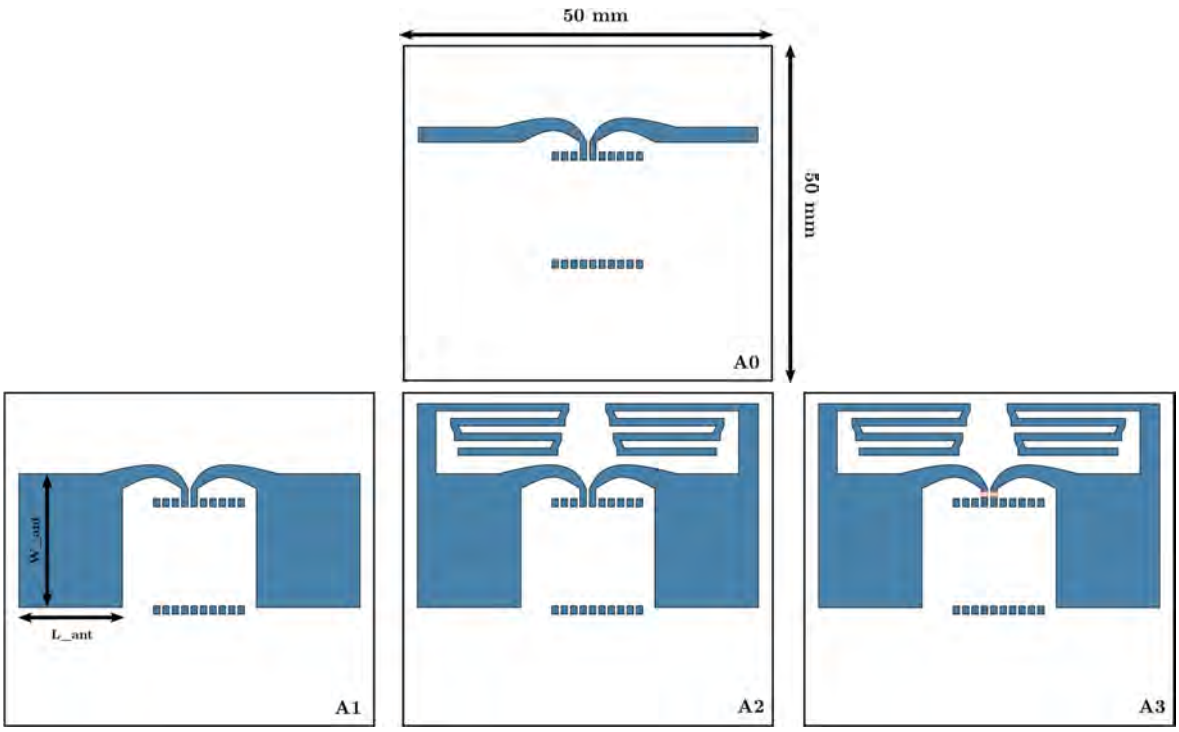

Figure V.2. Design steps of the UHF proposed antenna on rigid substrate (W_ant = 18 mm ; L_ant = 14 mm).

The initial design named A0, features a horizontal short dipole antenna with curved arms (width of 2 mm) connected to the input differential input pads of the UGM module. However, the imaginary part of the antenna (-411 Ω) did not match the impedance required (250 Ω). To address this impedance mismatch, the width of the rectangular part (W_ant) of the dipole arms is adjusted. This adjustment helped to better align the impedance of the antenna with the targeted impedance of the UGM. Despite the advantage of using lumped inductors for miniaturization, theses also induces losses due the presence of series resistance. The ohmic losses is also qualified by the Quality (Q) factor that should be higher as possible for the inductor selection. Murata LQW Wirewound inductor with a high Q will be used for the prototyping . The equivalent series resistance of the inductor is not introduced in the simulation parameters yet and will be accounted from the datasheet of the inductor once the target value is obtained . The smith chart in , shows the evolution of the antenna impedance with different values of inductor. We finally get close the targeted impedance with a lumped inductor of 30 nH.

As depicted in Figure V.3 (a), increasing the width of the antenna arms leads to a higher imaginary part of the impedance. However, it also increased the real part of the impedance. To ensure proper integration of the UWB antenna and avoid occupying the entire surface of the tag, we limited the width (W_Ant) to 18 mm. The obtained imaginary part of the impedance increases to approximately -200 Ω. To achieve the desired imaginary part close to +250 Ω from the A1 design, the next step involved introducing a 1 mm width meander line. However, this still resulted in an impedance mismatch, with an impedance of [4.515 - j·99.195] Ω. Given the size limitations of the tag, we loaded the antenna using two identical lumped inductors to increase the imaginary part. The lumped inductors were simulated by assigning boundaries to small rectangular sheets at the antenna input as shown in Figure V.2 (A3).

The use of lumped inductors enables antenna miniaturization but introduces losses due to its inherent series resistance. The ohmic losses are quantified by the quality factor (Q-factor) of the inductor, which should be as high as possible. For prototyping purposes, Murata LQW Wirewound inductors family with high Q were used. During the tuning steps, the equivalent series resistance of the inductor has not been included in the simulation parameters yet. It was considered from the inductor datasheet once the targeted value is achieved.

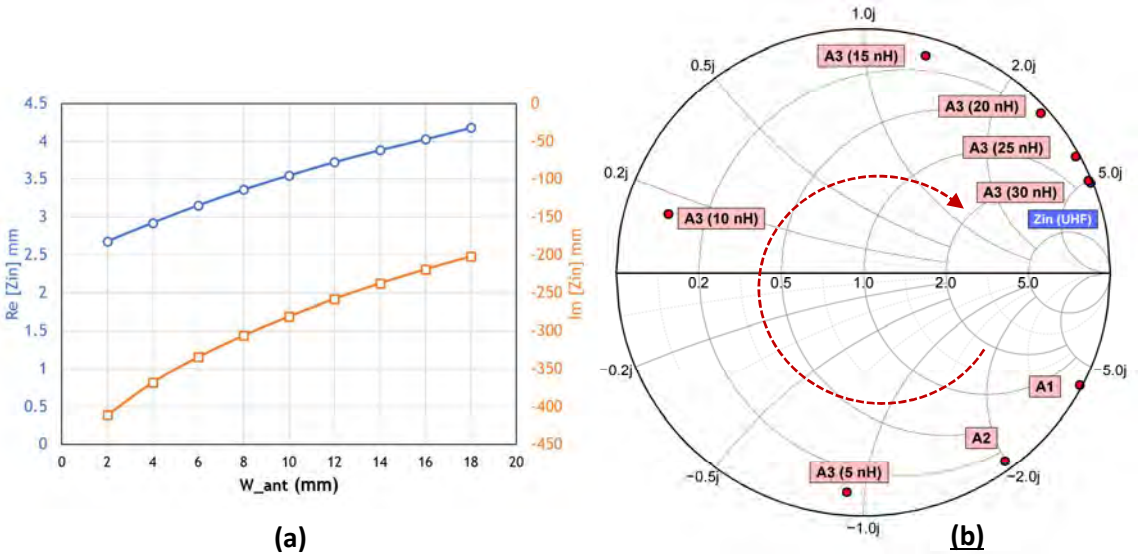

Figure V.3. (a) Input impedance of the A1 antenna as a function of W_ant parameter variation with fixed L_ant; (b) Evolution of the reflexion coefficient of antenna A1 on the Smith chart as a function of the loaded inductor value.

The Smith chart in Figure V.3 (b), illustrates the evolution of the antenna impedance with different values of the inductors. Finally, we were able to reach the complex conjugate impedance by using a lumped inductor of 30 nH (the last red marker closed to blue one).

After designing the complex conjugate UHF antenna, the next step consisted in integrating the UWB antenna and conducting a co-simulation to mitigate any coupling effects with the UHF antenna. To facilitate the design, the rounded bowtie antenna used in the current version of the tag (shown in Figure V.1) was used as the UWB antenna. Adjustments were made to fit the antenna into the 50 mm x 50 mm area, and a triangular shape was added near the feed point for impedance matching as shown in Figure V.5 (a). The simulated return loss (S11) of the UWB antenna, normalized to the complex conjugate impedance of the UGM ([25+j·9]) Ω, exhibited a bandwidth of 18.35% ranging from 3.86 GHz to 4.64 GHz (considering S11<-10 dB). However, the radiation pattern of the UWB antenna was affected by the larger size of the loaded dipole antenna. As shown in .Figure V.4, the UWB antenna alone, when placed on the substrate, exhibited a quite omnidirectional radiation pattern like a donut shape. However, the presence of the UHF antenna acted as a reflector element and modified the radiation pattern of the UWB antenna to become more directive in the horizontal plane (H-plane), resulting in a maximum gain of +3.9 dBi (at 4 GHz) at theta angles of 0° and 90°.

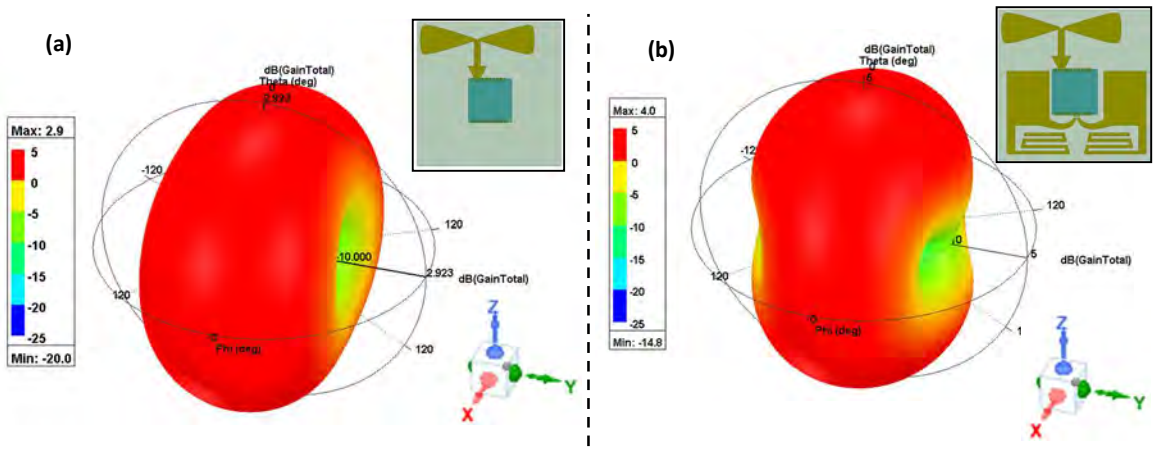

Figure V.4. 3D polar plot of the UWB antenna gain at 4 GHz: (a) UWB antenna only ; (b) UWB antenna considering the UHF antenna effect.

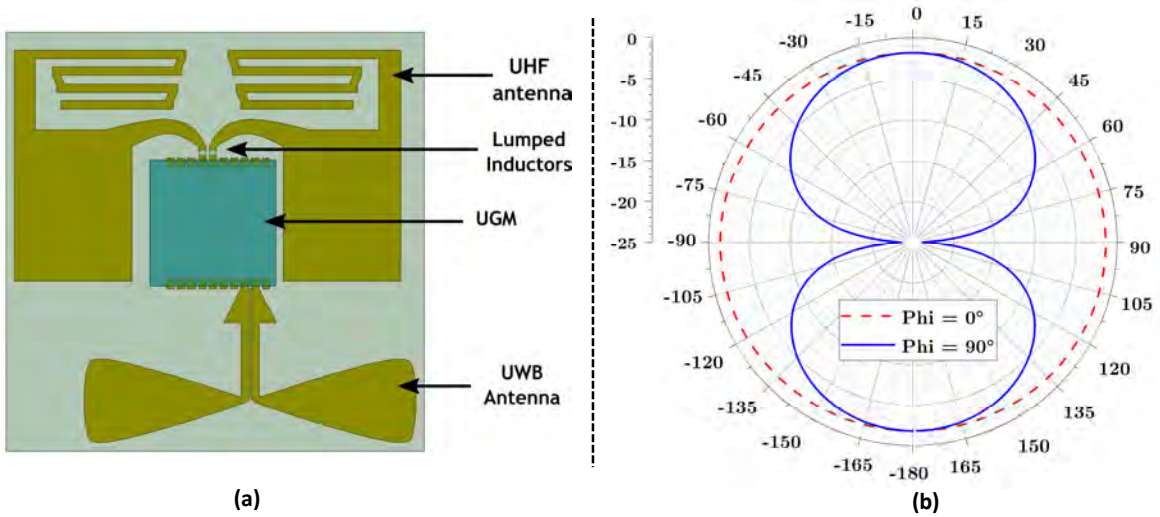

Figure V.5. (a) Top view of the designed tag on HFSS software with both antenna and UGM; (b) Simulated radiation pattern of the loaded UHF antenna (with UWB antenna and with UGM) at 868 MHz.

The final design of the geolocation tag, incorporating both the UWB and UHF antennas, is depicted in Figure V.5 (a). The LQW18AN30G00 inductance model was chosen for a more accurate simulation of the antenna. The serial resistance value to be introduced into the simulation (1.86 Ω) was calculated from its quality factor of 87.6 at the frequency of 860 MHz. Figure V.6 illustrates the impact of integrating the UWB antenna and UGM on the input impedance of the antenna. From the red line, the integration of the UWB antenna (green line) leads to a slight decrease of 0.3 Ω (at 870 MHz) in the real part of the impedance, while the imaginary part increases of 5 Ω. Considering the final functioning tag, the presence of the UGM is also considered in the simulation, with a 1 mm thick FR4 substrate placed on top of the pads (blue line). The results show that the impedance of the antenna is more impacted by the UGM module. The real part and imaginary part of the impedance increases when both the UGM and UWB antenna are present. Consequently, the input impedance of the UHF antenna (with UGM&UWB) reaches [11.2+j·276] Ω at 868 MHz, which is close to the targeted conjugate matching impedance of [8+j·250] Ω. The radiation patterns at 868 MHz of the UHF antenna in Figure V.5 (b), shows an omnidirectional radiation pattern that is not significantly affected by the presence of the UWB antenna.

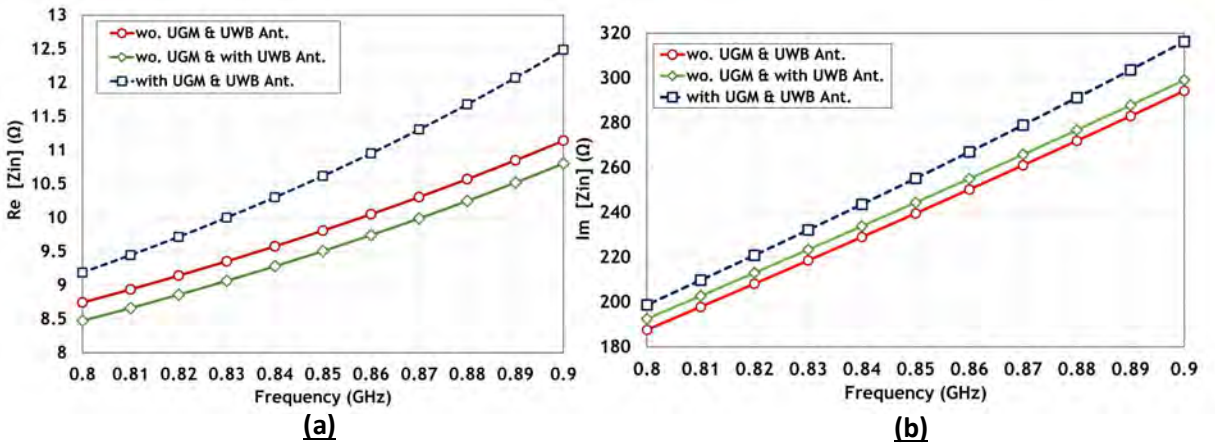

Figure V.6. Comparison of the input impedance of the UHF antenna with and without the presence of the UWB antenna and the UGM; (wo. = without).: (a) Real part of the antenna input impedance; (b) Imaginary part of the antenna input impedance.

However, it's important to note that the radiation efficiency is significantly reduced due to the series resistance of the loaded lumped inductor. The simulated radiation efficiency at 868 MHz is approximately 78 % and 41% without and with considering the series resistance of lumped inductor, respectively. In terms of maximum gain, in the H-plane (Phi = 0°), the antenna achieves a gain of approximately -1.8 dBi at a theta angle of 0°, and -1.4 dBi at a theta angle of 90°. Without considering series resistance in the simulation parameters, the maximum gain is higher +1.37 dBi at 868 MHz.

3.2. Measurement of the fabricated antenna

The return loss of the fabricated antenna was measured using a homemade RF probe made from a coaxial cable and a Vector Network Analyzer (VNA) Anritsu 37394D. The Short Open Load Thru (SOLT) calibration procedure was employed with an adequate calibration kit. The choice of the homemade RF probe was based thanks to its availability for experimentation and its fast and cost-effective measurement procedure as seen in Figure V.7 (b). This probe facilitated the tuning of the antenna's input impedance by replacing the SMD inductor. It is important to note that the fabricated probe connected to the VNA may introduce some measurement uncertainty. However, prior verification by comparing the characterization method with both the homemade probe and an adequate differential RF probe did not reveal a significant discrepancy in the measurements.

During the characterization process, the antenna was placed on a Rohacell foam to minimize any effects from the measurement table. The prototyped antenna required a higher inductance value compared to the simulation in order to achieve the targeted impedance. Two lumped inductors from the Murata LQW18AN series (27 nH and 30 nH) were soldered and tested. As depicted in Figure V.7 (b), both inductors resulted in a significant increase in the real part of the impedance, along with an increase in the imaginary part. However, an exact complex conjugate matching was not achieved, and a trade-off was necessary to avoid excessively high values of the real part by using a higher inductor value. While the radiation pattern was not measured in this particular instance, it can be done using a balun transformer and RF connector. For now, we will rely on the simulated gain obtained from HFSS. The simulated gain obtained on HFSS will be used for any calculation. The series resistance is 1.86 Ω with both used LQW18AN inductor (27 nH and 30 nH). Thus, we can expect to have about the same gain of 0.86 dBi as in the simulation.

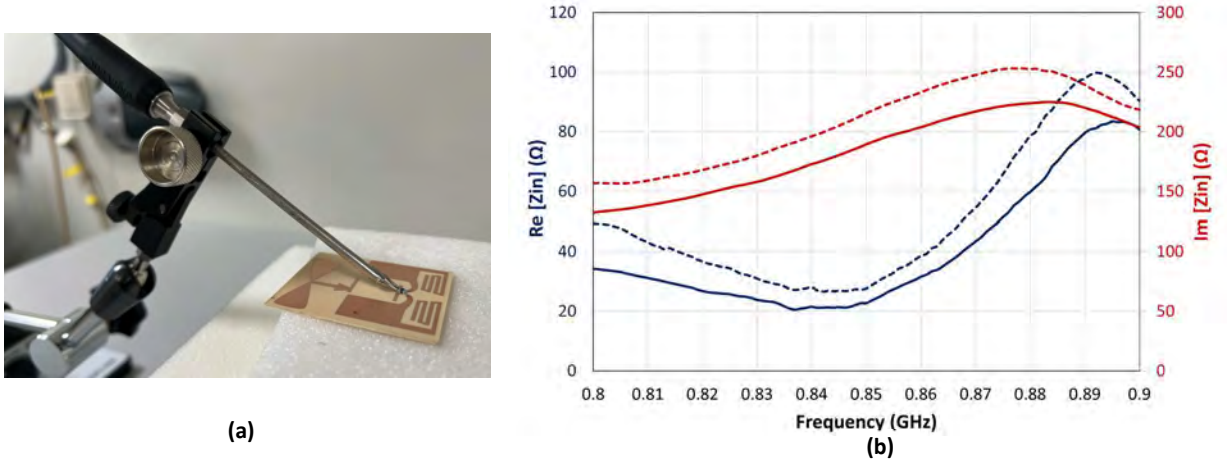

Figure V.7. (a) Measurement setup for the antenna characterization; (b) Input impedance of the loaded antenna with a lumped inductor : 27 nH (solid lines) and 30 nH (dashed lines).

We can see that for an impedance adaptation criterion generally set to return loss below -10 dB (maximum mismatch loss of 10%), the UHF antenna is suitable for the UGM module over the entire power range but more than 0 dBi. The antenna with an inductance value at 30 nH has a better adaptation and we can therefore estimate a loss by mismatch of 0.5% over for low power levels. These results are satisfactory to test the features of the tag on this prototype despite the low gain value of -1.8 dBi evaluated in simulation. The mismatch loss was calculated to evaluate the amount of power reflected (mismatch losses) and the received power by the antenna. To ensure accurate calculations, the input impedance of the harvester part of the UGM was measured using the same setup presented in Figure V.7 (a) with the homemade probe. It is important to note that the harvester of the UGM is a non-linear circuit thus its input impedance varies function of the input power. The measurements were performed for different RF input power levels configured on the VNA. The obtained results, shown in Table V.1, exhibit an imaginary part close to -250 Ω as expected. However, the real part of the impedance is higher. The return loss (S_{11}) was calculated using the equation (V.1), normalized by the equivalent complex conjugate impedance of the UGM at each RF input power level. Z_{Ant} is the input impedance of the UHF antenna measured earlier. It can be observed that, according to the impedance matching criterion typically set as a return loss below -10 dB (maximum mismatch loss of 10%), the UHF antenna is suitable for the UGM module across the entire power range. The antenna with an inductance value of 30 nH exhibits better impedance matching (better at 0 dBi).

We can expect an estimated mismatch loss of 0.5% for low power levels. These results are satisfactory for testing the tag's features on this prototype, despite the low simulated efficiency and gain value of -1.8 dBi at 868 MHz.

$$\boldsymbol{S_{11}(dB) = -20 \cdot log(|\Gamma|) = -20 \cdot log\left(\left|\frac{Z_{Ant} - Z_{UGM}^{*}}{Z_{Ant} + Z_{UGM}^{*}}\right|\right)} \quad \textbf{(V.1)}$$

$$Reflected\ Power\ (\%) = 100 \cdot |\Gamma|^2 \quad \text{(V.2)}$$

Table V.1. Measured impedance at 868 MHz of the UGM (Z_{UMG}) for different RF input power level from the VNA and the equivalent return loss and reflected power of the UHF antenna.

RF Pin (dBm)	Re [Z_{UGM}] (Ω)	Im [Z_{UGM}] (Ω)	Normalized Return loss of the UHF antenna (dB)		Estimation of the reflected power by the UHF antenna (%)	
			27 nH	30 nH	27 nH	30 nH
+5	92.228	-206.206	-18.25	-18.44	1.50 %	1.43 %
0	58.279	-239.456	-23.47	-34.69	0.45 %	0.03 %
-5	26.361	-254.018	-21.23	-25.68	0.75 %	0.27 %
-10	17.262	-257.886	-19.9	-22.95	1.02 %	0.51 %
-15	17.197	-258.101	-19.87	-22.92	1.03 %	0.51 %
-20	17.620	-258.134	-19.9	-23.02	1.02 %	0.50 %

4. Antennas based on semi-flex substrate (SMTag)

To address more use cases as in retail or industrial environment with objects with non-planar surfaces, the tag should be compact as well as conformable. A study was therefore carried out on the tag design with a rigid part to keep the structural integrity of the prototype and a flexible part allowing it to be folded. Beforehand, the manufacturing process was studied. Advanced solutions allow to meet our needs. It can either be a hybrid circuit board named semi-flex or flex-rigid PCB or by a single standard rigid FR4 substrate name semi-flex PCB.

Flex-Rigid or Rigid-Flex circuit is made from a combination of a flexible material as polyimide sandwiched between rigid layers. This technique is generally used to easily integrate multi-board systems in a single package. Rigid-flexible devices have always been present in our daily life. We can find them in wireless applications, in laptops and nowadays in the new generations of foldable smartphones and connected objects as in [219]. A practical devices which is a wireless electro-optic platform is fabricated with this process in order to be folded around the battery to achieve a very compact size [220]. Moreover, this technique has often been used in the development of antennas. In [221], is made a circular dipole antenna using flex-rigid structure using polyimide material for the flexible part. A more sophisticated design is presented in [222] for a conformal antenna at 17.2 GHz with multilayer PCB technology and uses Pyralux as the flexible material.

The semi-flex design consists in a tradition process with a mono-material FR4 substrate. The flexible element is a thin layer obtained by removing material from a certain portion of the same rigid substrate. A depth milling is applied on the z-axis to have a thin remaining material on the flexible part. This process is widely used in automotive applications and consumer electronics with cell phones.

Several reasons lead us to use a semi-flex process. It is approximately three times cheaper than the equivalent rigid-flex prototype. The manufacturing process is relatively simple and build time are more favourable. However, this technique presents some disadvantages. Semi-flex circuit is fragile, and the number of possible bending cycles is limited (less than 10) compared to the flex-rigid that is indefinitely bendable. As the aim is to potentially attach to tag to a mobile object, a dynamic use is not an option. Furthermore, it is important to note that the device can only be bent on one side, specifically the side that does not contain the copper trace.

We proposed in here a geolocation based on semi-flex substrate named SMtag. The global geometry of the SMtag is first specified before designing the antenna. The selection of a 0.8 mm thick FR4 substrate is determined by the requirements of the manufacturing process. Among the manufacturing specifications, the design is printable on copper ink of 35 µm and the flexible part of the substrate FR4 has a thickness of 0.25 mm (±0.05mm). As seen in Figure V.8, the semi-flex tag includes two rigid sections (B1 and B3) which carried the antennas and the UGM. For the flexible part (B2) of 10 mm x 30 mm, it was wise to add transmission lines connected to the UGM input pins to increase the imaginary part of the antenna. The PCB has a total dimension of 70 mm x 50 mm. The rigid panels are located within a 50 mm x 30 mm rectangle, which represents the final planar size when the PCB is bent at a 180° angle.

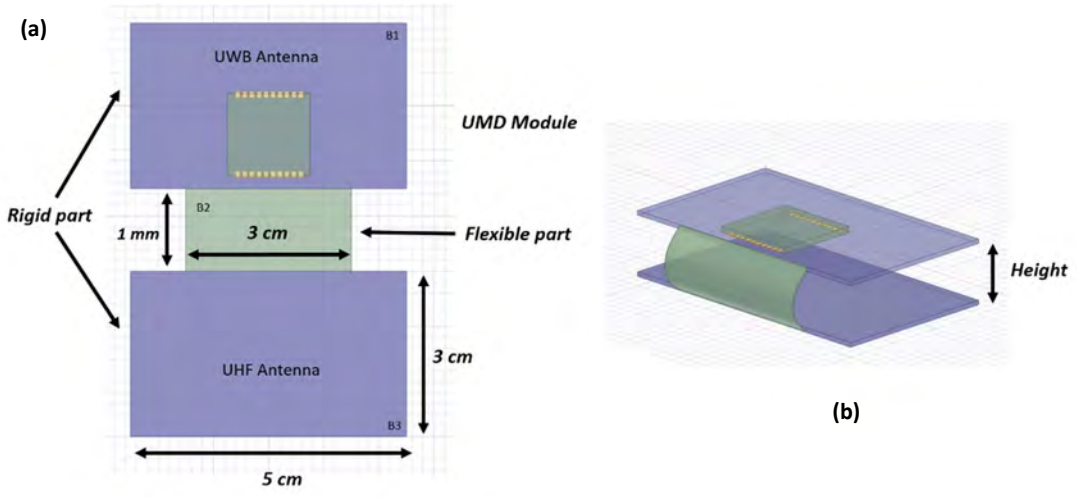

Figure V.8. Geometries of the semi-flex tag without antenna patterns; (a) top view in flat condition ; (b) Isometric view in 180° folded position (height = 0.8 mm).

4.1. Optimization of the UWB Bowtie antenna

The bowtie antenna is still used for the UWB part positioned on the B1 section of the tag. Due to the dimensions and dielectric properties of the FR4 substrate, the UWB antenna needs to be optimized to match the complex conjugate impedance of the UGM (25+j·9). Apart from the impedance matching, the antenna must provide a bandwidth (BW) of at least 500 MHz or 20% of the center frequency at 4 GHz. To ensure accurate simulation, the antenna was co-designed with the UHF antenna which is discussed in the following section.

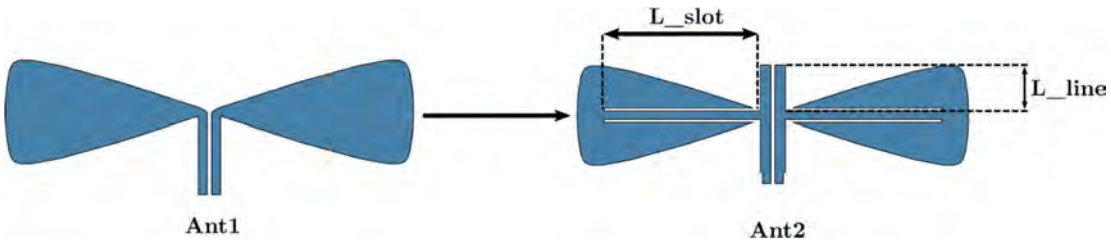

Figure V.9. Geometry of the proposed UWB Bowtie antenna. The final value of the parameters after optimization and co-simulation is L_slot = 16 mm and L_line = 4.6 mm.

As shown in Figure V.9, the initial optimization technique involves extending the upper portion of the antenna feeding lines in the Ant1 design (L_line = 0). This approach allows us to improve the impedance matching and avoid lengthening the lower part of the antenna feeding lines, which would increase its bulkiness. The variation of the parameter L_line, depicted in the Smith chart in Figure V.10 (a), shows a rotation of the antenna input impedance along a circle with a constant real part as L_line increases from 0 mm to 4.6 mm. We were constrained to a maximum length of 4.6 mm to ensure that the antenna fits within the rigid section of the prototype (B1), which already includes the UGM. We can see on the smith chart that the impedance of the antenna (red marker) is not yet adapted to that of the module (blue marker).

Secondly, two thin slot lines of 0.3 mm were included into each rounded bowtie arms. This modification aimed to increase the imaginary part of the impedance by altering the current distribution on the antenna. The variation of this parameters is reported on the graph in Figure V.10 (b). At 4 GHz, the antenna's impedance goes from a negative imaginary part and reach a maximum before decreasing. With a slot length of 15 mm, the corresponding impedance (Zant = 24+j·8.9 Ω) matched well with the targeted impedance (Z_{UWB}* = 25+j·9 Ω), but the bandwidth was reduced due to the presence of slot lines. Finally, the length of the slots (L_slot) was fixed to 16 mm which provide the best trade-off between bandwidth and impedance matching.

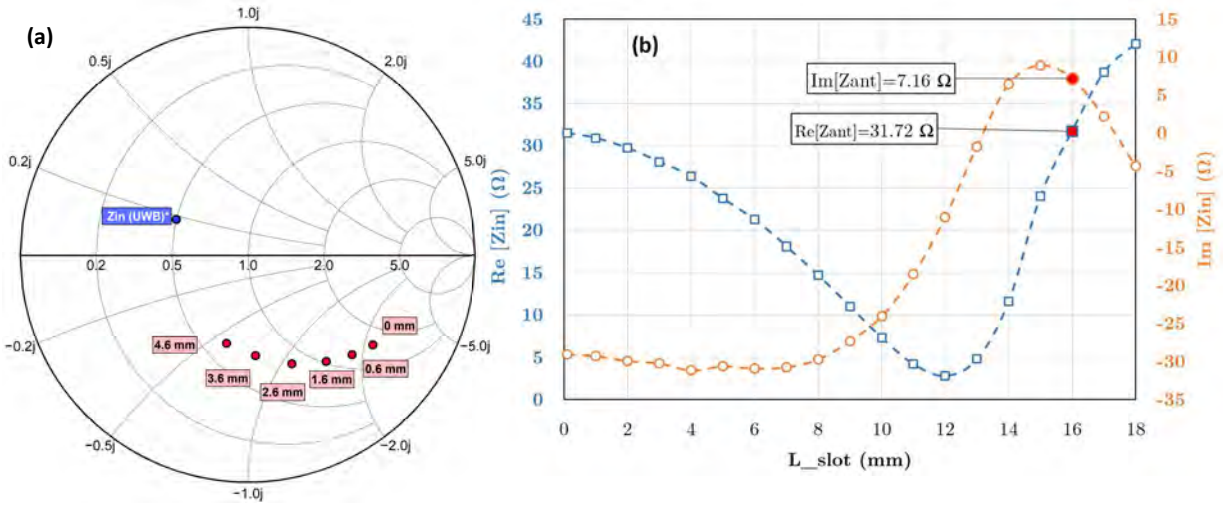

Figure V.10. Evolution of the simulated impedance of the UWB bowtie antenna at 4 GHz: (a) Smith chart with L_line variation; (b) Graph of the real and imaginary part with L_slot variation.

The normalized return loss in Figure V.11, shows a good impedance matching under -10 dB within the bandwidth of 3.64 GHz to 4.92 GHz. Interestingly, the antenna's performance is not significantly affected by the 180° folded position of the tag, maintaining the same bandwidth. This exceeds the requirement of at least 500 MHz bandwidth for our UWB application.

Regarding the radiation characteristics, both in the flat and 180° folded positions, the radiation pattern is influenced by the symmetrical positioning of the antenna arms, resulting in a gain variation of less than +1 dBi from -60° to 60° in the H-plane. The antenna has a peak gain of +3.66 dBi in the H-plane at theta=158°.

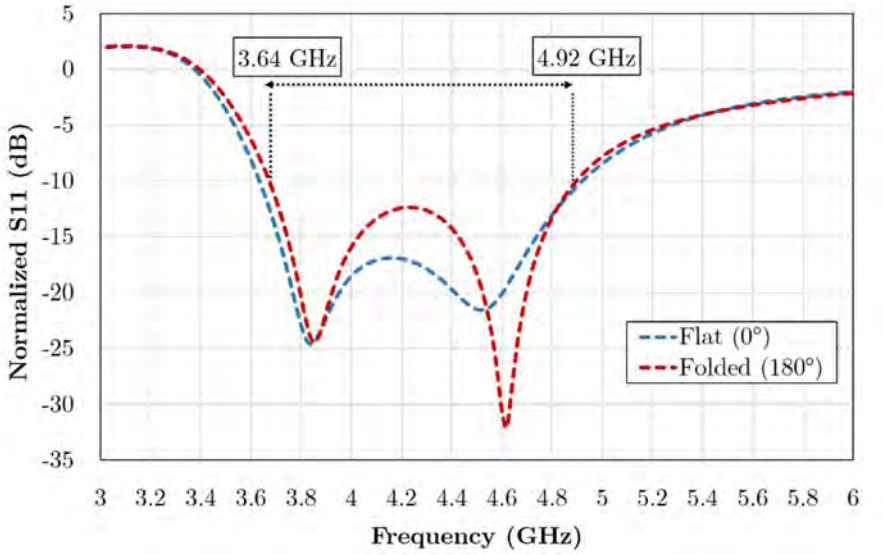

Figure V.11. Simulation of the UWB antenna (Ant2) return loss (normalized at Zin [UWB] = 25+j·9 Ω) in flat and folded position.*

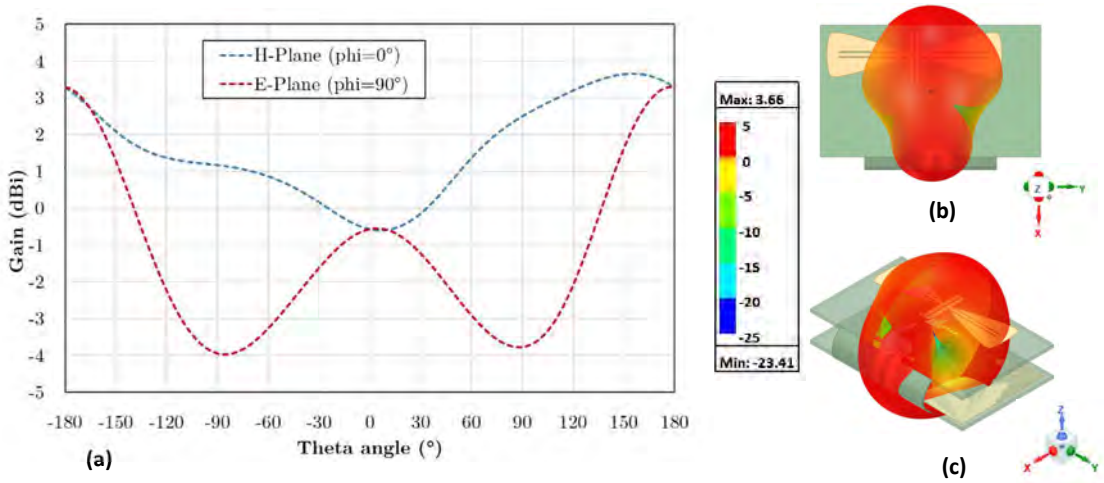

Figure V.12. Radiation performances of the UWB antenna : (a) Simulated gain at 4 GHz as a function of the theta angle; (b) Top view of the 3D polar plot of the gain at 4 GHz; (c) Isometric view of the 3D polar plot of the gain at 4 GHz.

4.2. UHF antenna design

The UHF antenna design proposed in Figure V.13, is a large pattern dipole antenna located in the B3 section of the semi-flex tag, which is connected to 1 mm length transmission lines (width of 2.55 mm). Due to the low imaginary part of the input impedance of the antenna, a pair of lumped inductors is used to reduce to increase the electrical dimensions to reach the target complex conjugate impedance of the UGM. The shape of the UHF antenna in the B3 section was optimized to ensure good radiation efficiency. Moreover, a short tapered line was added at the end of transmission lines to fit the dimensions of the input pads of the UGM.

To ensure accurate simulation results, the antenna was co-designed with the UWB bowtie antenna and the UGM module, both placed in the B1 section of the prototype.

After conducting multiple simulations by tuning the inductor values, the UHF antenna is complex conjugate matched to the module within the range of 24 nH to 30 nH. For practical reasons, the inductance values of 24 nH and 27 nH from the Murata LW15AN series are chosen based on their availability. The equivalent series resistance of these inductors is determined through the quality factor provided in the datasheet. The 27 nH inductance has a quality factor of 56 at 870 MHz, resulting in a series resistance of 2.61 ohms. Similarly, the 24 nH inductance has a quality factor of 59.1 at 870 MHz, corresponding to a series resistance of 2.2 ohms. These specific values were considered in the subsequent measurement results. These values were considered for the simulation results presented later.

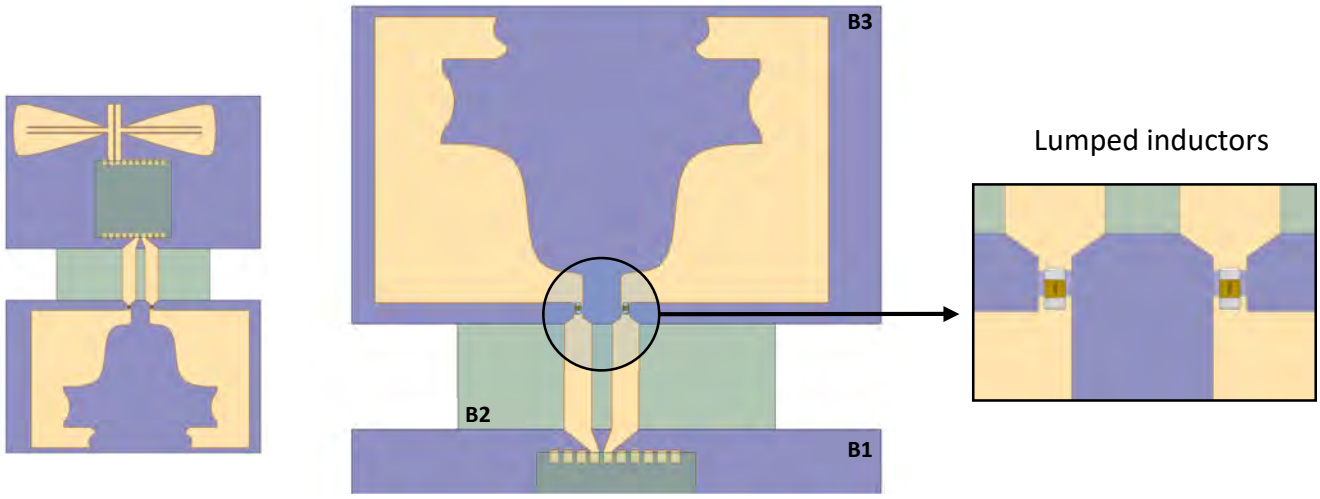

Figure V.13. Image of the loaded UHF dipole antenna.

A compact 3D tag with dimensions of 50 mm x 30 mm x 7 mm is obtained by folding the rigid section over the flexible one at a 180° angle, as shown in Figure V.8 (b). Simulation results indicate a satisfactory complex conjugate matching with the same inductor values in the 3D configuration. The imaginary part of the antenna's impedance is more affected when the prototype is in its compact 3D shape, while the real part is slightly modified. This indicates that the folding and miniaturization process has a greater impact on the reactive component of the impedance. Due to the folding of the transmission line connected to the UHF antenna, the current distribution is modified, resulting in a reduction in radiation efficiency. Nonetheless, this configuration does not affect the omnidirectional radiation pattern of the antenna.

In this section, we also focused the study on the impact of the series resistance of the inductors on the antenna's performance. Table V.2 presents the results of the UHF antenna in a flat and 180° folded position without considering the series resistance value, while Table V.3 includes the series resistance value. Contrary to the geometric effect, the series resistance affects more the resistive part of the antenna impedance. Although the antenna exhibits good impedance matching, the results show that the series resistance significantly reduce the antenna's performance, particularly in terms of radiation efficiency. Considering the series resistance, the gain values are below -2.5 dBi, and the radiation efficiency is below 40%. The use of FR4 material for the design is also constraining. The radiation efficiency is expected to be higher with a material that has lower dielectric losses.

To justify this, we simulated the same UHF antenna with an inductance value of 24 nH (considering its series resistance) on an Itera-MT40 substrate with a thickness of 0.8 mm and a loss tangent of 0.0031. With this substrate having lower dielectric losses, we expect to achieve a radiation efficiency of 45.9% (with a maximum gain of -1.2 dBi) in the flat position, and 39.9% (with a maximum gain of -1.8 dBi) in the folded position. The UHF antenna with ITera-MT40 substrate as for the first prototype exhibits approximately the same performance.

Given the requirement for a compact geolocation tag smaller than 65 mm x 45 mm, the next design based the same miniaturization technique (using lumped component) and the same antenna. However, the improvement of the antenna radiation efficiency was ensured through the choice of a low dielectric losses substrate. This helps to enhance the antenna performances (as demonstrated earlier) and thus the overall performance of the tag.

Table V.2. Simulation results of the semi-flex antenna in flat and folded position at 868 MHz without series resistance.

Configuration	Inductance (nH)	Zin (Ω)	Gain (dBi) at Phi=0° Min / Max	Radiation efficiency (%)
Flat	24	10.71 + j·183.55	+0.42 / +0.85	69.8
	27	13.58+ j·256.65	+ 0.29 / + 0.65	69.8
Folded (180°)	24	10.37 + j·218.79	+0.11/ +0.35	61.6
	27	13.47 + j·298.56	-0.16 / +0.04	61.7

Table V.3. Simulation results of the semi-flex antenna in flat and folded position at 868 MHz with the equivalent series resistance.

Configuration	Inductance (nH)	Zin (Ω)	Gain (dBi) at Phi=0° Min / Max	Radiation efficiency (%)
Flat	24	19.49 + j·180.50	-2.25 / -1.80	39.5
	27	27.69 + j·260.01	-2.74 / -2.34	36.9
Folded (180°)	24	20.56 + j·215.26	-2.94 / - 2.7	32.6
	27	29.3 + j·299.48	-3.49 / -3.31	28.4

4.3. UHF Antenna characterization

The design was fabricated by NCAB Group [223] using a specific rigid-flex process using 0.8 thick FR4 rigid substrate. The flexible part is 0.25 mm thick with a tolerance for depth control routing of ±0.05 mm. Based on the simulation results, RF wound type LQW15AN inductors with values of 24 nH and 27 nH were selected for the prototyping. Characterization of the fabricated tag was carried out using the same setup as before, with a positioner arm connected to the home-made probe, and the antenna placed on a rohacell foam. The impedance matching of the loaded antenna was measured in various positions, including the flat position, as well as folded angles of 90° and 180°. Over the frequency band, the impedance of the loaded antenna increases with the effect of the curvature of the flexible part. The measurement results were normalized with a reference impedance of the UGM at -20 dBm. Contrary to the simulation, it was observed that the 27 nH inductor provided a better complex conjugate impedance matching, with an imaginary part close to 250 Ω. In Table V.4, it can be noted that with the 27 nH inductor, the normalized impedance in both the flat position and the full 180° folded position was lower than -15 dBm, indicating a reflected power of over 1%.

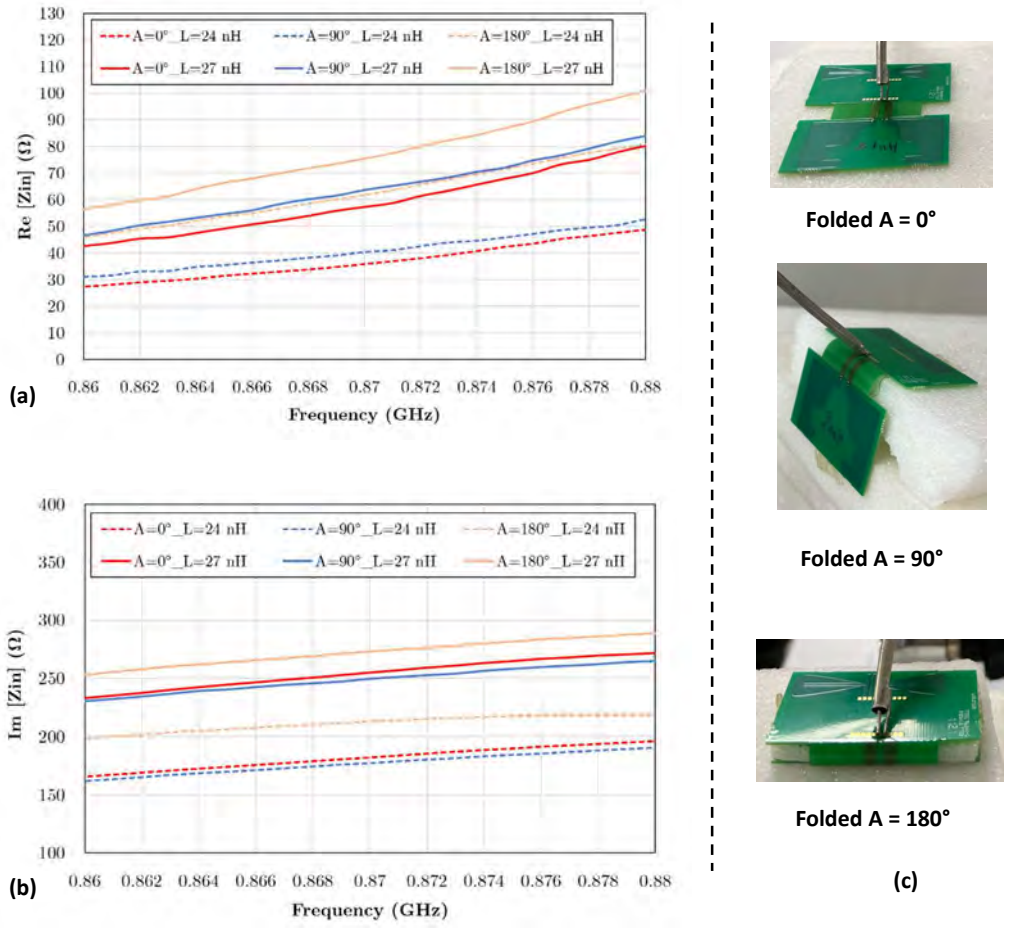

Figure V.14. The measured input impedance of the loaded UHF antenna on different folded angle (0° correspond to the flat position) : (a) Real part of the input impedance of the characterized antenna; (b) Imaginary part of the input impedance of the characterized antenna; (c) Photo of prototyped antenna under test.

Table V.4. Evaluation of the return loss and reflected power of the semi-flex loaded UHF antenna at 868 MHz with a normalized UGM impedance at -20 dBm.

Ind. (nH)	Folded angle	Re [Zin] (Ω)	Im [Zin] (Ω)	Normalized Return loss (dB)	Estimation of the reflected power (dBm)
24 nH	0°	33.679	178.864	-14.71	3.38 %
	90°	38.257	174.42	-14.08	3.91 %
	180°	58.554	210.44	-17.56	1.75 %
27 nH	0°	53.96	250.625	-22.83	0.52 %
	90°	60.133	245.503	-21.21	0.76 %
	180°	71.772	268.964	-19.72	1.07 %

The use of such an original design in semi-flex technology ensures a good return loss even with the high real part of the impedance. However, this results do not guarantee optimal performance of the geolocation tag, as the low radiation efficiency observed in the simulation can impact its sensitivity. In addition to the mismatch loss, the overall antenna efficiency and tag sensitivity are affected by dielectric losses. Therefore, an alternative approach was explored to optimize all antenna parameters and address these challenges.

5. A Full Flexible Tag Design based on Polyimide (Ftag)

The design proposed in the previous section using semi-flex technology (SMtag) allowed a smaller size in the 3D configuration, measuring 50 mm x 30 mm x 9.6 mm compared to the initial design on a rigid substrate. However, the radiation performance of the UHF antenna was significantly affected due to the use of the FR4 substrate, which has higher dielectric losses. In order to design an efficient UHF antenna for energy harvesting at low RF power levels, it is crucial to minimize dielectric losses. Therefore, the proposed design in this section named Ftag is based on a fully flexible substrate (polyimide). Polyimide material offers interesting properties such as low dielectric loss, heat resistance, and high mechanical stability. By using a fully flexible prototype, the tag can conform to different configurations, and the manufacturing process is faster, cheaper and less complex. To simplify the design and facilitate comparison with the previous semi-flex prototype (SMtag), the same antennas design was adapted on the polyimide-based substrate. The planar dimensions of the tag remain at 70 mm x 50 mm, and the dimensions of the antennas were not modified. The simulation was performed using a thin substrate of 125 µm, with a dielectric constant of 3.4 and a loss tangent of 0.012. The antenna pattern was assigned to a 35-µm thick copper boundary. This new design using a fully flexible polyimide substrate is expected to improve the radiation performance of the antenna by minimizing dielectric losses, enabling more efficient energy harvesting at low power input levels.

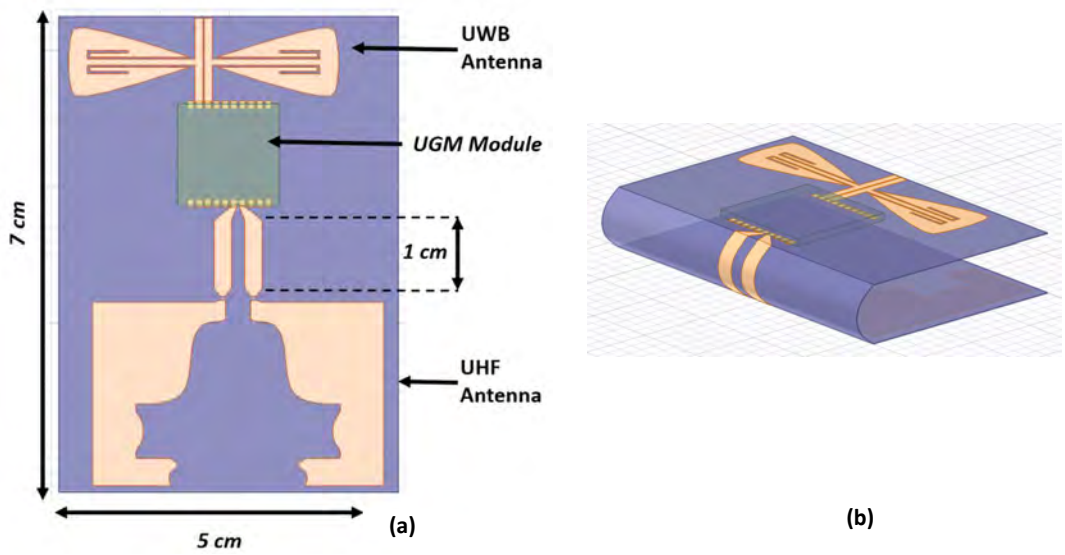

Figure V.15. Geometry of the new geolocation tag in flexible substrate with the top view in (a) and the isometric view of in 180° folded positions in (b).

5.1. Simulation of the UWB Bowtie antenna

Firstly, the bowtie antenna was simulated using the new flexible substrate material. Due to changes in the dielectric constant and thickness, the simulated impedance of the antenna also changed. At 4 GHz, the antenna exhibited a negative imaginary part of approximately -56 Ω. To achieve impedance matching with the flexible substrate, further investigation was conducted using the previously mentioned impedance matching technique. Similar to the previous design discussed in section 4.1, the parameter L_Line was initially increased from 4.6 mm to 6 mm. Additionally, the length of the slot lines was adjusted to achieve the desired imaginary part. To prevent splitting of the antenna arms, the slot lines were meandered, resulting in an effective antenna design as shown in Figure V.15.

In the new version of the UWB antenna, depicted in Figure V.16 (a), a successful complex conjugate impedance matching was achieved from 3.94 GHz to 5.2 GHz. When the tag is folded in the 180° position, the coupling effect with the UHF antenna enhances the depth of the return loss. Examining the radiation pattern at 4 GHz, the antenna exhibits an oval shape at Phi = 0° in both positions, with a gain of approximately +2 dBi and a variation of ±0.5 as a function of the theta angle. In the E-plane at phi = 90°, the folding of the antenna has a more pronounced effect.

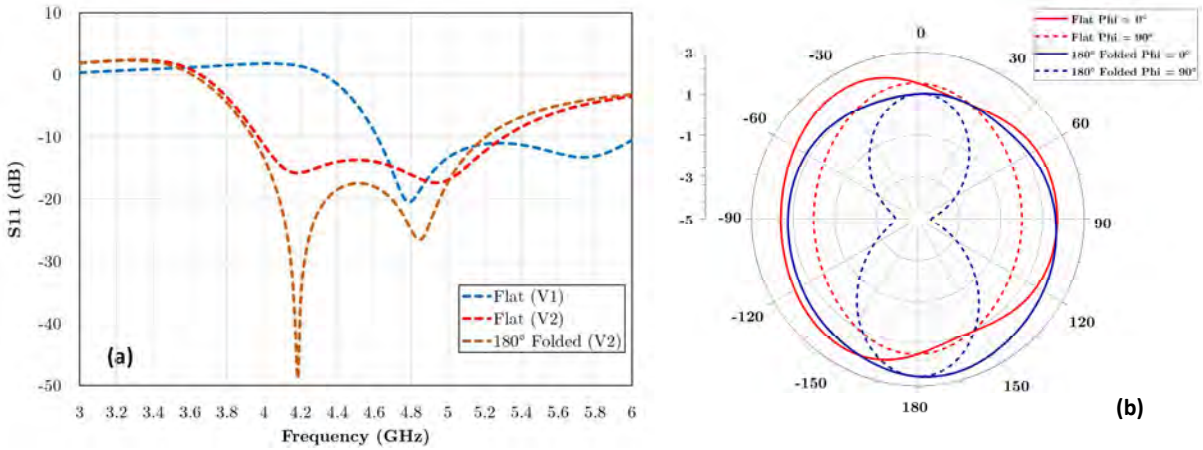

Figure V.16. (a) Comparison of the simulated return loss of the bowtie antenna unmatched (V1) and optimized (V2) in flat and folded position; (b) Radiation pattern at 4 GHz in at phi=0° and phi = 90°.

5.2. Simulation of the loaded UHF antenna

The impedance matching of the UHF antenna on the flexible substrate was achieved with relative ease. The use of lumped components provided enough flexibility to adjust the imaginary part of the antenna. By incorporating 30 nH and 33 nH inductors, we achieved the desired complex conjugate impedance values. The input impedance and efficiency of the UHF antenna can be found in Table V.5. The simulation considered the serial resistance values of the inductors, obtained from Murata's LWQ18AN series datasheet (based on quality factor). The simulated values for the 30 nH and 33 nH inductors at 870 MHz were 1.9 Ω and 2.24 Ω, respectively. As expected, the antenna's gain exceeded that achieved with a semi-flex substrate, resulting in a radiation efficiency improvement of at least 12%. The antenna demonstrated better impedance matching with a 30 nH inductance value in both the flat and folded configurations.

Table V.5. Simulation results of the loaded UHF flexible antenna in flat and folded position at 868 MHz.

Configuration	Inductance (nH)	Zin (Ω)	Gain (dBi) at Phi=0° Min / Max	Radiation efficiency (%)
Flat	30	18.11 + j·216.59	-1.35 / -1.25	53.8
	33	22.6 + j·279.97	-1.72 / -1.61	49.2
Folded (180°)	30	17.12+j·238.27	-2.11 / -1.98	45
	33	22.55 + j·316.21	-2.6 / -2.47	40.4

5.3. Loaded UHF antenna characterization

The substrate chosen for manufacturing is a polyimide film with a thickness of 125 µm, coated with a 35 µm thick copper layer (AP9151) [224]. This material offers several advantages, including good performance, temperature resistance, and high reliability. The antenna fabrication was carried out in the clean room of the LAAS-CNRS using photolithography process facilities. The prototypes were then loaded with lumped inductors from the Murata LQW18AN series through hand soldering. It should be noted that using other substrate types such as PET would have required an additional low-temperature process [225]. Once the assembly was complete, the impedance measurements were obtained using the home-made probe connected to the VNA, as described earlier. Similar to the previous antenna on a semi-flex substrate, we conducted tests for all three configurations as shown in Figure V.17: flat (0° angle), folded at a 90° angle, and folded at a 180° angle.

Figure V.17. Fabricated flexible antennas on polyimide substrate: (a) Flat, (b) 90° Folded, (c) 180° Folded.

The measurements gave successful results, showing a good input impedance for the UHF antenna, with a normalized return loss lower than -17 dBm. Regardless of the configuration (flat, bent 90°, or bent 180°), the impedance matching remained suitable for the integration of the antennas with the Geolocation Module (UGM). The optimized prototype used a pair of 33 nH inductors, resulting in less than 0.7% loss in received power by the UHF antenna in all configurations.

Table V.6. Evaluation of the return loss and reflected power of the flexible loaded UHF antenna at 868 MHz with a normalized UGM impedance at -20 dBm.

Ind. (nH)	Folded angle	Re [Zin] (Ω)	Im [Zin] (Ω)	Normalized Return loss (dB)	Estimation of the reflected power (dBm)
30 nH	0°	33.8	201.6	-17.92	1.61 %
	90°	33.7	205	-18.48	1.42 %
	180°	43	194	-16.41	2.29 %
33 nH	0°	45	250	-25.07	0.31 %
	90°	49.7	275	-23.42	0.42 %
	180°	59	252	-21.82	0.66 %

6. Wireless Power Performances of the Geolocation Tags.

Previously, three types of design were prototyped on different substrates, and it was concluded that certain antennas exhibited better performance due to the low dielectric losses of the substrate. In this section, the focus is on validating the efficiency of the designed and manufactured antennas by evaluating their radiated performances in the geolocation tag. The emphasis was not on the UWB part, as it will only serve to receive UWB signals through a receiver. The antennas presented above are now combined with the UGM, which is welded on manually without any particular hybridization process. The sample on a 0.8 mm thick rigid Itera substrate referred to as Rtag, the one on semi-flexible FR4 as SMtag, and the one on a 125 µm flexible polyimide as Ftag.

To ensure accurate emission rate estimations, the measurements were conducted in an anechoic chamber, as depicted in Figure V.18 (a). The sample as shown in Figure V.18 (b) were also tested un the same condtions. The setup involved an energy source consisting of an RF power generator connected to a transmitting antenna via a coaxial cable. This setup allowed for illuminating the tag directly at a distance of 2 meters and at the same height. The transmitting antenna used was a circular polarized patch antenna with a frequency range of 868 MHz to 960 MHz and a gain exceeding +9 dBic. This type of antenna is commonly employed in RFID applications. In fact, it necessarily induces a loss of 3 dB when receiving through a linear polarized antenna on the tag. The losses incurred by the cables were evaluated using the Anritsu ML2437A power meter. The wireless power transmission was achieved using a continuous wave signal at 868 MHz. Once the tag was placed on rohacell foam, the UHF antenna collected sufficient energy, enabling the emission of a UWB signal. This UWB signal was then received by a beacon provided by UIWNLOC Company. The received data, including the unique identification of the UGM and the emission timestamp, were displayed on a PC. The time interval between two emissions was used to evaluate the efficiency of the UHF energy harvesting component.

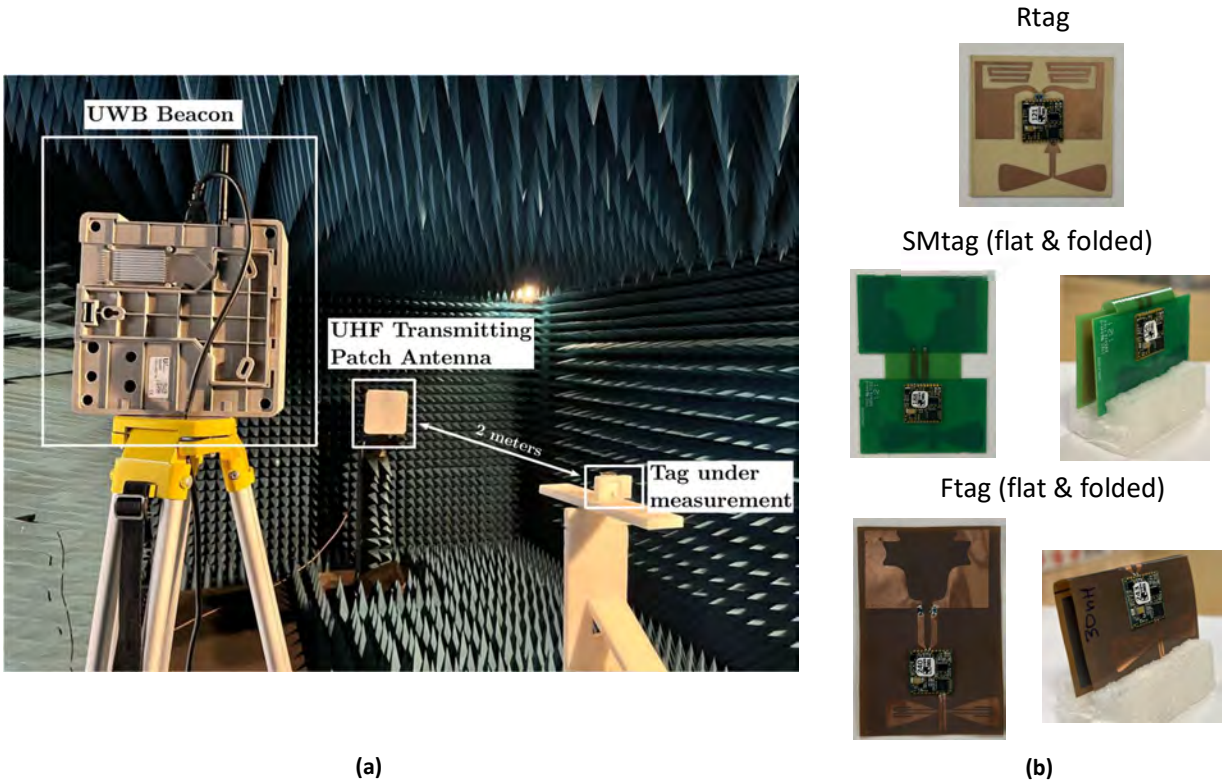

Figure V.18. (a) Measurement setup of the geolocation tags into the anechoic chamber; (b) Photos of the propotyped geolocation tags on different substrate.

Wires have not been connected to the UGM's capacitor to evaluate the charging times required for data transmission, as connecting them to the oscilloscope modifies the output impedance seen by the tag and thus alters the expected performance. To characterize the SMtag and Ftag tags in the folded position, they were held in place by a small rohacell cage to maintain the folded shape during testing, as shown in Figure V.18 (b). However, the aim is to integrate the tag into a protective case, which is not the subject of our preliminary study here.

For the test, the power source connected to the patch antenna was set with an RF output power of 24 dBm at 868 MHz. Figure V.19 shows a comparison of the emission rates of UWB signals at different orientations of the tag. This was done to evaluate the tag's performance in different positions, considering the unequal gain values depending on the shape of the radiation pattern. The associated images of the tag in each graph represent the orientation of the tag under test relative to the transmitting antenna. The tag was tested horizontally and vertically in both polarizations of the UHF antenna to evaluate performance in realistic scenarios with random tag placement. The rates depicted in the graph are averages of several receiving data time intervals.

Regarding the rigid tag Rtag, a pair of 30 nH inductors was used for impedance matching. As shown in Figure V.19 (a), regardless of the position, the tag can transmit the signal at least every seven seconds. In the horizontal position (represented in red), the rate is 3.6 seconds, while vertically, the rate can be lower (1.6 seconds) or higher (5.8 seconds) depending on the polarization of the UHF tag antenna.

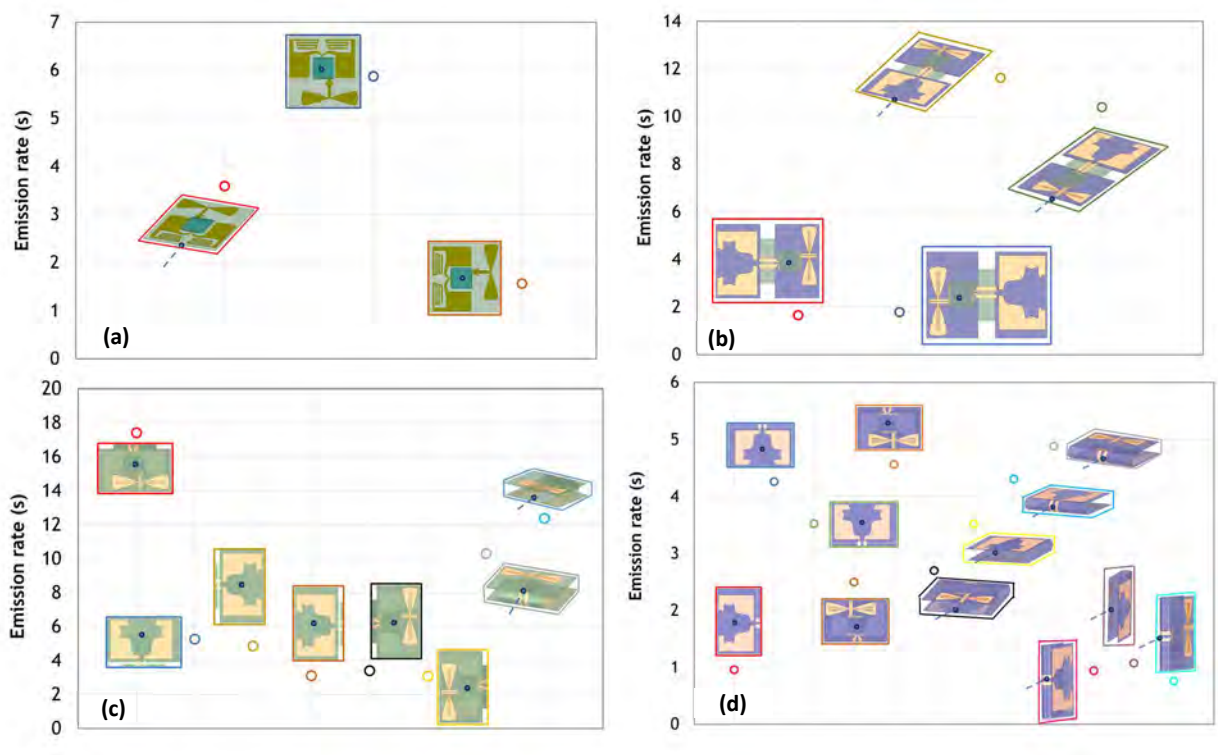

Figure V.19. Graph representing the emission rate of the developed geolocation tag as a function of the orientation from the power source : (a) Rigid tag named Rtag using 30 nH ; (b) Semi-flexible tag named SMtag in flat condition using 30 nH; (c)) Semi-flexible tag named Smtag in folded position using 27 nH; (d) Full flexible tag named Ftag in folded condition using 30 nH.

With the semi-flexible substrate-based SMTag, which is smaller than Rtag, it was expected to be less efficient due to higher dielectric losses. The SMTag with a pair of 27 nH inductors was chosen for the experiments. In the flat position, as shown in Figure V.19 (b), when placed vertically, the SMTag has an emission rate of less than 2 seconds, but horizontally, it exceeds 10 seconds.

In the folded position, which corresponds to the expected tag configuration, the emission rate is higher than in the flat position but remains around 5 seconds when placed horizontally in front of the transmitting antenna. The maximum rate in a single orientation is obtained at 17 seconds.

Finally, the experiments were carried out using the fully flexible tag named Ftag. It uses the same design as the SMTag but is improved with a better substrate that reduces dielectric losses. The design with a pair of 30 nH inductors was used. As expected, Figure V.19 (d) shows that the emission rate does not exceed 5 seconds regardless of the tag's position. When comparing the same orientation with the SMTag, the Ftag takes half the time to harvest energy and transmit the location signal to the UWB beacon. Thus, starting from the rigid tag Rtag, optimization in terms of design, configuration, and substrate selection has resulted in a more performant and compact tag, the Ftag.

7. Conclusion

In this chapter, our focus was on the miniaturization of the geolocation tag while maintaining its performance. The economic challenges were considered in order to ensure that the final product would be cost-effective. Initially, we attempted to design a small-sized antenna on a rigid substrate. However, this approach did not yield satisfactory results in terms of both size and performance. To overcome this limitation, we adopted a new manufacturing process that allow the use of a semi-flexible substrate. This allowed us to achieve a smaller size when the tag was folded. However, we encountered issues with the antenna's efficiency, and the tag took longer to harvest enough energy for UWB signal transmission.

To address these challenges, we decided to maintain the same design used for the SMtag, as it provided a small size. However, we made a crucial change by using a low-loss dielectric material, specifically polyimide, as the substrate. The use of polyimide substrate offered several advantages, including the ability to further reduce the size of the geolocation tag and improve the radiation efficiency of the UHF antenna for energy harvesting features. Comparing the SMtag on FR4 substrate and the Ftag based on polyimide substrate, we observed a significant improvement of about 12% in the radiation efficiency. This improvement translated into a higher sensitivity in energy harvesting for the geolocation tag, enabling it to collect sufficient energy for its operations.

The experimental test of the developed tag, reveals that the strategy by reducing the size of the tag through its geometry and using a low loss dielectric material, can give satisfaction. The full flexible tag Ftag of about 50 mm x 30 mm x 10 mm placed at 2 meter from the transmitting antenna spreading an equivalent EIRP power of 29.5 dBm can the harvest the energy and transmit the signal in some cases at less than 1 second and in certain orientation, the emission rate never exceed 5 seconds. These interesting results point the way to tag miniaturization using flexible materials. Future research will focus more on the type of flexible material, as polyimide remains relatively expensive compared with paper substrates. We'll also have to think about the protection and encapsulation of the flexible tag, which remains fragile compared with the rigid substrate.

VI. Development of a flexible battery-free geolocation tag based on advanced materials

1. Introduction

One of UWINLOC's objectives is to develop a flexible tag that is small in size and can conform to curved surfaces, enabling it to be easily attached to various objects. In the previous chapter, we explored solutions for creating battery-free geolocation tags using low-loss and flexible materials. However, to keep up with the evolving landscape of electronic devices that rely on low power consumption, alternative substrates and miniaturization, this chapter focuses on the development of a flexible battery-free geolocation tag on paper-based substrates.

The use of paper as a substrate offers several advantages. Firstly, it enables a less complex and more cost-effective manufacturing process. Additionally, paper is highly recyclable, making it an environmentally friendly alternative. The flexibility provided by paper-based substrates opens up new market opportunities and applications in areas such as retail, logistics, healthcare, and wearables.

In this presentation, we will introduce the Madras project, which focuses on the development of a geolocation tag based on organic flexible materials. We will discuss the project's objectives and specifications, and then present the design, development, and characterization of the flexible geolocation tag using advanced materials and transparent conducting inks.

2. About the Madras Project

Madras [226] is a European project that focuses on advancing the development of materials and processes for organic electronics, particularly in the field of Organic and Large Area Electronics (OLAE). The project's primary goal is to enhance the production capabilities of OLAE devices by optimizing the conductivity, transparency, and recyclability of the materials involved. The materials developed within the project are required to exhibit reliability, cost-effectiveness, and compatibility with high-volume production processes. Special attentions are given to improving the durability and lifespan of flexible electronics by utilizing robust materials and encapsulation technologies. Additionally, the project aims to establish a new manufacturing platform that enables rapid and efficient industrial production of OLAE devices.

To validate and apply the outcomes of the project, two demonstrators have been developed. The first demonstrator is a flexible geolocation tag designed for object identification and tracking within the industrial sector. The second demonstrator involves a fingerprint biometric reader based on photodetection, which serves as a means of user identification. These demonstrators serve as examples to showcase the capabilities of the materials and processes developed through the Madras project.

During the three-year development period, the Madras project involved 12 partners from five European countries, consisting of universities, research centers, industry players, and a standardization body. Among these collaborators, several key partners were involved in the development of the geolocation tag:

1. Uwinloc (UWL): As the primary partner, Uwinloc played a crucial role as the end-user of the geolocation tag. Their involvement aimed to emphasize the necessity of flexible electronics in the context of industry 4.0. Uwinloc was responsible for defining the specifications of the tag, designing its structure, and conducting material and prototype characterization.

2. Eurecat (EUT) [177]: A technology center based in Spain, Eurecat is responsible for project coordination, dissemination of activities, and technical aspects related to printing and the development of the encapsulation process.

3. Genesink (GNK) [227]: A French manufacturer specializing in advanced materials for conductive and semi-conductive inks. Genesink's role within the project is to enhance the electrical properties and adhesion of conductive inks for the development of the tag.

4. Arjowiggins (AJWG) [228]: A private company that specializes in the production of paper for printed electronics, with applications including RFID and NFC. Arjowiggins contributes to the project by developing an improved version of translucent paper, focusing on enhancing transparency and dielectric properties.

The remaining partners may have their specific roles in the final phase of the project or contribute indirectly to the development of the flexible tag.

3. Development of the flexible geolocation tag

3.1. Specifications

As part of the Madras project, Uwinloc is participating as a demonstrator for a new flexible tag. The current tag solution used a conventional rigid substrate, and has dimensions of approximately 68 mm x 48 mm (Figure VI.1 (a)). However, Uwinloc aims to significantly reduce the size of the electronic components to around 1 square centimeter (0.12 square inch), allowing for the creation of much smaller tags. One of the primary challenges is the space occupied by the antennas, which is influenced by the wavelength at the operating frequency and the dielectric properties of the substrate used. The final version of the tag should incorporate both the miniaturized electronic components and flexible antennas printed on a paper-based substrate (Figure VI.1 (c)).

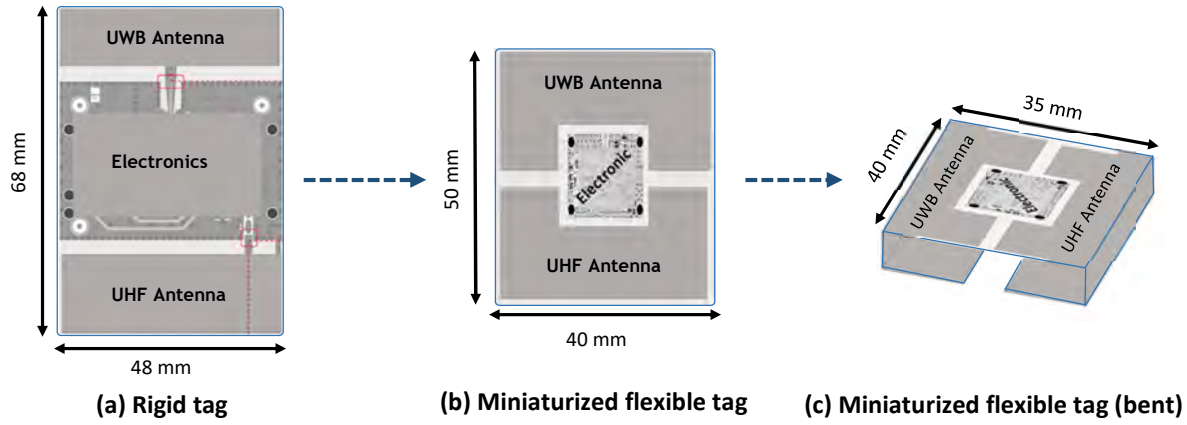

Figure VI.1. Miniaturizing step for the flexible geolocation tag.

As mentioned in the previous chapter, the geolocation tag works through two different frequencies: UHF for harvesting the surrounding electromagnetic waves from the source, and UWB at 4 GHz for transmitting the position to a dedicated beacon within the same area. The significant innovation of the flexible geolocation tag as demonstrator lies in a specific production process depicted in Figure VI.2. It involves several steps, starting with the selection of a nanocellulose foil as the material. This is followed by the printing process using advanced and transparent conductive ink, as well as SMD (Surface Mount Device) assembly. The key aspect of this process is the adoption of the In-Mold Electronic (IME) strategy, which integrates the electronics with traditional injection plastic transformation. IME involves embedding the electronics inside the plastic through thermoforming (where the conductive surface is shaped in 3D using heat and pressure) or injection molding (where the electronics are embedded within a single piece of injected resin). This approach provides numerous advantages, including improved reliability and durability, increased design freedom and flexibility, and reduced weight. IME is already being widely used in various applications, such as aerospace (e.g., integrated antennas) and automobile (e.g., touch sensors) [229].

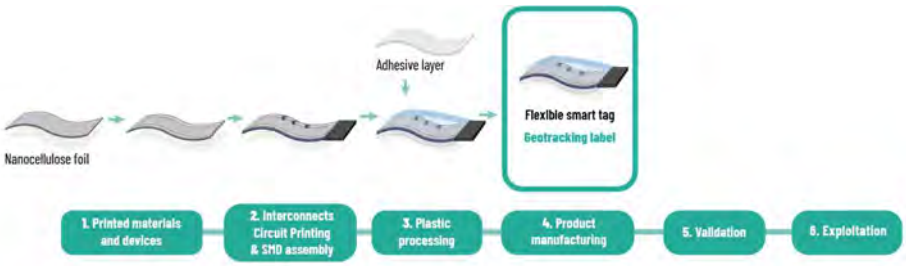

Figure VI.2. Production process of the flexible geolocation tag.

For the development of the flexible paper-based tag, the antennas had to be designed with material dielectric and electrical properties, and the electronic part embedded in the UWINLOC Geolocation Module (UGM) had to be assembled with the antennas, then overmolded to protect the tag. Several parameters must be considered when designing functional antennas, as the dielectric parameters and the thickness of the substrate and the ink conductivity. As studied in the previous chapter V, the tag antennas require low dielectric and ohmic losses. Consequently, the technical specifications was elaborated for the materials to develop, the fabrication process and the final demonstrator for an efficient and reliable flexible geolocation tag.

It was agreed to develop conductive inks with a low resistivity of less than 100 mΩ/sq for desired screen-printing technique. In our use case, the optical transparency of final demonstrators is not a necessity.

3.2. Materials development

The printed circuit board (PCB) substrate material is the fundamental part in any electronics devices, and even determining for performances in RF applications. Recent development on an alternative of conventional substrate in the field of OLEA are presented on the literature [230].

3.2.1. Definition of the substrate

The choice to use a nanocellulose-based substrate in the project aims to develop a scalable, transparent, and cost-effective material. Nanocellulose is considered a promising material for electronic production on flexible substrates due to its desirable properties such as lightweight, flexibility, and transparency [[231], [232]. It is derived from the nanometric structure of cellulose, a widely available and sustainable material known for its mechanical strength. Cellulose, the most abundant polymer on Earth, is produced through photosynthesis in plants.

There are two main categories of nanocellulose: nanocrystals of cellulose (CNC), which are produced through a chemical process, and cellulose nanofibrils (CNF), derived from cellulose fibers using mechanical treatment. The implementation of Nanocellulose Foil (NCF) substrates for industrial-scale electronic devices presents challenges due to the time and energy-intensive fabrication process involved, including steps such as nanocellulose extraction, dewatering, and the formation of high-quality films. The CNF from the wood structure through microscopy image as represented in Figure VI.3.

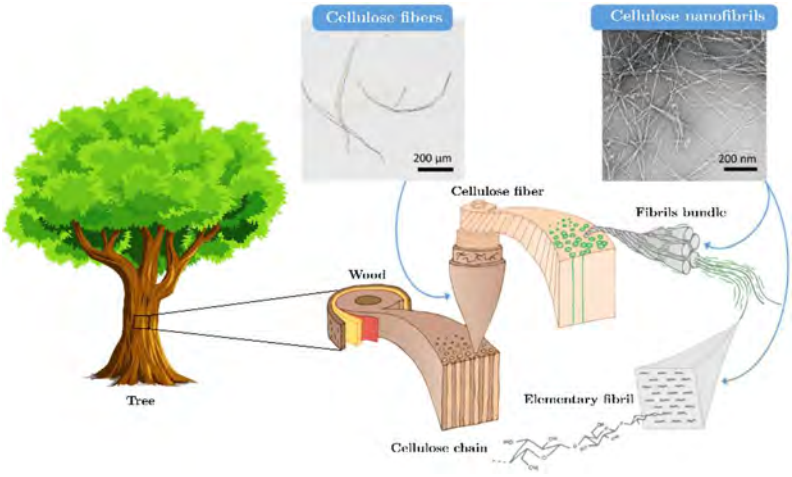

Figure VI.3. Representation of the wood structure, optical microscopy image of birch fibers and transmission electron microscopy image of birch CNF (Reproduced from Madras Blog post in[233]).

The nanocellulose stands out from other materials due to its outstanding properties and can be used in different applications in printing electronics. Nanocellulose has attracted much interest in the development of new biodegradable materials. Nanocellulose films coated with graphite ink via screen printing are demonstrated to be suitable materials for sustainable and green electronics [234]. Because of it several advantages (as renewability, flexibility and mechanical strength), the nanocellulose has gain a great interest in applications of sensors. The review [235] has introduce the applications of nanocellulose-based sensors in the fields of biomedicine, environmental monitoring, food safety, and wearable devices.

The advantage of using an innovative nano-cellulose based substrate is to give customers the opportunity to target new applications and develop smart systems for other use-cases. In energy harvesting field, the CNF has also proved his attractive potential in wearable electronics. As in where the CNF from carrots is used as piezoelectric composite film for collecting mechanical energy generated by foot and hand joints [236]. In this project, the nanocellulose is used to demonstrate it potentiality to be used as green, flexible and optically transparent paper-based substrate for RF applications.

The paper substrate used in the antenna design was produced by AJWG and contains 60% cellulose nanofibrils (CNF), resulting in a transparency of 79%. This paper is made from pure cellulose that undergoes enzymatic treatment using endoglucanase, followed by mechanical treatment using refiners. One of the objectives of using this substrate was to facilitate the coating of silver nanoinks on its surface. Table VI.1 presents a comparison of the dielectric properties of the MCF substrate with the AJWG commercialized sheet, which is not transparent (Powercoat Paper). These properties were determined using the cavity resonator method.

Table VI.1. Dielectric properties of substrates (powercoat foil and nanocellulose foil) from AJWG.

Substrates	Thickness (um)	Dielectric constant @900MHz	Loss tangent Tan δ @1GHz
NCF Foil	60	4.2 (±0.2)	0.135 (±0.015)
Powercoat paper	90 and 125	3.3	0.12

The nanocellulose-based substrate offers the advantages of transparency and being ultra-thin. However, it has a relatively high dielectric loss compared to the paper substrate used for the antenna in reference [237] (with a loss tangent, tanδ, of 0.09). The dielectric loss of the nanocellulose-based substrate is similar to the one used in reference [238], which is not specifically mentioned by name, but has a loss tangent of 0.125.

3.2.2. Developed conductive inks

The objective of the project is to develop advanced ink materials that have desirable characteristics such as transparency, conductivity, and resistance to moisture and ambient oxygen. To assess the performance of these materials, tests are conducted on both PET and NCF substrates. Adhesion tests follow the standard set by the American Society for Testing and Materials (ASTM) as outlined in ASTM D3359 [239]. Method B, which involves a perpendicular line model, is employed to evaluate adhesion on a scale ranging from 0 to 5. A rating of 5B indicates the highest level of adhesion with no defects and completely smooth edges. Resistivity, on the other hand, is measured using a 4-point probe.

Silver nanowires (Ag NWs) have gained significant popularity in the field of flexible electronic devices due to their excellent electrical conductivity and flexibility [240]. These properties make them well-suited for use in flexible devices. In this project, GNK has developed AgNW inks; however, they do not provide sufficient conductivity to achieve optimal antenna efficiency. As a result, the focus shifted to screen printing with silver nanoparticles (AgNP) ink. The applications of AgNP-based ink include transparent conductive film (TCF), thin film transistor (TFT), biosensors, radio frequency identification (RFID) antennas, and stretchable electronics. These applications have shown promise in the field of flexible and printed electronics [241].

Table VI.2. Electrical properties of the developed inks obtained (@140°C, 30 min).

Ink name	Rs (mΩ.cm)	Thickness (µm)	Resistivity (µΩ.cm)
Ag-NP1	19	2.2	4.1
Ag-NP2	20	2.7	5.4

In this study, GNK developed two Ag NP inks, namely Ag-NP1 and Ag-NP2, for applications in geolocation tag antennas. These inks contain nanocellulose crystals (CNC) and fibers (CNF), respectively. The electrical properties of these inks were measured and are provided in Table VI.2. Ag-NP1 ink, which contains nanocrystal cellulose (CNC), demonstrates better conductivity with a value of 4.1 µm.cm. It also exhibits good printability, allowing for a resolution of 100 µm linewidth and 150 µm gap between lines. However, Ag-NP1 ink shows poor adhesion on PET and NCF substrates. To address this issue, a new ink with improved adhesion properties has been developed and will be discussed later in this study.

3.3. Preliminary antenna design (V1)

After the development of the substrate and conductive ink, their properties were validated by testing their performance in an antenna performances. A modified loop antenna is designed on 60 µm thick NCF substrate with the highly conductive ink AgNP1. To consider the tolerance, the simulated resistivity is defined to 5.5 µm. The loop antenna structure was optimised after several simulations steps to improve the return loss and the realized gain. The PCB and the connector to be used for the characterisation were clearly modelled in the software to faithfully reproduce the fabricated samples.

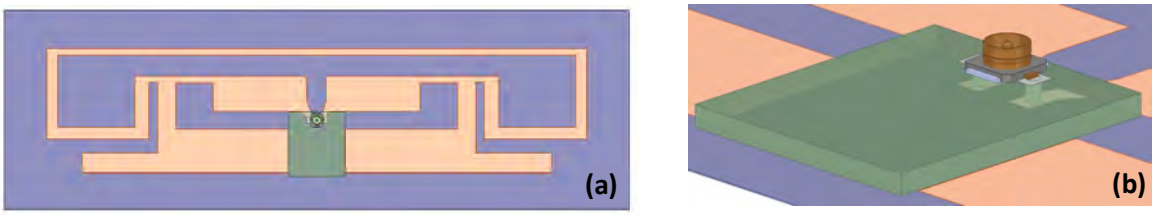

Figure VI.4. (a) Geometries of the designed antenna; (b) Representation of the excitation strategy with a hybridized PCB with U.FL connector; (c) Detailed view of the modelled U.FL connector with assigned materials.

To facilitate the characterization of the antenna on a paper substrate, a UFL connector was chosen and soldered onto a 1 mm thick printed circuit board (PCB), which was then adhered to the substrate using adhesive. The electrical connection between the antenna pads and the was established using a metallic via and conductive paste. This PCB was also designed to replicate the effect of the UWINLOC Geolocation Module (UGM) module. The simulated return loss of the antenna, as shown in Figure VI.5, indicates a resonant frequency of 855 MHz with a bandwidth of 67 MHz, reaching a return loss of under -10 dB. The antenna exhibits an omnidirectional radiation pattern at 867 MHz, with a maximum simulated gain of +1.9 dBi.

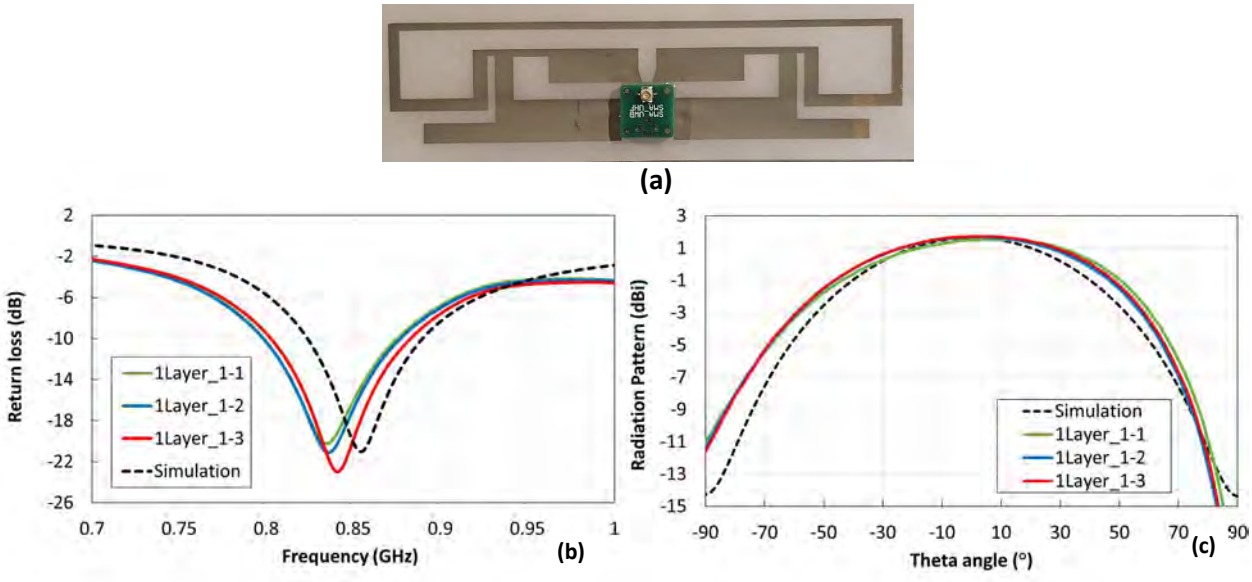

Figure VI.5. Comparison between simulation and measurements of the 3 samples : (a) Photo of the fabricated antenna on NCF with hybridized connecter; (b) Return loss; (c) Gain in the E-plane (φ=90°) at 867 MHz.

In the latter stage, the design was carried out at Eurecat center with screen-printed Ag-NP1 ink on the NCF substrate. The nominal thickness of the single-layer ink coated on NCF is 2.7 µm, which is indeed less than the skin depth. However, the power losses caused by the skin effect were evaluated through simulations beforehand, indicating a minimal impact of only 2% efficiency or 0.25 dBi gain reduction compared to a thicker 9 µm ink layer.

During characterization, three samples were tested in an anechoic chamber. Figure VI.5 (a) shows that the measured return loss of the three samples aligns well, but there is a slight shift of 14 MHz (at the peak resonant frequency) compared to the simulation. This deviation is probably due to the influence of the U.FL to SMA cable used in the measurement setup. Nonetheless, the measured gain of each sample corresponds to the simulated values, with a maximum of +1.6 dBi (±0.1) in the E-plane at 867 MHz. The measurement results are closed to the simulation results obtained with HFSS, confirming the validation of the dielectric and electrical parameters of the materials developed by the project partners.

Despite exhibiting good performance, Ag-NP1 ink showed poor adhesion on the NCF substrate, as previously mentioned. Cracks were observed on the antenna pattern of some samples during measurements, even when bent. To address this issue, GNK developed a new ink formulation named Ag-NP3, which incorporates an additive based on vinyl acrylic copolymer. Ag-NP3 ink demonstrated improved adhesion, achieving a rating of 5B according to ASTM D3359 standard, and it exhibited good printability through screen printing on the NCF substrate. However, despite the adhesion improvement on the substrate, the formulated Ag-NP3 ink has a higher resistivity compared to Ag-NP1 ink, with a factor of 4. This implies that the electrical conductivity of Ag-NP3 ink is lower than that of Ag-NP1 ink.

To evaluate the effect of the ink formulation change on antenna performance, simulations were carried out to compare the radiation efficiency and gain between the use of Ag-NP1 ink and Ag-NP3 ink. The resistivity variation is particularly significant for the UHF antenna, which plays a crucial role in energy harvesting. According to the simulations, the antenna's radiation efficiency decreases by 7% when using Ag-NP3 ink compared to Ag-NP1 ink. Indeed, a trade-off between resistivity and adhesion was crucial to establish a robust connection between the ink and the paper-based substrate.

While the compromise is to enhance the adhesion properties on the substrate. By prioritizing adhesion, the ink can adhere more effectively to the paper-based substrate, ensuring better durability and stability of the antenna structure.

Table VI.3. Electrical properties of the new formulated ink with better adhesion compared to the high conductive ink (with sintering at 150°C for 30 min).

Ink name	Rs (mΩ.cm)	Thickness (µm)	Resistivity (µOhm.cm)	Adhesion on NCF
Ag-NP1	22 ± 8	2.3 ± 0.3	4.8 ± 0.8	3B
Ag-NP3	130 ± 30	1.7 ± 0.3	20 ± 1	5B

3.4. Antenna design including in-mold process (V2).

The second iteration of the design aims to achieve both antenna performance and print reliability by incorporating the in-mould process. One of the key constraints of this process is that the overall size of the tag should not exceed a 70 mm x 70 mm square area. In this design stage, the UWB antenna is also developed to ensure a 50 Ω impedance and compatibility with the manufacturing processes.

When selecting the material for encapsulation, the primary considerations are transparency and adhesion with the NCF substrate. After evaluating various resins and considering the technical capabilities of EUT, Thermoplastic Polyurethane (TPU) material is chosen. TPU is a commonly used thermoplastic for injection moulding flexible plastic parts in electronic devices. [242]. It offers favorable elastic and mechanical properties, making it suitable for the desired application.

A study presented in a previous paper [243] demonstrates the feasibility of screen-printed epidermal antennas using elastic silver ink on an 89 µm thick TPU substrate for monitoring human health. This further supports the selection of TPU as the encapsulation material in the current design, given its proven compatibility with flexible antennas and its advantageous properties.

3.4.1. TPU material characterization

The choice of TPU grade for injection molding is crucial to meet the specifications for RF transparency and minimize the impact on radiation efficiency. EUT conducted experiments using three TPU grades: standard TPU 15N80 [244], TPU15N85 [245], and bio-based TPU D12T80E [246]. The bio-based TPU is not only environmentally friendly but also exhibits properties similar to the standard TPU of the same hardness, including excellent mechanical properties and abrasion resistance.

To determine the dielectric parameters of the TPU materials, a simple transmission line resonator method is employed. The dielectric permittivity of the material is extracted by measuring the S-parameters of resonators. Half-wavelength open-stub and ring resonators are initially designed with a relative permittivity of 4.8 and a dissipation factor of 0.05, based on the provided dielectric parameters from the vendor [247]. The resonator designs for TPU characterization have been previously simulated on ADS and are shown in Figure VI.6. These resonators are then screen printed on 1.25 mm thick TPU using a UV curable standard silver ink (ELG-410S from Norcode [248]).

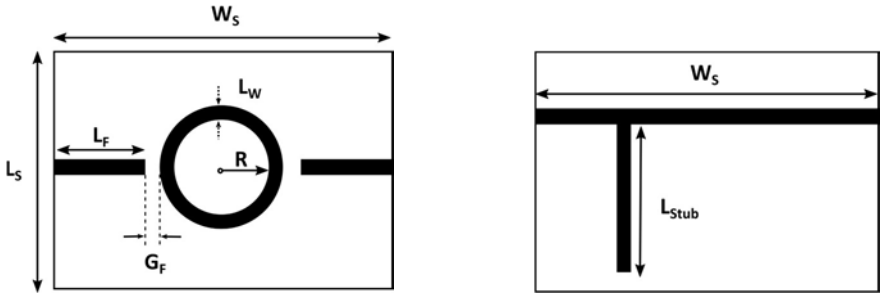

Figure VI.6. Geometry of the ring resonator stub and the quarter wavelength stubs. The parameters are: LF = 19 mm; GF = 0.2 mm; R=50.6 mm; LW = 2.25 mm; Lstub = 45 mm; Wstub = 70 mm.

Two samples of standard TPU 15N80 grade and one of the TPU ECO were fabricated and measured. The transmission coefficient |S12|response of the resonators are shown in Figure VI.7 © &(d). The calculation of the dielectric constant from the quarter wavelength resonator is calculated using the equation (IV.10).and (IV.13), providing an approximate value depicted in Table VI.4 and Table VI.5. For the ring resonator sample, the effective permittivity was obtained through the measured resonance frequencies and the mean radius of the ring (R_{mean}) with the equation (VI.1). The loss tangent has not been extracted due to the inaccuracy of the transmission line technique. For the next simulations, we will refer to the value provided in the datasheet.

$$R_{mean} = \frac{n \cdot \lambda_g}{2\pi} \tag{VI.1}$$

Based on the experimental results, both TPU grades exhibit a dielectric permittivity of approximately 3.3 (±0.12). The measured resonance frequencies were further validated through a retrospective simulation using ADS software, confirming the dielectric constant of 3.3. This value will be utilized in future antenna simulations with TPU to ensure the resonance frequency aligns with the desired specification of 868 MHz.

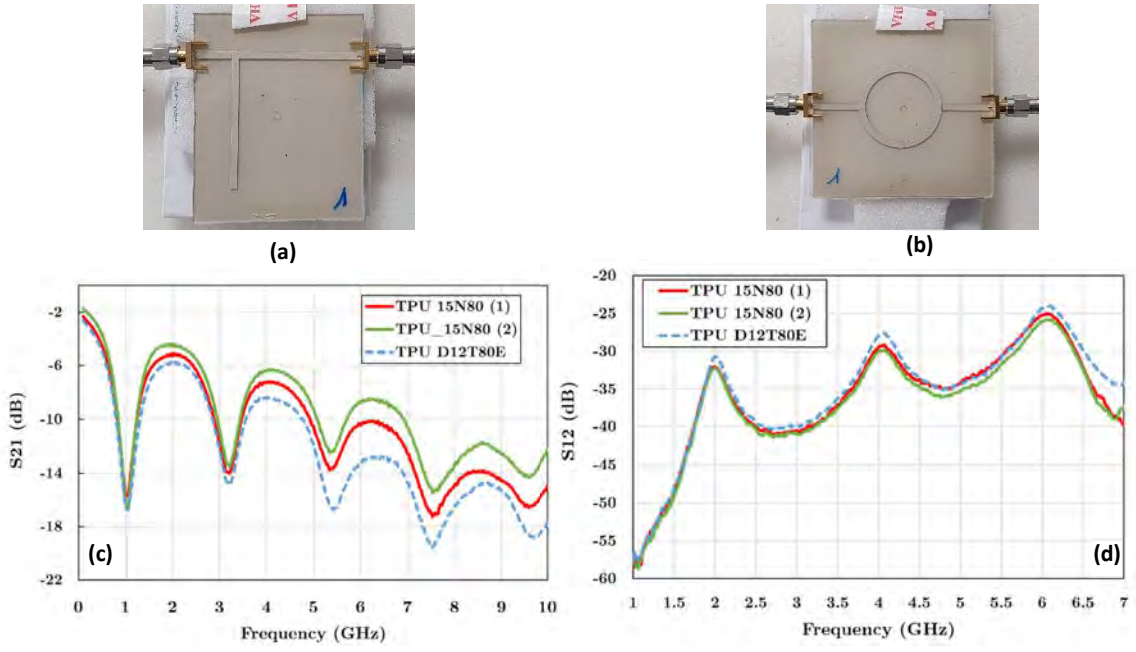

Figure VI.7. Photo of the resonator printed on TPU material and measured transmission coefficient for different TPU grade: Quarter wavelength stub resonator (a & c); Ring resonator (b &d).

Table VI.4. Measured resonance frequency and extracted dielectric constant for each TPU grade with the stub resonator method.

	TPU D12T80E			TPU 15N80 (1)			TPU 15N80 (2)		
N	1	3	5	1	3	5	1	3	5
Freq. (GHz)	1.05	3.22	5.42	1.03	3.22	5.35	1.04	3.22	5.41
ε_{eff}	2.63	2.53	2.48	2.75	2.53	2.55	2.7	2.53	2.49
ε_r	3.4	3.25	3.18	3.57	3.25	3.28	3.5	3.25	3.19

Table VI.5 – Measured resonance frequency and extracted dielectric constant for each TPU grade with the ring resonator method.

	TPU D12T80E			TPU 15N80 (1)			TPU 15N80 (2)		
N	1	2	3	1	2	3	1	2	3
Freq (GHz)	2.01	4.07	6.06	1.99	4.07	6.05	2	4.07	6.05
ε_{eff}	2.57	2.51	2.55	2.63	2.51	2.56	2.60	2.51	2.56
ε_r	3.31	3.22	3.28	3.39	3.22	3.29	3.35	3.22	3.29

3.4.2. Simulation and experimental results of the antennas

The design proposed here, intend test the in-mold process with TPU material, its compatibility with NFC substrate and silver nanoparticules inks, and to validate its extracted parameters. The TPU layer should protect the final demonstrator of the tag on the printed side according to EUT facilities. Two separate antennas working independantly at UHF frequency band and UWB at 4 GHz are presented in Figure VI.8.

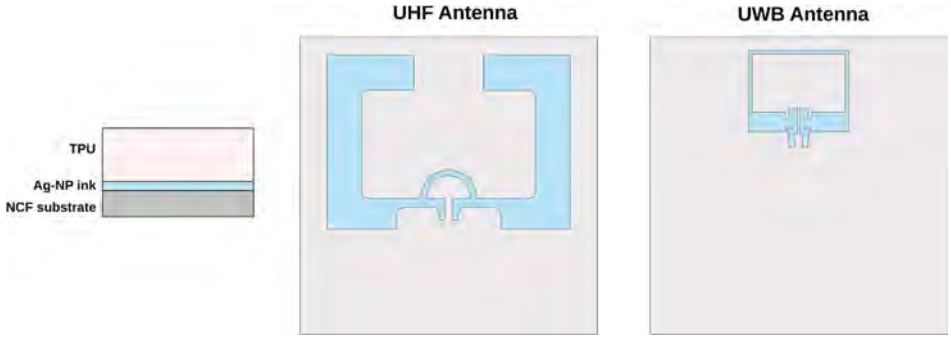

Figure VI.8. Cross section view of the in-molded antennas with different materials and image of the UHF and UWB antennas into a 70 mm x 70 mm area.

- *Simulation of UHF antenna (V2)*

The UHF antenna named V2 presented in this section builds upon the design developed previously on a PET substrate in Chapter IV. It is a modified dipole structure combined with a T-match structure to enhance impedance matching at 50 Ω. This type of design is quite practical and simple to design for applications requiring an antenna size on an area smaller than a half-wave dipole. In the simulations, both types of conductive inks, namely Ag-NP1 with good conductivity and Ag-NP3 with improved adhesion, are evaluated to estimate the potential decrease in antenna efficiency.

The feeding technique remains consistent, utilizing a U.FL connector that is electrically connected through vias on a 1 mm thick FR4 substrate, as depicted in Figure VI.9. Both in the simulations and during the manufacturing process, the electrical connection is established on the non-metallized side of the NCF substrate. As a reminder, the dielectric and electrical properties of the materials employed in the simulations are outlined in Table VI.6.

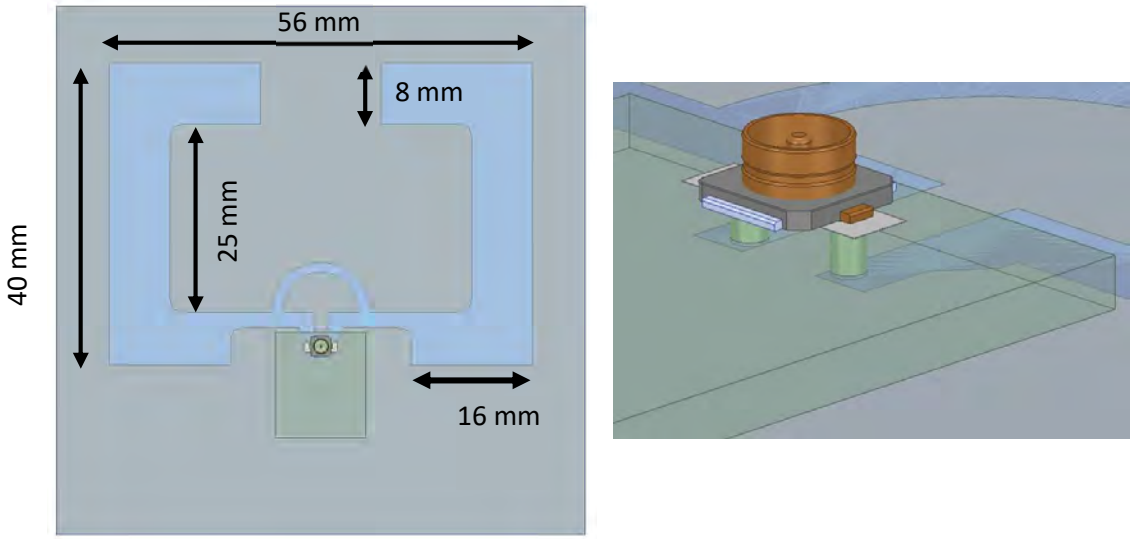

Figure VI.9. Geometry of the UHF Antenna_V2 with connector and rigid PCB.

Table VI.6. Summary of electrical and dielectric properties of materials defined in simulation.

	Dielectric constant	**Loss Tangent**	**Thickness (µm)**		**Resistivity (µΩ.cm)**	**Thickness (µm)**
NCF	4.4	0.15	60	Ag-NP1	5.5	2.3
TPU	2.57	2.51	1.25	Ag-NP3	21	2

In accordance with the manufacturing process from Eurecat, there are two options for encapsulation thickness: 1.25 mm and 1.5 mm. A simulation study was conducted to examine the impact of TPU thickness on the performance of the antenna using Ag-NP1 ink. As reported in Figure V.10 (a) **Error! Reference source not found.**, the results indicate that increasing the TPU thickness leads to an increase in the imaginary part of the antenna, as reflected in the equivalent effective permittivity, causing a shift in the resonance frequency. This effect is also noticeable in the losses induced by the material. The radiation efficiency of the antenna decreases with a thicker TPU substrate, as depicted in Figure V.10 (a). Hence, it is preferable to establish a plastic molding process with the thinnest possible TPU thickness, while considering its fragility.

Furthermore, a simulation was conducted to compare the antenna performance using a hypothetical scenario with a perfect silver ink having a resistivity of 1.59 µΩ.cm and the formulated silver nanoparticle inks (Ag-NP1 and Ag-NP3). Table VI.7 presents the results, indicating that even when using Ag-NP3 ink, the radiation efficiency of the antenna is not significantly affected.

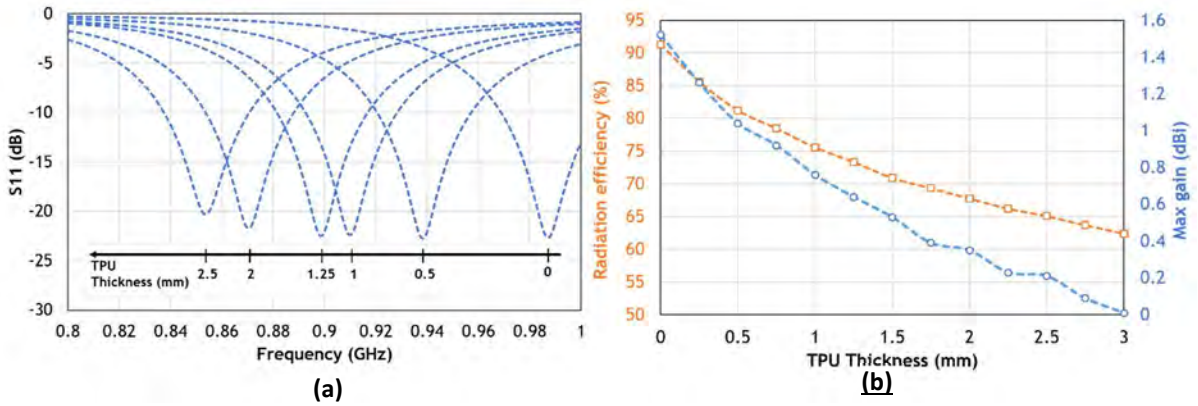

Figure VI.10. Simulation of the return loss for different the TPU thickness; (b) Simulated the radiation efficiency and maximum gain at each resonant frequency as a function of the TPU thickness.

Table VI.7.Radiative performance of the UHF Antenna_V2 for different silver inks

Ink name	Resonant Frequency f_0	Radiation efficiency	Maximum realized gain at f_0
Silver (1.59 µΩ.cm)	897.5	73.6 %	0.67 dBi
Ag-NP1	898.5 MHz	73.0 %	0.59 dBi
Ag-NP2	895.5 MHz	71.7 %	0.57 dBi

- *Simulation of UWB antenna_V2*

The UWB antenna presented in this part is based on the antenna developed on Polyimide substrate in appendix 3 . A 1.25 mm thick TPU layer is added to the top to optimize the antenna performance at the same time. At this stage of the simulation, the excitation is ensured with a lumped port between the pads and Ag-NP1 ink is used as a conductive ink. The PCB with the UFL connector were used once the optimized finished. Based on the previous studies, this UWB antenna is obtained from a rectangular loop with an electrical length equivalent to the full wavelength at the frequency of 4 GHz. Then, it was shown that the proximity of the feed pads ensured a capacitive coupling allowing to improve the bandwidth. As reported in the Figure VI.11, starting from the Ant1, this coupling is improved by adding small rectangles of 2.6 mm x 2 mm at the slot of the loop with the same gap of 0.56 mm. From Ant2 to Ant3, the matching is improved while not decreasing the bandwidth.

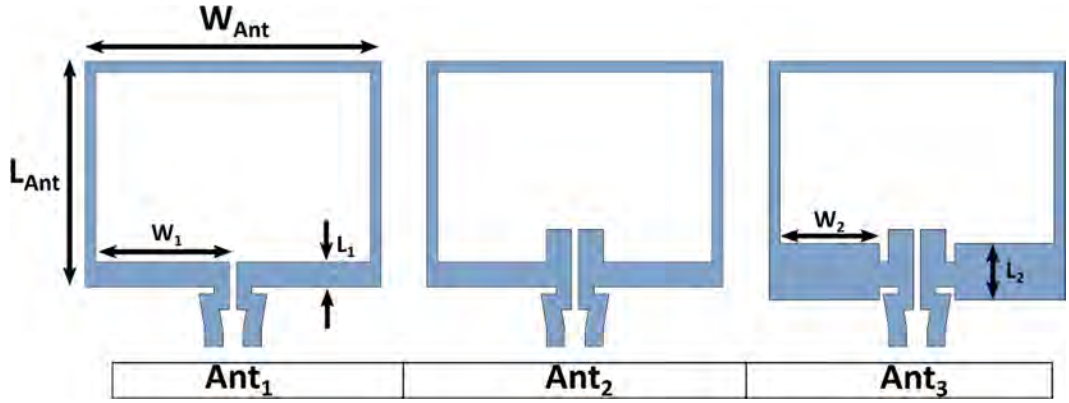

Figure VI.11. Design steps of the UWB antenna from Ant1 to Ant3: WAnt = 23.52 mm; LAnt = 18.96 mm; W1 = 12.64 mm; L1 = 1.96 mm; W2 = 7.926 mm; L2 = 4.5 mm.

The simulation results are presented in Figure VI.12. It is important to consider all the information provided for an accurate simulation. In Figure V.13 (a), we demonstrate the impact of ink thickness in the simulation. The sheet layer of Ant3 was converted into a solid by applying a thicker sheet. It is observed that with a thickness of 2.7 µm, the return loss is significantly affected due to the edge coupling effect of the antenna. Since our antenna relies on coupling for improved bandwidth and operates at higher frequencies, it is crucial to consider this effect through 3D modelling. The final designed antenna exhibits good matching within a bandwidth of 1.89 GHz (ranging from 3.12 GHz to 5 GHz), exceeding the requirements.

Furthermore, the simulation takes into account the addition of the PCB and connector for characterization, although the differences are not significant when simulating the same antenna (Ant3) with a 2 µm Ag-NP3 ink. The overall geometry of the antenna remains largely unchanged, maintaining a donut-shaped radiation pattern. However, for Ag-NP1 ink, the realized gain in the H-plane varies from +1.48 dBi at theta = 0° to a lower gain of +0.3 dBi at theta = 90°. Thus, we can expect to reach higher antenna radiation efficiency with the use of Ag-NP1 ink will result in a more efficient antenna.

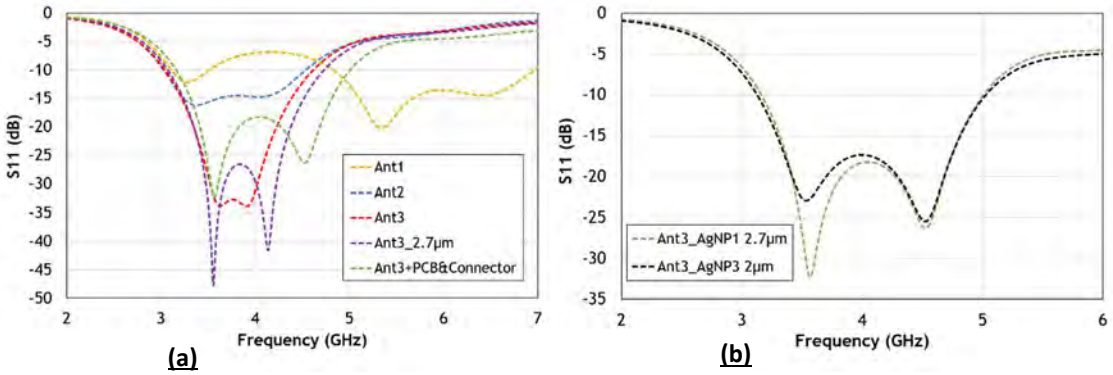

Figure VI.12. Simulation of the UWB antenna return loss: (a) Results from Ant1 to Ant3 and effect of the sheet thickness and hybridized PCB with connector; (b) Comparison between the silver conductive inks.

Table VI.8.Radiative performance of the UWB Antenna at 4 GHz for both silver nanoparticles inks

Ink name	Radiation efficiency	Maximum realized gain
Ag-NP1	81.3 %	1.97 dBi
Ag-NP2	76.9 %	1.78 dBi

- *Manufactured Antennas_V2*

The initial injection molding trials using TPU on NCF revealed limited adhesion and substrate fragility when subjected to bending. To address this issue, different materials were tested to ensure compatibility between the paper-based substrate and the plastic. ARJW and EUT conducted several steps, and it was found that using a TPU thickness of 1.25 mm prevented the appearance of cracks in the nanocellulose foil. However, the injection of TPU ECO resulted in the formation of bubbles between the printed Ag-NP3 layer and the NCF substrate. Consequently, alternative materials were explored to improve adhesion between the substrate and the plastic. One approach involved applying an NCF coating, which made the substrate rougher but compromised its transparency. Another material, Poly-Vinylidene Chloride (PVDC), provided a good moisture barrier but did not offer optimal TPU adhesion. PU (Polyurethane) showed promising results in terms of improved TPU adhesion and good moisture resistance, although the manufacturing process for this material is slightly more expensive. Preliminary tests also demonstrated the successful encapsulation of the electronic and rigid part (UGM) that was already hybridized on the substrate.

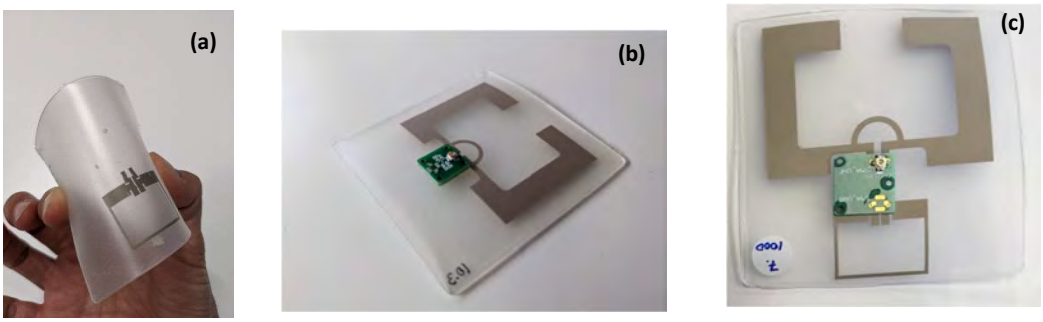

Figure VI.13. Photo of the in-molded antennas on TPU: (a) UWB antenna without connector in bent condition; (b) UHF antenna with PCB and hybridized connector; (c) UHF and UWB printed on the same 7 x 7 cm substrate.

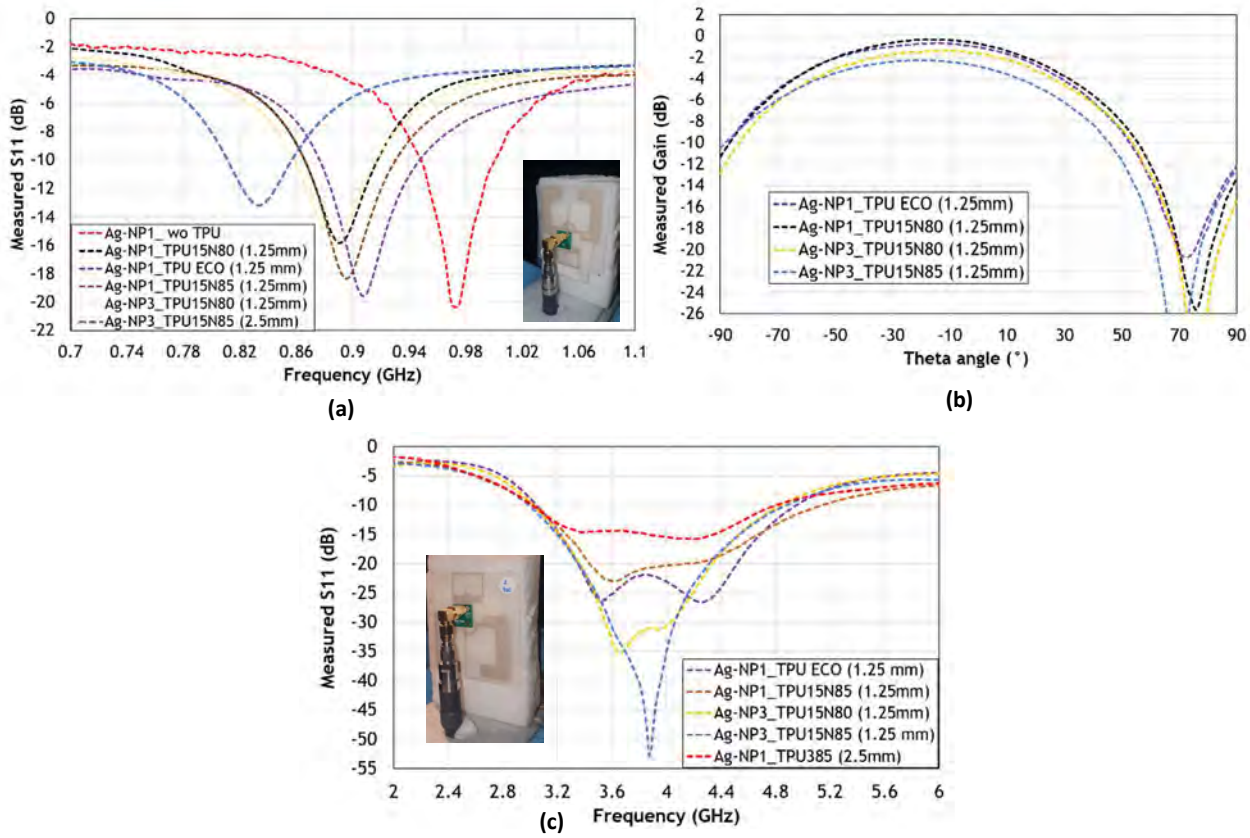

Figure VI.14. Experimental results of the return loss and gain of the in-molded antenna.: (a) & (b) UHF antenna; (c) UWB antenna.

The samples were manufactured by EUT using both Ag-NP inks (improved adhesion and high conductivity) and different TPU grades. For return loss (S_{11}) measurement, the antennas were placed on a rohacell substrate in an anechoic chamber. The experimental results, shown in Figure II.15 (a), match perfectly with the simulations conducted using the extracted TPU dielectric parameter. The UHF antenna exhibits resonance frequencies of approximately 840 MHz, 900 MHz, and 980 MHz for TPU thicknesses of 0 mm (wo), 1.25 mm, and 2.5 mm, respectively.

As predicted in the simulation, antennas manufactured with Ag-NP1 and Ag-NP3 inks show no significant differences in terms of impedance matching, but the choice of TPU grade can slightly affect the resonance frequency. Gain measurements were performed only on samples with a 1.25 mm TPU thickness. The gain at the frequency of 890 MHz in the Y-Z plane, or at Phi = 0°, is presented in Figure II.15.

The deviation in the radiation pattern is likely caused by the presence of the cable and the SMA adaptor in front of the antenna, as shown in the inset. However, the results are reasonably acceptable, with a maximum gain of approximately -0.3 dBi for the antenna with Ag-NP1 (better conductivity) and -1.4 dBi for Ag-NP2 (better adhesion). The results are not accurate enough to draw conclusions regarding the advantage of using a specific TPU grade in terms of antenna performance. However, the decision was made based on the TPU grade that exhibited better adherence to the NCF substrate.

The characterization of the UWB antenna samples reveals a good impedance matching within the frequency range of 3 GHz to 5.14 GHz (S11 ≤ -10 dB), which is roughly in line with the simulation results. Irrespective of the TPU grade and silver nanoparticles inks used, the bandwidth remains consistent, although the depth of the return loss may vary. However, at these higher frequencies, certain factors become more noticeable during measurements, such as the imperfect electrical connection of the connector to the antenna pads, the cable orientation relative to the antenna, and the accuracy of the VNA calibration. Unfortunately, it was not possible to measure the radiation performance of the UWB antennas due to unavailable samples and the inaccuracy of the measurements.

3.5. Complex conjugate antennas for the flexible geolocation tag

3.5.1. Antennas simulation for the final version of the flexible tag

The previous version of the battery-free geolocation module, as discussed in Chapter V, was optimized for extremely low power consumption. In this new version, the UGM has been designed with two differential inputs to enable energy harvesting capabilities. The energy harvester is based on a Greinacher doubler topology, which has been optimized for low-power density and is powered by a dedicated RF energy source operating in the Industrial Scientific Medical (ISM) frequency band at 868 MHz. The new UGM significantly reduces the energy requirements to approximately 5 - 10 µJ for a single UWB transmission. This reduction in power consumption has been achieved by minimizing the power requirements of the microcontroller, transmitter, and leakage current of the storage capacitor (60 µF). With a sensitivity of -27 dBm, a TAG-to-source distance of up to 30 meters can be easily achieved. Furthermore, by using appropriate technology, the capacitor voltage can be lowered, resulting in further power leakage reduction and increased gain. The harvester efficiency reaches 33%, delivering 1.3 µW. Additional details about the energy harvesting circuit can be found in the patent [170]. The UHF input impedance of the UGM has changed to approximately 24 + j·270 Ω for an RF input power of -27 dBm. This value was obtained using a coaxial RF Ground-Signal (GS) probe from Fairview Microwave [249]. The UWB part remains unchanged from the previous version, with an impedance of 25 + j·9 Ω.

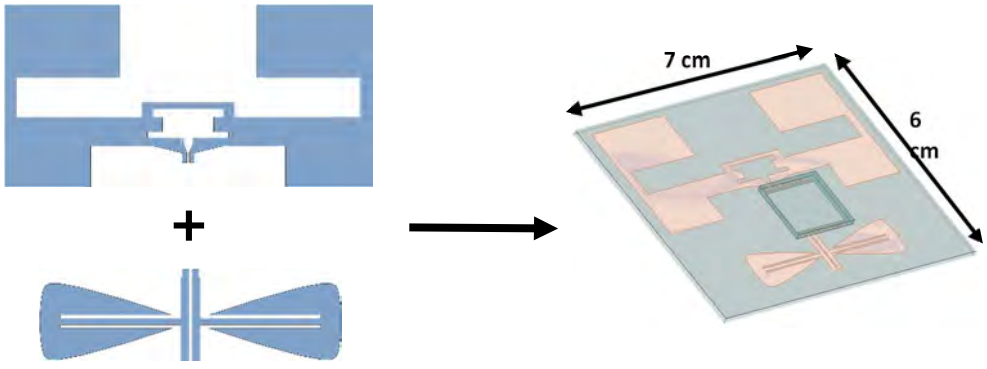

Figure VI.15. Final antennas design in complex conjugate impedance for the flexible geolocation tag.

The UHF antenna, previously designed for operation at 50 Ω impedance, has been modified to operate at a different input impedance. The updated version of the tag design, depicted in Figure VI.15, uses the bowtie antenna from Chapter V to achieve a more compact form. Through a co-design process involving all the elements, the antenna dimensions were adjusted for improved optimization. The simulation results, displayed in the Figure VI.16 (a), indicate that the UHF antenna exhibits a complex impedance that is relatively close to the targeted impedance. During the optimization process, the parameters were adjusted to ensure that the real part of the impedance remained within the desired range while maintaining an appropriate imaginary part.

The selected Ag NP-based ink does not significantly alter the impedance characteristics of the antenna, and the antenna still exhibits positive gain at Phi = 0°. However, the radiation efficiency is not particularly high due to various losses associated with the material properties and the coupling effects between antenna elements.

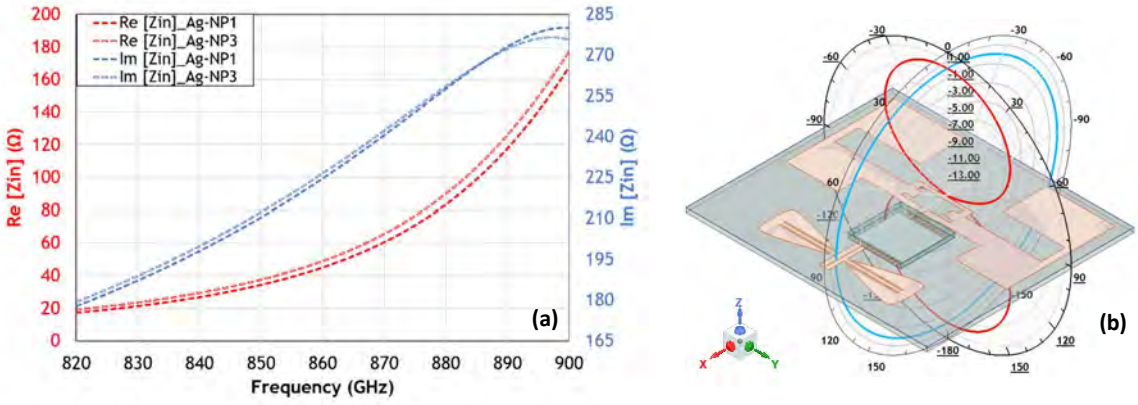

Figure VI.16. Simulation of the UHF Antenna: (a) Input impedance for both Ag NP-based inks; (b) Radiation pattern overlay of 3D view design at 868 MHz for Ag-NP1 ink.

Table VI.9. Summary of the UHF antennas parameters for both Ag NP-based inks.

Ink name	Input impedance (Ω)	Radiation efficiency	Maximum gain at Phi = 0°	Minimum gain at Phi = 0°
Ag-NP1	57 + j·237.28	66.94 %	+ 0.52 dBi	+ 0.25 dBi
Ag-NP3	60 + j·237.32	63.86 %	+ 0.33 dBi	+ 0.02 dBi

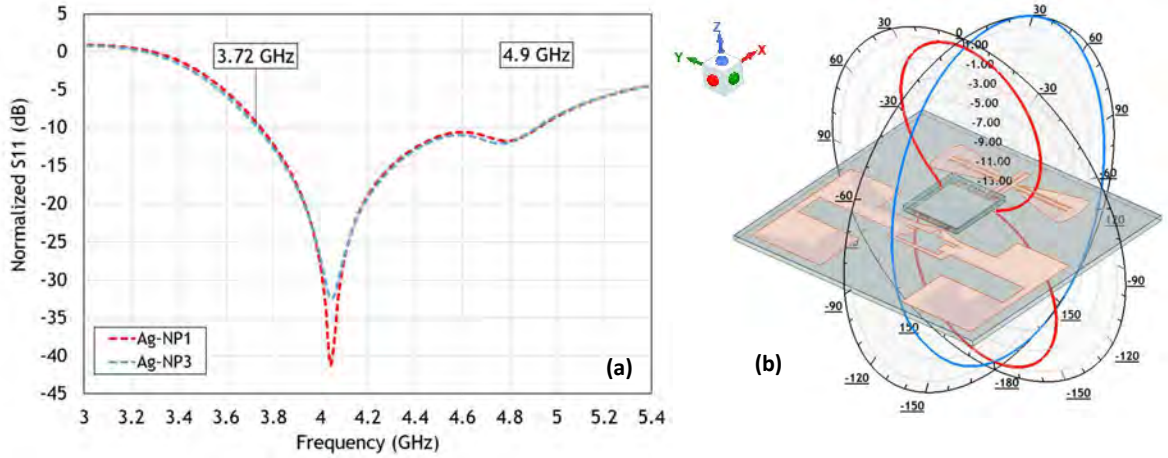

Figure VI.17. Simulation of the UWB bowtie antenna: (a) Normalized return loss for both Ag NP-based inks; (b) Radiation pattern overlay of 3D view design at 4 GHz with Ag-NP1 ink.

The UWB antenna has been tuned to achieve a match with the NCF substrate and the presence of the TPU material. The normalized return loss at the impedance of 25+j·9 Ω is shown in Figure VI.17 (a). It can be observed that the antenna meets the return loss criterion of -10 dB and is well matched between 3.72 GHz and 4.9 GHz, with a peak around 4 GHz. The results are roughly the same for both silver inks (Ag NP1 and Ag NP2). However, the antenna efficiency is relatively low, with a value of approximately 57%. The maximum gain achieved is around +1.9 dBi. It is worth noting that the bowtie antenna exhibits a more directive behaviour with the presence of the UHF antenna, as the UHF antenna behaves like a reflector in this configuration.

3.5.2. Fabrication of the flexible geolocation tag

A tag sample was first fabricated without the electronic components to validate the simulated complex conjugate impedance of the two antennas. Hybridized metal contacts were established at the pads of the antennas to facilitate the measurement using RF probes. To create the contact points, holes were carefully dug into the antenna pads, and conductive epoxy resin (EPO-TEK H20E) was filled in them to ensure electrical interconnection with the antennas. To prevent any damage to the substrates and plastic protection, the resin curing process was performed at a low temperature. EUT carried out the curing process at 90ºC for 1 hour before applying adhesive for mechanical contact.

An insert with dimensions of 70 mm x 70 mm x 1.25 mm, featuring a 4 mm thick housing for the UGM, was manufactured by EUT, as shown in Figure VI.18. After conducting several printing tests, the adhesion of the high-conductivity Ag-NP1 ink was improved to a rating of 4B with a PU coating on the NCF substrate. The measured layer resistivity of the PU coating was found to be 23 mΩ/sq. A TPU thickness of 1.25 mm was selected to ensure better adherence and flexibility of the entire encapsulated tag.

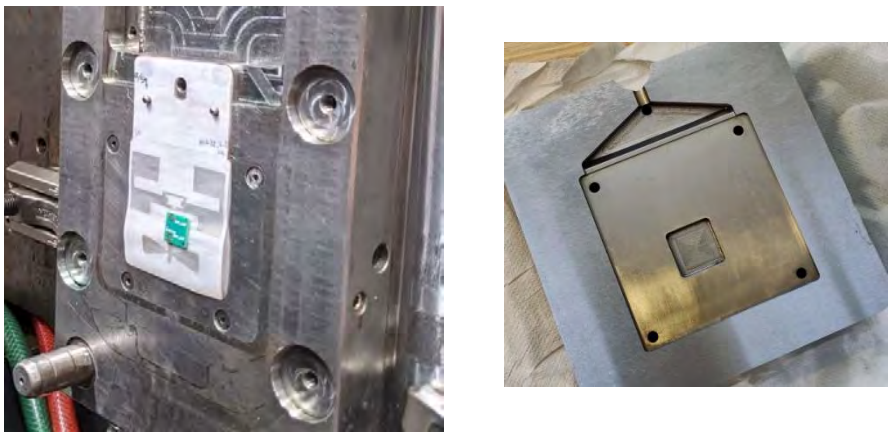

Figure VI.18. Manufactured insert: (a) Injection side; (b) Ejection side.

At the end of the process, after conducting numerous tests and optimizations, the overmoulded tags were successfully produced, as depicted in Figure VI.19. The final validation of the flexible geolocation beacon was planned to include measurements of UHF sensitivity by assessing the emission rate via the beacon under various orientations. Additionally, the maximum transmission range of the UWB signal emitted by the tag was intended to be measured. Furthermore, an evaluation of the tag geolocation coverage was meant to be conducted in preparation for marketing and wide-scale deployment to customers. Unfortunately, the desired results could not be obtained due to administrative issues at UWINLOC.

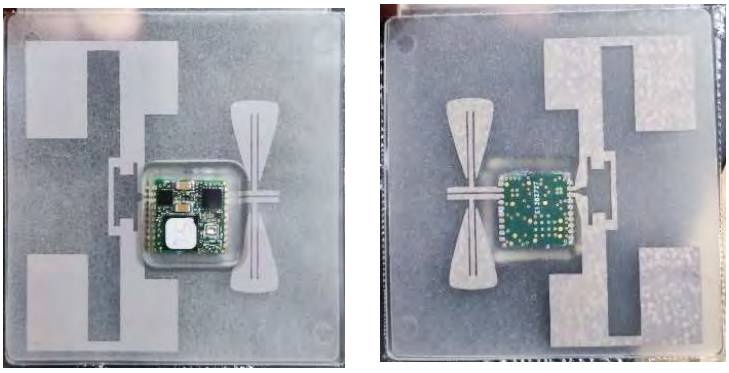

Figure VI.19. Front view (left) and back view (right) of the flexible geolocation tag on NCF injected with the UGM.

4. Conclusion

This chapter presents the manufacturing process of a flexible geolocation tag on advanced materials as part of the Madras project, with the goal of achieving large-scale production. The tag is designed to be flexible, durable, recyclable, mechanically robust, and to have excellent performance for energy harvesting and geolocation features. The focus is primarily on designing the antenna part of the tag, with careful consideration given to the choice of substrate and conductive ink.

The antennas developed in this project were designed on Nanocellulose foil, developed by AJRWG, which offers advantages such as recyclability, low weight, abundance, and high mechanical resistance, as studied in [249]. Printing the antennas requires customized inks that are also recyclable and possess good electrical properties. GNK has developed a silver nanoparticle ink with superior conductivity compared to silver nanowire ink. Two Ag NP-based inks were formulated, one with high conductivity and the other with an adhesion promoter.

The initial version of the UHF antenna, designed for 50 Ω impedance at 868 MHz for energy harvesting, was used to validate the properties of the materials and the manufacturing process conducted by project partners. The results demonstrated good performance in line with the simulations. To ensure reliability and mechanical resistance, an encapsulation technique with TPU material was investigated, which is commonly used in the field of in-mould electronics. The dielectric parameters were measured and incorporated into the simulation of new antenna designs with varying dimensions. The conductive Ag NP inks were specifically developed to be compatible with in-mould electronics.

An approach was proposed to improve the adhesion of TPU, address the fragility of the NCF upon bending, and enhance resistance to high relative humidity (RH) conditions in climate chambers. A second batch of UHF and UWB antennas was manufactured to validate the simulation results before proceeding to the final phase. For the functional demonstrator, antennas tailored to the input impedance of the UGM (Ubiquitous Green Mesh) module were designed, considering the same dielectric and electrical parameters of the materials. The overall tag fits within a 70 mm x 60 mm area with a TPU thickness of 1.25 mm.

For the final production, an Ag-NP1 ink with better conductivity can be used, thanks to the PU coating that ensures improved adhesion between the NCF and TPU. Due to time constraints, the functional tests could not be completed within the project timeline, which concludes in April 2023.

VII. Conclusion and Prospects

1. Conclusion

This manuscript resumes the various work carried out on the development of a RF wireless power transmission system for compact battery-free geolocation tags, as well as the development of battery-free wireless sensor node for structural health monitoring. The activities focused mainly on electromagnetic energy harvesting through a dedicated source or far field wireless power transmission.

A comprehensive review of the subject provided a global state-of-the-art understanding of battery-free devices and their significance in our increasingly interconnected world. The study revealed that several energy sources can effectively power these battery-free devices, and numerous research advancements have yielded promising results. Through an exploration of the history of wireless power transmission, different architectures were identified, tailored to specific specifications such as size, sensitivity, frequency, and required power levels. This knowledge served as a foundation for the subsequent research and development activities conducted in this study.

In the initial phase of the research, a rectenna (rectifying antenna) was proposed on a rigid substrate FR4 to convert electromagnetic waves at 868 MHz. The design objective was to achieve a high-power conversion efficiency (PCE) at low RF power levels and a smaller size compared to existing state-of-the-art designs. An innovative approach was taken to develop an electrically small antenna with a positive gain. By employing miniaturization techniques, the antenna's electrical length was preserved while reducing its overall dimensions in a 3D shape. Two versions of the antenna, namely A1_3D and A2_3D, were fabricated with dimensions of 52 mm x 32 mm x 10 mm and 40 mm x 30 mm x 10 mm, respectively. Both antennas exhibited a gain higher than +1 dBi. To maintain the compact size, a rectifier was cleverly integrated into the design, forming an electrically small rectenna. Each rectenna achieved a PCE of over 40% when illuminated with a power density of 1 µW/cm², using a non-optimum load of 10 kΩ. Notably, the proposed rectenna R1_3D outperformed existing designs, showcasing an ultra-compact size and excellent performance, with a PCE of 35% for -15 dBm RF power. These successful developments of the antenna (A1_3D) and the rectenna (R1_3D) served as foundational elements for the subsequent work on the battery-free sensor node, forming key components in its design.

In continuation of the research, the electrically small rectenna (R1_3D) developed, was used to wirelessly power a battery-free sensing node (BF-SN) designed to be embedded into concrete cavity.

It consists of developing “communicating materials” through the physical parameters monitoring. This aspect of the project is mainly the subject of another thesis conducted by a colleague within the laboratory [150]. Four prototypes of the BF-SN were developed, with two based on LoRaWAN technology and the other two using Bluetooth Low Energy (BLE) technology. The aim was to optimize the DC power harvested by the sensing node, to reduce the power consumption and one approach involved adding a reflector to the design to achieve a more directive antenna configuration. Furthermore, a cooperative prototype that combines BLE and Ultra-Wideband (UWB) technology was proposed. This design aimed to leverage the capabilities of both the geolocation and the physical parameters monitoring. Additionally, the efficient harvester integrated into the UWL module could be used to power the sensing node, ensuring a self-sustaining power supply.

The development of a geolocation tag for UWINLOC focused on achieving miniaturization and performance optimization while considering economical constraints, such as low manufacturing cost. Initially, the Ultra High Frequency (UHF) part of the energy harvesting feature was studied, with a specific emphasis on miniaturization using a flexible PET substrate. The flexible nature of the PET substrate allowed for reducing the antenna size by conforming to different shapes and surfaces. To further enhance the performance, a rectenna was co-designed and manufactured on the PET substrate. The rectenna combined the functions of the antenna and rectifier, enabling efficient energy harvesting. The performance of the rectenna, when integrated with the harvester part of the tag, demonstrated competitive and satisfactory results, paving the way for future advancements and achievements.

This first study led us to a global design of the tag considering the UWB part. The electronic part of the tag was miniaturized in a small 15 mm x 15 mm PCB module by UW and we only worked on the antenna part of the tag. New antenna designs (UHF and UWB) have been proposed. A first tag with compact antennas on a rigid substrate was not satisfactory due to the low radiation efficiency of the antenna for energy collection. Another solution was proposed to ensure miniaturization of the overall size of the tag with a semi-flexible substrate. However, the use of lumped components plays favorably on the complex conjugate impedance matching but unfavorably on the radiation efficiency. In order to compensate the losses, while keeping the conformability with a flexible substrate, a 3rd design was proposed on a polyimide substrate (that has fewer dielectric losses than those of FR4 and PET). On the other hand, this type of substrate has a certain purchase and manufacturing cost for a large-scale geo-locatable tag deployment.

For the miniaturization and performance optimization purposes, this initial study led us to the design of the full geolocation tag (including the Ultra-Wide Band part). The electronic component of the tag was miniaturized into a compact 15 mm x 15 mm PCB module by the company, while our focus was primarily on the antenna aspect of the tag. We proposed new antenna designs for both UHF and UWB frequencies. Initially, we attempted to develop a tag with compact antennas on a rigid substrate. However, the radiation efficiency of the antenna for energy harvesting was found to be insufficient. As an alternative, we proposed a semi-flexible substrate to achieve overall size reduction of the tag. However, the use of lumped components, although beneficial for achieving complex conjugate impedance matching, and the use of lossy substrate had a negative impact on the radiation efficiency. To address these challenges and maintain flexibility with the substrate, we proposed a third antenna design on a polyimide substrate. Polyimide offers lower dielectric losses compared to FR4 and PET substrates. The obtained tag on flexible Kapton substrate satisfied our technical requirements. However, it is important to note that this type of substrate incurs a certain cost for purchasing and manufacturing, which could be a consideration for large-scale deployment of geolocation tags.

Finally, through the Madras a low-cost alternative with advanced materials was proposed. The partners worked on the development of materials with interesting properties to low-cost alternative with advanced materials . The achievements were the result of several meetings between partners, and decisions on scientific, technical and economic aspects. The prototypes are presented from the specifications phase to the final phase of obtaining the tag on encapsulated NCF substrate. Unfortunately the timing did not allow us to reach the final phase of the project, but more details are available on the site of the Madras project [226].

In the final step through the MADRAS project, a low-cost alternative using advanced materials was proposed through the collaboration of 161European partners. Extensive work was done on the development of materials with desirable properties, including satisfactory electric and dielectric characteristics, good flexibility, and effective tag protection through encapsulation techniques.

The achievements made during the project were the result of numerous meetings and discussions among the partners, where decisions were made regarding scientific, technical, and economic aspects. Prototypes were developed and progressed from the initial specification phase to the final stage of obtaining the tag on an encapsulated Nanocellulose Foil (NCF) substrate. Although the project timeline did not allow for completion of the final phase, more detailed information about the project can be found on the Madras project website [226]. The website provides additional insights into the project's objectives, progress, and outcomes.

Other notable accomplishments include the publication of conference papers and journal articles highlighting the development of antennas/rectennas using a polyimide substrate, as well as a miniature drone antenna designed for airliner detection. These publications have contributed to the dissemination of knowledge and advancements in the field.

2. Prospects and feasibility

We have conducted studies on various antenna types to achieve miniaturization of the geolocation tag and rectennas for efficient harvesting of electromagnetic waves. In our designs, a trade-off is made between size and overall performance. While miniaturizing the antennas can result in a decrease in radiation efficiency (gain) and bandwidth, this is not critical for our specific use case within the narrow band ISM 865-868 MHz range. However, we can note that compact antennas with high gain can be achieved using unconventional substrates such as metamaterials. However, these substrates require complex manufacturing processes and come with a significant cost. Therefore, opting for flexible substrates allows us to meet both miniaturization and cost requirements, even if it means sacrificing RF performance to some extent. Additionally, as mentioned in the state of the art, there are several parameters that can be optimized to improve the efficiency of RF-DC conversion for wireless power transmission.

- *Antenna and rectenna gain :*

An antenna array can provide benefits such as increased antenna gain, allowing for energy harvesting at low power density levels or over longer distances. It can also offer a wider aperture area and higher aperture efficiency, enabling energy harvesting independently of the beam direction of the energy source, as demonstrated in *[250], [251]*. However, due to our miniaturization constraints, utilizing an antenna array is not suitable for our specific application. On the other hand, the use of a reflector plane can be employed to reduce the radiation pattern (in the case of a dipole antenna) and create a directional antenna.

This technique allows us to focus on the electromagnetic field and capture maximum RF power. While this approach has been successfully utilized for wirelessly powering battery-free sensing

nodes, it is not suitable for compact geolocation tag and small IoT devices due to the constraints of miniaturization.

- *Harvested dc power and sensitivity:*

The performance of the energy harvester and the output power are influenced by the architecture and components used in the design. Currently, Skyworks' Schottky diodes from the SMS7630 family are widely considered suitable for low-power applications. However, to further enhance the efficiency of the harvester and increase the output power, multistage rectifiers or CMOS charge pump designs, as demonstrated in *[252]–[254]* can be implemented.

Previous research has shown that the power conversion efficiency (PCE) and harvested power can be improved by optimizing the waveform of the transmitted signal. The performance of the rectifier or rectenna, due to their inherent non-linearity, is affected by the Peak-to-Average Power Ratio (PAPR) of the received signal *[255]–[258]*.

This technique has been explored in ongoing research while considering the maximum Effective Isotropic Radiated Power (EIRP) within the targeted frequency band, in accordance with FCC standards.

- *Multisource or multiband harvesting :*

In order to optimize the harvested DC power for powering active circuits, it is possible to explore energy harvesting from multiple power sources across a wide frequency range or multiple frequencies *[259]*. One approach is the use of a serially combined multiband rectenna array, which has been demonstrated to significantly increase the DC power output *[260]*

Preliminary work has been conducted on rectennas designed for dual-band operation, specifically targeting energy harvesting from waves in different Wi-Fi frequency bands (2.4 GHz and 5.2 GHz). This research incorporates a new double-sided dual-band bowtie antenna design and a triple-band rectifier, as depicted in Figure VII.1.

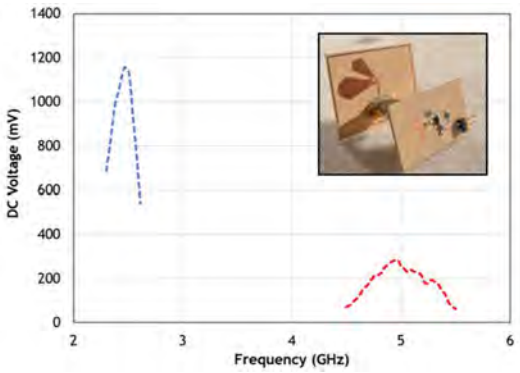

Figure VII.1. Dual -Band Rectenna : Measured harvested dc voltage of the rectenna across a 10 kΩ for an estimated received power of -2.2 dBm (low band) and -7 dBm (high band). The inset shows a photo of the prototyped rectenna.

VIII. Appendix

1. Schematic and Layout of the BLE-based SN : Prototype 1

1.1. Schematic of BSN1

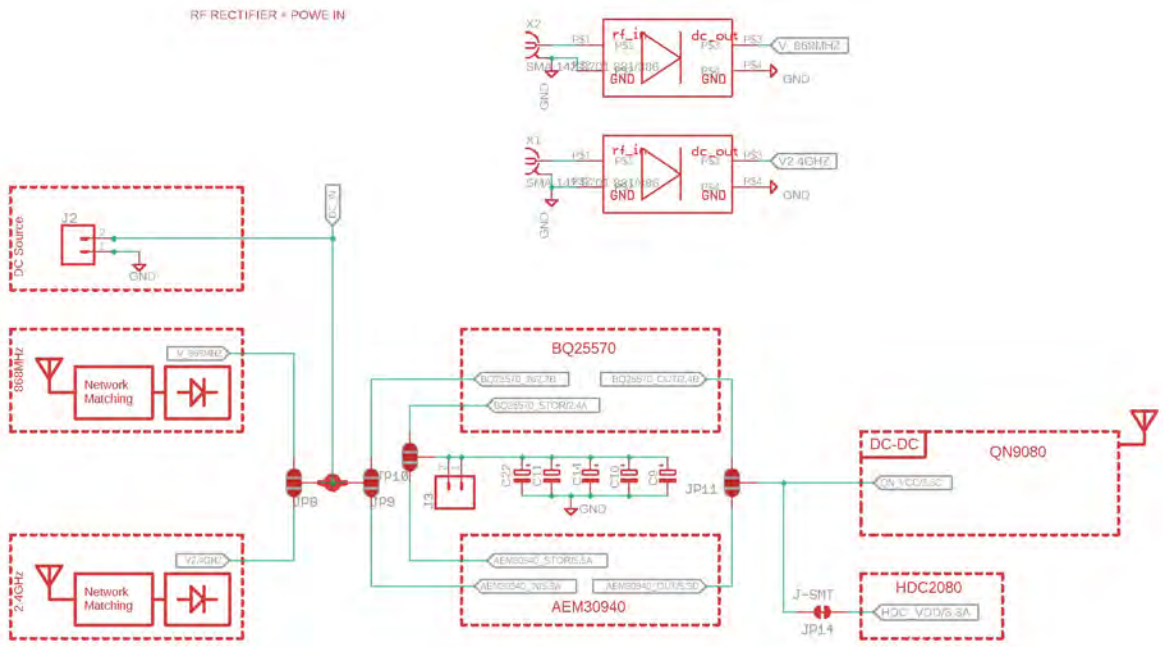

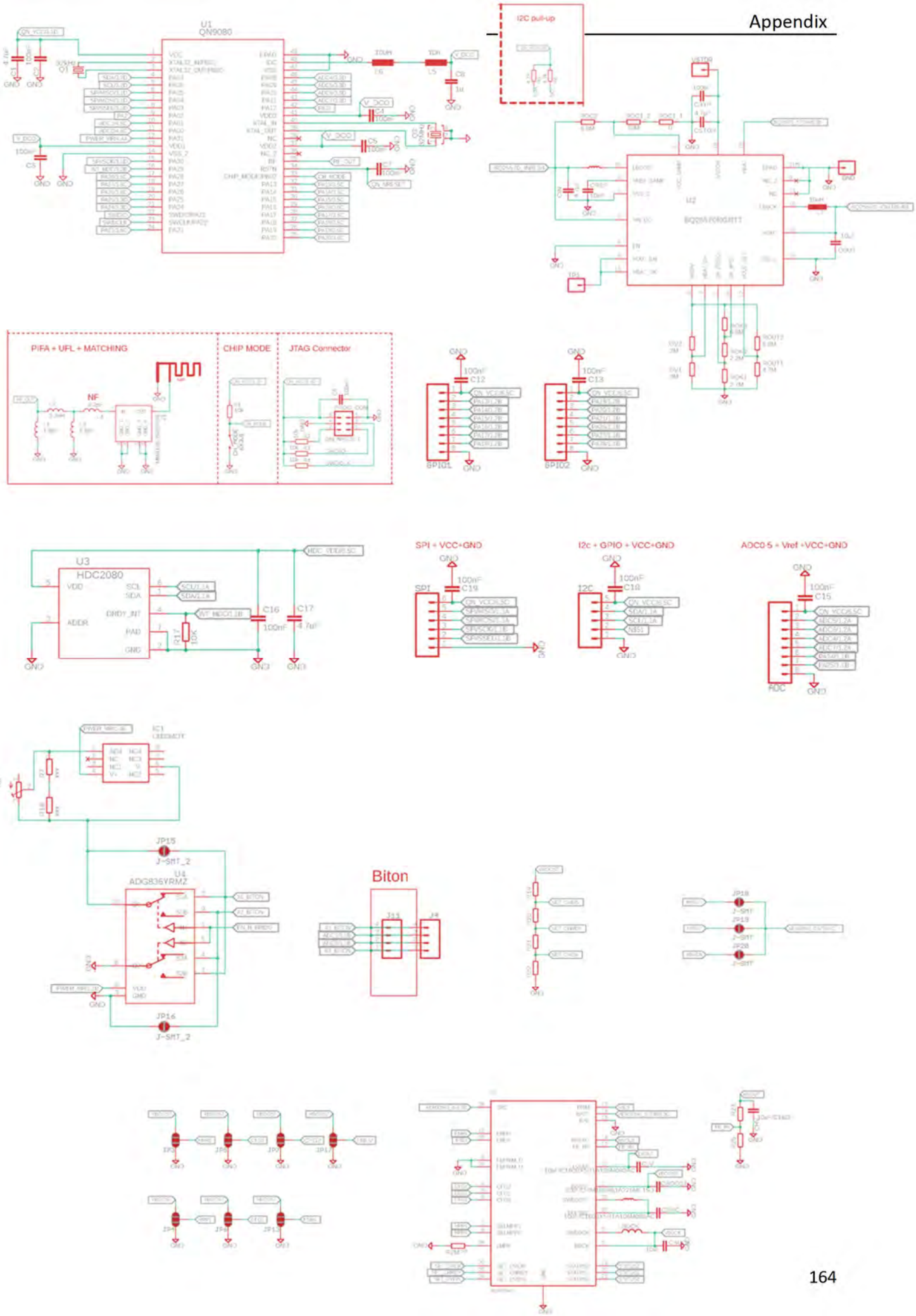
U1
QN9080
I2C pull-up
PIFA + UFL + MATCHING
CHIP MODE
JTAG Connector
U3
HDC2080
SPI + VCC+GND
I2c + GPIO + VCC+GND
ADC0.5 + Vref +VCC+GND
U4
ADG836YRMZ
Biton
JP15
JP16
J-SMT_2

1.2. Layout of BSN1

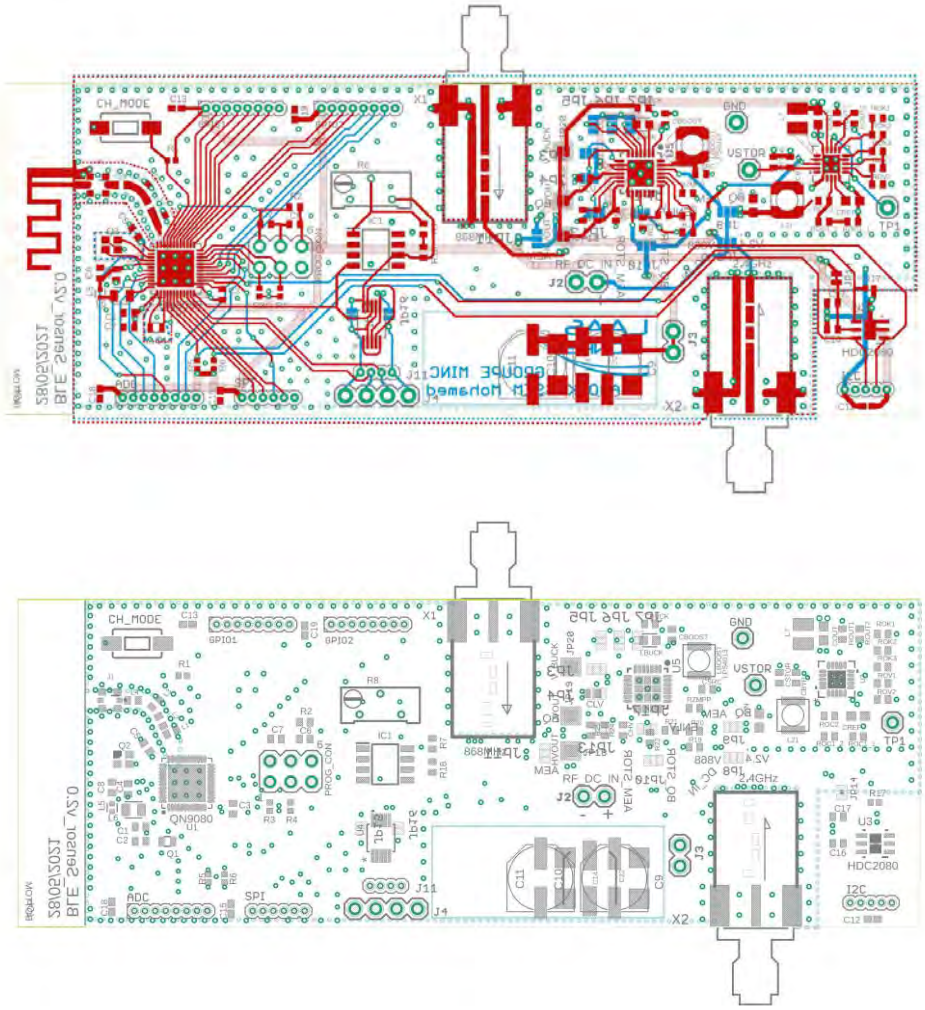

2. Schematic and Layout of the BLE-based SN : Prototype 2

2.1. Schematic of BNS2

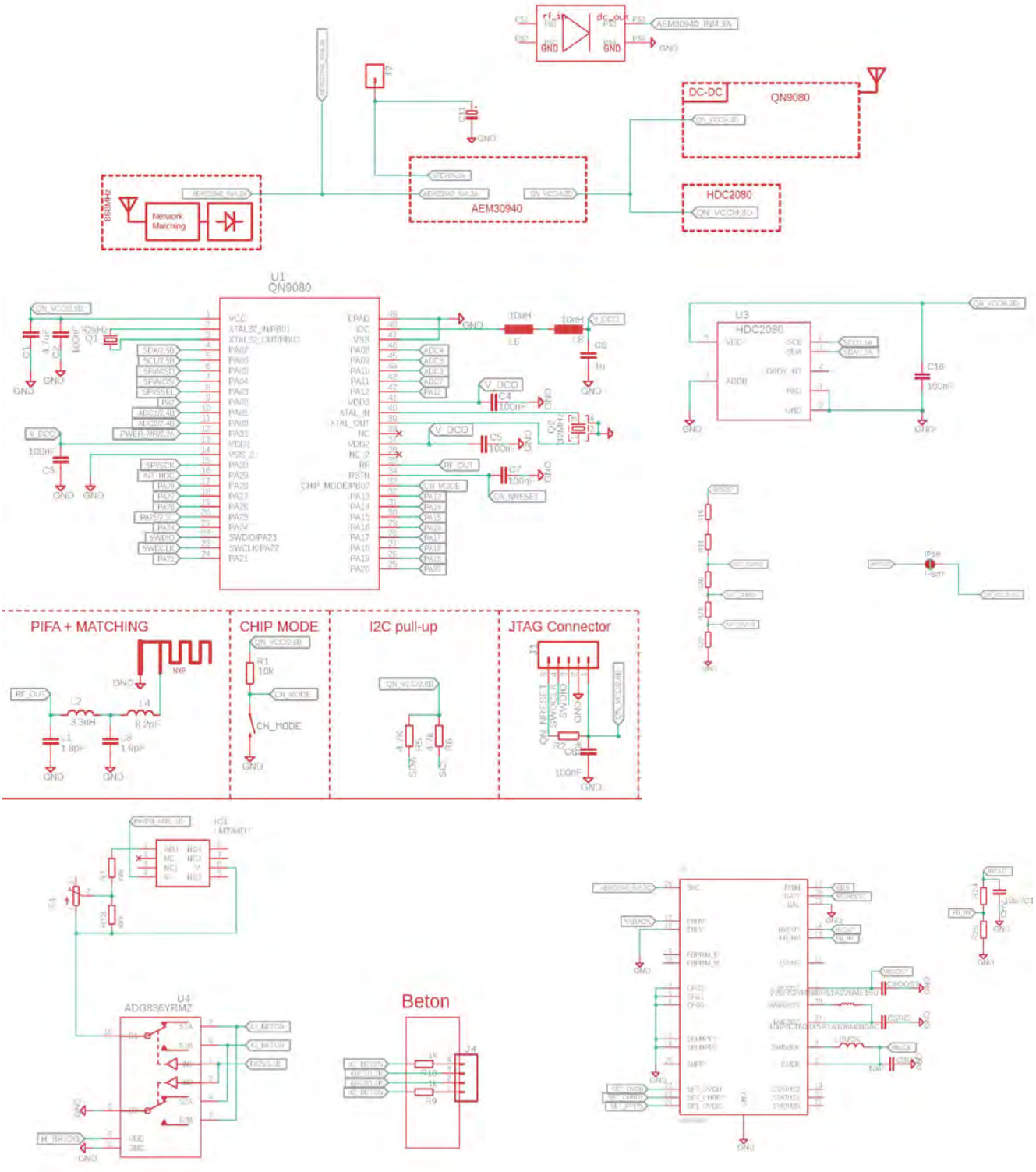

2.2. Layout of BSN2

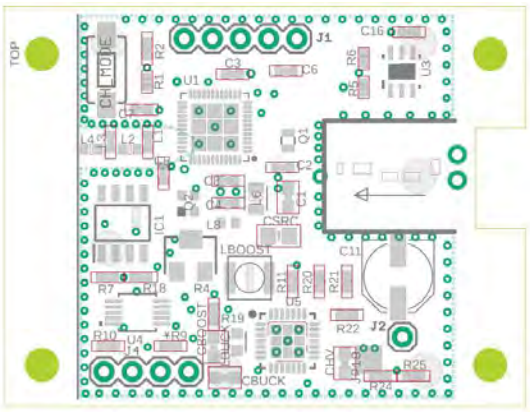

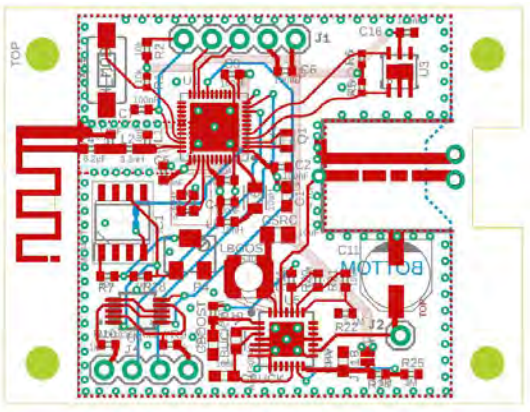

3. Exploitation of flexible Polyimide based material for antenna and rectenna design.

This appendix section showcases additional work conducted during the thesis years, focusing on antenna and rectenna designs implemented on a flexible substrate. The objective was to explore novel structures using substrates other than the conventional rigid substrates commonly employed. By using a flexible substrate, we could achieve miniaturization, significant weight reduction, and conformability, regardless of the shape of the object being mounted.

The designs presented in this section were implemented on a polyimide substrate with a thickness of 125 µm. This choice of substrate was based on its availability and familiarity with the manufacturing process within our laboratory. Furthermore, polyimide exhibits desirable properties for our work. Its high temperature resistance, in particular, enables convenient prototyping of circuits and facilitates characterization through hand soldering.

The polyimide substrate, also known by its commercial name Kapton (developed by DuPont), is a highly flexible and thin film made of polymer. It possesses excellent dielectric properties with a low loss tangent, surpassing those of paper and PET substrates. Moreover, it exhibits outstanding mechanical and thermal resistance, allowing it to be utilized in extreme conditions, including temperatures up to 400°C. Thanks to its reliable performance, the polyimide substrate finds extensive use across various industries for the development of flexible electronics. It is particularly well-suited for applications in demanding environments such as the automotive, aerospace, and space industries, where its resilience and durability are highly valued.

Table VIII.1. Comparison of commonly used flexible substrates for antenna design.

Substrates	ε_r (1 KHz)	tanδ (1 KHz)	Thickness	Prototyping complexity
Polyimide/ Kapton [261]	3.4 - 3.6 (HIGH)	0.0018-0.0026 (LOW)	7.5 µm-125 µm	Simple
PTFE/ Teflon [262]	2.1 - 2.5 (LOW)	0.0002-0.0025 (LOW)	1.5mm-6 mm	Complex
PET/ Melinex 506 [263]	2.9 - 3.0 (Medium)	0.002 (LOW)	35 µm-175 µm	Moderate
PDMS [264]	2.76 - 3.8 (HIGH)	0.015-0.02 (Medium)	-	Complex
PEN [265]	2.9 - 3.2 (HIGH)	0.0048 (LOW)	12µm - 250 µm	Moderate
Paper [238], [266]	3-5 (HIGH)	0.05-0.13 (HIGH)	50 µm - 250 µm	Moderate

When compared to other commonly used substrates for antenna design (as shown in Table VIII.1), polyimide emerges as the substrate that offers a better compromise between low dielectric losses and ease of prototyping. In our specific use case, which involves antenna and rectifier design, it is crucial to accurately characterize the substrate to ensure precise simulation results. The dielectric properties of the polyimide substrate have been extensively studied in a previous thesis conducted by our research team in the laboratory, providing us with a comprehensive understanding of its behavior.

We present two designs that have garnered attention and were the subject of articles at the EuCAP conference. These designs leverage the unique advantages offered by the polyimide substrate, highlighting our advancements and innovations in the field of antenna and rectifier design.

- *A Novel Polyimide Flexible Antenna Design for S-Band Applications*
- *A Dual-Band and Flexible CPW-Fed Antenna for RF Energy Harvesting Applications*

A Novel Polyimide Flexible Antenna Design for S-Band Applications

Alassane Sidibe[1,2], Alexandru Takacs[1], Daniela Dragomirescu[1], Samuel Charlot[1] , Jan Mennekens[2]
[1] LAAS-CNRS, Université de Toulouse, CNRS, INSA, UPS, Toulouse, France, alassane.sidibe@laas.fr, alexandru.takacs@laas.fr, daniela.dragomirescu@laas.fr, samuel.charlot@laas.fr
[2] Uwinloc, Toulouse, France, alassane.sidibe@uwinloc.com, jan@uwinloc.com

***Abstract*— The technological advances in electronic devices and the Internet of Things bring us to be surrounded by multiple sensors in the coming years. These devices should be conformable and adapted to small or irregular shapes and surfaces. This is why flexible materials are becoming important in this field thanks to their lightness, stretchability and robustness especially in wearable electronics to get integrated on clothes for biomonitoring. Our proposal in this paper concerns the design, printing process, and performance of a novel antenna on a polyimide flexible substrate. It is based on a loop antenna and has dimensions of 40 mm × 35 mm × 0.127 mm. Its very wideband behavior from 2.4 GHz to 4 GHz allows targeting S-Band applications such as LTE and Wi-Fi. Interesting performances are also achieved in terms of radiation patterns. At 2.45 GHz, the maximum antenna gain is about +2.6 dBi with an omnidirectional pattern but at higher frequencies, the antenna is more directive with a higher gain.**

***Index Terms*—Flexible antenna, polyimide, wideband, flexible electronic devices, S-Band, wireless applications.**

I. INTRODUCTION

Faced with the new demand on thermal, moisture and, water resistance devices and on new applications such as medical, wearable, mobile, aerospace, and retail, the rigid Printed Circuit Board (PCB) made of conventional materials is being limited. Electronic devices tend to be more flexible, stretchable, foldable, and recyclable by using non-conventional materials. The new generation of consumer electronics products aims to cover several markets and are motivated by using flexible electronics. The use of alternative substrates also allows the development of smart wearable devices for sensing and communication applications. In addition, in the context of the Internet of Things (IoT), recent developments in printed electronics demonstrate the ability to use organic and inorganic materials allowing a new form factor, a high-volume manufacturing, and a huge deployment [1]. Research is also being carried out on flexible microfluidics, which has an impact on the chemistry, electronics, biology, and medicine areas [2]. Wireless communicating devices require the use of an antenna to transmit and receive the data wirelessly. Depending on the frequency range, flexible material can be used for a large application. In [3], a review of many flexible antennas in different material types and applications is presented. For instance, at Microwaves Frequencies, a 60 GHz patch antenna is designed and fabricated with Kapton substrate in [4]. However, the use of a flexible antenna is more relevant when operating in the low frequency range with a large radiative surface. The flexibility allows the sheet to be bent into different geometries and to have a smaller final antenna.

The proposed design of the antenna is based on polyimide substrate for S-band applications. The S-Band is a part of the electromagnetic spectrum from 2 to 4 GHz. It is mainly used for mobile Long-Term Evolution (LTE) and Wireless Fidelity (Wi-Fi) applications, and for several practical radar applications, as well as for the communication between satellites. This band also covers 5G Sub-6GHz (3-4 GHz band) which is intended to connect devices to each other.

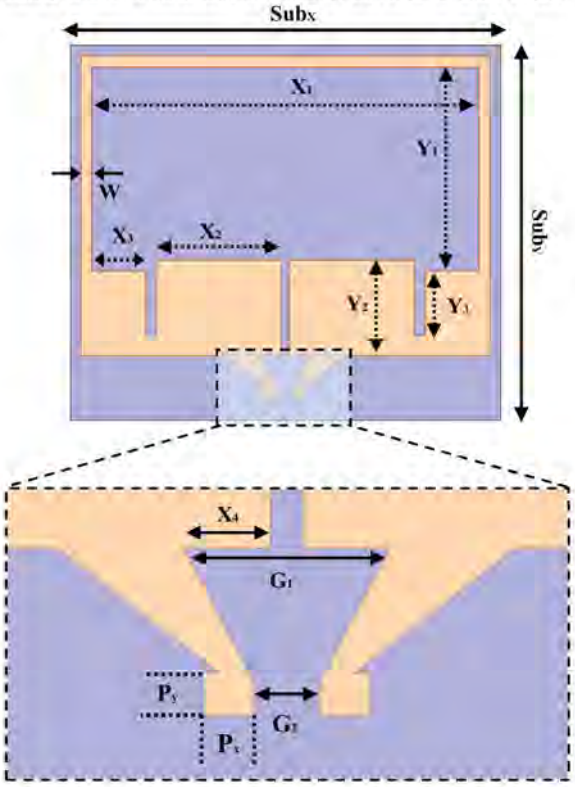

Fig. 1. Layout and main dimensions of the proposed antenna and the feed pad (metallization is represented by gold color)

TABLE 1. DIMENSIONS OF THE PROPOSED ANTENNA

Dimensions (mm)												
SubX	*SubY*	*X1*	*X2*	*X3*	*Y1*	*Y2*	*Y3*	*W*	*Px*	*Py*	*G1*	*G2*
40	35	36	11.6	5	19	9	6	1	1.2	1	5	1.5

This paper focuses first on the presentation of flexible materials and their characteristics, and then in a second part the design of the proposed antenna, optimized for S-Band applications, is presented. The last part of this paper is devoted to the fabrication process and characterization of the flexible antenna.

II. FLEXIBLE SUBSTRATE MATERIAL

The replacement of conventional rigid substrates has facilitated the development and improvement of several flexible materials with different properties. These can offer several advantages such as flexibility, stretchability, compactness, moisture resistance, low cost. Flexible materials can be separated in categories: synthetic and natural polymers, paper, and textile materials. There are several polymer materials: polydimethylsiloxane (PDMS), liquid crystal polymer (LCP), Parylene, polyethylene naphtalate (PEN), Polyethylene terephthalate (PET), and Polyimide (PI). They are considered as the best candidate for flexible antenna design [3]. Paper substrates also offer advantages such as printability with an easy printing technique, and recyclability. In addition, scientists have been working on flexible electronic devices based on nanocellulose [5]. The first flexible design started with polyimide material. Due to its good Radiofrequency (RF) performance and heat resistance, it is mostly used for wireless applications using an antenna. In [6], a novel multiband monopole CPW antenna is proposed. In some applications, the substrate should be carefully chosen considering its dielectric parameters, the environment resistance and the fabrication process.

III. ANTENNA DESIGN AND SIMULATION

The proposed antenna in this paper is a novel design based on a loop antenna, modified to increase the bandwidth and efficiency for the S-band frequencies range. The simulation was performed by Ansys HFSS software on polyimide substrate (dielectric constant = 3.4; loss tangent = 0.012; thickness = 127 µm; copper thickness = 35 µm). The geometry and dimensions of the proposed antenna are presented in Fig.1 and Table 1. It is based on a full-wave loop antenna approximately at 2.5 GHz with a width of 1 mm as presented in Fig. 2 (A1). Then, a feeding pad was carefully designed to characterize the antenna easily and carefully with a soldered SMD connector in Fig 2 (A2). Thus, a U. FL connector from Hirose [7] was chosen but may have limitations above 6 GHz. In the same step, the width Y_2 was adjusted to optimize the return loss and bandwidth. As seen in Fig. 3, the A2 antenna with Y_2 equals to 3 mm, has three resonant frequencies spaced approximately by 2 GHz from each other (@f1 = 2.5 GHz, @f2 = 4.4 GHz, and @f3 = 6.7 GHz.

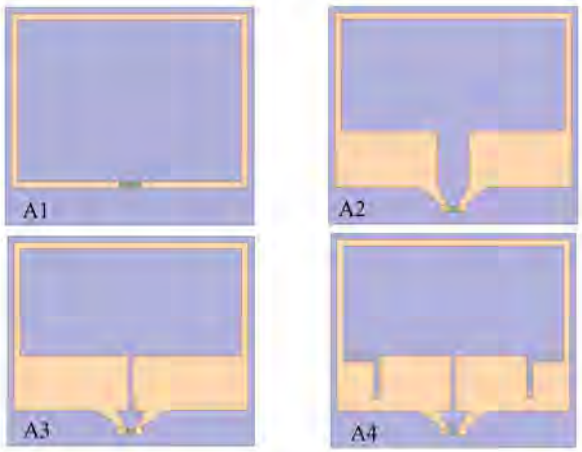

Fig. 2. Antenna design evolution (green rectangle is the lumped port on simulation).

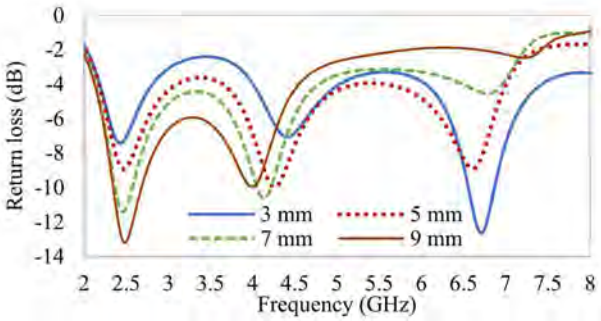

Fig. 3. Simulated return loss of antenna A2 with different Y_2 values.

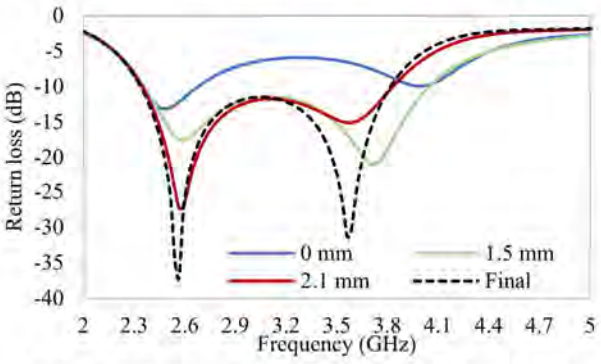

Fig. 4. Simulated return loss of antenna A3 with different X_4 values.

By increasing Y2, the total real part of the antenna decreases and the imaginary part increases at a higher frequency (around @f3), thus improving the bandwidth of the antenna between @f1 and @f2. The second step of the optimization is to decrease the real part of the impedance again achieve a good matching at 50 ohms (S11 ≤ -10 dB). It is presented on A3 by tuning the X_4 parameter. Reducing this parameter tends to decrease the real part of the impedance (at 3 GHz it goes from 134 Ω to 76 Ω) and make @f2 at 3.55 GHz, first located at 4 GHz (Fig.4).

At the last step, the return loss is optimized by adding an inverted L slot (1mm width) at the inner corner of the antenna as presented in Fig.2 (A4). Thus, it can be observed that in Fig.4, the increase of the peak resonance at 2.55 GHz and 3.5 GHz.

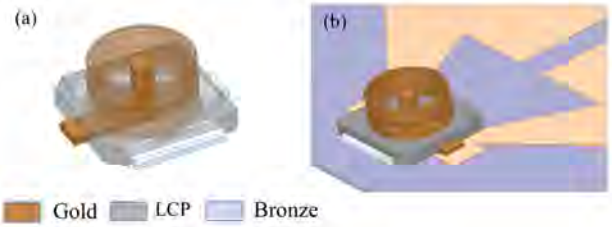

Fig. 5. (a) 3D model of the U.FL connector and materials assignement, LCP (Liquid Crystal Polymer) ; (b) Connector placement on the antenna feed pad.

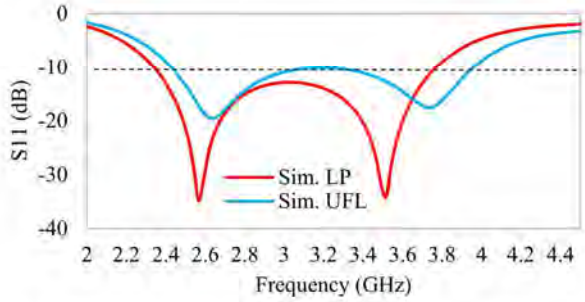

Fig. 6. Simulated antenna return loss with the U.FL connector model and LP (Lumped Port without connector).

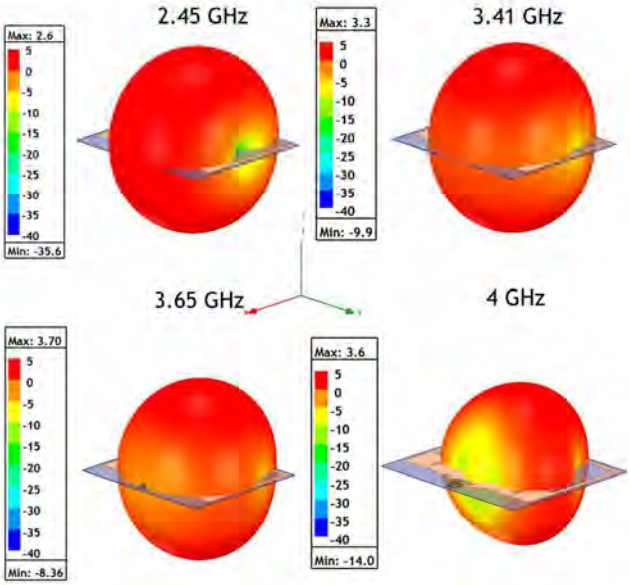

Fig. 7. 3D radiation pattern simulation of the realized gain of the proposed antenna at different frequencies.

An accurate simulation must include the effect of the used connector for measurement. The U. FL 3D model is shown in Fig.5. It consists of a Liquid Crystal Polymer (LCP) housing and gold-plated brass contacts. In the simulation performed, the larger pads constituting the ground were affected as the bronze part. A comparison of the return loss (S11 in dB) between the excitation with lumped port assigned to an rectangle between pads and the excitation thanks to the connector, is shown in Fig.6. Despite the effect of the connector as expected, the antenna remains matched for 50 Ω but the return loss is slightly shifted of 100 MHz. The antenna has a very wide bandwidth from 2.3 GHz to 4 GHz for S11 ≤ -10 dB. Fig.7 presents the simulated 3D radiation patterns for the proposed antenna. At 2.45 GHz, the antenna radiates as an omnidirectional antenna and is more directive at high frequency. It is noticed that the antenna radiation pattern is more oriented on the YZ plane with an improvement gain.

IV. Printed Antenna Prototype

A. Printing processing of the flexible antenna

Various printing processes on flexible material exist. They can be separated into two categories: subtractive (Laser ablation, dry or wet etch) and Additive (photolithography, flexography, inkjet, and screen-printing). Each process is specific in terms of ink thickness and adhesion on substrate, printing resolution, mass production, etc. The photolithography technic was the one be used for the antenna printing process as seen in Fig 9. The sheet used is 127 µm thick polyimide film coated on both sides with 35 µm thick copper (AP9151) [8]. It is cut to size with a cutter and then covered with a 1 µm thick ECI photosensitive resin. The resin is first annealed on a hot plate at 90°C for 60 s. The sheet with the resin is UV exposed through a glass mask with the desired pattern. The sheet is then annealed on a 110°C hot plate for 60 s, and some areas of the resin are dissolved in a developing solution to reveal the copper. The remaining resin hides the copper parts corresponding to the desired structures. The foil is then immersed in an acid bath to etch the copper that is not protected by the resin. Once the copper is etched, the foil is rinsed with water. The resin is then removed with acetone, rinsed with water and dry with nitrogen (N2). This leaves the polyimide and some copper depending on the desired shape. The photo of the obtained antenna after the process is presented in Fig. 8.

Fig. 8. Photo of the manufactured antenna in cleanroom and with U.FL connector and SMA adaptator mounted.

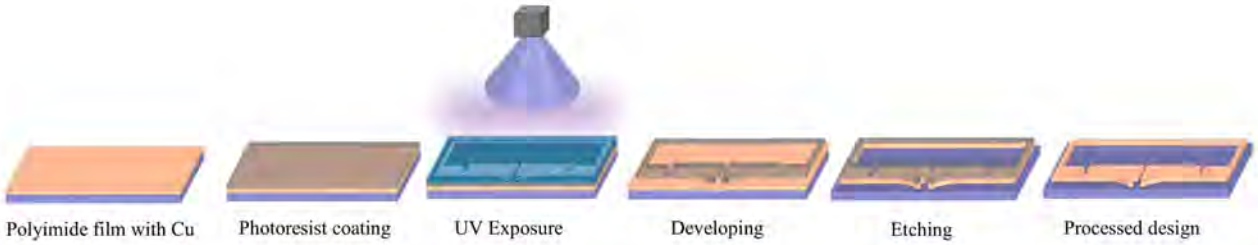

Fig. 9. Schematic representation of the photolithographic process.

B. *Antenna Characterization: Results and Discussion*

The performance of the antenna is tested in flat position. To perform the characterization accurately, the antenna was fixed on a flat Rohacell (with a dielectric constant around 1.03) surface, and the connector soldered at the feeding pad as located in Fig. 5 (b). An U. FL to SMA adapter is plugged to allow measurement with the Vector Network Analyzer (VNA). It can be noted that the measurement with the U. FL connector fits very well with the simulation. The same bandwidth from 2.3 GHz to 3.8 GHz is obtained as expected (Fig.10).

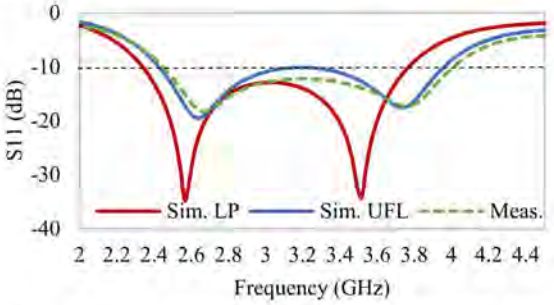

Fig. 10. Comparison of the simulated and measured return loss of the printing antenna.

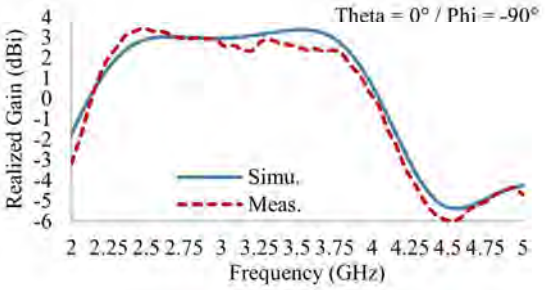

Fig. 11. Comparison between measured and simulated Realized Gain as function of the frequency on the E-plane.

In addition, the radiation pattern measurement is performed in an anechoic chamber (by using the far-field antenna measurement facilities existing at LAAS-CNRS) and was carried out in the E-plane where the antenna under test is rotated in the azimuth plane. In Fig.11, a good agreement between simulation and measurement of the gain as a function of the frequency is obtained.

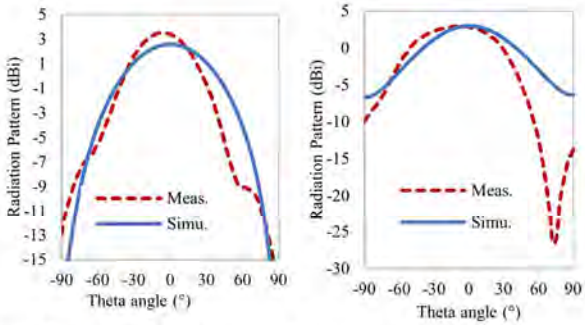

Fig. 12. Comparison of the measured and simulated radiation pattern in the E-plane (Phi = -90°) at 2.45 GHz (left) and 3.41 GHz (right).

It can be observed that the maximum gain on the E-plane stays around +3 dBi in the bandwidth matched 50 Ω (S11≤-10 dB). The simulation performed at 2.45 GHz for the radiation pattern at 2.45 GHz is equal to the measurement of the E-plane. However, the measurement and simulation at higher frequency (3.41 GHz) have the same maximum but the radiation pattern is modified as a function of the theta angle. This difference can probably be justified by the measurement uncertainty at higher frequency.

V. CONCLUSION

Flexible antennas take an important part in wireless devices and allow a great freedom in the design and operation of the target application while rigid PCB antennas are limited. In this paper, is proposed a novel antenna design that offers a very wide bandwidth. In the literature, such ultra-wide band antenna are most often designed with a Coplanar Waveguide (CPW) fed technique, as presented in Table 2. Our proposal consists of a modified loop antenna covering a very large bandwidth from 2.45 GHz to 4 GHz. This antenna may offer the possibility to be used for LTE, Wireless Local Area Network (WLAN) applications as well as for Wi-Fi and 5G Sub-6GHz (3.4 GHz to 3.8 GHz) mobile networks. The radiative behaviour at a higher frequency can be useful when transmitting or receiving the signal in a specific direction where the antenna radiates especially in certain directions. In conclusion, the proposed antenna of flexible polyimide substrate is a novel design and offers a good trade-off between bandwidth, compactness, and gain as compared with the state of the art.

TABLE 2. COMPARISON WITH THE STATE OF THE ART.

Ref.	Type	Substrate // Conductive ink	Process	Bandwidth & Frequency	Gain (dBi)	Dimensions
[9]	CPW Monopole	Kapton // Silver	Inkjet	54.4 % (1.2 GHz) / 14 % (2 GHz) / 23.5 % (2.6 GHz / 17.2 % (3.4 GHz)	-1.2 / + 0.6 / + 2.1	70×20×0.11 mm^3
[10]	Loop	Polyimide // Copper	Chemical Etching	BW 35MHz at 2.45 GHz	--	55×50×0.05 mm^3
[11]	CPW Monopole	Paper // Silver	Inkjet	2 - 10 GHz	-0.92 (2.45 GHz) / +1.52 (5.5 GHz)	50×28×0.254 mm^3
[12]	Microstrip Patch	SU-8/PDMS // Copper	Photo.	6.2 - 6.4 GHz	+2.17	46.4×20×0.5 mm^3
[13]	Inverted F-shaped monopole	Kapton // Silver	--	2.4 - 5 GHz / 3 GHz	+1.5	25×32×0.125 mm^3
[14]	CPW-fed T-shaped patch	PET // Silver	Inkjet	26 - 40 GHz 42 % (33 GHz)	+4.35 (27GHz) / +7.44 (39GHz)	16×16×0.135 mm^3
This work	Modified loop	Polyimide / Copper	Photo.	2.45 - 4 GHz 48% (3.225 GHz)	+2.6 (2.45 GHz) / +3.3 (3.41 GHz)	40×35×0.127 mm^3

ACKNOWLEDGMENT

The authors acknowledge the French technological Network RENATECH through the LAAS-CNRS cleanroom for its support. We acknowledge UWINLOC Company and the support of the French region OCCITANIE through the research project OPTENLOC. The works were also supported by the French National Research Agency (ANR) through the McBIM Project (Communicating Material at the disposal of the Building Information Modelling), under Grant ANR-17-CE10-0014.

REFERENCES

[1] Wiklund, Jenny, Alp Karakoç, Toni Palko, Hüseyin Yiğitler, Kalle Ruttik, Riku Jäntti, and Jouni Paltakari, "A Review on Printed Electronics: Fabrication Methods, Inks, Substrates, Applications and Environmental Impacts," Journal of Manufacturing and Materials Processing 5, 89, 2021.

[2] Fallahi H, Zhang J, Phan HP, Nguyen NT, "Flexible Microfluidics: Fundamentals, Recent Developments and Applications," Micromachines (Basel) 10(12):830, 2019.

[3] Kirtania, Sharadindu G., Alan W. Elger, Md. R. Hasan, Anna Wisniewska, Karthik Sekhar, Tutku Karacolak, and Praveen K. Sekhar, "Flexible Antennas: A Review," Micromachines 11, no. 9:847, 2020.

[4] Z. Yang, A. Takacs, S. Charlot and D. Dragomirescu, "Design of Kapton based passive circuits at microwave frequencies," 2015 European Microwave Conference (EuMC), 2015, pp. 873-876.

[5] Use of nanocellulose in printed electronics: a review, Hoeng et al. - Nanoscale, 2016.

[6] S. Ahmed, F. A. Tahir, A. Shamim and H. M. Cheema, "A Compact Kapton-Based Inkjet-Printed Multiband Antenna for Flexible Wireless Devices," IEEE Antennas and Wireless Propagation Letters, vol. 14, pp. 1802-1805, 2015

[7] U.FL Series Connector HIROSE Electric Group. Available online: https://www.hirose.com/product/series/U.FL?lang=en (accessed on 12 October 2021).

[8] DuPont Pyralux AP Flexible circuit materials datasheet [online], https://www.dupont.com/content/dam/dupont/amer/us/en/products/ei-transformation/documents/EI-10124-Pyralux-AP-Data-Sheet.pdf (accessed by 12 October 2021).

[9] Cang, Dingyong, Zhiliang Wang, and Huiwen Qu, "A Polyimide-Based Flexible Monopole Antenna Fed by a Coplanar Waveguide" Electronics 10, no. 3: 334, 2021.

[10] H. A. Elmobarak, S. K. A. Rahim, M. Himdi, X. Castel and T. A. Rahman, "Low cost instantly printed silver nano ink flexible dual-band antenna onto paper substrate," 11th European Conference on Antennas and Propagation (EUCAP), 2017, pp. 3061-3063.

[11] H. P. Phan, T. Vuong, P. Benech, P. X. P. Borel and A. Delattre, "Low-cost wideband antenna on paper substrate," 11th European Conference on Antennas and Propagation (EUCAP), 2017, pp. 2168-2171.

[12] C. Lin, C. Chang, Y. T. Cheng and C. F. Jou, "Development of a Flexible SU-8/PDMS-Based Antenna," IEEE Antennas and Wireless Propagation Letters, vol. 10, pp. 1108-1111, 2011.

[13] T. Leng, K. Pan, X. Zhou, Y. Li, M. A. Abdalla and Z. Hu, "Non-Volatile RF Reconfigurable Antenna on Flexible Substrate for Wireless IoT Applications," IEEE Access, vol. 9, pp. 119395-119401, 2021.

[14] S. F. Jilani, Q. H. Abbasi and A. Alomainy, "Inkjet-Printed Millimetre-Wave PET-Based Flexible Antenna for 5G Wireless Applications," IEEE MTT-S International Microwave Workshop Series on 5G Hardware and System Technologies (IMWS-5G), 2018, pp. 1-3.

A Dual-Band and Flexible CPW-Fed Antenna for RF Energy Harvesting Applications

Alassane Sidibe[1], Alexandru Takacs[1], Daniela Dragomirescu[1], Samuel Charlot[1]
[1] LAAS-CNRS, Université de Toulouse, CNRS, INSA, UPS, Toulouse, France, alassane.sidibe@laas.fr, alexandru.takacs@laas.fr, daniela.dragomirescu@laas.fr, samuel.charlot@laas.fr

***Abstract*—This paper addresses a new design of a dual-band monopole antenna on a Polyimide flexible substrate fed by coplanar waveguide technique. The final purpose of the antenna will aim to be used with a rectifier circuit as part of a rectenna for RF energy harvesting in the ISM Band. Consequently, the layout of the rectifier was considered in the simulation step. The proposed topology of this CPW-feed dual band antenna is based on a modified monopole antenna combined with a rectangular loop ring and has dimensions of 38 mm × 30 mm × 0.125 mm. Interesting performances are achieved in terms of radiation patterns. On the first band at 2.42 GHz, the maximum antenna gain is about +2.29 dBi with a quite omnidirectional pattern but in the second band, the antenna is more directive with a higher gain +3.97 dBi at 5.84 GHz.**

***Index Terms*— Flexible antenna, polyimide, dual-band antenna, rectenna, wireless power transmision, energy harvestion.**

I. INTRODUCTION

The expansion of certain electronics markets, such as medical, retail, and wearable, has significantly drawn the attention of the scientific and engineering community to the development of flexible materials, manufacturing processes and new associated electronics functionalities [1]–[3]. This is radically a game changer for the next generation of electronic devices that will no longer be limited by the integration and can match with the shape of any mount.

The benefits of using flexible electronics are multiple. Unlike the traditional rigid substrate, it is light and thin thus the weight of the electronic devices will be going to decrease considerably. It allows to reduce the size by bending or folding them according to the geometry needed. Some of these materials (such as polyactide PLA and nanocellulose-based paper) are biodegradable and other material-based polymers (PET, Polyimide, PEN…) can be easily recyclable in order to reduce the environmental footprint [4]. Furthermore, flexible electronics may require complex and costly manufacturing and assembly processes. The risk of breakage due to electronically mounted components is also high. The targeted applications for flexible electronics in this paper is Radiofrequency (RF) Energy Harvesting (RFEH) or Wireless Power Transmission (WPT). For example in the literature, a textile-based flexible rectenna is designed for wearable energy harvesting at millimeter-wave bands [5].

II. THE PROPOSED DESIGN

Basically, a rectenna stands for a *rect*ifier and an*tenna* that is used to convert electromagnetic waves to DC power in order to power supply active components such as microcontrollers, transceivers and sensors. In a rectenna, the antenna captures the EM waves (at the same frequency band) from any EM energy sources or data transmitters and provides an RF signal (P_{RF}) to the connected rectifier. An adequate matching network is used to optimize the power transfer from the output of the antenna to the input of the rectifier diode. Once the RF signal is rectified, it is then filtered to get a DC voltage that will be finally boosted, managed and stored in a storage capacitor for supplying the load. The architecture of a conventional rectenna is presented in Figure 1.

One of the main challenges of a rectenna design is the optimization of the power transmission from the antenna to the rectifier. A compact rectenna which consists of a Coplanar Waveguide (CPW) feed antenna and a microstrip rectifier connected by a 35 mm long Surface Mounted Assembly (SMA) connector and adaptor is proposed in [6]. It was clearly noted that variation between simulation and measurement results is due to soldering effects, quality of SMA connector, discontinuities of substrate dielectric constant and manufacturing tolerance. Another design of dual-band CPW rectenna first started with the design of a CPW antenna with a limited size of its ground plane and then the matching network of the CPW rectifier is modified to optimize the RF-to-DC conversion efficiency [7]. However, it is obvious that the radiation performances of such an antenna (CPW feed) will not be the same with the presence of the rectifier ground plane and would not be able to properly reach its maximum efficiency at the targeted frequency band.

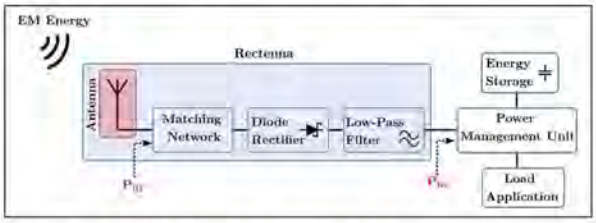

Figure 1. Schematic of a rectenna connected to a power management unit to power supply the load application with the harvested DC power from incident EM waves.

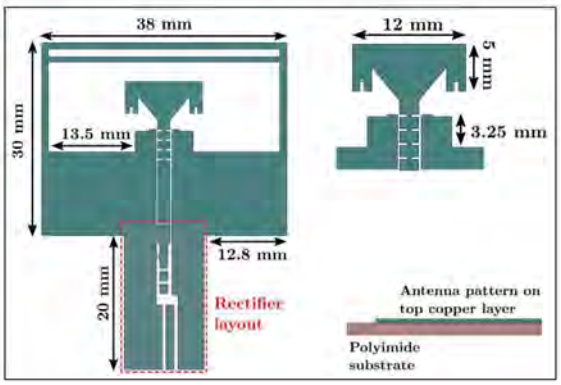

Figure 2. Layout of the proposed rectenna and side view of the design.

A 2.45 GHz broadband rectenna using a Grounded Coplanar Waveguide with a high gain of +10 dBi was presented in [8]. The drawback of this design using a 1.5 mm thick rigid substrate is the size (115 mm x 91 mm) of the use of a reflector plane at a distance of 22 mm. In our work, the final design of the proposed rectenna targeting Bluetooth and WIFI band is depicted in Figure 2. This paper will be more focused on the antenna part; its design and optimization step during simulation, and the measurement of its performances. Among all materials used for printing electronics, Polyimide material seems to be a suitable candidate as substrate thanks to its advantages (low dielectric losses, heat resistance and mechanical stability) for our needs.

III. Simulation of the Dual-Band Antenna

The antenna structure should be wisely chosen to obtain a compact design and interesting radiation performances. It can either be excited by different feeding techniques (coaxial probe, microstrip feed line, couple feed and CPW feed). The fact of using CPW feeding technique, allows the propagation of the EM field between the conduction and enable Wide-Band (WB) or dual-band features. For this purpose, an interesting CPW feed antenna at 2.45 GHz was designed with R03003 flexible material [9] and PET substrate [10]. The antenna was simulated on the Polyimide substrate (dielectric constant = 3.4; loss tangent = 0.012; thickness = 125 µm) by HFSS software from Ansys.

Two excitation/feeding approaches are used for the simulations. During the first optimization procedure of the antenna, a lumped port was used. The excitation is ensured with a Perfect Electric Conductor (PEC) bridge normal to the CPW plane and connecting the adjacent ground planes with rectangular faces (2 mm wide) as shown in Figure 3. The technique of exciting the CPW mode with air-bridge is common for antenna simulations as in [11], [12]. For highest fidelity to the manufactured sample, the RF connecter is 3D modeled and excited with a lumped port. It was previously demonstrated that this model can reliably reproduce the experimental results [13].

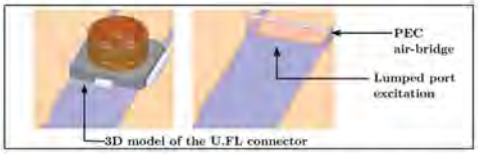

Figure 3. Feeding techniques used on the simulation.

The CPW antenna design has followed the optimization steps shown in Figure 4, Figure 5 and Figure 6. Figure 5. First, it started with a basic 11 mm length monopole antenna fed by CPW (**S1**) designed on a substrate with a size of 40 mm x 52 mm. The monopole length with a symmetrical ground plane of 11 mm x 17.75 mm presents a resonance frequency at 5.75 GHz. Then, a 70 mm length square loop element is added to connect the symmetrical ground plane in order to improve the return loss (**S2**). It can also be seen that the short-circuited loop acts as a full wavelength loop and create a resonance at 2.44 GHz as seen in Figure 4. At this step of optimization, we considered the rectifier layout. However, the transmission lines of the RF part (before the diode location) were removed to ease the use of a connector for the characterization (inset **S3**).

As expected, the rectifier layout has shifted the first resonant frequency and enhanced the bandwidth at the higher resonance mode. Therefore, improvement should be made at the first resonance created by the loop.

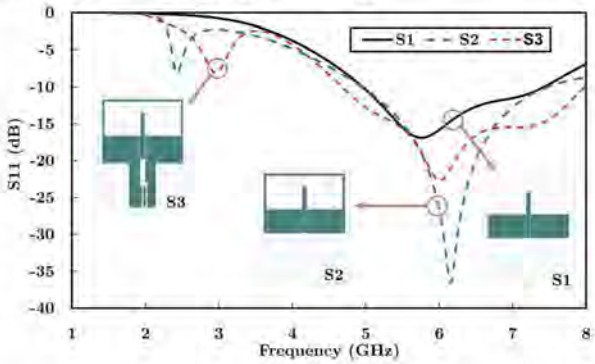

Figure 4. Simulated return loss S_{11} (dB) of the antenna at different design steps (from S1 to S3).

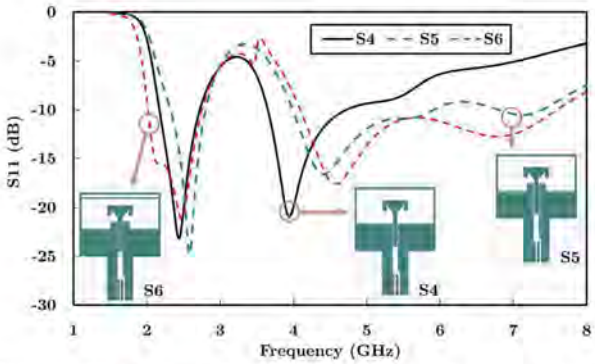

Figure 5. Simulated return loss S_{11} (dB) of the antenna at different design steps (from S4 to S6).

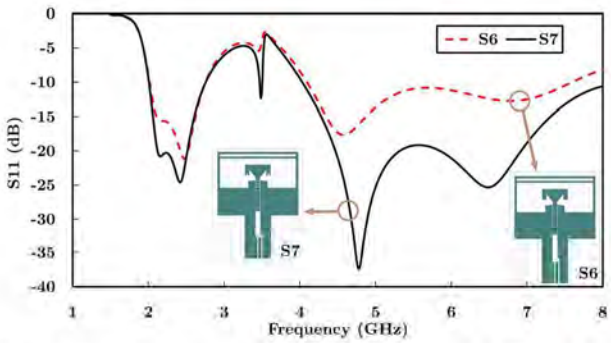

Figure 6. Simulated return loss S11(dB) of the antenna at different design steps (S4 and S6).

As seen in Figure 5, it was possible to ensure this need by changing the shape of the monopole with a triangular element on top with two rectangular arms at the ends (**S4**). On the other hand, it significantly modifies the higher resonance bandwidth that is then enhanced by adding a rectangular element on the ground plane to improve the CPW mode (**S5**). The undesired resonance around 3.5 GHz is due to the coupling between the horizontal line added for the bandwidth improvement and the head of the monopole (**S6**). Finally, short slots were added to the monopole part to improve the return loss (their length was optimized during the simulation) as seen in Figure 6.

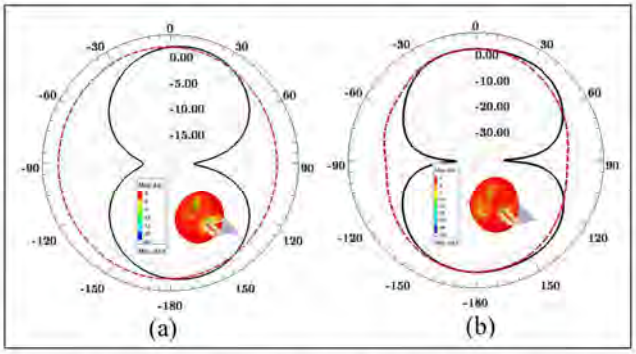

Figure 7. Simulation results of the realized gain in radiation pattern at 2.45 GHz (a) and 5.8 GHz (b) at Phi = 0 (black line) and Phi = +90° (red dashed line) ; Inset of the 3D radiation pattern (realized gain).

Figure 7 presents the simulated radiation patterns for the proposed antenna. At 2.45 GHz, the antenna radiates as an omnidirectional antenna and is more directive at high frequency.

IV. Implementation and Tests

A. *Manufactutring process of the flexible antenna*

The printing process of photolithography is the same as that used in our previous paper [13]. We use a special foil from DuPont named Pyralux AP9151R [14] to fabricate the antenna. This substrate is a 125-µm Polyimide film with a 35 µm copper foil laminated on top and bottom of it (Figure 8a).

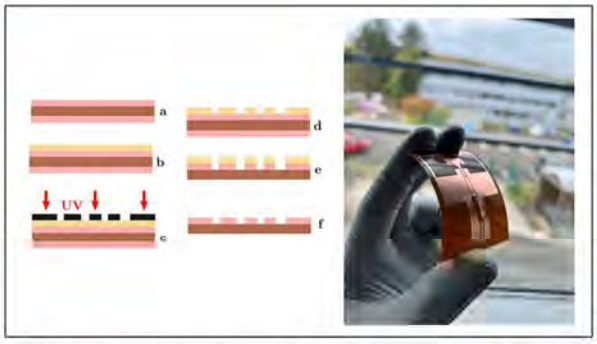

Figure 8. Description of the antenna manufacturing process (left); Photo of the manufactured antenna on polyimide substrate with a soldered U.FL connector for characterization (right).

The process flow to build the antenna is done in a clean room with photoresist equipment to allow resolution down to 10 µm. For that, a 1µm thick positive resin from Shipley (ECI 3012) is spin-coated on the substrate (Figure 8b), then bake and UV insolated through a chromium mask (Figure 8c) with the antenna design. The exposed resin then disappears in a remover (Figure 8d). The next step is the etching of the top copper not protected by the resin (Figure 8e) in a chloride iron (III) solution to minimize the lateral copper etched and keep the desired antenna layout. The back copper film is also removed at this same step. Finally, the resin is removed by acetone (Figure 8f).

The use of a U.FL connector for the characterization of such a flexible antenna is the simplest. It does not require any additional process to be assembled and can only be attached to the antenna by directly hand soldering the pads with tin.

B. *Experimental results*

The performance of the antenna is evaluated on an anechoic chamber in flat position. A U. FL to SMA adapter is connected to a cable from the Vector Network Analyzer (VNA). Figure 9 presents the comparison between the simulation done with the U.FL connector 3D model, the PEC air-bridge and the measurement. It can clearly be seen that the results fit well in the first desired region (cream color) at up to 4 GHz. The antenna is matched in a bandwidth of 690 MHz (2.06 GHz to 2.75 GHz). But there is a difference between measured and simulated return loss starting from 4 GHz. It is probably due to the inaccuracy of the measurement with the connector-adaptor at a higher frequency. The fabricated antenna stays matched under -10 dB in the band from 4.79 GHz to 7 GHz (more). The results were not plotted up to 7 GHz because of the frequency range limitation of the U.FL connector.

The gain of the antenna is measured in an anechoic chamber (by using the far-field antenna measurement facilities existing at LAAS-CNRS). A good correlation was obtained on the antenna gain as a function of the frequency with a measured gain of +2 dBi and +3.67 dBi at 2.42 GHz and 5.78 GHz, respectively (Figure 11). The radiation pattern was carried out in the E-plane where the antenna under test rotates in the azimuth plane.

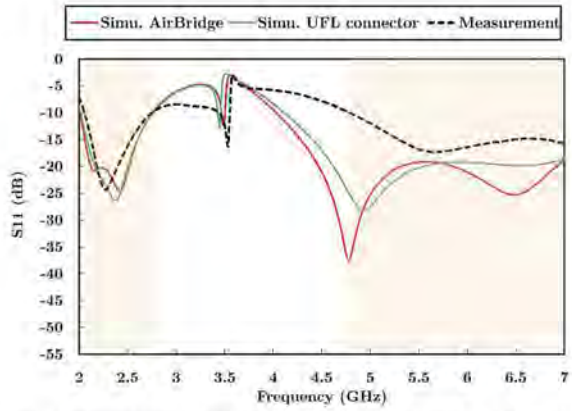

Figure 9. Comparison of the simulated return loss (with an air-bridge lumped port and U.FL) and the measurement on anechoic chamber.

As shown in Figure 11, the radiation pattern is quite omnidirectional at 2.42 GHz with a maximum gain of +2.29 dBi (Theta = +26°) and an aperture angle of 116°. The radiation pattern is a bit more directive at 5.84 GHz on some angles with a maximum gain of +3.97 dBi (Theta = -6°).

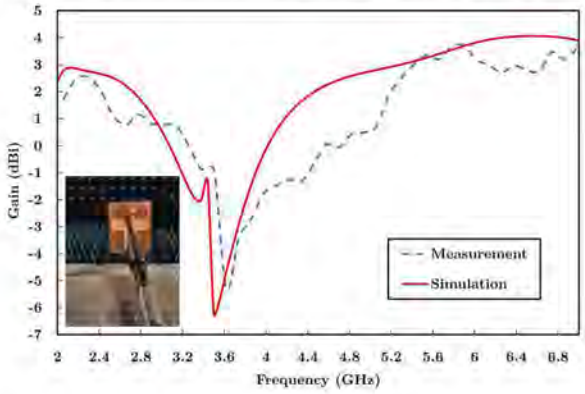

Figure 10. Comparison between measured (in anechoic chamber) and simulated realized gain (with connector) of the proposed antenna as function of the frequency on the E-plane.

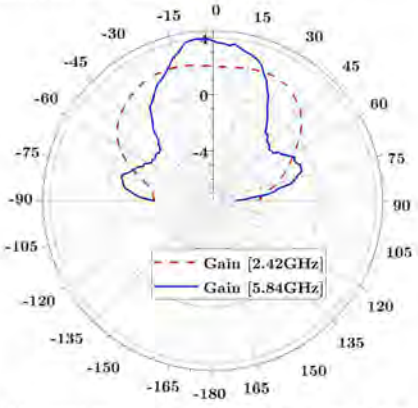

Figure 11. Measured radiation pattern in the E-plane (Phi = -90°) at 2.42 GHz (red dashed line) and 5.84 GHz (blue solid line).

V. Conclusion

In this paper, a new dual-band and flexible antenna using CPW feeding (designed for a CPW supported rectenna) has been proposed and accurately characterized. The rectifier layout has been considered during the simulation and optimizing stage. By co-designing the antenna with the rectifier layout, we can consider the electromagnetic coupling between the antenna and rectifier layout. As proved by experimental results, the proposed CPW dual band antenna covers the frequency bands (measured S11<-15 dB) of 2.08 GHz – 2.675 GHz (measured gain G> +1 dBi) and 5.29 GHz – 7 GHz (measured gain G> +2 dBi).

Acknowledgment

The authors acknowledge the French technological Network RENATECH through the LAAS-CNRS cleanroom for its support. We acknowledge UWINLOC Company and the support of the French region OCCITANIE through the research project OPTENLOC. The works were also supported by the French National Research Agency (ANR) through the McBIM Project (Communicating Material at the disposal of the Building Information Modelling), under Grant ANR-17-CE10-0014.

References

[1] C. Kallmayer, D. P. Parekh, V. Atluri, and K. Erickson, 'New Materials and Processes for Flexible Electronics'.

[2] Z. Zhou, H. Zhang, J. Liu, and W. Huang, 'Flexible electronics from intrinsically soft materials', *Giant*, vol. 6, p. 100051, 2021.

[3] D. A. Corzo Diaz, G. Tostado-Blázquez, and D. Baran, 'Flexible Electronics: Status, Challenges and Opportunities', 2020.

[4] Z. Zhai, X. Du, H. Zheng, and Y. Long, 'Biodegradable Polymeric Materials for Flexible and Degradable Electronics', *Frontiers in Electronics*, p. 26.

[5] M. Wagih, G. S. Hilton, A. S. Weddell, and S. Beeby, 'Broadband millimeter-wave textile-based flexible rectenna for wearable energy harvesting', *IEEE Transactions on Microwave Theory and Techniques*, vol. 68, no. 11, pp. 4960–4972, 2020.

[6] Q. Awais, Y. Jin, H. T. Chattha, M. Jamil, H. Qiang, and B. A. Khawaja, 'A compact rectenna system with high conversion efficiency for wireless energy harvesting', *IEEE access*, vol. 6, pp. 35857–35866, 2018.

[7] M. Aboualalaa *et al.*, 'Dual-band CPW rectenna for low input power energy harvesting applications', *IET Circuits, Devices & Systems*, vol. 14, no. 6, pp. 892–897, 2020.

[8] M.-J. Nie, X.-X. Yang, G.-N. Tan, and B. Han, 'A compact 2.45-GHz broadband rectenna using grounded coplanar waveguide', *IEEE antennas and wireless propagation letters*, vol. 14, pp. 986–989, 2015.

[9] K. Aljaloud and K.-F. Tong, 'A flexible 2.45 GHz rectenna using electrically small loop antenna', 2018.

[10] X. Guo, Y. Hang, Z. Xie, C. Wu, L. Gao, and C. Liu, 'Flexible and wearable 2.45 GHz CPW-fed antenna using inkjet-printing of silver nanoparticles on pet substrate', *Microwave and optical technology letters*, vol. 59, no. 1, pp. 204–208, 2017.

[11] S.-S. Hsu, K.-C. Wei, C.-Y. Hsu, and H. Ru-Chuang, 'A 60-GHz Millimeter-Wave CPW-Fed Yagi Antenna Fabricated by Using 0.18-µm CMOS Technology', *IEEE Electron Device Letters*, vol. 29, no. 6, pp. 625–627, 2008.

[12] Y. Dong, T. K. Johansen, V. Zhurbenko, and P. J. Hanberg, 'A rectangular waveguide-to-coplanar waveguide transition at D-band using wideband patch antenna', in *2018 48th European Microwave Conference (EuMC)*, 2018, pp. 1045–1048.

[13] A. Sidibe, A. Takacs, D. Dragomirescu, S. Charlot, and J. Mennekens, 'A Novel Polyimide Flexible Antenna Design for S-Band Applications', in *2022 16th European Conference on Antennas and Propagation (EuCAP)*, 2022, pp. 1–5.

[14] DuPont Pyralux AP Flexible circuit materials datasheet [online], https://www.dupont.com/content/dam/dupont/amer/us/en/products/ei-transformation/documents/EI-10124-Pyralux-AP-Data-Sheet.pdf (accessed by 13 October 2022).

4. Article from International Journal of Microwave and Wireless Technologies

International Journal of Microwave and Wireless Technologies

cambridge.org/mrf

Research Paper

Cite this article: Sidibe A, Loubet G, Takacs A, Ferré G, Ghiotto A (2020). Miniature drone antenna design for the detection of airliners. *International Journal of Microwave and Wireless Technologies* 1–7. https://doi.org/10.1017/S1759078720000896

Received: 10 September 2019
Revised: 15 June 2020
Accepted: 15 June 2020

Keywords:
PIFA antenna; circular polarization; Automatic Dependence Surveillance-Broadcast system (ADS-B); airliners detection

Author for correspondence:
Alassane Sidibe,
E-mail: asidibe@laas.fr

Miniature drone antenna design for the detection of airliners

Alassane Sidibe[1,2], Gaël Loubet[1], Alexandru Takacs[1], Guillaume Ferré[3] and Anthony Ghiotto[3]

[1]LAAS-CNRS, Université de Toulouse, CNRS, UPS, 7, Avenue du Colonel Roche, 31400 Toulouse, France; [2]Uwinloc, 9, Rue Humbert Tomatis, 31200 Blagnac, France and [3]IMS Laboratory, Université de Bordeaux-IPB ENSEIRB-MATMECA, 351, cours de la libération, 33400 Talence, France

Abstract

In this paper, the design of a miniature antenna dedicated to the detection of airliners through the demodulation of Automatic Dependence Surveillance-Broadcast system (ADS-B) signals is presented. This antenna is designed for being embedded on the top of a drone in order to detect and avoid collisions with airliners. This antenna consists of an array of Planar Inverted-F Antennas, a quadrature feed network (FN) and a reflector plane (RP). The FN is designed to have output signals with the same amplitude and a 90° phase difference between each other. It achieves circular polarization and maintains the axial ratio of the antenna under −3 dB at the desired frequency (1.09 GHz). The antenna with the FN was manufactured and characterized. It weighs approximately 145 kg with its RP. The measured gain of the proposed antenna is about +3.7 dBi. To validate the design, the manufactured antenna was tested with a Universal Software Radio Peripheral for the processing of ADS-B signals at the French National Microwaves Days 2019 (JNM) student contest. The detection of airliners can reach up to 437 km.

Introduction

With the emergence of drones in the last years, new problems arise especially concerning the sharing and the safety of the airspace. Thus, the detection and the localization of aircraft by unmanned aerial vehicles are essential to avoid collisions. The Automatic Dependent Surveillance-Broadcast (ADS-B) surveillance technology is more and more used by aircraft to broadcast periodically some information like their position to the air traffic control stations and/or to other aircraft. It is above all a cheap, simple, and reliable alternative to using expensive Radar technologies to locate aircraft from the ground. The position of aircraft is no more calculated and approximated from the Radars data but send by the aircraft themselves from embedded Global Positioning System. Nevertheless, the transmitted unscrambled information like location can be easily received and used by non-targeted users like drones or radio-amateurs.

Within the framework of the 21st French National Microwaves Days (JNM) at Caen (France) in 2019, a student contest was organized to highlight the best miniature receiving antenna for drones dedicated to the detection, localization, and avoidance of airliners by the use of ADS-B signals. During this contest, different antennas were tested and the most efficient was defined as the one, which has detected the farthest aircraft.

The signal processing needed to parse ADS-B messages and locate the aircraft during this competition was processed thanks to the Software Defined Radio (SDR) solution presented in [1, 2].

This paper presents the winning antenna, which is a compact array of four three-dimensional Planar Inverted-F Antenna (PIFA). According to the constraints imposed by the contest organization, this antenna is fully passive, has a maximal size inferior or equal to 80 mm × 80 mm × 20 mm, placed above the center of a 200 mm × 150 mm reflector plan emulating the top of a drone and connectable through a female SMA connector. This miniature antenna is tuned to be effective in the ADS-B band used in Europe, which is around 1090 MHz. It also has nearly circular polarization, a high aperture angle of 97° and a gain of +3.7 dBi.

Proposed antenna design

For the detection of ADS-B signals, patch and quasi-omnidirectional antennas are generally used. In [1], a circularly polarized patch antenna by corner cut dedicated to ADS-B systems is presented. In [3], this is a compact T-Slot patch antenna, which is presented for the same application. In order to detect the farthest aircraft, a quasi-omnidirectional and circularly

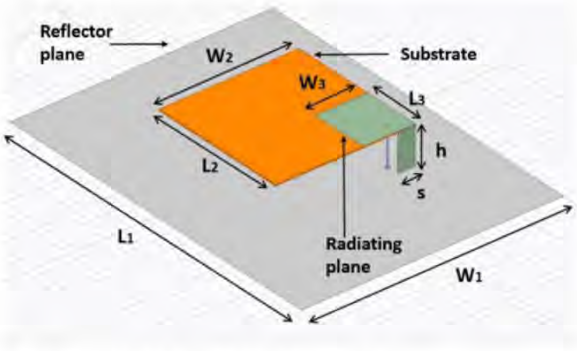

Fig. 1. Configuration of the antenna with single PIFA.

Table 1. Geometrical parameters of a single PIFA antenna

Parameter	Value (mm)
Length of the ground plane (L_1)	200
Length of the substrate (L_2)	80
Length of the radiating plane (L_3)	$\lambda/4$ | ~68.75
Width of the ground plane (W_1)	150
Width of the substrate (W_2)	80
Width of the radiating plane (W_3)	30
Height (h)	20
Shorting pin width (s)	10

polarized antenna seemed to us the appropriate choice. Moreover, the designed antenna should have good efficiency and a gain as high as possible. Thus, the proposed design consists of an array of four PIFA. Thanks to the compactness of each PIFA, it is possible to place four of them in the specified area and, thus, increase the global gain of the array. For instance, the design of a PIFA array with circular polarization for Nanosatellite application is proposed in [4]. Its size is about 100 mm × 100 mm and has a gain of +4.78 dBi at 2.35 GHz.

Antenna design

First, a single PIFA was simulated and optimized with HFSS software. Its geometry in Fig. 1 consists of a radiating element short-circuited to a ground/reflector plane (RP) by a shorting pin and a feeding point placed between the two planes (and close to the shorting pin). The RP size and position were chosen according to the contest size requirements. It has a dimension of 150 mm × 200 mm and the antenna size (without reflector) should not exceed 80 mm × 80 mm with a maximum height of 20 mm above the reflector.

The antenna was designed on a FR4 substrate (thickness: 0.8 mm, dielectric constant: 4.4, dielectric loss tangent: 0.02). Table 1 shows the dimensions of the designed single PIFA that is not centered on the ground plane, thus anticipating the mounting position in the antenna array.

The position of the feed point is controlled to have an input impedance of 50 Ω at the targeted frequency. The measured reflection coefficient as a function of the frequency plotted in Fig. 2(a) shows a good matching with less than −15 dB at 1.09 GHz. As seen in the radiation pattern in Fig. 2(b), the maximum gain of +4 dBi at 1.09 GHz was obtained for an elevation angle of 60° or equivalently for $\theta = 30°$; where theta is the angle relative to the *Oz*-axis that is perpendicular to the antenna plane (i.e. the horizontal or *xOy* plane).

An array of four PIFA was designed by adding three other identical single PIFA at each corner of the FR4 substrate as presented in Fig. 3. Circular polarization was obtained with the relative phases of 0°, 90°, 180°, and 270° at the source ports.

With previous parameters depicted in Table 1, the antenna array does not operate at the targeted frequency. Moving the feeding point at the center of each single patch surface (radiating plane), allows reaching a good matching at 1.09 GHz. The radiating surface has also been modified to a square ($W_3 = L_3 = \lambda/4$).

Figure 4(a) shows the reflection coefficient of the array of PIFA at each input port. The port 1 and 3 with a respective excitation of 0° and 180° give the same simulated value of the reflection coefficient while the ones at the port 2 (90°) and port 4 (270°) are the same.

As depicted in Fig. 4(b), the miniature antenna array with quadrature feed can reach a maximum gain of +4.85 dBi oriented over the *Oz*-axis that is perpendicular to the antenna plane.

The rotation of the antenna array above the RP has an important impact on the axial ratio (AR). As a result of an optimization

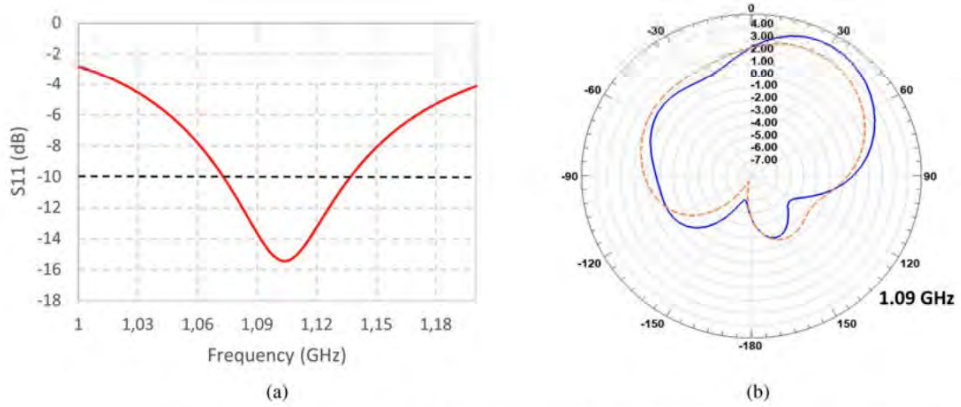

Fig. 2. (a) Simulated reflection coefficient and (b) radiated pattern of a single PIFA antenna ($xOz/\varphi = 0°$ cut – blue solid line – and $yOz/\varphi = 90°$ – orange dash line –).

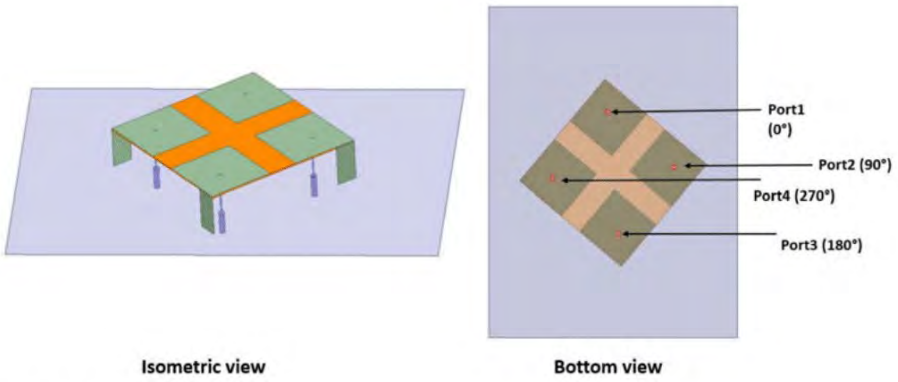

Fig. 3. Isometric and bottom view of the array PIFA antenna.

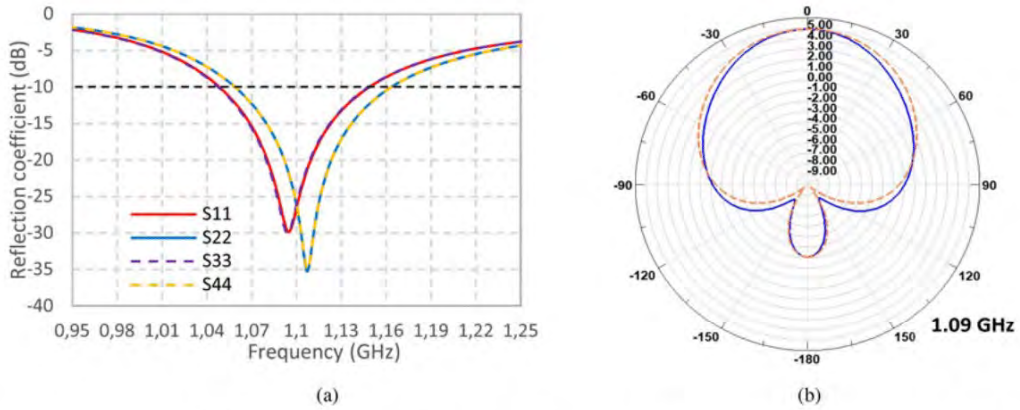

Fig. 4. (a) Simulated reflection coefficient at each port of the antenna; (b) the radiation pattern of the PIFA antenna array in two vertical planes: $xOz/\varphi = 0°$ (blue solid line) and $yOz/\varphi = 90°$ (orange dash line).

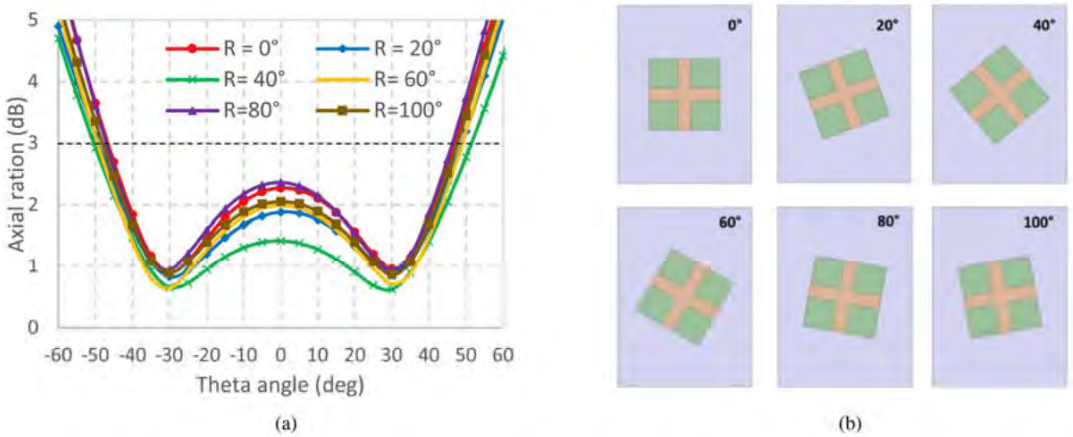

Fig. 5. (a) Variation of the axial ratio as function of the antenna rotation angle at $\varphi = 0°$ and 1.09 GHz; (b) antenna rotation angle with the respect to the reflector.

process, we found that the rotation of the array about 40° on the RP improves the most the AR. As seen in Fig. 5(a), the antenna has an AR bandwidth (AR < 3 dB) about [−50°; 50°].

Feed network

Instead of using four ports to feed the four PIFA, we decide to design a feed network (FN) based on the circuital model

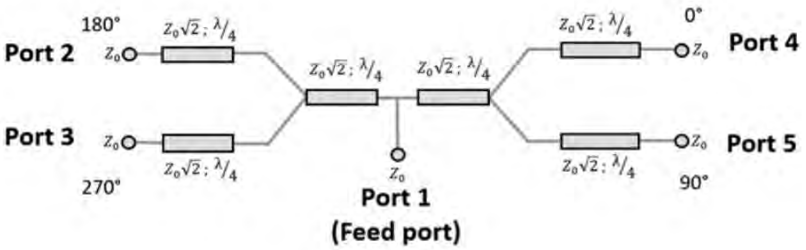

Fig. 6. Circuit model of the feed network.

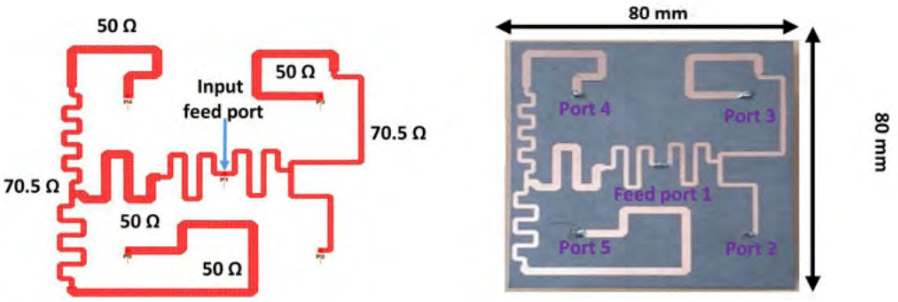

Fig. 7. Layout and photograph of the fabricated quadrature feed network.

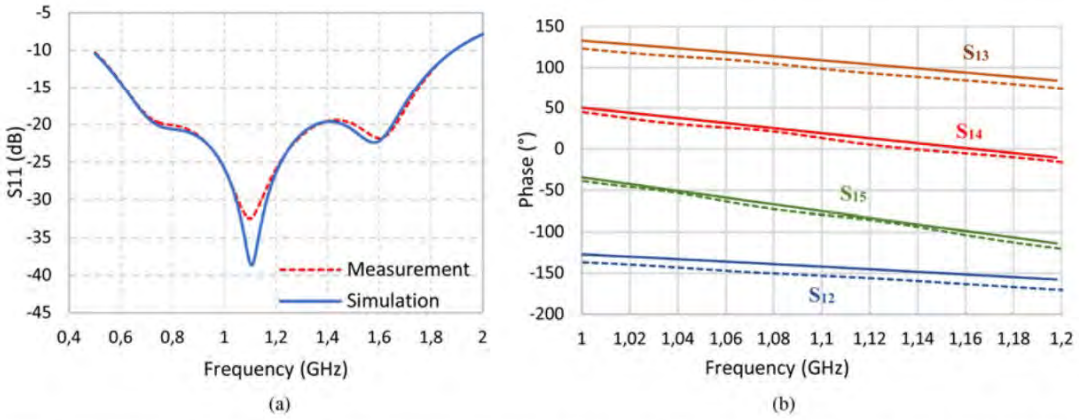

Fig. 8. (a) Simulated (line) and measured (dashed line) of the reflection coefficient (at the input of the feed port); (b) The phase delay between port 1 and each of the others.

represented in Fig. 6. It was designed to have equal 6 dB power splitting and create 90° phase shift between each output signal.

Different structures of the feeding network are proposed in the literature. The system designed in [5] is a combination of Wilkinson power dividers and two branch-line couplers in the 2.5 GHz band. Another design is proposed in [6], consists of three T-junction in phase power dividers for 30 GHz frequency band. It exists a sequential rotation network (SRN) too, which could answer to our constraints [7]. Figure 7 shows the chosen layout of the feeding network. It consists of a combination of transmission lines with different characteristic impedances and lengths connected by using a T-junction. They are used as an impedance transformer and a 90° phase shifter. Additionally, microstrip meander lines were used for the compactness in order to respect the specified area. Advanced Design System (ADS) Keysight software was used for the design, the simulation, and the optimization of this circuit. For accurate simulation, a Momentum simulation was performed. As presented in Fig. 7, the length of 50 Ω line was adjusted to $\lambda/4$ to allow the targeted phase shift between each antenna port. Z_o corresponds to the equivalent impedance of the connected antenna in the port (50 Ω).

The FN was fabricated on Duroïd substrate (substrate thickness: 0.787 mm, relative permittivity: 2.3 and loss tangent: 0.0012) to allow lower losses. For the measurement, the four end-line ports were connected to a 50 Ω load to replace the impedance of the miniature antenna.

The input reflection coefficient of the circuit is presented in Fig. 8. The agreement between measurement and simulation is

Table 2. Measured power split and phase at each port of the feed network at 1.09 GHz

S-Parameters	S_{12}	S_{13}	S_{14}	S_{15}
Measured power split (dB)	−6.1	−6.94	−5.93	−5.69
Simulated phase (degree)	−140.3	111.9	22.8	−70.4
Measured phase (degree)	−151.8	101.7	17.5	−76.6

Table 3. Measured phase difference between output ports of the feed network at 1.09 GHz

Output Port	S_{14}–S_{15}	S_{14}–S_{12}	S_{14}–S_{13}
Phase difference (degree)	94.1	169.3	−84.2 (modulo 2π) = 275.8

very good and the input reflection coefficient is less than −15 dB for the targeted frequency.

The measured power division/split shown in Table 2 is approximatively equal to 6 dB at each output port. The slight difference is mainly due to the compact size of the feeding network that does not allow a fully optimized design in the targeted area that is mainly identical with the maximum allowed surface (according to the JNM contest) for our antenna array (80 mm × 80 mm × 20 mm).

The port 4 with the lowest phase was chosen as the port reference of the FN. As depicted in Table 3, the FN satisfies a progressive 90° phase delay for other ports. The maximum phase error obtained is about +16.5° for the port 2. This difference is due to the last line connected to port 2, which is not exactly equal to $\lambda/4$.

Experimental results and discussion

A prototype of the array of PIFA with the F was manufactured and characterized (Fig. 9). The FN is placed at the top of the RP to have a compact prototype. In order to place the SMA connector and to avoid the short-circuit of the feeding point and the ground plane, a small gap was added between the RP and the circuit. With its RP and FN, the antenna array weighs approximately 145 g.

As seen in Fig. 10(a), a good correlation of the S_{11} between simulation and measurement was obtained with a frequency shift of only 30 MHz.

The measured gain presented in Fig. 10(b) was performed in an anechoic chamber. The φ angle corresponds to the cut plane of the RP. Φ angle equal to 45° means that the PIFA array without RP is perpendicular to the *xOz* plane. The measured result shows that the antenna has a maximum gain of +2.44, +3.7, and +1.94 dBi respectively, at $\varphi = 0°$, $\varphi = 45°$, and $\varphi = 90°$.

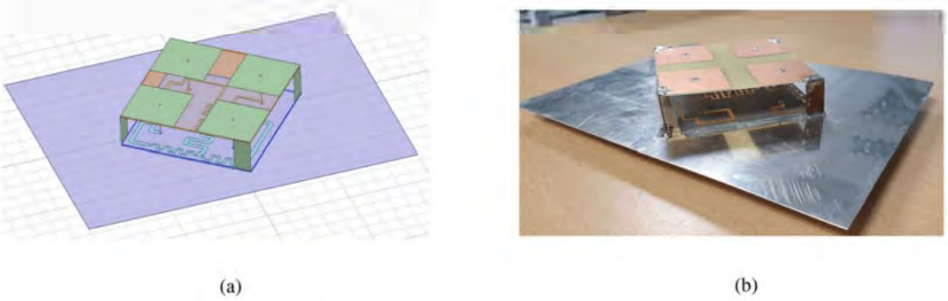

(a) (b)

Fig. 9. (a) Designed antenna on HFSS Software; (b) Photograph of the manufactured antenna.

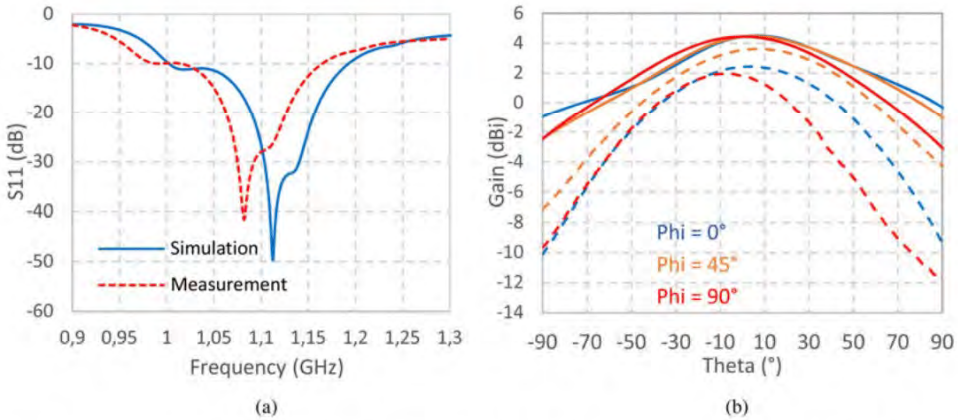

(a) (b)

Fig. 10. (a) Measured (dashed line) and simulated (continuous line) reflection coefficient at the input of the feed port of the PIFA array; (b) the simulated (continuous line) and measured (dashed line) gain for three vertical cut planes ($\varphi = 0°$, $\varphi = 45°$, and $\varphi = 90°$).

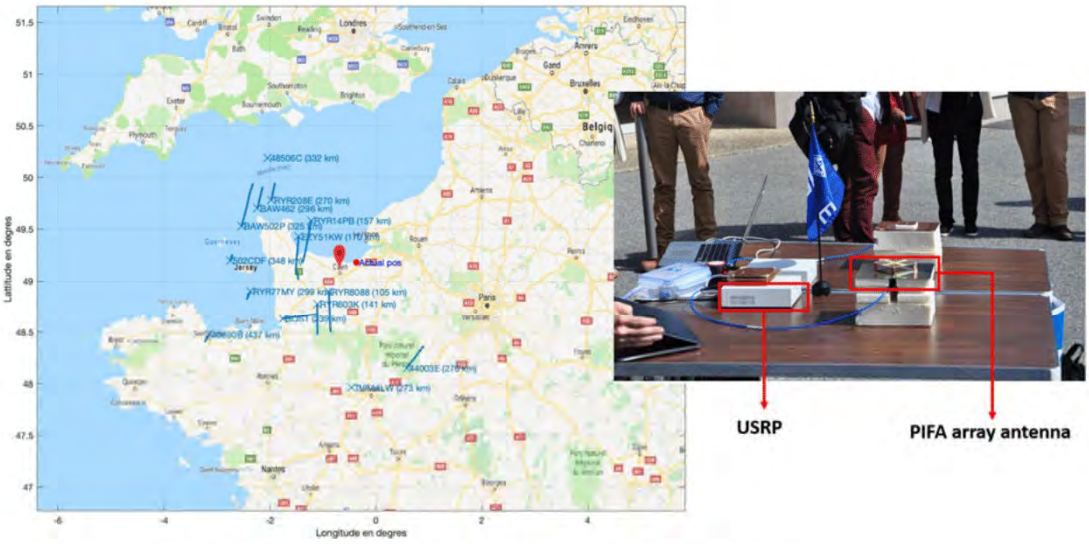

Fig. 11. Real-time trajectory on the map of the detected aircraft and a photo of the antenna during tests at the contest.

Comparing to the state of the art, the design proposed in this paper is a compact antenna array that worked at 1.09 GHz band with the highest gain. The antenna in [2] work at higher frequency (2.35 GHz) and have approximately the same size (100 mm × 100 mm) with a gain of +4.56 dBi. A compact circular polarized antenna of $0.11{\cdot}\lambda_0 \times 0.11{\cdot}\lambda_0 \times 0.02{\cdot}\lambda_0$ at 1.21 GHz is presented in [8] but with a low gain of +0.1 dBi.

Contest measurement results

Functional tests of the manufactured miniature PIFA (array) antenna were performed during the contest at the JNM conference in Caen with a radio software described in [1]. This section presents the result of the detection global system (no ADS-B signal transmission) with the proposed manufactured antenna. An Universal Software Radio Peripheral (USRP) is used to process real ADS-B signals sent by the aircraft. Then, by using MATLAB and the algorithms presented in [2], we are able to decode in real-time the ADS-B baseband signals. In addition, we developed a MATLAB code that allows displaying the aircraft trajectories over a figure using an open street map. To validate the decoded trajectories, we can compare the results with the trackers available on the Internet (for example http://www.flightradar24.com). The USRP model employed during the challenge was a USRP B100. This USRP provides up to 16 MHz of bandwidth and it has a Xilinx Spartan 3A-1400 FPGA. However, the demodulation can be implemented on other SDRs. More details about the ADS-B standard and the decoding algorithm can be found in [2].

Figure 11 displays in real-time on a map, the trajectories of air traffic over the actual position with different airliners detected during the test. The maximum range of detection with the PIFA array antenna was 437 km.

Conclusion

In this work, a miniature antenna consisting of an array of four PIFA antenna above a RP for the detection of airliners through the demodulation of ADS-B communications was proposed. The reflector emulates the top side of a drone. A quadrature FN was proposed, designed, and manufactured to achieve circular polarization of the array of PIFA.

The proposed antenna array is more compact than standard circular polarized patch antennas. Measured results demonstrate that the antenna provides a gain about +3.7 dBi with an AR under 3 dB. The performance of the antenna was validated with an adequate USRP receptor for ADS-B signal during the functional tests performed for the JNM'2019 antenna design contest and the maximum detection range of airliners was 437 km.

Acknowledgement. The authors wish to acknowledge the organizers of the JNM design contest. IEEE-MTT, AP France and Rogers Corporation supported this contest.

References

1. **Ferre G, Tajan R and Ghiotto A** (2016) Simulation d'un émetteur / récepteur ADS-B et décodage temps réel à l'aide : de Matlab, d'une radio logicielle et d'une antenne patch. *J3eA, Journal sur l'enseignement des sciences et technologies de l'information et des systèmes* **15**, 17–22, 6–17. https://www.j3ea.org/articles/j3ea/pdf/2016/01/j3ea160003.pdf.
2. **Laporte-Fauret B, Tajan R and Ferré G** (2019) ADS-B transmitter/receiver simulation to decode real aircraft trajectories with software defined radios. *29th Annual Conference of the European Association for Education and Information Engineering (EAEEIE)*, pp. 1–6.
3. **Babani S, Khamis NHH, Bala BD, Mohammed TAA and Communication Engineering Department** (2014) A compact microstrip patch antenna for ADS-B operation. *Asia Pacific Microwave Conference*, pp. 1–3.
4. **Kurnia GF, Nugrobo FS and Prasetyo AD** (2014) Planar Inverted-F Antenna (PIFA) array with circular polarization for nano satellite application. *International Symposium on Antennas and Propagation Conference Proceedings*, Kaoshiung, Taiwan, December 2–5, pp. 1–2.
5. **Mohammadi P, Piroutiniya A and Rasekhmanesh MH** (2016) A novel compact feeding network for array antenna. *Progress In Electromagnetics Research Letters* **59**, 1–6.
6. **Akbari M, Farahbakhsh A and Sebak A-R** (2019) Ridge gap waveguide multilevel sequential feeding network for high-gain circularly polarized

array antenna. *IEEE Transactions on Antennas and Propagation* **67**, 253–254.
7. **Jazi MN and Azarmanesh MN** (2006) Design and implementation of circularly polarised microstrip antenna array using a new serial feed sequentially rotated technique. *IEEE Proceedings-Microwaves, Antennas and Propagation* **153**, 133–140.
8. **Ali T, Saadh MAW, Pathan S and Biradar RC** (2017) A miniaturized circularly polarized coaxial fed superstrate slot antenna for L-band application. *Internet Technology Letters* **1**, e21.

Alassane Sidibe was born in Dakar, Senegal, in 1994. He received the M. Sc. degree in electronics of embedded system and telecommunications from the University Paul Sabatier of Toulouse in 2018. He is currently pursuing a Ph.D. degree in communication engineering with the French company Uwinloc. He has authored seven research articles and his current research interests include wireless power transmission and energy harvesting for battery-free tags.

Gael Loubet was born in Toulouse, France, in 1994. He received the Engineer Diploma in Electronics and Automation Engineering from the National Institute of Applied Sciences, Toulouse, in 2017, where he is currently pursuing his Ph.D. degree in micro- and nano-systems for wireless communications. He has authored three articles in refereed journals. His research interests include communicating materials paradigm, electromagnetic wireless power transfer, wireless communication for the Internet-of-Things applications, and wireless sensor networks for structural health monitoring applications.

Alexandru Takacs (M'12) was born in Simleu Silvaniei, Romania, in 1975. He received the Engineer Diploma in electronic engineering from the Military Technical Academy, Bucharest, Romania, in 1999, and the master's and Ph.D. degrees in the microwave and optical communications from the National Polytechnic Institute of Toulouse, Toulouse, France, in 2000 and 2004, respectively. From 2004 to 2007, he was a Lecturer with the Military Technical Academy, and an Associate Researcher with the Microtechnology Institute, Bucharest. From 2008 to 2010, he occupied a postdoctoral position with the Laboratory for Analysis and Architecture of Systems (LAAS), National Center for Scientific Research (CNRS), Toulouse. During 2011, he was a Research and Development RF Engineer with Continental Automotive SAS France, where he was in charge of antenna design and automotive electromagnetic simulation. Since 2012, he has been an Associate Professor with the University Paul Sabatier, Toulouse, where he performs research within LAAS–CNRS. He has authored or co-authored five international patents, 30 papers in refereed journals, one book, one book chapter, and over 90 communications in international symposium proceedings. His research interests include the design of microwave and RF circuits, energy harvesting and wireless power transfer, small antenna design, electromagnetic simulation techniques, and optimization methods.

Guillaume Ferré (Member, IEEE) graduated in electronic and telecommunication engineering (ENSIL) from the University of Limoges, France, in 2003. He received the Ph.D. degree in digital communications and signal processing from the Limoges University of Technology, Limoges, in 2006. From 2006 to 2008, he was a Post-Doctoral Researcher of the Limoges XLIM laboratory and the Laboratoire de l'Intégration du Matériau au Système (IMS), Bordeaux, France. Since 2008, he has been an Associate Professor with the Ecole Nationale Supérieure d'Electronique, Informatique, Télécommunications, Mathématique et Mécanique (ENSEIRB-MATMECA), an engineering school of Bordeaux INP. After several administrative responsibilities at the Telecommunications Department of ENSEIRB-MATMECA, he is currently the Director of industrial relations. He carries out his research activities at the IMS Laboratory, Signal and Image Team. These fields of research concern the circuits and systems for digital communications, including signal processing and digital communications for 5G, IoT, digital enhancement for wideband power amplifiers, and time-interleaved analog-to-digital converters. He is the author of more than 100 papers in international conferences. He is also the author of seven patents. He currently supervises five Ph.D. students with a significant part of industrial research activities. He is the Principal Investigator (PI) of many national and international projects. At the local level, he is responsible for two research activities related to the Internet of Things, including one to investigate on the smart campus. Dr. Ferré is a member of several technical program committees, including ICC, Globecom, ICT, and ICECS. In the IMS Laboratory, he holds the position of Vice-President of the Scientific Council. In 2019, he received as the author the Best Paper Award at the IEEE International Symposium on Personal, Indoor, and Mobile Radio Communications (IEEE PIMRC 2019), Track 4, entitled "An Enhanced LoRa-Like Receiver for the Simultaneous Reception of Two Interfering Signals."

Anthony Ghiotto (S'05–M'09–SM'15) was born in Aubenas, France, in 1982. He received the M.Sc. and Ph.D. degrees (Hons.) in optics, optoelectronics, and microwave engineering from the Grenoble Institute of Technology, Grenoble, France, in 2005 and 2008, respectively. From 2009 to 2012, he has held a postdoctoral research associate position at the Polytechnique Montréal, Montreal, QC, Canada. In 2012, he joined the Department of Electronics, ENSEIRB-MATMECA Engineering School, Bordeaux Institute of Technology, University of Bordeaux, Talence, France, and the Laboratory of Integration from Materials to Systems (IMS), University of Bordeaux, where he is currently an Associate Professor (with Full Professor habilitation). In 2016 and 2017, he has been a Guest Professor with the University of Pavia, Pavia, Italy. His current research interests include analysis, design, and integration of microwave and millimeter wave passive and active circuits in PCB [including substrate integrated waveguide (SIW) and air-filled SIW], dielectric waveguide, and BiCMOS and complementary metal-oxide-semiconductor (CMOS) technologies. Dr. Ghiotto was an Organization Committee Member of the 2015 European Microwave Week and the 2015 French National Microwave Days. He is a member of the Technical Coordinating Committee (TCC), the MTT-8 Filters and Passive Components Technical Committee, and the MTT-15 Microwave Field Theory Committee of the IEEE Microwave Theory and Technique Society (MTT-S). He was a recipient of the Young Scientist Award of the International Union of Radio Science in 2008, the Post-Doctoral Fellowship from the Merit Scholarship Program for Foreign Students of the Fonds Québécois de la Recherche sur la Nature et les Technologies of Québec in 2009, and the IEEE SPI Young Investigator Training Program Award in 2016 and 2017. Since 2017, he has been the Chair of the IEEE MTT French Chapter. He is the TPC Chair of the 2019 European Microwave Conference. He is an Associate Editor of the EuMA International Journal of Microwave and Wireless Technologies. He is a Technical Reviewer of the IEEE TRANSACTIONS ON MICROWAVE THEORY AND TECHNIQUES, the IEEE TRANSACTIONS ON ANTENNA AND PROPAGATION, the IEEE MICROWAVE AND WIRELESS COMPONENTS LETTERS, and the IEEE ANTENNAS AND WIRELESS PROPAGATION LETTERS. Since 2013, he has been the Counselor of the IEEE Student Branch of Bordeaux: the BEE Branch, and the Advisor of the MTT and AP BEE Branch Chapters.

References

[1] Carnegie Mellon University, "The "Only" Coke Machine on the Internet" https://www.cs.cmu.edu/~coke/history_long.txt (Accessed Mar. 13, 2023).

[2] B. Nagajayanthi, 'Decades of Internet of Things towards twenty-first century: a research-based introspective', *Wireless Personal Communications*, vol. 123, no. 4, pp. 3661–3697, 2022.

[3] IoT Analytics, 'State of IoT 2022: Number of connected IoT devices growing 18% to 14.4 billion globally', May 18, 2022. https://iot-analytics.com/number-connected-iot-devices/ (accessed Mar. 13, 2023).

[4] S. Kumar, P. Tiwari, and M. Zymbler, 'Internet of Things is a revolutionary approach'.

[5] A. Toor, A. Wen, F. Maksimovic, A. M. Gaikwad, K. S. Pister, and A. C. Arias, 'Stencil-printed Lithium-ion micro batteries for IoT applications', *Nano Energy*, vol. 82, p. 105666, 2021.

[6] E. F. Garay and R. Bashirullah, 'Biofluid activated microbattery for disposable microsystems', *Journal of Microelectromechanical Systems*, vol. 24, no. 1, pp. 70–79, 2014.

[7] L. Hu, H. Wu, F. La Mantia, Y. Yang, and Y. Cui, 'Thin, flexible secondary Li-ion paper batteries', *ACS nano*, vol. 4, no. 10, pp. 5843–5848, 2010.

[8] Y. Li, S. Yong, N. Hillier, S. Arumugam, and S. Beeby, 'Screen printed flexible water activated battery on woven cotton textile as a power supply for e-textile applications', *IEEE Access*, vol. 8, pp. 206958–206965, 2020.

[9] R. Tajima *et al.*, 'Truly wearable display comprised of a flexible battery, flexible display panel, and flexible printed circuit', *Journal of the Society for Information Display*, vol. 22, no. 5, pp. 237–244, 2014.

[10] S. Mukherjee, A. Albertengo, and T. Djenizian, 'Beyond flexible-Li-ion battery systems for soft electronics', *Energy Storage Materials*, vol. 42, pp. 773–785, 2021.

[11] A. Poulin, X. Aeby, and G. Nyström, 'Water activated disposable paper battery', *Scientific Reports*, vol. 12, no. 1, p. 11919, 2022.

[12] C. García Núñez, L. Manjakkal, and R. Dahiya, 'Energy autonomous electronic skin', *npj Flexible Electronics*, vol. 3, no. 1, p. 1, 2019.

[13] S. Kim *et al.*, 'Ambient RF energy-harvesting technologies for self-sustainable standalone wireless sensor platforms', *Proceedings of the IEEE*, vol. 102, no. 11, pp. 1649–1666, 2014.

[14] S. K. Ram, S. R. Sahoo, B. B. Das, K. Mahapatra, and S. P. Mohanty, 'Eternal-thing: A secure aging-aware solar-energy harvester thing for sustainable IoT', *IEEE Transactions on Sustainable Computing*, vol. 6, no. 2, pp. 320–333, 2020.

[15] A. Páez-Montoro, M. García-Valderas, E. Olías-Ruíz, and C. López-Ongil, 'Solar energy harvesting to improve capabilities of wearable devices', *Sensors*, vol. 22, no. 10, p. 3950, 2022.

[16] X. Xiao, Y. Fu, Y. Yang, and X. Zhang, 'Sustainable solar powered battery-free wireless sensing for food cold chain management', *Sensors International*, vol. 3, p. 100157, 2022.

[17] L. Hou, S. Tan, Z. Zhang, and N. W. Bergmann, 'Thermal energy harvesting WSNs node for temperature monitoring in IIoT', *IEEE Access*, vol. 6, pp. 35243–35249, 2018.

[18] J.-H. Bahk, H. Fang, K. Yazawa, and A. Shakouri, 'Flexible thermoelectric materials and device optimization for wearable energy harvesting', *Journal of Materials Chemistry C*, vol. 3, no. 40, pp. 10362–10374, 2015.

[19] D. Enescu, ‘Thermoelectric energy harvesting: basic principles and applications’, *Green energy advances*, p. pp-1, 2019.
[20] N. Sezer and M. Koç, ‘A comprehensive review on the state-of-the-art of piezoelectric energy harvesting’, *Nano Energy*, vol. 80, p. 105567, 2021.
[21] Y. Liu *et al.*, ‘Piezoelectric energy harvesting for self-powered wearable upper limb applications’, *Nano Select*, vol. 2, no. 8, pp. 1459–1479, 2021.
[22] M. K. Mishu *et al.*, ‘Prospective efficient ambient energy harvesting sources for iot-equipped sensor applications’, *Electronics*, vol. 9, no. 9, p. 1345, 2020.
[23] X. Gu, L. Grauwin, D. Dousset, S. Hemour, and K. Wu, ‘Dynamic ambient RF energy density measurements of Montreal for battery-free IoT sensor network planning’, *IEEE Internet of Things Journal*, vol. 8, no. 17, pp. 13209–13221, 2021.
[24] Z. Liang and J. Yuan, ‘Modelling and prediction of mobile service channel power density for RF energy harvesting’, *IEEE Wireless Communications Letters*, vol. 9, no. 5, pp. 741–744, 2020.
[25] Z. Liang and J. Yuan, ‘A Compact Dual-Band Four-Port Ambient RF Energy Harvester With High-Sensitivity, High-Efficiency, and Wide Power Range’, *IEEE Transactions on Microwave Theory and Techniques*, vol. 70, no. 1, pp. 641–649, 2021.
[26] S. Shen, Y. Zhang, C.-Y. Chiu, and R. Murch, ‘A triple-band high-gain multibeam ambient RF energy harvesting system utilizing hybrid combining’, *IEEE Transactions on Industrial Electronics*, vol. 67, no. 11, pp. 9215–9226, 2019.
[27] D. Galante-Sempere, D. Ramos-Valido, S. Lalchand Khemchandani, and J. Del Pino, ‘Low-power RFED wake-up receiver design for low-cost wireless sensor network applications’, *Sensors*, vol. 20, no. 22, Art. no. 22, 2020.
[28] ‘Energy Harvesting | Making Devices Energy Autonomous’, *E-peas*, Apr. 11, 2023. https://e-peas.com/ (accessed Apr. 11, 2023).
[29] ‘Power management | TI.com’, Apr. 11, 2023. https://www.ti.com/power-management/overview.html (accessed Apr. 11, 2023).
[30] Y. Shafiq, J. S. Gibson, H. Kim, C. P. Ambulo, T. H. Ware, and S. V. Georgakopoulos, ‘A reusable battery-free RFID temperature sensor’, *IEEE Transactions on Antennas and Propagation*, vol. 67, no. 10, Art. no. 10, 2019.
[31] F. Costa, S. Genovesi, M. Borgese, A. Michel, F. A. Dicandia, and G. Manara, ‘A review of RFID sensors, the new frontier of internet of things’, *Sensors*, vol. 21, no. 9, Art. no. 9, 2021.
[32] N. Khalid, R. Mirzavand, H. Saghlatoon, M. M. Honari, A. K. Iyer, and P. Mousavi, ‘A Batteryless RFID sensor architecture with distance ambiguity resolution for smart home IoT applications’, *IEEE Internet of Things Journal*, vol. 9, no. 4, Art. no. 4, 2021.
[33] D. Dardari *et al.*, ‘An ultra-wideband battery-less positioning system for space applications’, in *2019 IEEE International Conference on RFID Technology and Applications (RFID-TA)*, IEEE, 2019, pp. 104–109.
[34] X. Gu, W. Lin, S. Hemour, and K. Wu, ‘Readout distance enhancement of battery-free harmonic transponder’, *IEEE Transactions on Microwave Theory and Techniques*, vol. 69, no. 7, Art. no. 7, 2021.
[35] M. Wagih, ‘Battery-Free Wireless Node Powered using High-Efficiency Harvesting of 900 MHz GFSK-Modulated Packets with a Compact Rectenna’, in *2022 Wireless Power Week (WPW)*, IEEE, 2022, pp. 162–165.
[36] V. Talla, B. Kellogg, S. Gollakota, and J. R. Smith, ‘Battery-free cellphone’, *Proceedings of the ACM on Interactive, Mobile, Wearable and Ubiquitous Technologies*, vol. 1, no. 2, Art. no. 2, 2017.

[37] A. Rigi, A. J. Mugisha, A. Arefian, S. R. Khan, and S. Mitra, 'Wireless battery-free body temperature sensing device for key workers', *IEEE Sensors Letters*, vol. 6, no. 2, Art. no. 2, 2021.
[38] M. Boada, A. Lazaro, R. Villarino, and D. Girbau, 'Battery-less soil moisture measurement system based on a NFC device with energy harvesting capability', *IEEE Sensors Journal*, vol. 18, no. 13, Art. no. 13, 2018.
[39] D. Dardari *et al.*, 'An ultra-low power ultra-wide bandwidth positioning system', *IEEE Journal of Radio Frequency Identification*, vol. 4, no. 4, pp. 353–364, 2020.
[40] D. Fabbri, A. Romani, A. Costanzo, and D. Masotti, 'An orientation-independent UHF battery-less Tag for extended-range Applications', in *2020 XXXIIIrd General Assembly and Scientific Symposium of the International Union of Radio Science*, 2020, pp. 1–4. doi: 10.23919/URSIGASS49373.2020.9231982.
[41] J. Garnica, R. A. Chinga, and J. Lin, 'Wireless power transmission: From far field to near field', *Proceedings of the IEEE*, vol. 101, no. 6, pp. 1321–1331, 2013.
[42] S. Y. Choi, B. W. Gu, S. Y. Jeong, and C. T. Rim, 'Advances in wireless power transfer systems for roadway-powered electric vehicles', *IEEE Journal of emerging and selected topics in power electronics*, vol. 3, no. 1, pp. 18–36, 2014.
[43] C. H. Lee, G. Jung, K. Al Hosani, B. Song, D. Seo, and D. Cho, 'Wireless power transfer system for an autonomous electric vehicle', in *2020 IEEE Wireless Power Transfer Conference (WPTC)*, IEEE, 2020, pp. 467–470.
[44] G. L. Barbruni, P. M. Ros, D. Demarchi, S. Carrara, and D. Ghezzi, 'Miniaturised Wireless Power Transfer Systems for Neurostimulation: A Review', *IEEE Transactions on Biomedical Circuits and Systems*, 2020.
[45] W. Lin and R. W. Ziolkowski, 'Far field wireless power transfer for IoT applications enabled by an ultra-compact and highly-efficient Huygens rectenna', in *2020 IEEE Wireless Power Transfer Conference (WPTC)*, IEEE, 2020, pp. 69–71.
[46] H. Lyu, X. Liu, Y. Sun, Z. Jian, and A. Babakhani, 'A 915-MHz far-field energy harvester with- 22-dBm sensitivity and 3-V output voltage based on antenna-and-rectifier codesign', *IEEE Microwave and Wireless Components Letters*, vol. 29, no. 8, pp. 557–559, 2019.
[47] K. Jin and W. Zhou, 'Wireless laser power transmission: A review of recent progress', *IEEE Transactions on Power Electronics*, vol. 34, no. 4, pp. 3842–3859, 2018.
[48] J. C. Maxwell, *The Scientific Papers of James Clerk Maxwell...*, vol. 2. University Press, 1890.
[49] H. Hertz, 'Dictionary of Scientific Biography, vol', *VI. New York: Scribner*, pp. 340–349, 1990.
[50] C. Hirlimann, 'Understanding the Branly effect', *arXiv preprint cond-mat/0703495*, 2007.
[51] N. Tesla, 'The transmission of electrical energy without wires', *Electrical World and Engineer*, vol. 1, pp. 21–24, 1904.
[52] W. C. Brown and R. H. George, 'Rectification of microwave power', *IEEE spectrum*, vol. 1, no. 10, pp. 92–97, 1964.
[53] W. Brown, J. Mims, and N. Heenan, 'An experimental microwave-powered helicopter', in *1958 IRE International Convention Record*, IEEE, 1966, pp. 225–235.
[54] W. C. Brown, 'Experiments involving a microwave beam to power and position a helicopter', *IEEE Transactions on Aerospace and Electronic Systems*, no. 5, pp. 692–702, 1969.
[55] W. C. Brown, 'The history of power transmission by radio waves', *IEEE Transactions on microwave theory and techniques*, vol. 32, no. 9, pp. 1230–1242, 1984.
[56] V. Marian, B. Allard, C. Vollaire, and J. Verdier, 'Strategy for microwave energy harvesting from ambient field or a feeding source', *IEEE Transactions on Power Electronics*, vol. 27, no. 11, pp. 4481–4491, 2012.

[57] C. R. Valenta and G. D. Durgin, 'Harvesting wireless power: Survey of energy-harvester conversion efficiency in far-field, wireless power transfer systems', *IEEE Microwave Magazine*, vol. 15, no. 4, pp. 108–120, 2014.
[58] U. Guler and M. Ghovanloo, 'Power management in wireless power-sipping devices: A survey', *IEEE circuits and systems magazine*, vol. 17, no. 4, pp. 64–82, 2017.
[59] T. Soyata, L. Copeland, and W. Heinzelman, 'RF energy harvesting for embedded systems: A survey of tradeoffs and methodology', *IEEE Circuits and Systems Magazine*, vol. 16, no. 1, pp. 22–57, 2016.
[60] Y.-S. Chen and C.-W. Chiu, 'Maximum achievable power conversion efficiency obtained through an optimized rectenna structure for RF energy harvesting', *IEEE Transactions on Antennas and Propagation*, vol. 65, no. 5, pp. 2305–2317, 2017.
[61] H. Sun, Y. Guo, M. He, and Z. Zhong, 'A dual-band rectenna using broadband Yagi antenna array for ambient RF power harvesting', *IEEE Antennas and Wireless Propagation Letters*, vol. 12, pp. 918–921, 2013.
[62] K. Niotaki, S. Kim, S. Jeong, A. Collado, A. Georgiadis, and M. M. Tentzeris, 'A compact dual-band rectenna using slot-loaded dual band folded dipole antenna', *IEEE Antennas and Wireless Propagation Letters*, vol. 12, pp. 1634–1637, 2013.
[63] C. Liu, F. Tan, H. Zhang, and Q. He, 'A novel single-diode microwave rectifier with a series band-stop structure', *IEEE transactions on microwave theory and techniques*, vol. 65, no. 2, pp. 600–606, 2016.
[64] S.-E. Adami *et al.*, 'A Flexible 2.45-GHz Power Harvesting Wristband With Net System Output From −24.3 dBm of RF Power', *IEEE Transactions on Microwave Theory and Techniques*, vol. 66, no. 1, pp. 380–395, Jan. 2018, doi: 10.1109/TMTT.2017.2700299.
[65] A. Okba, A. Takacs, and H. Aubert, 'Compact rectennas for ultra-low-power wireless transmission applications', *IEEE Transactions on Microwave Theory and Techniques*, vol. 67, no. 5, pp. 1697–1707, 2019.
[66] D. Masotti, A. Costanzo, M. Del Prete, and V. Rizzoli, 'Genetic-based design of a tetra-band high-efficiency radio-frequency energy harvesting system', *IET Microwaves, Antennas & Propagation*, vol. 7, no. 15, pp. 1254–1263, 2013.
[67] J.-H. Chou, D.-B. Lin, K.-L. Weng, and H.-J. Li, 'All polarization receiving rectenna with harmonic rejection property for wireless power transmission', *IEEE Transactions on Antennas and Propagation*, vol. 62, no. 10, pp. 5242–5249, 2014.
[68] W. Lin and R. W. Ziolkowski, 'Electrically small, single-substrate huygens dipole rectenna for ultracompact wireless power transfer applications', *IEEE Transactions on Antennas and Propagation*, vol. 69, no. 2, pp. 1130–1134, 2020.
[69] M. Zeng, A. S. Andrenko, X. Liu, Z. Li, and H.-Z. Tan, 'A compact fractal loop rectenna for RF energy harvesting', *IEEE Antennas and Wireless Propagation Letters*, vol. 16, pp. 2424–2427, 2017.
[70] K. Miwatashi, T. Hirakawa, N. Shinohara, and T. Mitani, 'Development of High-Power Charge Pump Rectifier for Microwave Wireless Power Transmission', *IEEE Journal of Microwaves*, vol. 2, no. 4, pp. 711–719, 2022.
[71] T. Mitani, S. Kawashima, and T. Nishimura, 'Analysis of voltage doubler behavior of 2.45-GHz voltage doubler-type rectenna', *IEEE Transactions on Microwave Theory and Techniques*, vol. 65, no. 4, pp. 1051–1057, 2017.
[72] Q. Ren *et al.*, 'A Security-Enhanced, Charge-Pump-Free, ISO14443-A-/ISO10373-6-Compliant RFID Tag With 16.2-$$\backslash$mu $ W Embedded RRAM and Reconfigurable Strong PUF', *IEEE Transactions on Very Large Scale Integration (VLSI) Systems*, 2022.

[73] D. De Donno, L. Catarinucci, and L. Tarricone, 'An UHF RFID energy-harvesting system enhanced by a DC-DC charge pump in silicon-on-insulator technology', *IEEE Microwave and Wireless Components Letters*, vol. 23, no. 6, pp. 315–317, 2013.
[74] 'On-chip high-voltage generation in MNOS integrated circuits using an improved voltage multiplier technique | IEEE Journals & Magazine | IEEE Xplore'. https://ieeexplore.ieee.org/document/1050739 (accessed Mar. 08, 2023).
[75] S.-C. Lin, C.-Y. Cheng, C.-Y. Hsu, and Z.-M. Tsai, 'Compat wireless energy harvesting rectenna and measurement configuration with multiple continuous-wave transmitters', in *2016 IEEE International Symposium on Radio-Frequency Integration Technology (RFIT)*, Aug. 2016, pp. 1–4. doi: 10.1109/RFIT.2016.7578189.
[76] 'A Hybrid Cockcroft–Walton/Dickson Multiplier for High Voltage Generation | IEEE Journals & Magazine | IEEE Xplore'. https://ieeexplore.ieee.org/document/8767979 (accessed Mar. 08, 2023).
[77] H. Zhang, Z. Zhong, Y.-X. Guo, and W. Wu, 'Differentially-fed charge pumping rectifier design with an enhanced efficiency for ambient RF energy harvesting', in *2017 IEEE MTT-S International Microwave Symposium (IMS)*, IEEE, 2017, pp. 613–616.
[78] W. Liu, K. Huang, T. Wang, J. Hou, and Z. Zhang, 'A Compact Ultra-Broadband RF Rectifier Using Dickson Charge Pump', *IEEE Microwave and Wireless Components Letters*, vol. 32, no. 6, pp. 591–594, 2022.
[79] 'An RF-to-DC Rectifier With High Efficiency Over Wide Input Power Range for RF Energy Harvesting Applications | IEEE Journals & Magazine | IEEE Xplore'. https://ieeexplore.ieee.org/document/8790985 (accessed Mar. 08, 2023).
[80] K. Gharehbaghi, F. Koçer, and H. Külah, 'Optimization of Power Conversion Efficiency in Threshold Self-Compensated UHF Rectifiers With Charge Conservation Principle', *IEEE Transactions on Circuits and Systems I: Regular Papers*, vol. 64, no. 9, pp. 2380–2387, Sep. 2017, doi: 10.1109/TCSI.2017.2695650.
[81] M. Wagih, A. S. Weddell, and S. Beeby, 'Rectennas for radio-frequency energy harvesting and wireless power transfer: A review of antenna design [antenna applications corner]', *IEEE Antennas and Propagation Magazine*, vol. 62, no. 5, pp. 95–107, 2020.
[82] Y.-S. Chen and C.-W. Chiu, 'Insertion loss characterization of impedance matching networks for low-power rectennas', *IEEE Transactions on Components, Packaging and Manufacturing Technology*, vol. 8, no. 9, pp. 1632–1641, 2018.
[83] J.-K. Huang and S.-Y. Chen, 'A compact slot loop rectenna for dual-band operation at 2.4- and 5.8-GHz bands', in *2016 IEEE International Symposium on Antennas and Propagation (APSURSI)*, IEEE, 2016, pp. 411–412.
[84] S. Yoshida, S. Asakura, S. Yamanokuchi, and K. Nishikawa, '152.6% Fractional Bandwidth UHF-to-Microwave Band Compact Rectifier Utilizing the Conditions for Flat Frequency Characteristics of RF–DC Conversion Efficiency', *IEEE Microwave and Wireless Components Letters*, vol. 32, no. 6, pp. 595–598, 2022.
[85] J. Tissier and M. Latrach, 'Appropriate conventional rectifier topology for low-power RF energy harvesting', in *2022 Wireless Power Week (WPW)*, IEEE, 2022, pp. 644–648.
[86] H. Sun and W. Geyi, 'A new rectenna with all-polarization-receiving capability for wireless power transmission', *IEEE Antennas and Wireless Propagation Letters*, vol. 15, pp. 814–817, 2015.
[87] S. Li, F. Cheng, C. Gu, S. Yu, and K. Huang, 'Efficient dual-band rectifier using stepped impedance stub matching network for wireless energy harvesting', *IEEE Microwave and Wireless Components Letters*, vol. 31, no. 7, pp. 921–924, 2021.
[88] S. Ahlawat, N. Singh, B. K. Kanaujia, and K. Rambabu, 'A Dual Band Differential Intraoral Antenna and System for Wireless Data and Radiative Near-field Power Transfer', *IEEE Transactions on Antennas and Propagation*, 2023.

[89] H. He, H. Lin, P. Wu, Q. Li, and C. Liu, 'Compact High-Efficiency Broadband Rectifier Based on Coupled Transmission Line', *IEEE Transactions on Circuits and Systems II: Express Briefs*, vol. 69, no. 11, pp. 4404–4408, 2022.
[90] W. Liu, K. Huang, T. Wang, Z. Zhang, and J. Hou, 'A broadband high-efficiency RF rectifier for ambient RF energy harvesting', *IEEE Microwave and Wireless Components Letters*, vol. 30, no. 12, pp. 1185–1188, 2020.
[91] Z. He and C. Liu, 'A compact high-efficiency broadband rectifier with a wide dynamic range of input power for energy harvesting', *IEEE Microwave and Wireless Components Letters*, vol. 30, no. 4, pp. 433–436, 2020.
[92] S. Yu, F. Cheng, C. Gu, C. Wang, and K. Huang, 'Compact and efficient broadband rectifier using T-type matching network', *IEEE Microwave and Wireless Components Letters*, vol. 32, no. 6, pp. 587–590, 2022.
[93] A. Takacs, A. Okba, and H. Aubert, 'Compact planar integrated rectenna for batteryless IoT applications', in *2018 48th European Microwave Conference (EuMC)*, IEEE, 2018, pp. 777–780.
[94] A. M. Jie, M. F. Karim, K. T. Chandrasekaran, and others, 'A wide-angle circularly polarized tapered-slit-patch antenna with a compact rectifier for energy-harvesting systems [Antenna Applications Corner]', *IEEE Antennas and Propagation Magazine*, vol. 61, no. 2, pp. 94–111, 2019.
[95] J. Kim and J. Oh, 'Compact rectifier array with wide input power and frequency ranges based on adaptive power distribution', *IEEE Microwave and Wireless Components Letters*, vol. 31, no. 5, pp. 513–516, 2021.
[96] F. S. e Serpa, H. D. Hernandez, and R. L. da S. Adriano, 'A Compact High-Efficiency Broadband RF Rectifier for Energy Harvesting Applications', in *2021 SBMO/IEEE MTT-S International Microwave and Optoelectronics Conference (IMOC)*, IEEE, 2021, pp. 1–3.
[97] P. Wu *et al.*, 'High-efficient rectifier with extended input power range based on self-tuning impedance matching', *IEEE Microwave and Wireless Components Letters*, vol. 28, no. 12, pp. 1116–1118, 2018.
[98] Z. He, H. Lin, and C. Liu, 'Codesign of a Schottky diode's and loop antenna's impedances for dual-band wireless power transmission', *IEEE Antennas and Wireless Propagation Letters*, vol. 19, no. 10, pp. 1813–1817, 2020.
[99] C. Song *et al.*, 'Matching network elimination in broadband rectennas for high-efficiency wireless power transfer and energy harvesting', *IEEE Transactions on Industrial Electronics*, vol. 64, no. 5, pp. 3950–3961, 2016.
[100] A. Hirono, N. Sakai, and K. Itoh, 'High efficient 2.4 GHz band high power rectenna with the direct matching topology', in *2019 IEEE Asia-Pacific Microwave Conference (APMC)*, IEEE, 2019, pp. 1268–1270.
[101] M. Wagih, A. S. Weddell, and S. Beeby, 'High-efficiency sub-1 GHz flexible compact rectenna based on parametric antenna-rectifier co-design', in *2020 IEEE/MTT-S International Microwave Symposium (IMS)*, IEEE, 2020, pp. 1066–1069.
[102] Z. Dan, Z. He, H. Lin, and C. Liu, 'A Patch Rectenna With an Integrated Impedance Matching Network and a Harmonic Recycling Filter', *IEEE Antennas and Wireless Propagation Letters*, vol. 21, no. 10, pp. 2085–2089, 2022.
[103] H. Zhang, S.-P. Gao, W. Wu, and Y.-X. Guo, 'Uneven-to-even power distribution for maintaining high efficiency of dual-linearly polarized rectenna', *IEEE Microwave and Wireless Components Letters*, vol. 28, no. 12, pp. 1119–1121, 2018.
[104] Y. Park, K. Kim, and D. Youn, 'Rectenna Array Design for Receiving High Power in Beam Type Wireless Power Transmission', in *2018 Asia-Pacific Microwave Conference (APMC)*, IEEE, 2018, pp. 440–442.

[105] E. Choi *et al.*, '$-$11 to 7 dBm Power Range, Triple Band RF Energy Harvesting System With 99.9% Peak Tracking Efficiency and Improved PCE', *IEEE Transactions on Circuits and Systems I: Regular Papers*, 2022.
[106] M. A. Halimi, T. Khan, S. K. Koul, and S. R. Rengarajan, 'A Dual-Band Rectifier Using Half-Wave Transmission Line Matching for 5G and Wi-Fi Bands RFEH/MPT Applications', *IEEE Microwave and Wireless Components Letters*, 2022.
[107] Y. Chen, X. Liu, Y. Li, and Z. Huang, 'Super-Broadband Rectifier with Expanded Input Power Range for Microwave Power Transmission', in *2022 IEEE 5th International Conference on Electronic Information and Communication Technology (ICEICT)*, IEEE, 2022, pp. 1040–1042.
[108] X. Tang, G. Xie, and Y. Cui, 'Self-sustainable long-range backscattering communication using RF energy harvesting', *IEEE Internet of Things Journal*, vol. 8, no. 17, pp. 13737–13749, 2021.
[109] D. Liu, L. Wang, Z. He, and C. Liu, 'A Self-Packaged SISL Low-Power Rectifier Based on a High-Impedance Line for $ C $-Band Applications', *IEEE Microwave and Wireless Components Letters*, 2022.
[110] M. Wagih and S. Beeby, 'Thin Flexible RF Energy Harvesting Rectenna Surface With a Large Effective Aperture for Sub μW/cm 2 Powering of Wireless Sensor Nodes', *IEEE Transactions on Microwave Theory and Techniques*, vol. 70, no. 9, pp. 4328–4338, 2022.
[111] Z. Yue, X. Xu, S. Li, Y. H. Zhu, and X. Q. Lin, 'Efficient and Compact Tri-Band Rectifier With Large Frequency Ratio for WPT', *IEEE Microwave and Wireless Components Letters*, 2022.
[112] Y. Wang, X.-X. Yang, G.-N. Tan, and S. Gao, 'Study on millimeter-wave SIW rectenna and arrays with high conversion efficiency', *IEEE Transactions on Antennas and Propagation*, vol. 69, no. 9, pp. 5503–5511, 2021.
[113] S. Ladan, A. B. Guntupalli, and K. Wu, 'A high-efficiency 24 GHz rectenna development towards millimeter-wave energy harvesting and wireless power transmission', *IEEE Transactions on Circuits and Systems I: Regular Papers*, vol. 61, no. 12, pp. 3358–3366, 2014.
[114] M. Wagih, N. Hillier, S. Yong, A. S. Weddell, and S. Beeby, 'RF-powered wearable energy harvesting and storage module based on E-textile coplanar waveguide rectenna and supercapacitor', *IEEE Open Journal of Antennas and Propagation*, vol. 2, pp. 302–314, 2021.
[115] Skyworks Schottky diodes datasheet, Accessed: Oct. 24, 2022. [Online]. Available: https://www.skyworksinc.com/-/media/A36775836A4E4BA8A92104088692424F.ashx
[116] 'SMS7630-005LF Skyworks Solutions, Inc. Diode-Schottky|Skyworks'. https://store.skyworksinc.com/products/detail/sms7630005lf-skyworks-solutions-inc/113182/ (accessed Feb. 13, 2022).
[117] Skyworks application note, 'APN1001: Circuit Models for Plastic Packaged Microwave Diodes'. Accessed: Oct. 25, 2022. [Online]. Available: https://www.skyworksinc.com/-/media/2D9AE5CC1CD6411F94EF8DAB11AA7BDE.pdf
[118] H. Packard, 'Linear models for diode surface mount packages', *Application Note 1124*, 1997.
[119] 'AEM20940 RF Energy Harvesting | Radio Frequency Harvesting', *E-peas*. https://e-peas.com/product/aem30940/ (accessed Feb. 13, 2022).
[120] 'BQ25570 datasheet | TI.com'. https://www.ti.com/document-viewer/BQ25570/datasheet/revision-history-slusbh21212#SLUSBH21212 (accessed Dec. 06, 2021).
[121] H. Wheeler, 'Small antennas', *IEEE Transactions on Antennas and Propagation*, vol. 23, no. 4, pp. 462–469, 1975, doi: 10.1109/TAP.1975.1141115.

[122] H. A. Wheeler, ‘The radiansphere around a small antenna’, *Proceedings of the IRE*, vol. 47, no. 8, pp. 1325–1331, 1959.
[123] W. A. Davis, T. Yang, E. D. Caswell, and W. L. Stutzman, ‘Fundamental limits on antenna size: a new limit’, *IET microwaves, antennas & propagation*, vol. 5, no. 11, pp. 1297–1302, 2011.
[124] R. H. Patel, A. Desai, and T. Upadhyaya, ‘A discussion on electrically small antenna property’, *Microwave and Optical Technology Letters*, vol. 57, no. 10, pp. 2386–2388, 2015.
[125] H. A. Wheeler, ‘Fundamental limitations of small antennas’, *Proceedings of the IRE*, vol. 35, no. 12, pp. 1479–1484, 1947.
[126] G. Marrocco, ‘The art of UHF RFID antenna design: Impedance-matching and size-reduction techniques’, *IEEE antennas and propagation magazine*, vol. 50, no. 1, pp. 66–79, 2008.
[127] ‘U.FL series - HIROSE Electric Group [Connector]’. https://www.hirose.com/product/series/U.FL?lang=en# (accessed Nov. 22, 2022).
[128] S. Zahid, A. Quddious, F. A. Tahir, P. Vryonides, M. Antoniades, and S. Nikolaou, ‘Dual-band compact antenna for UHF and ISM systems’, in *2019 13th European Conference on Antennas and Propagation (EuCAP)*, IEEE, 2019, pp. 1–5.
[129] L. H. Trinh *et al.*, ‘Miniature antenna for IoT devices using LoRa technology’, in *2017 International Conference on Advanced Technologies for Communications (ATC)*, IEEE, 2017, pp. 170–173.
[130] F. A. Asadallah, A. Eid, G. Shehadeh, J. Costantine, Y. Tawk, and E. M. Tentzeris, ‘Digital Reconfiguration of a Single Arm 3-D Bowtie Antenna’, *IEEE Transactions on Antennas and Propagation*, vol. 69, no. 7, pp. 4184–4188, 2020.
[131] S. D. Assimonis, V. Fusco, A. Georgiadis, and T. Samaras, ‘Efficient and sensitive electrically small rectenna for ultra-low power RF energy harvesting’, *Scientific reports*, vol. 8, no. 1, pp. 1–13, 2018.
[132] V. Palazzi, M. Del Prete, and M. Fantuzzi, ‘Scavenging for energy: A rectenna design for wireless energy harvesting in UHF mobile telephony bands’, *IEEE Microwave Magazine*, vol. 18, no. 1, pp. 91–99, 2016.
[133] Y. Muramoto, N. Sakai, and K. Itoh, ‘A 920 MHz band rectenna with the impedance transfomed small loop antenna (IT-SLA)’, in *2022 Wireless Power Week (WPW)*, IEEE, 2022, pp. 400–403.
[134] S. Keyrouz, ‘Practical Rectennas, RF Power Harvesting and Transport’, *PhD-Thesis*, 2014.
[135] W. Lin and R. W. Ziolkowski, ‘Wirelessly powered light and temperature sensors facilitated by electrically small omnidirectional and Huygens dipole antennas’, *Sensors*, vol. 19, no. 9, p. 1998, 2019.
[136] ‘Projet McBIM’, *McBIM*. http://mcbim.cran.univ-lorraine.fr/front-page (accessed Feb. 02, 2023).
[137] G. Loubet, ‘Autonomous wireless sensor networks for the implementation of communicating materials. Application to civil engineering industry’, PhD Thesis, INSA Toulouse, 2021.
[138] J. H. Bungey and M. G. Grantham, *Testing of concrete in structures*. Crc Press, 2006.
[139] S. K. Verma, S. S. Bhadauria, and S. Akhtar, ‘Review of nondestructive testing methods for condition monitoring of concrete structures’, *Journal of construction engineering*, vol. 2013, no. 2008, pp. 1–11, 2013.
[140] P. Kot, M. Muradov, M. Gkantou, G. S. Kamaris, K. Hashim, and D. Yeboah, ‘Recent advancements in non-destructive testing techniques for structural health monitoring’, *Applied Sciences*, vol. 11, no. 6, p. 2750, 2021.

[141] S. Taheri, 'A review on five key sensors for monitoring of concrete structures', *Construction and Building Materials*, vol. 204, pp. 492–509, 2019.
[142] S. Kubler, W. Derigent, A. Thomas, and E. Rondeau, 'Problem definition methodology for the "Communicating Material" paradigm', *IFAC Proceedings Volumes*, vol. 43, no. 4, pp. 198–203, 2010.
[143] 'en_30022002v030201p.pdf'. Accessed: Feb. 07, 2023. [Online]. Available: https://www.etsi.org/deliver/etsi_en/300200_300299/30022002/03.02.01_60/en_30022002v030201p.pdf
[144] LoRaWAN module, 'Type ABZ(CMWX1ZZABZ-078) | LPWA Products', *Murata Manufacturing Co., Ltd.* https://www.murata.com/en-eu/products/connectivitymodule/lpwa/overview/lineup/type-abz-078 (accessed Feb. 07, 2023).
[145] LoRa transceiver, 'SX1276'. https://www.semtech.fr/products/wireless-rf/lora-connect/sx1276 (accessed May 23, 2023).
[146] ARM Microcontrollers, 'stm32l072cz.pdf'. Accessed: May 23, 2023. [Online]. Available: https://www.st.com/resource/en/datasheet/stm32l072cz.pdf
[147] 'ETSI TR 102 436 V2.1.1 (2014-06) - Electromagnetic compatibility and Radio spectrum Matters (ERM); Short Range Devices (SRD) intended for operation in the bands 865 MHz to 868 MHz and 915 MHz to 921 MHz; Guidelines for the installation and commissioning of Radio Frequency Identification (RFID) equipment at UHF', *iTeh Standards Store*. https://standards.iteh.ai/catalog/standards/etsi/8e50724b-db29-45ad-8e8b-d5681b109ee8/etsi-tr-102-436-v2-1-1-2014-06 (accessed Apr. 22, 2022).
[148] G. Roqueta, S. Irteza, J. Romeu, and L. Jofre, 'A novel compact UHF wideband antenna for near field electrical characterization of Steel Fiber Reinforced Concrete', in *2009 3rd European Conference on Antennas and Propagation*, IEEE, 2009, pp. 2393–2397.
[149] S.-H. Jeong and H.-W. Son, 'UHF RFID tag antenna for embedded use in a concrete floor', *IEEE Antennas and Wireless Propagation Letters*, vol. 10, pp. 1158–1161, 2011.
[150] G. Loubet, 'Réseaux de capteurs sans fil autonomes pour la fabrication de matériaux communicants. Application au domaine du génie civil.', PhD Thesis, Toulouse, INSA, 2021.
[151] G. Loubet, A. Takacs, E. Gardner, A. De Luca, F. Udrea, and D. Dragomirescu, 'LoRaWAN battery-free wireless sensors network designed for structural health monitoring in the construction domain', *Sensors*, vol. 19, no. 7, p. 1510, 2019.
[152] 'AEROTEK CO.,LTD.' http://www.aerotek.co.th/classic/coaxstd.php (accessed May 24, 2023).
[153] Bluetooth technology overview. Accessed: Dec. 06, 2021. [Online]. Available: https://www.bluetooth.com/learn-about-bluetooth/tech-overview/
[154] Bluetooth blog, 'What You Need to Know About Periodic Advertising Sync Transfer'. Accessed: Mar. 02, 2022. [Online]. Available: https://www.bluetooth.com/blog/periodic-advertising-sync-transfer/
[155] 'QN908x: Ultra-Low-Power Bluetooth Low Energy System on Chip (SoC) Solution | NXP Semiconductors'. https://www.nxp.com/products/wireless/bluetooth-low-energy/qn908x-ultra-low-power-bluetooth-low-energy-system-on-chip-solution:QN9080 (accessed Dec. 06, 2021).
[156] Bluetooth Low-Energy MCU, 'QN9090/30(T)'. https://www.nxp.com/products/wireless/bluetooth-low-energy/qn9090-30-bluetooth-low-energy-mcu-with-armcortex-m4-cpu-energy-efficiency-analog-and-digital-peripherals-and-nfc-tag-option:QN9090-30 (accessed Apr. 20, 2022).
[157] Nordic Semiconductor Bluetooth SoC, 'nRF52833'. https://www.nordicsemi.com/Products/nRF52833 (accessed Apr. 20, 2022).

[158] ‘BlueNRG-LP - Programmable Bluetooth® LE 5.2 Wireless SoC - STMicroelectronics’. https://www.st.com/en/wireless-connectivity/bluenrg-lp.html (accessed Apr. 20, 2022).
[159] ‘Radio SoC, Bluetooth 5 Certified’. https://www.onsemi.com/products/wireless-connectivity/wireless-rf-transceivers/rsl10 (accessed Apr. 20, 2022).
[160] ‘EFR32BG22 Series 2 Bluetooth Low Energy (SoC) - Silicon Labs’. https://www.silabs.com/wireless/bluetooth/efr32bg22-series-2-socs (accessed Apr. 20, 2022).
[161] ‘SmartBond DA14530 and DA14531 | Dialog’. https://www.dialog-semiconductor.com/products/bluetooth-low-energy/da14530-and-da14531 (accessed Apr. 20, 2022).
[162] Z.-X. Du and X. Y. Zhang, ‘High-efficiency single-and dual-band rectifiers using a complex impedance compression network for wireless power transfer’, *IEEE Transactions on industrial electronics*, vol. 65, no. 6, pp. 5012–5022, 2017.
[163] M. Huang *et al.*, ‘Single-and dual-band RF rectifiers with extended input power range using automatic impedance transforming’, *IEEE Transactions on Microwave Theory and Techniques*, vol. 67, no. 5, pp. 1974–1984, 2019.
[164] ‘HDC2080 datasheet | TI.com’. https://www.ti.com/document-viewer/HDC2080/datasheet/GUID-5AB554A1-5F5B-4CF8-B0D0-9590654E767A#TITLE-SNAS678SNAS6781218 (accessed Dec. 06, 2021).
[165] ‘Compact Planar Antennas for 2.4 GHz Communication’, p. 48.
[166] M. Ghamari *et al.*, ‘Detailed examination of a packet collision model for Bluetooth Low Energy advertising mode’, *IEEE Access*, vol. 6, pp. 46066–46073, 2018.
[167] ‘QN9080SIP Development Kit’. https://www.nxp.com/design/development-boards/freedom-development-boards/wireless-connectivy/a-highly-extensible-platform-for-application-development-of-qn9080sip:QN9080SIP-DK (accessed Feb. 14, 2022).
[168] ‘QN9080DK: A highly extensible platform for application development of QN908x | NXP Semiconductors’. https://www.nxp.com/products/wireless/bluetooth-low-energy/a-highly-extensible-platform-for-application-development-of-qn908x:QN9080DK (accessed Apr. 12, 2022).
[169] ‘865080143008.pdf’. Accessed: Apr. 14, 2022. [Online]. Available: https://www.we-online.com/catalog/datasheet/865080143008.pdf
[170] USPTO.report, ‘Radio-frequency Energy Harvesting Circuit And Communication Device Integrating Such A Radio-frequency Energy Harvesting Circuit Patent Application’, *USPTO.report*. https://uspto.report/patent/app/20210249901 (accessed Apr. 22, 2022).
[171] USPTO.report, ‘Method And Device For The Detection Of A Pulse Of A Signal Patent Application’, *USPTO.report*. https://uspto.report/patent/app/20200091956 (accessed Apr. 22, 2022).
[172] ‘UWINLOC | New Indoor Location System for assets tracking’, *UWINLOC | Indoor Location System*. https://uwinloc.com/ (accessed Feb. 09, 2022).
[173] D. A. Corzo Diaz, G. Tostado-Blázquez, and D. Baran, ‘Flexible Electronics: Status, Challenges and Opportunities’, 2020.
[174] Y. Khan, A. Thielens, S. Muin, J. Ting, C. Baumbauer, and A. C. Arias, ‘A new frontier of printed electronics: flexible hybrid electronics’, *Advanced Materials*, vol. 32, no. 15, p. 1905279, 2020.
[175] S. Wang, T. Chinnasamy, M. A. Lifson, F. Inci, and U. Demirci, ‘Flexible substrate-based devices for point-of-care diagnostics’, *Trends in biotechnology*, vol. 34, no. 11, pp. 909–921, 2016.

[176] Executive Agency for Small and Medium sized Enterprises. and Technopolis Group., *Advanced technologies for industry: product watch : flexible and printed electronics.* LU: Publications Office, 2021. Accessed: May 26, 2023. [Online]. Available: https://data.europa.eu/doi/10.2826/295137
[177] 'Eurecat Centre Tecnològic - Innovant per a les empreses', *Eurecat*. https://eurecat.org/ (accessed Feb. 09, 2022).
[178] V. T. Nguyen and C. W. Jung, 'Impact of dielectric constant on embedded antenna efficiency', *International Journal of Antennas and Propagation*, vol. 2014, 2014.
[179] X. Yi, T. Wu, Y. Wang, and M. M. Tentzeris, 'Sensitivity modeling of an RFID-based strain-sensing antenna with dielectric constant change', *IEEE Sensors Journal*, vol. 15, no. 11, pp. 6147–6155, 2015.
[180] T. Inui, H. Koga, M. Nogi, N. Komoda, and K. Suganuma, 'A miniaturized flexible antenna printed on a high dielectric constant nanopaper composite', *Advanced Materials*, vol. 27, no. 6, pp. 1112–1116, 2015.
[181] 'EI-10206-Kapton-HN-Data-Sheet.pdf'. Accessed: Aug. 26, 2022. [Online]. Available: https://www.dupont.com/content/dam/dupont/amer/us/en/products/ei-transformation/documents/EI-10206-Kapton-HN-Data-Sheet.pdf
[182] 'ST506-Datasheet.pdf'. Accessed: Aug. 26, 2022. [Online]. Available: https://usa.dupontteijinfilms.com/wp-content/uploads/2017/01/ST506-Datasheet.pdf
[183] M. Ercoli, M. Kraemer, D. Dragomirescu, and R. Plana, 'A high performance integrated balun for 60 GHz application in 65nm CMOS technology', in *2010 Asia-Pacific Microwave Conference*, IEEE, 2010, pp. 1845–1848.
[184] A. Dianat, A. Attaran, R. Muscedere, and B. A. Chronik, 'PCB Fabricated Passive RF Balun for 3 T MRI Applications', in *2019 IEEE Canadian Conference of Electrical and Computer Engineering (CCECE)*, IEEE, 2019, pp. 1–4.
[185] C.-S. Lin *et al.*, 'Analysis of multiconductor coupled-line Marchand baluns for miniature MMIC design', *IEEE Transactions on microwave theory and techniques*, vol. 55, no. 6, pp. 1190–1199, 2007.
[186] M. Martelius *et al.*, 'A class-D tri-phasing CMOS power amplifier with an extended Marchand-Balun power combiner', *IEEE Transactions on Microwave Theory and Techniques*, vol. 68, no. 3, pp. 1022–1034, 2019.
[187] S.-H. Yang and C.-K. C. Tzuang, '130-nm CMOS K-band two-element differential power-combining oscillators', *IEEE transactions on microwave theory and techniques*, vol. 61, no. 3, pp. 1174–1185, 2013.
[188] M. Zeng, A. S. Andrenko, X. Liu, B. Zhu, Z. Li, and H.-Z. Tan, 'Differential topology rectifier design for ambient wireless energy harvesting', in *2016 IEEE International conference on RFID technology and applications (RFID-TA)*, IEEE, 2016, pp. 97–101.
[189] M. M. Mansour, X. Le Polozec, and H. Kanaya, 'Compact and wide-band efficiency improved RF differential rectifier for wireless energy harvesting', in *2018 IEEE/MTT-S International Microwave Symposium-IMS*, IEEE, 2018, pp. 972–975.
[190] Q. W. Lin and X. Y. Zhang, 'Differential rectifier using resistance compression network for improving efficiency over extended input power range', *IEEE Transactions on Microwave Theory and Techniques*, vol. 64, no. 9, pp. 2943–2954, 2016.
[191] 'HSMS-285x.pdf'. Accessed: Aug. 19, 2022. [Online]. Available: https://media.digikey.com/pdf/Data%20Sheets/Avago%20PDFs/HSMS-285x.pdf
[192] 'INDQ (Inductor with Q) - ADS 2009 - Keysight Knowledge Center'. https://edadocs.software.keysight.com/pages/viewpage.action?pageId=5924474 (accessed Aug. 25, 2022).

[193] K. Saeed, M. F. Shafique, M. B. Byrne, and I. C. Hunter, 'Planar microwave sensors for complex permittivity characterization of materials and their applications', *Applied Measurement Systems*, pp. 319–350, 2012.
[194] 'Basics of Measuring the Dielectric Properties of Materials'.
[195] D. Zhou, Y. Zhang, S. Shi, J. Zhang, R. Yue, and Y. Wang, 'Dielectric Constant Determination for Thin Film by Using Reflection Resonance Microstrip Line Method', *IEEE Transactions on Dielectrics and Electrical Insulation*, vol. 29, no. 1, pp. 15–21, 2022.
[196] K.-P. Latti, M. Kettunen, J.-P. Strom, and P. Silventoinen, 'A review of microstrip T-resonator method in determining the dielectric properties of printed circuit board materials', *IEEE Transactions on Instrumentation and Measurement*, vol. 56, no. 5, pp. 1845–1850, 2007.
[197] L. Cai, Z. H. Jiang, Y. Huang, and W. Hong, 'Ungrounded coplanar waveguide based straight line methods for broadband and continuous dielectric characterization of microwave substrates', *IEEE Access*, vol. 8, pp. 32624–32631, 2020.
[198] A. Zahedi, F. A. Boroumand, and H. Aliakbrian, 'Analytical transmission line model for complex dielectric constant measurement of thin substrates using T-resonator method', *IET Microwaves, Antennas & Propagation*, vol. 14, no. 15, pp. 2027–2034, 2020.
[199] 'Dimatix Materials Printer DMP-2850: Support | Fujifilm [United States]'. https://www.fujifilm.com/us/en/business/inkjet-solutions/deposition-products/dmp-2850/support (accessed Aug. 09, 2022).
[200] B. C. Wadell, *Transmission line design handbook*. Artech House Microwave Library, 1991.
[201] 'End Launch Connectors Archives', *Southwest Microwave*. https://mpd.southwestmicrowave.com/product-category/end-launch-connectors/ (accessed Sep. 14, 2022).
[202] 'A CPW T-Resonator Technique for Electrical Characterizati... - Google Scholar'. https://scholar.google.com/scholar?hl=fr&as_sdt=0%2C5&q=A+CPW+T-Resonator+Technique+for+Electrical+Characterization+of+Microwave+Substrates&btnG= (accessed May 30, 2023).
[203] 'H20E.pdf'. Accessed: Jun. 01, 2023. [Online]. Available: https://www.epotek.com/docs/en/Datasheet/H20E.pdf
[204] M. Fallahpour and R. Zoughi, 'Antenna miniaturization techniques: A review of topology-and material-based methods', *IEEE Antennas and Propagation Magazine*, vol. 60, no. 1, pp. 38–50, 2017.
[205] A. Okba, A. Takacs, and H. Aubert, 'Compact flat dipole rectenna for IoT applications', *Progress In Electromagnetics Research C*, vol. 87, pp. 39–49, 2018.
[206] H. Nakano, H. Tagami, A. Yoshizawa, and J. Yamauchi, 'Shortening ratios of modified dipole antennas', *IEEE Transactions on Antennas and Propagation*, vol. 32, no. 4, pp. 385–386, 1984.
[207] G. Marrocco, A. Fonte, and F. Bardati, 'Evolutionary design of miniaturized meander-line antennas for RFID applications', in *IEEE Antennas and Propagation Society International Symposium (IEEE Cat. No. 02CH37313)*, IEEE, 2002, pp. 362–365.
[208] M. Rokunuzzaman, M. T. Islam, W. S. Rowe, S. Kibria, M. Jit Singh, and N. Misran, 'Design of a miniaturized meandered line antenna for UHF RFID tags', *PloS one*, vol. 11, no. 8, p. e0161293, 2016.
[209] A. M. Marindra, P. Pongpaibool, W. Wallada, and S. Siwamogsatham, 'An optimized ink-reducing hollowed-out arm meander dipole antenna structure for printed RFID tags', *International Journal of Microwave and Wireless Technologies*, vol. 9, no. 2, pp. 469–479, 2017.

[210] ‘Fractal antennas: A novel antenna miniaturization... - Google Scholar’. https://scholar.google.com/scholar?hl=fr&as_sdt=0%2C5&q=Fractal+antennas%3A+A+novel+antenna+miniaturization+technique%2C+and+applications&btnG= (accessed Jun. 01, 2023).
[211] H.-K. Ryu, G. Jung, D.-K. Ju, S. Lim, and J.-M. Woo, ‘An electrically small spherical UHF RFID tag antenna with quasi-isotropic patterns for wireless sensor networks’, *ieee antennas and wireless propagation letters*, vol. 9, pp. 60–62, 2010.
[212] S. H. Kim and J. H. Jang, ‘Compact folded monopole antenna with LC-loadings’, in *2010 International Workshop on Antenna Technology (iWAT)*, IEEE, 2010, pp. 1–4.
[213] S. Das, D. J. Sawyer, N. Diamanti, A. P. Annan, and A. K. Iyer, ‘A strongly miniaturized and inherently matched folded dipole antenna for narrowband applications’, *IEEE Transactions on Antennas and Propagation*, vol. 68, no. 5, pp. 3377–3386, 2020.
[214] S. Das, H. Saghlatoon, P. Mousavi, and A. K. Iyer, ‘A highly miniaturized and inherently conjugately matched folded dipole-based RFID tag antenna’, *IEEE Access*, vol. 7, pp. 101658–101664, 2019.
[215] A. A. Babar *et al.*, ‘Inkjet-printable UHF RFID tag antenna on a flexible ceramic-polymer composite substrate’, in *2012 IEEE/MTT-S International Microwave Symposium Digest*, IEEE, 2012, pp. 1–3.
[216] Y. Takigawa, S. Kashihara, and F. Kuroki, ‘Integrated slot spiral antenna etched on heavily-high permittivity piece’, in *2007 Asia-Pacific Microwave Conference*, IEEE, 2007, pp. 1–4.
[217] K. Li, C. Zhu, L. Li, Y.-M. Cai, and C.-H. Liang, ‘Design of electrically small metamaterial antenna with ELC and EBG loading’, *IEEE Antennas and Wireless Propagation Letters*, vol. 12, pp. 678–681, 2013.
[218] ‘Td and Dk - Very Low-Loss Laminate and Prepreg.pdf’. Accessed: Jun. 01, 2023. [Online]. Available: https://www.isola-group.com/wp-content/uploads/data-sheets/i-tera-mt40.pdf?t=945025256
[219] T. Wu, F. Wu, C. Qiu, J.-M. Redouté, and M. R. Yuce, ‘A rigid-flex wearable health monitoring sensor patch for IoT-connected healthcare applications’, *IEEE Internet of Things Journal*, vol. 7, no. 8, pp. 6932–6945, 2020.
[220] G. Bilodeau *et al.*, ‘A wireless electro-optic platform for multimodal electrophysiology and optogenetics in freely moving rodents’, *Frontiers in Neuroscience*, p. 990, 2021.
[221] M. Karlsson and S. Gong, ‘Circular dipole antenna for mode 1 UWB radio with integrated balun utilizing a flex-rigid structure’, *IEEE transactions on antennas and propagation*, vol. 57, no. 10, pp. 2967–2971, 2009.
[222] A. Enayati, M. Libois, W. De Raedt, and G. A. Vandenbosch, ‘Conformal antenna-in-package solution implemented in a 3D flex-rigid multilayer PCB technology’, in *Asia-Pacific Microwave Conference 2011*, IEEE, 2011, pp. 118–121.
[223] ‘Nous fabriquons des circuit imprimés’, *NCAB Group France*. https://www.ncabgroup.com/fr/ (accessed Jan. 09, 2023).
[224] ‘EI-10124-Pyralux-AP-Data-Sheet.pdf’. Accessed: Jan. 12, 2023. [Online]. Available: https://www.dupont.com/content/dam/dupont/amer/us/en/products/ei-transformation/documents/EI-10124-Pyralux-AP-Data-Sheet.pdf
[225] ‘MELINEX® ST505 | Tekra, LLC’. https://www.tekra.com/products/films/polyester-films/heat-stabilized-pet/melinex-st505 (accessed Jan. 16, 2023).
[226] ‘MADRAS - Advanced materials and processing in organic electronics’, *madras-project.eu*. https://madras-project.eu/ (accessed Sep. 18, 2022).
[227] ‘Conductive ink for printed electronics : IOT, display and more’, *GenesInk*. https://www.genesink.com/ (accessed Feb. 09, 2022).
[228] ‘Home’, *Arjowiggins*. https://www.arjowiggins.com/ (accessed Feb. 09, 2022).

[229] M. Beltrão, F. M. Duarte, J. C. Viana, and V. Paulo, 'A review on in-mold electronics technology', *Polymer Engineering & Science*, vol. 62, no. 4, pp. 967–990, 2022.
[230] 'C.-S.-Buga-et-al.-2021-A-Review-on-Materials-and-Technologies-for-Organic-Large-Area-Electronics.pdf'. Accessed: Jan. 19, 2023. [Online]. Available: https://www.dtx-colab.pt/wp-content/uploads/2019/05/C.-S.-Buga-et-al.-2021-A-Review-on-Materials-and-Technologies-for-Organic-Large%E2%80%90Area-Electronics.pdf
[231] F. Hoeng, A. Denneulin, and J. Bras, 'Use of nanocellulose in printed electronics: a review', *Nanoscale*, vol. 8, no. 27, pp. 13131–13154, 2016.
[232] A. A. Septevani, D. Burhani, and Y. Sampora, 'Nanocellulose in electronics and electrical industry', in *Nanocellulose Materials*, Elsevier, 2022, pp. 217–246.
[233] 'Optimising the transparency of Cellulose Nano Fibrils Films for more sustainable electronics' manufacturing - madras-project.eu'. https://madras-project.eu/optimising-the-transparency-of-cellulose-nano-fibrils-films-for-more-sustainable-electronics-manufacturing/ (accessed Sep. 26, 2022).
[234] A. Pammo *et al.*, 'Nanocellulose films as substrates for printed electronics', in *2019 International Conference on Manipulation, Automation and Robotics at Small Scales (MARSS)*, IEEE, 2019, pp. 1–6.
[235] S. Li, H. Chen, X. Liu, P. Li, and W. Wu, 'Nanocellulose as a promising substrate for advanced sensors and their applications', *International Journal of Biological Macromolecules*, 2022.
[236] Y. Ba, J. Bao, R. Song, C. Zhu, and X. Zhang, 'Printing Paper-Like Piezoelectric Energy Harvesters Based on Natural Cellulose Nanofibrils', in *2019 20th International Conference on Solid-State Sensors, Actuators and Microsystems & Eurosensors XXXIII (TRANSDUCERS & EUROSENSORS XXXIII)*, IEEE, 2019, pp. 1451–1454.
[237] H. P. Phan, T. P. Vuong, P. Benech, P. Xavier, P. Borel, and A. Delattre, 'Novel ultra-wideband "robe" antenna on high-loss paper substrate', in *2017 IEEE International Symposium on Antennas and Propagation & USNC/URSI National Radio Science Meeting*, IEEE, 2017, pp. 319–320.
[238] E. Vandelle, T.-P. Vuong, G. Ardila, S. Hemour, and K. Wu, 'Miniaturized antenna on a paper substrate', in *2019 49th European Microwave Conference (EuMC)*, IEEE, 2019, pp. 73–76.
[239] 'Standard Test Methods for Rating Adhesion by Tape Test'. https://www.astm.org/d3359-22.html (accessed Jan. 19, 2023).
[240] N. Sharma, N. M. Nair, G. Nagasarvari, D. Ray, and P. Swaminathan, 'A review of silver nanowire-based composites for flexible electronic applications', *Flexible and Printed Electronics*, 2022.
[241] L. Mo *et al.*, 'Silver nanoparticles based ink with moderate sintering in flexible and printed electronics', *International journal of molecular sciences*, vol. 20, no. 9, p. 2124, 2019.
[242] M. Hubmann *et al.*, 'Process Optimization of Injection Overmolding Structural Electronics with Regard to Film Distortion', *Polymers*, vol. 14, no. 23, p. 5060, 2022.
[243] R. B. Simorangkir *et al.*, 'Screen printed epidermal antenna for IoT health monitoring', in *2021 IEEE Asia-Pacific Microwave Conference (APMC)*, IEEE, 2022, pp. 395–397.
[244] 'Pearlthane-CLEAR15N80_exp1.pdf'. Accessed: Jan. 24, 2023. [Online]. Available: https://www.lubrizol.com/-/media/Lubrizol/Engineered-Polymers/Documents/Engineered-Polymer-TDS/Pearlthane-CLEAR15N80_exp1.pdf
[245] 'Pearlthane-Clear-15N85.pdf'. Accessed: Jan. 25, 2023. [Online]. Available: https://www.lubrizol.com/-/media/Lubrizol/Engineered-Polymers/Documents/Engineered-Polymer-TDS/Pearlthane-Clear-15N85.pdf

[246] ‘ESTANE_ECO_12T80E.pdf’. Accessed: Jan. 24, 2023. [Online]. Available: https://www.lubrizol.com/-/media/Lubrizol/Engineered-Polymers/Documents/Engineered-Polymer-TDS/ESTANE_ECO_12T80E.pdf
[247] ‘Estane-ZHF_95AT3.pdf’. Accessed: Jan. 24, 2023. [Online]. Available: https://www.lubrizol.com/-/media/Lubrizol/Engineered-Polymers/Documents/Engineered-Polymer-TDS/Estane-ZHF_95AT3.pdf
[248] ‘elg-410s_04012016.pdf’. Accessed: Jan. 24, 2023. [Online]. Available: http://www.norcote.com/uploads/7/5/4/4/75449567/elg-410s_04012016.pdf
[249] O. A. T. Dias, S. Konar, A. L. Leão, W. Yang, J. Tjong, and M. Sain, ‘Current state of applications of nanocellulose in flexible energy and electronic devices’, *Frontiers in Chemistry*, vol. 8, p. 420, 2020.
[250] E. Vandelle *et al.*, ‘High gain isotropic rectenna’, in *2017 IEEE Wireless Power Transfer Conference (WPTC)*, IEEE, 2017, pp. 1–4.
[251] X. Qi, Z. Xu, and H. Li, ‘High-Efficiency 2-D Multibeam Rectenna Based on Gain Enhanced Patch Array’, *IEEE Antennas and Wireless Propagation Letters*, vol. 21, no. 12, Art. no. 12, 2022.
[252] A. C. C. Chun, H. Ramiah, and S. Mekhilef, ‘Wide power dynamic range CMOS RF-DC rectifier for RF energy harvesting system: A review’, *IEEE Access*, 2022.
[253] S. M. Noghabaei, R. L. Radin, Y. Savaria, and M. Sawan, ‘A high-sensitivity wide input-power-range ultra-low-power RF energy harvester for IoT applications’, *IEEE Transactions on Circuits and Systems I: Regular Papers*, vol. 69, no. 1, pp. 440–451, 2021.
[254] L. F. Rahman, M. Marufuzzaman, L. Alam, and M. B. Mokhtar, ‘Design topologies of a CMOS charge pump circuit for low power applications’, *Electronics*, vol. 10, no. 6, p. 676, 2021.
[255] S. Abeywickrama, R. Zhang, and C. Yuen, ‘Refined nonlinear rectenna modeling and optimal waveform design for multi-user multi-antenna wireless power transfer’, *IEEE Journal of Selected Topics in Signal Processing*, vol. 15, no. 5, pp. 1198–1210, 2021.
[256] B. Clerckx and E. Bayguzina, ‘Waveform design for wireless power transfer’, *IEEE Transactions on Signal Processing*, vol. 64, no. 23, pp. 6313–6328, 2016.
[257] A. Collado and A. Georgiadis, ‘Optimal waveforms for efficient wireless power transmission’, *IEEE microwave and wireless components letters*, vol. 24, no. 5, pp. 354–356, 2014.
[258] A. Collado and A. Georgiadis, ‘Improving wireless power transmission efficiency using chaotic waveforms’, in *2012 IEEE/MTT-S International Microwave Symposium Digest*, IEEE, 2012, pp. 1–3.
[259] H. S. Vu, N. Nguyen, N. Ha-Van, C. Seo, and M. T. Le, ‘Multiband ambient RF energy harvesting for autonomous IoT devices’, *IEEE Microwave and Wireless Components Letters*, vol. 30, no. 12, pp. 1189–1192, 2020.
[260] C. Song, P. Lu, and S. Shen, ‘Highly efficient omnidirectional integrated multiband wireless energy harvesters for compact sensor nodes of Internet-of-Things’, *IEEE Transactions on Industrial Electronics*, vol. 68, no. 9, pp. 8128–8140, 2020.
[261] ‘Kapton® Summary of Properties’.
[262] ‘datasheet-ptfe-virgin-uk.pdf’. Accessed: Apr. 11, 2023. [Online]. Available: https://www.polyfluor.nl/assets/files/datasheet-ptfe-virgin-uk.pdf
[263] ‘ST506-Datasheet.pdf’. Accessed: Apr. 11, 2023. [Online]. Available: https://usa.dupontteijinfilms.com/wp-content/uploads/2017/01/ST506-Datasheet.pdf
[264] A. A. Bakar *et al.*, ‘Polydimethylsiloxane as a Potential Antenna Substrate.’, *Acta Physica Polonica, A.*, vol. 135, no. 5, Art. no. 5, 2019.

[265] I. Marasco *et al.*, 'A compact evolved antenna for 5G communications', *Scientific reports*, vol. 12, no. 1, Art. no. 1, 2022.
[266] C. Beisteiner and B. G. Zagar, 'Dielectric permittivity measurement of paper substrates using commercial inkjet printers', *Procedia Engineering*, vol. 168, pp. 995–998, 2016.

List of achievements

Publications

National conference papers

[1] G. Loubet, A. Sidibe, A. Takacs, and D. Dragomirescu, “Réseau de capteurs sans fil et sans batterie télé-alimentés par transfert de puissance électromagnétique rayonnée destiné au suivi de l’état de santé structurelle des bétons armés,” 22ème Journées Nationales Microondes (JNM 2022), Jun 2022.

[2] G. Loubet, A. Sidibe, A. Takacs, and D. Dragomirescu, “Réseau de capteurs sans fil et sans batterie télé-alimentés par transfert d’énergie électromagnétique radiative,” Journées Scientifiques URSI France NANO, MESO, MICRO: Sciences et Innovations pour la radio et la photonique 2022.

International conference papers

[3] A. Sidibe, A. Takacs, A. Okba, and H. Aubert, “Design and characterization of a compact rectenna for structural health monitoring applications,” in 2019 IEEE International Symposium on Antennas and Propagation and USNC-URSI Radio Science Meeting, 2019, pp. 1803–1804.

[4] A. Sidibe, A. Takacs, A. Okba, and G. Loubet, “An Improved Rectenna Design for Battery-free Wireless Sensors and Structural Health Monitoring,” in 2019 IEEE Wireless Power Transfer Conference (WPTC), 2019, pp. 440–445.

[5] A. Sidibe, A. Takacs, B. Franciscatto, and J. Mennekens, “Design and Characterization of Differential Rectifier on Flexible Substrate for WPT/IOT Applications,” in 2019 SBMO/IEEE MTT-S International Microwave and Optoelectronics Conference (IMOC), 2019, pp. 1–3.

[6] A. Sidibe, G. Loubet, A. Takacs, and D. Dragomirescu, “Design and Characterization of Compact Antennas for Wireless Sensing Applications,” in 2020 International Workshop on Antenna Technology (iWAT), 2020, pp. 1–4.

[7] A. Sidibe, A. Takacs, G. Loubet, and D. Dragomirescu, “Ultra-compact and high-efficiency rectenna for wireless sensing applications in concrete structure,” in 2020 IEEE/MTT-S International Microwave Symposium (IMS), 2020, pp. 988–991.

[8] A. Sidibe and A. Takacs, “A Miniature and High-Efficiency Rectenna in ISM 868 MHz Frequency Band,” in 2020 IEEE International Symposium on Antennas and Propagation and North American Radio Science Meeting, 2020, pp. 1509–1510.

[9] A. Sidibe, G. Loubet, A. Takacs, and D. Dragomirescu, “Energy Harvesting for Battery-Free Wireless Sensors Network Embedded in a Reinforced Concrete Beam,” in 2020 23rd European Microwave Conference (EuMC), 2021, pp. 702–705.

[10] A. Sidibe and A. Takacs, “Compact 3D Rectenna for Low-Power Wireless Transmission,” in 2021 XXXIVth General Assembly and Scientific Symposium of the International Union of Radio Science (URSI GASS), 2021, pp. 1–4.

[11] G. Loubet, A. Sidibe, A. Takacs, J.-P. Balayssac, and D. Dragomirescu, “Battery-free Structural Health Monitoring System for Concrete Structures,” in 13^{h} International Workshop on Structural Health Monitoring (IWSHM), 2022.

[12] G. Loubet, A. Sidibe, A. Takacs, and D. Dragomirescu, “Battery-free Bluetooth Low Energy Sensing Nodes for Structural Health Monitoring of Concretes,” in 13th International Workshop on Structural Health Monitoring (IWSHM), 2022.

[13] A. Sidibe, A. Takacs, D. Dragomirescu, S. Charlot, and J. Mennekens, “A Novel Polyimide Flexible Antenna Design for S-Band Applications,” in 2022 16th European Conference on Antennas and Propagation (EuCAP), 2022, pp. 1–5.

[14] L. López-Mir et al., “Towards In-mould Antennas for Geolocation Tags,” in 2022 IEEE International Conference on Flexible and Printable Sensors and Systems (FLEPS), 2022, pp. 1–4.

[15] A. Sidibe, M. A. Kassem, A. Takacs, J. Mennekens, and J. Dachy, “Autonomous and Battery-Free Wireless Tag combining UWB and BLE Technology,” in 2022 Wireless Power Week (WPW), 2022, pp. 207–212.

[16] G. Loubet, J.-P. Balayssac, A. Sidibe, D. Dragomirescu, and A. Takacs, “Battery-free, Wirelessly Powered and Controlled Concrete Resistivity Sensing Node,” in 2022 Wireless Power Week (WPW), 2022, pp. 547–552.

[17] A. Sidibe, L. López-Mir, B. Dhuiège, G. Depres, A. Takacs and J. Mennekens, “A Thin Paper UHF Antenna on Nanocellulose Based Substrate for Battery-Free Geolocation Tags,” in 2022 IEEE International Symposium on Antennas and Propagation and North American Radio Science Meeting, 2022

[18] A. Sidibe, A. Takacs, D. Dragomirecu, S. Charlot, “A Dual-Band and Flexible CPW-Fed Antenna for RF Energy Harvesting Applications,” in 2023 17th European Conference on Antennas and Propagation (EuCAP), 2023.

[19] A. Sidibe, A. Takacs, T. Eddine Djidjekh, “A Compact Triple-Band Rectifier and Dual-Band Rectenna for IoT Applications,” in 2023 Wireless Power Technology Conference and Expo (WPTCE) 2023.

[20] A. Sidibe, A. Takacs, D. Dragomirecu, S. Charlot, “Flexible Printed Rectenna Based on a 2.45 GHz CPW Rectifier for Energy Harvesting Applications,” in 2023 26th European Microwave Conference (EuMC), 2023 (Accepted).

Journal papers

[21] A. Sidibe, G. Loubet, A. Takacs, G. Ferré, and A. Ghiotto, “Miniature drone antenna design for the detection of airliners,” *Int. J. Microw. Wirel. Technol.*, vol. 13, no. 1, pp. 21–27, 2021

[22] A. Sidibe, A. Takacs, G. Loubet, and D. Dragomirescu, “Compact Antenna in 3D Configuration for Rectenna Wireless Power Transmission Applications,” Sensors, vol. 21, no. 9, p. 3193, 2021.

[23] A. Sidibe, G. Loubet, A. Takacs, and D. Dragomirescu, “A Multifunctional Battery-Free Bluetooth Low Energy Wireless Sensor Node Remotely Powered by Electromagnetic Wireless Power Transfer in Far-Field,” Sensors, vol. 22, no. 11, p. 4054, 2022.

Awards

[24] Winner of antenna design competition at the 21st edition of the JNM (Journées Nationales Micro-ondes), IEEE MTT / AP France / Rogers Corporation · May 2019.